An Integrated Approach to Expansion Deflection Nozzle Analysis

by

Neil Vernon Taylor

A dissertation submitted to the University of Bristol in accordance with the requirements of the degree of Doctor of Philosophy in the Department of Aerospace, September 2002

58920 words

ORIGINAL COPY TIGHTLY BOUND

Abstract

Expansion Deflection (ED) nozzles have long been considered as an alternative to conventional bell and conical designs. The ED nozzle has two primary benefits over such nozzle configurations, being shorter, and with the potential for altitude compensation. However, the difficulties involved with modelling the complex flow interactions within the nozzle type have thus far prevented the creation of a reliable method for its design and analysis.

The work presented within this dissertation makes use of a combination of several different approaches to flow solution to provide a more complete analysis than previously achieved. The primary advance is the use of a CFD scheme to analyse the transonic throat region, the results of which are used as input to a Method of Characteristics based algorithm for the solution of the inviscid supersonic flow-field. This method is both efficient, and allows contour optimisation through the calculus of variations. The viscous flow region is treated in a partially or fully empirical manner, depending upon ambient pressure.

The results of this analysis reveal several previously unidentified flow-field behaviours and design parameter interactions. Careful selection of the variables used to define the throat region is shown to be of considerable importance, as they effect not just the thrust produced, but also whether a real flow through such a nozzle may exist. Secondly, the high probability of shock wave formation and interaction with the nozzle wall within length optimised ED nozzles is demonstrated. This has consequences for both the design and analysis of the ED nozzle.

Overall, a framework is established which allows the flow behaviour and performance characteristics of the nozzle type to be estimated in greater detail than previously possible. The performance increments demonstrated over conventional bell nozzles include an approximately 25 to 50 percent length reduction for nozzles designed for solely high altitude operation, and a similar reduction in length plus a noticeable increase in low altitude thrust for trans-atmospheric nozzles. However, before application of the ED nozzle concept to a real system becomes possible, several areas of uncertainty must be addressed, and these are highlighted at the end of this dissertation.

Acknowledgements

I would like to thank Mr. C. M. Hempsell of the Department of Aerospace Engineering for his time and effort in the supervision of this work, Drs Allen and Jones for their assistance in matters relating to CFD flow calculations, and Mr Alan Bond and associates at Reaction Engines Ltd. for their interest and advice. The financial assistance of the Engineering and Physics Research Council has also been much appreciated. Finally, special thanks must go to my friends and colleagues for providing entertaining diversions when required, and of course most of all to my parents for their support and understanding.

Declaration

The work in this dissertation was carried out in the Department of Aerospace Engineering at the University of Bristol. The work is original except where indicated by special reference in the text and no part of the dissertation has been submitted for any other degree. Any views expressed in the dissertation are those of the author and in no way represent those of the University of Bristol. The dissertation has not been presented to any other University for examination either in the United Kingdom or overseas.

N.V. Taylor, September 2002

Contents

List of Figures

List of Tables

Notation

a	Local speed of sound
a^*	The critical velocity.
A	Local nozzle cross secitonal area.
A_E	Nozzle exit cross sectional area.
A^*	Critical nozzle area.
A_b	Base area of pintle.
A_t	Throat area.
B	Shock entropy function.
c_{df}	Forebody drag coefficient.
c_p	Specific heat capacity at constant pressure.
c_{pb}	Base pressure coefficient.
C	Crocco number.
C_F	Thrust coefficient.
C_F^∞	Thrust coefficient in a vacuum.
C_{Fc}	Thrust coefficient due to input characteristic.
C_{Fw}	Thrust coefficient due to wall pressure.
C_{Fb}	Thrust coefficient due to base pressure.
CFL	Courant Friedrichs Lewy number.
d	Step height.
$d_{i+\frac{1}{2}}$	Downstream axial damping term.
$d_{i-\frac{1}{2}}$	Upstream axial damping term.
D	Drag.
	Body diameter.
$\underline{D}$	Dissipaton vector.
e_0	Total energy.
f_k	Control surface for entropy calculation.
f_N	Forcing function.
$f_{0,2,4}$	functions in an infinite power series.
$f_{1,2,3}$	functions input to the calculus of variations method.
F	Largest cross sectional area of body.

F_H	Base area.
$F1, F2$	Common compatablilty functions for the MoC.
$F1i, F2i$	Variable compatability functions for the MoC.
$\underline{F}$	x-direction flux vector.
G_t	Minimum separation of nozzle walls.
$\underline{G}$	y-direction flux vector.
h	Radial distance of nozzle wall from centreline.
	Cross sectional area of pintle used in drag calculations.
h_0	Total enthalpy.
$\underline{h}$	Axisymmetric remainder vector.
H	Shear layer height.
H^*	Height of shock formation.
H_B	Boat tail shear layer similarity constant.
$\underline{H}$	Distributed axisymmetric remainder vector.
i	Cell index in stramwise direction.
	RRC index.
j	Cell index in the cross flow direction.
	LRC index.
k	A scalar.
	Cell vertex number.
K^κ	Second order damping constant.
K^ξ	Fourth order damping constant.
K_1	First contour optimisation constant.
	Two-dimensional shear layer function.
K_2	Second contour optimisation constants.
K_{1R}	Axisymmetric shear layer function.
LRC	Left running characteristic.
$\dot{m}$	Mass flow rate.
M	Mach number.
M_∞	Upstream infinity Mach number.
MoC	Method of Characteristics.
n	Total number of cells in CFD mesh.
nb_1	Number of points before geometric minima, ED nozzles.
nb_2	Number of points after geometric minima, ED nozzles.
n_i	number of cells in i direction.
n_j	number of cells in j direction.
n_w	Number of points on contour.
N	Grid level in multigrid scheme.

N	Recompression factor.
P	Pressure.
P_0	Total pressue.
P_a	Atmospheric pressure.
P_b	Base pressure.
P_c	Chamber pressure.
P_r	Pressure at reattachement.
P_{rt}	Turbulent Prandtle number.
P_W	Sum of forces acting on pintle walls.
P_4	Pressure behind shock in closed wake mode.
P_∞	Upstream infinity pressure.
$\underline{P}$	Flux operator.
r	Recovery factor.
R	Universal gas constant.
R'	Empirical compressible divergence function.
R_c	Radius of pre throat contraction, ED nozzles.
R_p^-	Pre throat pintle wall radius.
R_p^+	Post throat pintle wall radius.
$R_p^=$	Pre and post throat pintle wall radius.
R_t	Throat radius (axisymmetric), half height (two dimensional).
R_w^-	Pre throat outer wall radius;
R_w^+	Post throat outer wall radius;
$R_w^=$	Pre and post throat outer wall radius;
$\underline{R}$	Residual vector.
Re	Mach number residual of CFD scheme.
RRC	Right running characteristic.
$\tilde{s}$	Specifc entropy.
$\tilde{s}_\infty$	Specifc entropy at upstream infinity.
S	Total entropy.
S_c	Separation criterion.
$\underline{S}$	Source vector.
t	Time.
Δt^*	Time step for CFL of unity.
T	Temperature.
T_0	Total temperature.
T_c	Chamber temperature .
T_t	Flow temperature at M=1.
T_∞	Upstream infinity temperature.

u	Velocity component in x-direction.
u_t	Axial velocity component at nozzle throat.
$\tilde{u}$	non dimensional velocity w.r.t a^* in x-direction.
$\hat{u}$	Small perturbation velocity, x-direction.
U_∞	Upstream infinity parallel flow velocity.
$\underline{U}$	Vector of conserved quantities.
v	Velocity component in y direction.
$\tilde{v}$	non dimensional velocity w.r.t a^* in y-direction.
$\hat{v}$	Small perturbation velocity, y-direction.
$\underline{V}$	Velocity vector.
V_n	Local velocity vector normal to surface.
W	Flux velocity.
x	Cartesian coordinate (axial).
x_0	Intersection of sonic and centre lines.
x_k	length of final cell in onlflow region.
$\bar{x}$	constant used in mesh spacing.
x_c	x coordinate of origin of contraction.
y	Cartesian coordinate (lateral 2D, radial axisymmetric).
y_d	Radial step for translating CFD mesh.
y_t	Average radius of nozzle throat.
Y	Elemental area in thrust calculations.
z	Steretched longtitudional coordinate
α	Constant defining velocity profile along nozzle centreline.
	Cone half angle
β	Shock angle.
	Ratio of total temperature in jet to still air region.
γ	Ratio of specific heats.
Γ	Ratio of minimum wake radius to pintle base radius.
δ	Shock deflection angle.
	Boundary layer thickness.
δ_T	Thermal boundary layer thickness.
ϵ	Nozzle expansion ratio, $\frac{A_E}{A_t}$.
	Dutton and Addy's expanspion parameter.
	Non dimensional perpendicular distance through shear layer.
φ	Stream function.
ϕ	Mixing layer non dimensional velocity profile.
ϕ_{n-1}	Halls throat flow function.
ϕ_L	Left running characterisic angle.

ϕ_R	Right running characterisic angle.
η	Dutton and Addy's expansion variable for small throats.
	Non dimensional distance through shear layer.
κ	Second order damping function.
$\lambda_{2,3}$	LaGrangian multipliers.
μ	Mach angle.
ν	Prandtle-Meyer function.
ϖ	Cell area.
ρ	Density.
ρ_0	Total density.
σ	Channapragada's compressable jet spread parameter.
	Scalar for converting G_t to R_t.
σ_{inc}	Incompressable jet spread parameter.
θ	Flow angle.
θ_e	Subtended angle at grid exit.
θ_i	Inflection angle.
θ_t	Nominal flow angle at throat.
ξ	Fourth order damping function.
ζ	Radial distance to local throat centreline.
ζ_t	Radial distance to geometrical throat centreline.
$\Delta\zeta$	Separation between nozzle walls.
Λ	Second difference of pressure.
Ω	Centre of curvature.

Chapter 1

Introduction

1.1 A Brief History of the Rocket Nozzle

The nozzle on a rocket motor performs the function of converting the randomly directed thermal energy released by the combustion process into a strongly directional, very high speed flow. The reaction to this momentum change effected on the propellant gas provides the thrust produced by the rocket, and hence the efficiency of the chosen nozzle design is of critical importance in determining the overall performance of the system.

Initially, the primary application of such motors was to artillery and bombardment weapon systems (although of course simple firework motors predate even this function). The perpetual need to compromise between performance and safety, reliability, and above all cost, meant that in general nozzle design was kept as simple as possible. For this reason, convergent only nozzles initially dominated [1], later followed by conical nozzles (e.g. Ref. 2), normally of a cone angle between 12 and 18 degrees. These offered adequate performance at minimal cost and complexity. It was not until the space age dawned, and vehicles capable of reaching orbit were seriously considered, that the performance demanded from rocket nozzles increased and conical designs were no longer sufficient. This need for greater efficiency lead to several new concepts being examined.

Foremost among these was the contoured, length optimised nozzle devised by Rao [3], [4]. Although shorter and lighter for a given thrust, this genre of nozzle shares many similarities with the more orthodox conical type. The throat region in particular is practically identical, allowing commonality of combustion chamber design. However, due to careful shaping of the nozzle wall contour, similar performance is achieved with a shorter nozzle, and hence a reduced mass. These two nozzle types have been used on virtually all previous and current rocket propulsion systems, the conical nozzle dominating for lower performance applications (such as small sounding rockets and missiles), and the length optimised contour

where higher performance is required, particularly in the various stages of launch vehicle systems. Indeed so common is the length optimised design in space applications that the term 'bell nozzle', originally encompassing any nozzle with curved walls (and hence a bell like appearance) has become synonymous with the type.

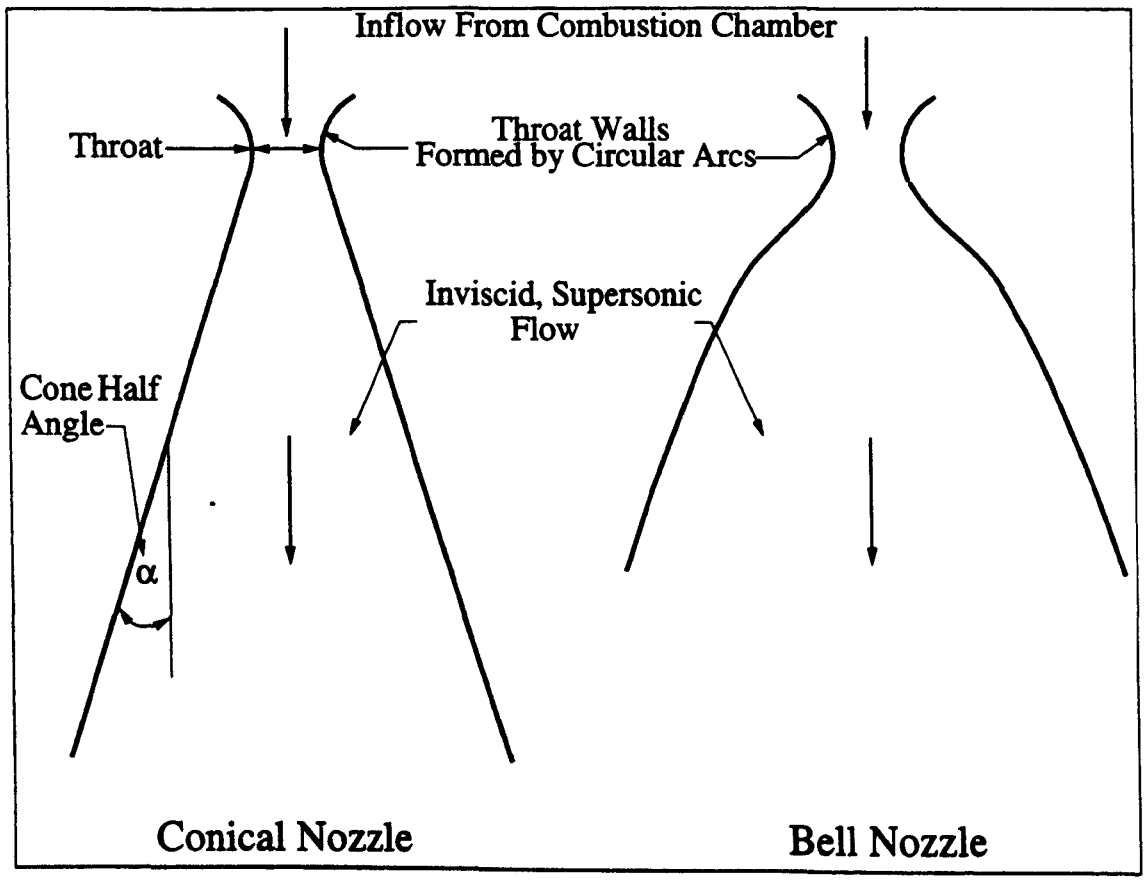

Figure 1.1: *Conventional Nozzle Types*

Fig. 1.1 shows these two conventional nozzle types in schematic form. The gases produced by the combustion process are accelerated through a contraction, until reaching the nozzle throat (defined as the minimum cross sectional area perpendicular to the nominal flow direction). After here achieving sonic speed, the flow is further accelerated by the diverging nozzle section. Although the flow within this region possesses viscosity, for practical nozzle sizes the magnitudes of the forces created by viscous interactions are sufficiently small to be considered negligible outside of a thin boundary layer attached to the nozzle walls. Therefore the majority of the flow may be treated as an inviscid fluid, simplifying analysis. Conventional nozzles are therefore generally designed assuming an entirely inviscid flow, a correction then being applied to account for boundary layer thickness [5].

Although these two designs account for nearly all nozzles current and historical, various other concepts have been devised and investigated. One such design is the Expansion Deflection (ED) nozzle, a member of a group of nozzle concepts collectively known as 'advanced' designs. The benefits theoretically provided by an ED nozzle include a further reduction in length, and a significant amount of altitude compensation (detailed in Sec. 1.2.2). However,

a certain degree of uncertainty and technical risk is associated with the type, primarily due to the flow processes which occur within an ED nozzle. These involve not only supersonic inviscid flow, but also regions of viscous mixing and recirculating flows, and hence are considerably more complex than equivalent conventional nozzle designs. The aim of the work described within this thesis is to reduce the uncertainty surrounding the ED nozzle concept, and hence increase the likelihood of its application to current and future space vehicles.

1.2 The Expansion Deflection (ED) Nozzle

1.2.1 Overview

The structure and nomenclature of an ED nozzle is shown in Fig. 1.2, along with the various regions of a typical (idealised) flow-field. The primary flow of gas follows a very similar pattern to that in a conventional nozzle. On exiting the combustion chamber, it is accelerated to supersonic speeds through the nozzle throat, which in an ED nozzle is displaced from, and at an angle to, the nozzle centreline. Throughout this process, the viscous forces present are sufficiently negligible for the flow to be treated as inviscid, outside of a thin boundary layer attached to the nozzle walls.

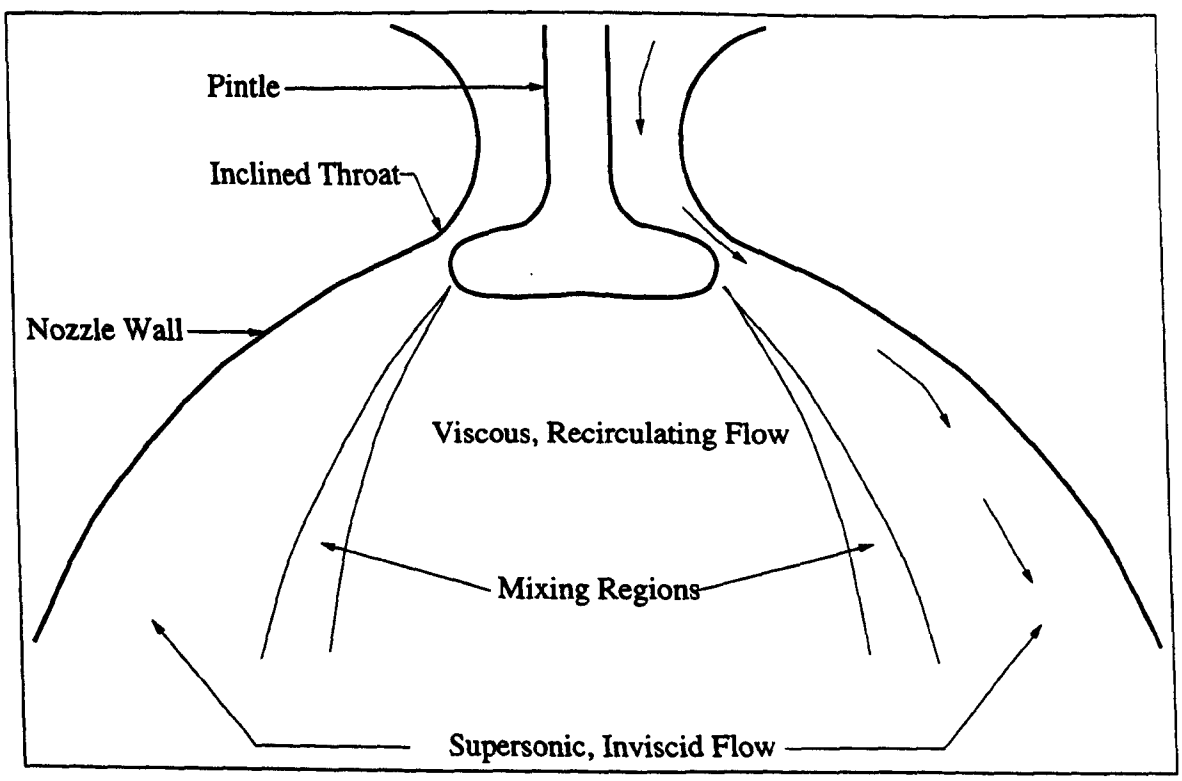

Figure 1.2: *ED Nozzle General Configuration*

The expansion of the inviscid flow takes place at the shoulder of the pintle, and the outer nozzle wall then causes compressive turning of the flow to provide thrust. As the expansion

takes place in a much shorter length than in a bell nozzle, the total length of the nozzle is greatly reduced (Rao, who devised a minimum length scheme for ED nozzles similar to his method for bell nozzles, claimed that the reduction could be as great as 50 percent [6]). This in turn should lead to an associated mass saving.

The separation point on the pintle creates a central portion of the flow which has a much lower velocity, and in which the effects of viscosity may no longer be ignored. Separating these two distinct flow regimes lies a mixing layer, generally assumed to be of negligible thickness. This mixing layer, however, provides an interface through which the pressure distribution within the viscous flow region may interact with the primary inviscid flow. If this central region is open to, and therefore effected by, the atmosphere, a mechanism is provided by which the flow may adapt to variations in ambient conditions. This process is known as altitude compensation.

1.2.2 Altitude Compensation

The exit area of a conventional nozzle is fixed by the physical structure. This means that if the chamber pressure is constant (usually a good approximation), a complete conversion of all the available random thermal energy into axially directed kinetic energy (ideal expansion) will only occur at a single ambient pressure. At any other, the flow will either over or underexpand, and if overexpansion is particularly severe, separation from the nozzle walls will occur. These four possible flow configurations are shown schematically in Fig. 1.3.

Underexpansion occurs at high altitude, where the ambient pressure is below that at which ideal expansion occurs. This leads to a small performance loss, as the thrust is partly comprised of random thermal energy. If the atmospheric pressure is above that associated with ideal expansion (i.e. at low altitudes), the flow overexpands, which causes a more significant performance loss and may lead to separation of the flow from the nozzle walls if the wall pressure is anywhere less than approximately 0.4 that of ambient (the Summerfield Criterion [7]).

Conical nozzles have a constant wall angle outside of the throat region, and separation has beneficial effects, allowing an amount of pressure recovery on sections of the nozzle walls that would otherwise experience pressures considerably below atmospheric. The wall angles of bell nozzles, however, vary with length and are much smaller near the exit plane. These factors allow the point of separation to move easily and unevenly in the axial direction under slight disturbances. This in turn may cause oscillations and vibrations of the primary flow, leading to side loads and possible structural failure. In general therefore, bell nozzles are designed so that they never operate overexpanded to such an extent that separation may occur. This places an effective maximum on the expansion ratio (the ratio of exit area to

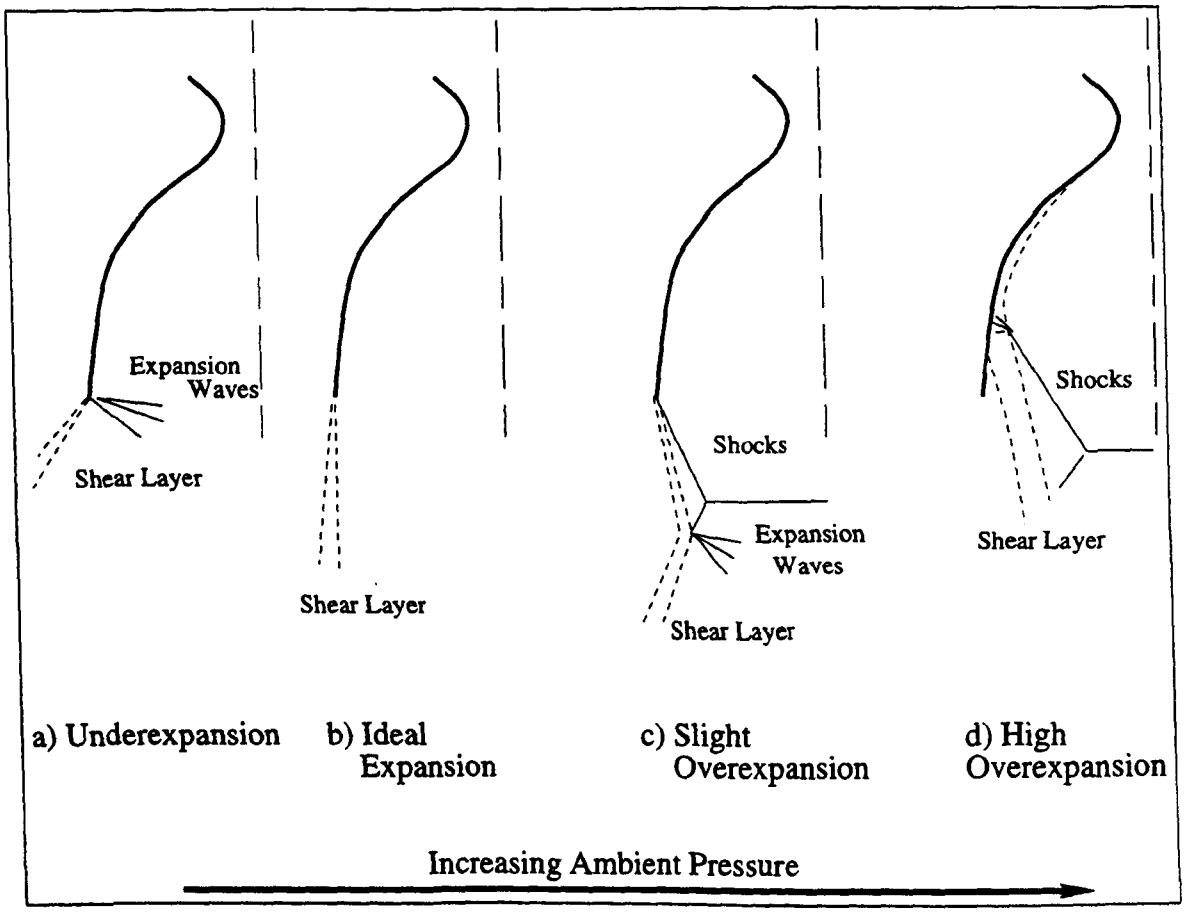

Figure 1.3: *Effect of Ambient Pressure on a Bell Nozzle Flow*

throat area) of a nozzle, determined by the ratio of chamber pressure to the highest ambient pressure in the operating range (i.e. sea level conditions for lower stages and Single Stage to Orbit (SSTO) vehicles). This in turn will result in a restriction on maximum vacuum performance, where large area ratios are beneficial.

For multiple stage vehicles, each stage may be designed to operate over a relatively narrow range of ambient pressures, reducing the risk of overexpansion and performance losses. However, for some vehicles (primarily most proposed SSTO's, but also some multiple stage vehicles like the Space Shuttle), the same propulsive unit operates over the entire trajectory from sea level to orbit. The atmospheric pressure at which perfect expansion occurs (and hence the expansion ratio) will be chosen so that the best compromise between high altitude (minimum underexpansion) and low altitude performance (minimum overexpansion), is achieved. Despite this, losses due to these flow conditions, coupled with the expansion ratio limit discussed above, may amount to 15 percent compared to a perfectly adapting nozzle [8]. If, however, the area ratio of the exit flow varies with altitude, the performance at pressure ratios other than design point improves.

An ED nozzle has two distinct modes of operation, as shown in Fig. 1.4. At low altitudes where the ambient pressure is high, the viscous wake region behind the pintle will be open to the atmosphere at the downstream boundary, as shown on the left of Fig. 1.4. This allows

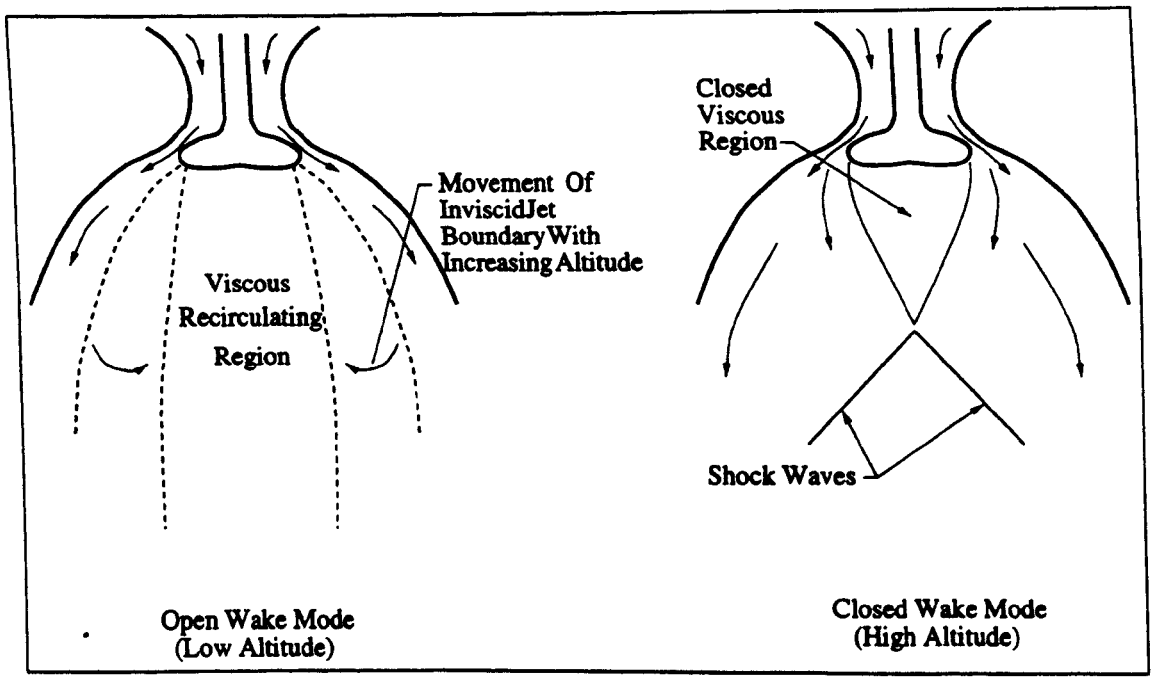

Figure 1.4: *Effect of Altitude on ED Nozzle Flow*

the ambient pressure to penetrate the nozzle flow-field, and act upon the inviscid flow. As a result, the supersonic flow containing the vast majority of the combustion products is forced into a thin layer against the outer nozzle walls, reducing its effective exit area. As altitude is gained the ambient pressure drops, causing the boundary of the viscous region to move in towards the centreline of the nozzle, and allowing the supersonic region to expand. This continuously varies the effective area ratio of the nozzle, ensuring that the expansion of the primary gas flow is always close to ideal.

Eventually, the inviscid jet boundary reaches the centreline of the nozzle, and the wake region becomes entirely enclosed within the outer supersonic flow (shown on the right hand side of Fig. 1.4). Once closed the region of recirculating fluid immediately behind the pintle is isolated from the atmosphere, and hence the pressure distributions along the pintle base and nozzle walls are no longer effected by reductions in ambient pressure. As this removes any further altitude compensating capability, the pressure ratio at which wake closure occurs is of some significance. Unfortunately, this process is complex and difficult to predict. It will be dependent upon many variables, including the throat angle, pintle and contour shape, and chamber pressure.

As separation occurs on the internal (pintle) wall where the curvature is much higher, it is more stable, and hence vibration and associated structural problems reduce. This removes the limit on the maximum expansion ratio of the nozzle, assuming that altitude compensation begins on the outer nozzle wall before the flow separates from it. Increasing the nozzle area ratio not only improves vacuum performance, but also raises the chamber to ambient pressure ratio at which the wake closes. This in turn will increase the range of altitudes at which the nozzle will compensate for atmospheric conditions for a given combustion cham-

ber design. The physical size of the nozzle will of course still be limited by other factors, such as allowable mass and aerodynamic drag.

1.2.3 Inherent Weaknesses

Ignoring for the present the complexity of analysis and design inherent in the ED concept, two further difficulties relating to the physics of the flow regime should be noted. The most significant relates to altitude compensation. The high speed gas surrounding the viscous flow 'pumps out' this region, reducing the pressure acting there. This produces a drag force on the pintle base during open wake operation, and reduces the pressures acting along the boundary between the viscous and inviscid flows (known as the free jet boundary) to below atmospheric. In effect, the nozzle will compensate to a higher altitude than that actually occurring, and this in turn will lead to a less than perfect altitude compensation. The severity of this effect is the subject of some debate, and is discussed in more detail in Ch. 4.

The unconventional throat configuration also increases the problem of cooling the nozzle, primarily due to the greater radius of the throat. The cross sectional area of the throat, A_t, is approximately

$$A_t = 2\pi y_t G_t \tag{1.1}$$

where G_t is the minimum separation between the inner and outer walls, and y_t is the average radial location of the throat. As the throat area will be linearly related to y_t, a greater radius requires a smaller G_t for the same throat area and mass flow. As a rough rule of thumb, the minimum gap between the nozzle walls is between 5 and 20 times smaller on an ED nozzle than that on an equivalent conventional type.

As it may be shown that the heat transfer at the throat is strongly related to the minimum gap between the walls and chamber pressure [9], this narrow throat may in effect limit the maximum chamber pressure allowable for a particular nozzle design. If this is the case, much of the advantage offered by altitude compensation compared to a conventional design with a higher chamber pressure may be lost [10]. This small throat gap will also increase the importance of manufacturing accuracy and tolerances, increasing the risk of asymmetric (and even oscillating) flow. However, as heat fluxes will depend to a significant degree upon the geometry and flow patterns of the throat region, precise estimates of the magnitude of this problem are difficult to make at the current time. Finally, it should be noted that there is some dispute as to whether the increase in total heat flux is due to the small gap, or the corresponding increase in surface area over which the boundary layer occurs. However, these two properties are directly related, so an increase in throat radius reduces the throat gap and increases the surface area, and hence the exact mechanism is unimportant.

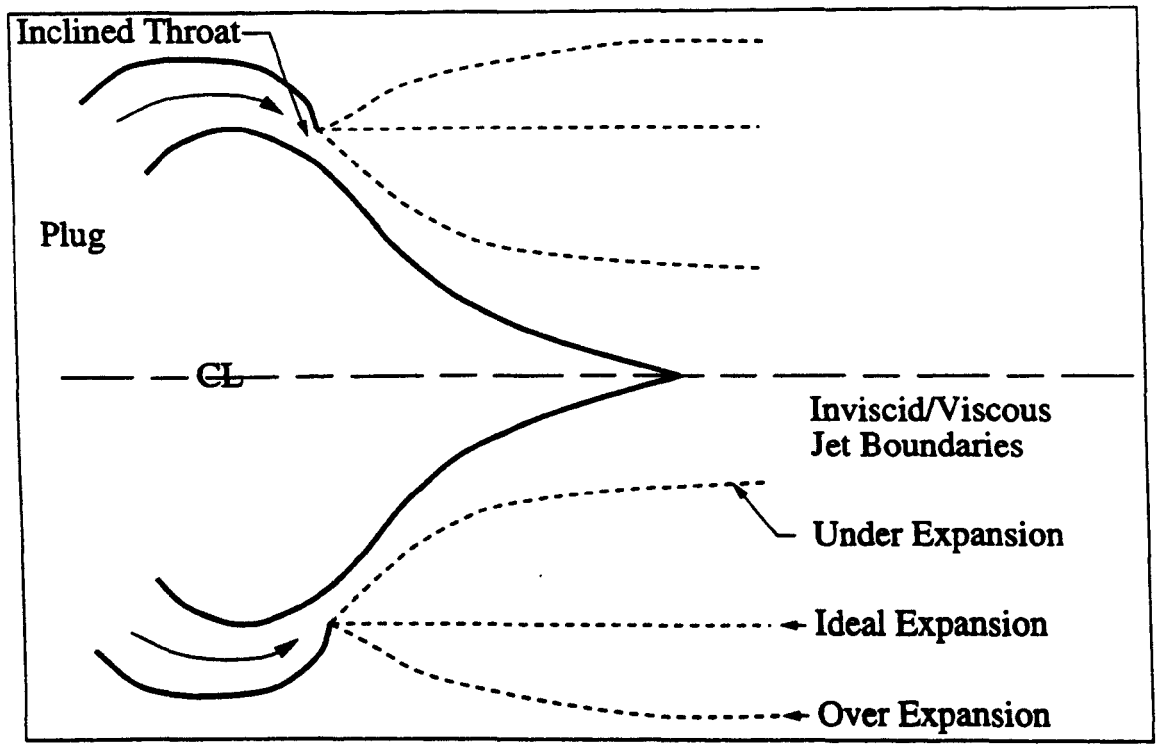

Figure 1.5: *The Plug Nozzle*

1.3 Comparison with other Advanced Nozzle Concepts

The ED nozzle is not the only unconventional nozzle type which potentially offers advantages of reduced length and/or altitude compensation. A brief summary of the alternative designs is therefore presented, particularly emphasising the relative advantages and disadvantages of the ED nozzle compared to the alternatives. Only a qualitative comparison is possible, however, as not only is the ED nozzle currently insufficiently understood to allow a more rigorous analysis, but the same is true for all other advanced nozzle concepts.

1.3.1 Plug and Aerospike Nozzles

The plug nozzle originated at approximately the same time as the ED, and is in many ways similar. In fact it is the most studied of any of the advanced nozzles (e.g. Refs. 11,12 and 13), and is often regarded to be superior in terms of both length reduction and altitude compensation. However, the reasons for this assumption are questionable, as shall be discussed in that which follows.

A generalised plug nozzle is shown in Fig. 1.5, and as may be seen it strongly resembles an ED. The principle difference between the two designs is that the atmospheric boundary on the plug nozzle is external to the inviscid flow, rather than internal as on an ED. This should provide an advantage for the plug, as the viscous region surrounds the high speed flow, and hence cannot be evacuated by it. This ensures that the boundary of the inviscid region will

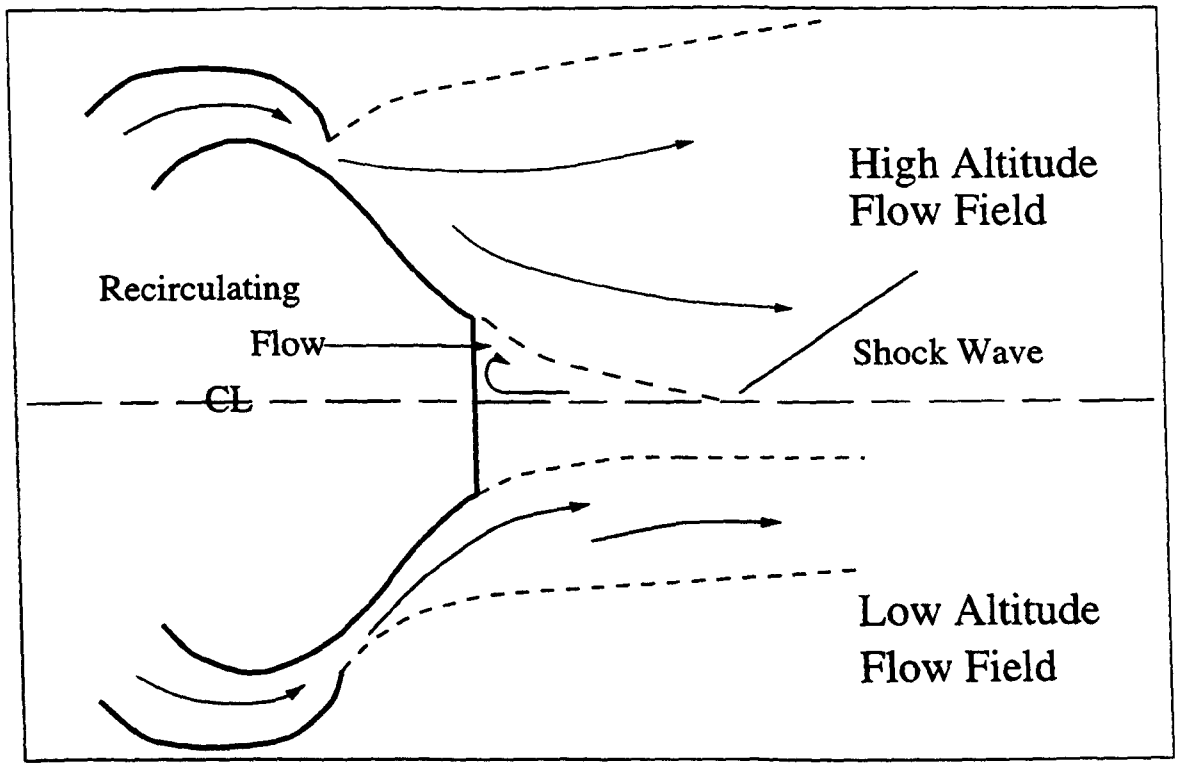

Figure 1.6: *The Truncated Plug (Aerospike) Nozzle*

be at atmospheric pressure, rather than slightly below.

Plug nozzle contours tend to belong to the class known as ideal contours, which ensure parallel flow at the nozzle exit, thus removing interference effects that would arise with the non zero radial velocity at the centreline resulting from length optimised contours. Whilst ideal contours reduce divergence losses, they are longer than the length optimised contour such as may be used with an equivalent ED nozzle. However, the length of the plug nozzle may be shortened to form a truncated plug (or aerospike) nozzle as shown in Fig. 1.6.

This design takes advantage of the fact that the extreme tail of the plug is close to the centreline, and thus this portion of the nozzle comprises only a relatively small part of the surface area and hence thrust produced. By removing this section, a considerable reduction in length (and more importantly mass) is achieved with only a small performance loss. This loss is reduced still further by the closure of the wake behind the base of the aerospike (much like that behind the pintle of an ED nozzle), trapping some viscous recirculating flow. As this region is sealed by the surrounding supersonic flow, the pressure will be invariant with ambient conditions, and hence at altitudes significantly above the wake closure a considerable thrust is produced.

Both these concepts (the aerospike in particular), appear to offer advantages not only over conical and bell nozzles, but also the ED concept. Whilst the plug nozzle would be of a greater length than an ED nozzle with the same throat angle and expansion ratio (due to the ideal contour necessary), the aerospike would be of similar length or even shorter. Further, the external pressure boundary should ensure more efficient altitude compensation,

and the base pressure exerted on the rear of the aerospike plug is likely to be higher than that on the rear of an ED pintle, due to the inward inclination of the flow at separation [14]. However, the plug and aerospike nozzle flow-fields are as complex as that of the ED, and hence have all the difficulties of analysis and design associated. Coupled to this, a more detailed examination of the plug nozzle concept reveals several problem areas.

The first of these is due to the fact that the radial location of the throat (y_t) on plug nozzles is much greater than that of an equivalent ED. For the same mass flow, the heat flux in the throat region is therefore considerably increased, as was discussed in Sec. 1.2.3. This large throat radius also impacts on the combustion chamber, requiring the use of annular designs. These are untried, and hence their efficiency is unknown. The burning surface will obviously be of a considerably different shape, the chamber walls being much closer together. As the surface of area these walls is much greater, the cooling requirements are also more severe. Whilst it is true that the ED nozzle combustion chamber would also require some modification of conventional designs due to the presence of the pintle, it would have a much greater degree of similarity, and therefore present a lesser risk.

The use of annular combustion chambers may be avoided by the clustered plug nozzle design, where a series of very small expansion ratio conventional bell nozzles form a ring around plug, replacing the throat and supplying the supersonic gas flow (e.g. as in Ref. 15). However this concept suffers from increased complexity in the exhaust flow-field (due to multiple nozzle flow interactions), and a reduction in overall combustion efficiency due to a loss of economy of scale.

The plug contour design also deviates more significantly from the inviscid flow contours derived in the design process, as the boundary layer grows very rapidly toward the tail of the nozzle due to flow convergence [16]. This means the boundary layer correction is more significant and hence of greater importance. However, accurate predictions of boundary layers on such doubly curved surfaces with pressure gradients are notoriously difficult to generate [5].

A second disadvantage of the plug concept is also indirectly related to the large throat radius. As is clear in Figs. 1.5 and 1.6, the nominal flow direction at the throat is inclined inwards, towards the nozzle centreline. To produce this effect, the flow leaving the combustion chamber must be brought to a greater radius than the throat, and then turned back in and accelerated towards the centreline. This requires a region of structure outside of the nominal nozzle exit area, and in atmospheric flight this will lead to a significant amount of base drag.

Fig. 1.7 demonstrates the difference in base area for plug and ED nozzles. The two nozzles shown are formed by the same two dimensional contour, the variation between type

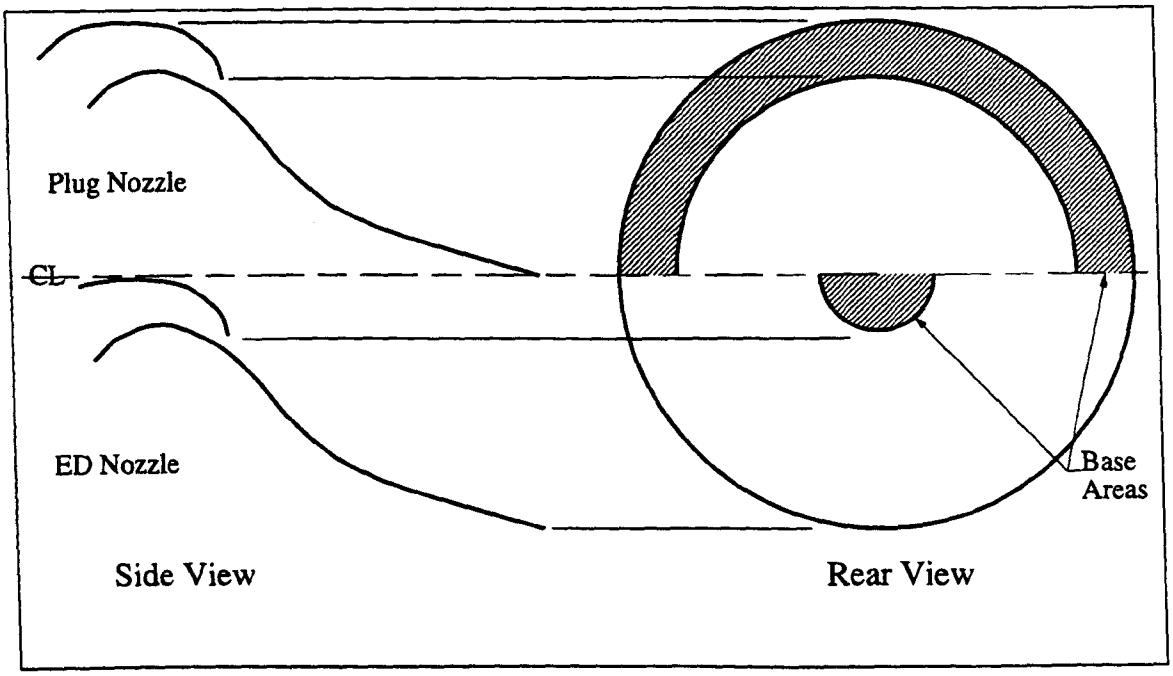

Figure 1.7: *Respective Base Areas of Equivalent Plug and ED Nozzles*

being created by the location of the axis of rotation. As may be seen, the base area of the ED nozzle is considerably smaller. This problem becomes more severe as the throat inclination is increased (required for larger expansion ratios), as the flow must be brought to an ever greater radius before the throat, to ensure a smooth profile in this region. Further, the clustered plug concept discussed previously will not reduce this problem, and may even exacerbate it as the combustion chambers and associated structure of all the small bell nozzles will lie outside the primary gas flow.

A final point to note is that the existence of this base drag will have implications for the altitude compensating capability of the plug nozzle. The presence of a base drag by definition implies that the pressure on this rearward face is less than atmospheric. This means that the initial expansion of the flow from the throat in low altitude flight will be into a region at below atmospheric pressure. In turn, this will result in the flow compensating to an apparently higher altitude than actually occurring, reducing the wall pressures and lessening the thrust relative to the still air case.

Whilst some cold flow tests suggest that losses due to this behaviour are confined to a narrow range of flight Mach numbers near unity [8], more recent work involving state of the art CFD schemes suggest that this effect is significant for all supersonic flight velocities [17]. As the freestream Mach number rises, the overexpansion of the rocket exhaust is increased, resulting in ever more severe thrust losses. In fact, in Ref. 17 it was found that for most supersonic flight conditions the performance loss was greater in magnitude than that due to the base drag discussed previously, and may have serious implications for the plug nozzle concept as a whole.

This behaviour is in some ways similar to the anticipated evacuating effect of the supersonic primary flow on the central viscous core within the ED nozzle. However, the fact that little impact on wall pressures was found for subsonic freestream conditions suggests that this effect may be minimal, as the wake behind the ED pintle will be subsonic. The freestream Mach number itself will have little or no effect on the wall pressures on an ED, as the primary inviscid flow only interacts with the freestream beyond the exit plane of the nozzle, and the viscous region within the nozzle interfaces with the atmosphere a significant distance downstream of this. Thus it is entirely possible that whilst in dead air conditions the compensating capability of the ED nozzle is less than that of the plug, for the majority of flight conditions it may well prove superior, even substantially so.

1.3.2 Linear Aerospike

The 'linear aerospike' (actually this is the planar, or two dimensional variant of the nozzle type) was developed in an attempt to avoid the difficulties associated with the plug nozzle, discussed previously. Primarily, the dependence of throat area on radial distance is removed, and hence the throat gap required for a constant mass flow is unaffected by the throat location. The base area produced by the turning of the subsonic flow is also rendered independent of radial distance, and hence will lie somewhere between the base area of an axisymmetric plug and an ED. Whilst the ingress of the atmospheric pressure at either end of the plug will effect the altitude compensating capability of the nozzle, this may be eliminated by side walls.

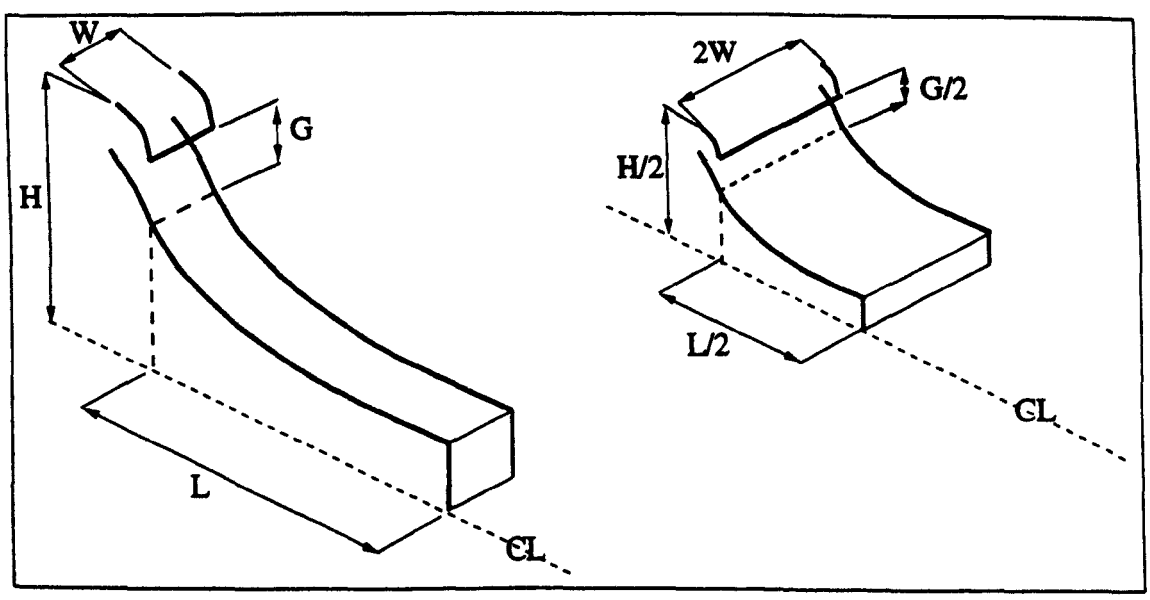

Figure 1.8: *Effect on a Linear Aerospike of Throat Geometry*

The length of any planar nozzle will always be greater than the equivalent thrust axisymmetric counterpart for a given thrust if the throat width is equal to the radius of the axisymmetric nozzle. However, in a linear nozzle the length and total height will be determined by the throat gap alone, independent of throat width. Therefore these dimensions will

be reduced if a rectangular throat section is used (see Fig. 1.8). Unfortunately, this in turn reduces the throat gap, and hence increases the heat flux. This has lead some to conclude that no advantage is gained by turning to the linear aerospike with respect to the problems associated with cooling the throat region [10].

Further to this, the increased width of the nozzle will increase the mass, and it is likely that the mass of a linear aerospike will be greater than an equivalent thrust axisymmetric plug or ED (note that linear versions of both conical and bell nozzles are possible, but never used). Finally the performance loss caused by overexpansion due to freestream Mach number noted at the end of the previous section will also effect the planar variant in the same manner as the axisymmetric.

Despite these apparent drawbacks, research into the linear aerospike continues [18], and it nearly became the first advanced nozzle type to fly, as it was the intended nozzle for the X33. It has also been proposed as the nozzle of choice for other aerospace programmes [19]. Therefore, throughout this thesis both linear and axisymmetric nozzles will be examined, partially because they generally represent simpler flow cases, and partly because a comparison with the linear aerospike nozzle is required. It should be noted that the ED nozzle also has a linear variant, which would be very similar to the linear aerospike. The ED nozzle would suffer from losses associated with the internal pressure compensating flow surface, but could gain from the fact that the heavy throat or clustered bell portion of the propulsive unit would be nearer the centreline of any vehicle to which it was integrated.

1.3.3 Controlled Flow Separation Nozzles

This nozzle category includes dual-bell nozzles, nozzles with both mechanically released and erodible inserts, nozzles with extendible skirts, and nozzles with boundary layer trips (Fig. 1.9). These nozzles achieve a measure of altitude compensation by behaving as a small expansion ratio nozzle at low altitude, and a larger one at higher altitudes. The difference between the nozzle types is created by the mechanism by which the transition between the two modes is achieved.

In a dual-bell nozzle, the flow is forced to separate in a controlled manner at low altitudes from an inflection in the contour. At higher altitudes, the flow expands sufficiently to negotiate the inflection [20], and the overall expansion ratio of the nozzle is increased. However, the transition between these modes has been found to be unstable, and hence create large side loads during transition [21].

Nozzles with releasable inserts incorporate an entirely separate nozzle for low altitude flight within the primary, whilst those with extendible skirts extend the nozzle contour at

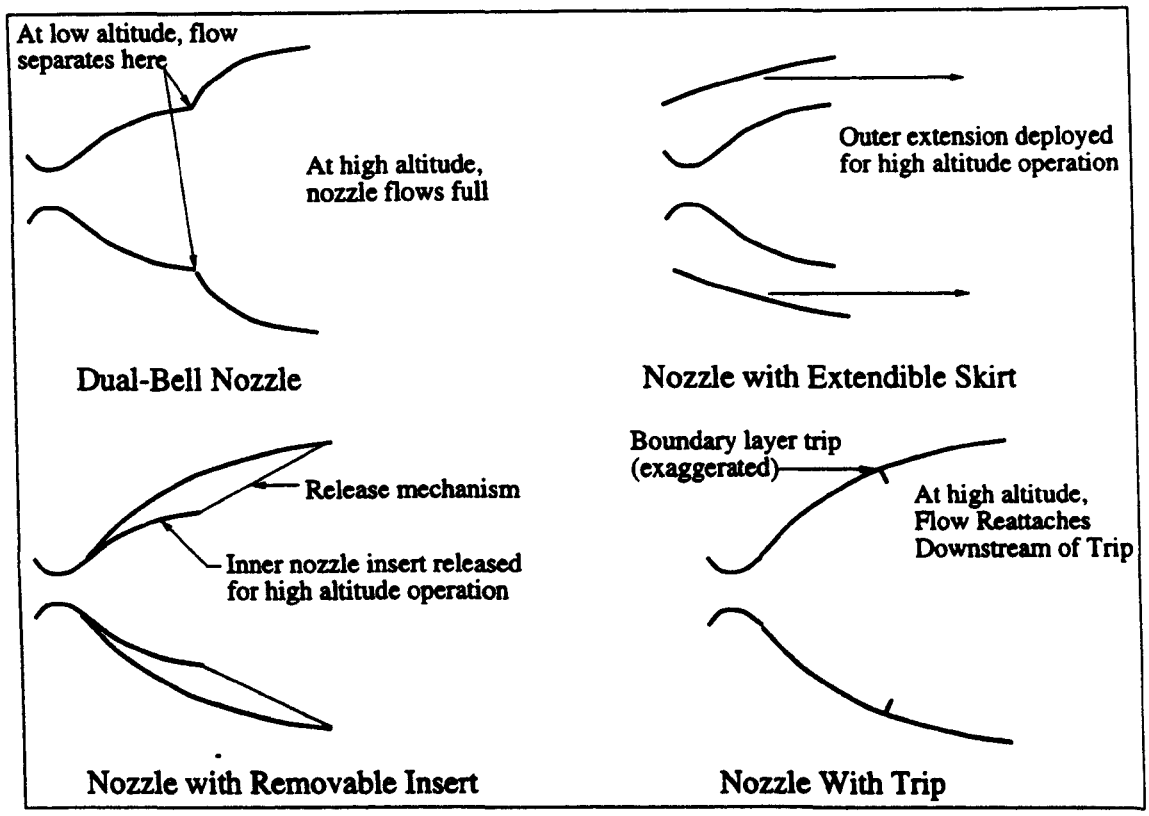

Figure 1.9: *Controlled Flow Separation Nozzle Types.*

high altitude. In both cases, transition between modes is achieved by a mechanical device. The boundary layer trip nozzle induces separation of the turbulent boundary layer at low altitudes, which re-attaches to the nozzle walls at higher altitudes.

The insert nozzle has the advantage that both nozzles may be of optimal contour, whereas the full flowing dual-bell nozzle and the low altitude nozzle of the extendible skirt may not be so designed. However, the release of the inner nozzle in the insert design has considerable risk, as it must exit the outer without striking it, and will also act as a blockage on the flow during release. The mass penalty of the system is larger, as there is no commonality between the nozzles. Both the insert and extendible nozzle suffer in comparison to the dual bell in terms of complexity, as they require mechanisms to provide the movement of the nozzle, increasing weight and reducing reliability. Finally, the boundary layer trip nozzle is the simplest to build and easiest to test, but has relatively poor performance. This is due to losses induced by the device used to trip the boundary layer, and is particularly severe with respect to vacuum thrusts.

These nozzles provide only a two stage altitude compensation, rather than the continuous adaption of plug and ED nozzles. Such continuous contour modification is provided by a variant of the insert nozzle, which employs a low altitude nozzle contour of a material that is gradually eroded by the hot gas. However, this concept suffers from the obvious difficulty in ensuring the smooth burn of the insert to the known and symmetrical intermediate contours required for controlled flow.

Both low and high altitude performance of these nozzles are slightly less than that of an optimised bell of the same area ratio, due to the obstructing effect of the transfer mechanisms. The nozzles will also be heavier than a bell nozzle designed for the same expansion ratio as the high altitude nozzle. However, as a nozzle with a larger overall expansion ratio may be used without risk of separation at low altitude, the vacuum performance will be significantly improved. As more efficient propulsion is achieved, the overall mass of the launch vehicle will be reduced. These nozzle concepts also share complete commonality with existing conventional combustion chambers and throat designs, and hence will be no more difficult to cool than conventional nozzles. The risk associated with the need to radically (plug) or slightly (ED) redesign the combustion chamber is also removed.

1.3.4 Dual-Mode Nozzles

This class of nozzle includes dual-throat and dual-expander types (Fig. 1.10). Both have two concentric throats; in a dual-throat nozzle they are supplied by the same combustion chamber, whereas in a dual-expander separate chambers are used, each of which may burn a different propellant combination or mixture ratio. Exhaust gas is passed through both throats during low altitude operation, but only one (usually the outer) at high altitude. This produces a reduction in throat area, and hence an increase in overall expansion ratio, increasing the efficiency of the nozzle. Whilst the total thrust of the nozzle is reduced due to the lower mass flow, thrust demands at high altitudes are lower.

The dual-expander nozzle necessitates the use of an annular combustion chamber surrounding one of conventional type, and therefore requires an extra component of unconventional technology. However, the radius is much less than the annular chamber of a plug nozzle, and would therefore present a lesser design challenge. The unique advantage offered by the dual-expander concept is the capability provided to tailor propellant combinations to the thrust regime required. Generally, the inner chamber will burn a denser combination, which is less efficient but provides higher thrust levels. At high altitude this chamber would be turned off, leaving only the outer chamber. This outer chamber would typically burn a less dense mixture, giving lower thrust but conversely a higher thrust coefficient [22].

As is the case for the physically adapting nozzle types discussed in the previous section, the altitude compensation is not continuous, and the bell nozzle may only be optimised for one of the two configurations (which would normally be the higher expansion ratio). In both designs, the outer throat will be at a significant radial distance, and hence the gap between the walls is likely to be small, again creating cooling problems. The radius of this throat is likely to be slightly greater than that of an ED (although still much less than a plug), and the material separating the two throats will be surrounded on all sides by hot gas, with minimal

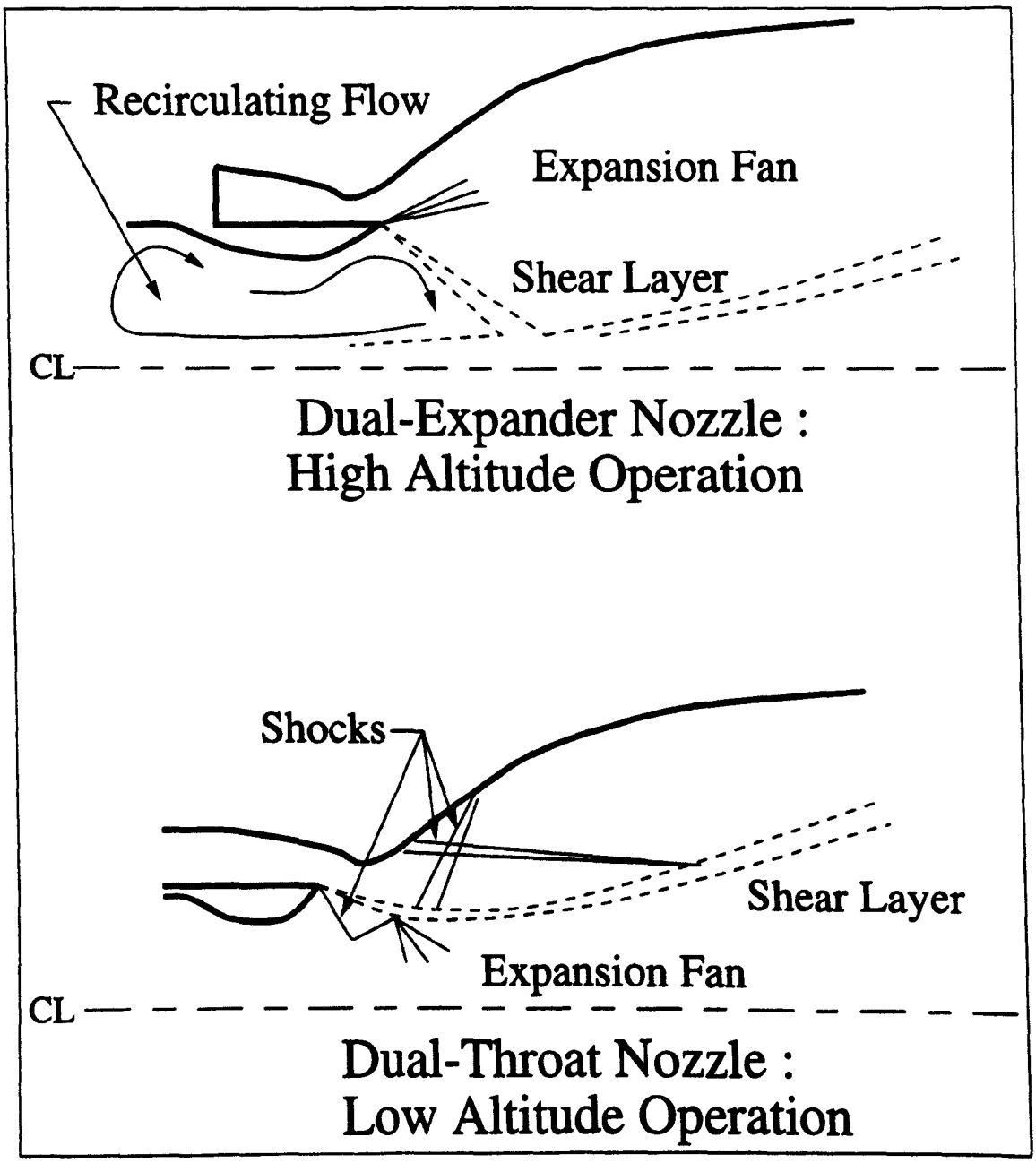

Figure 1.10: *Dual-Mode Nozzles*

thickness to allow for cooling mechanisms. It is therefore probable that the heating problem here is worse than that for an ED. Finally, as only altitude compensation and not length reduction is provided by these nozzle types, the mass of the nozzle is likely to be greater than that of an equivalent ED or plug. Indeed, due to the increased complexity in the throat region, and the need for two combustion chambers (one of unconventional annular design), the mass of a dual-expander nozzle is likely to exceed that of a conventional bell of similar overall expansion ratio.

1.4 Review of Previous Work on the ED Nozzle

The obvious advantages of reduced length and altitude compensation provided the impetus for a series of investigations into the ED concept in the 1960's. However, the analysis process of the ED nozzle is considerably more complex than that of conventional types, due to the large regions of viscous flow, and the presence of internal separations and mixing regions. The ED nozzle also has more variations in its geometric composition compared to conventional nozzles, especially with regard to the throat region. There was therefore a wide scope for differing approaches to the ED nozzle concept to develop, and in fact two schools of thought became apparent fairly early on. The primary contributer to the first was Rao, and the second Mueller.

1.4.1 Rao

In his initial paper on the subject, Rao developed a method for ED nozzle contour design based on his well established technique for minimum length bell nozzles [6]. This method makes use of the Method of Characteristics (MoC) to provide analysis of the supersonic, inviscid flow region. The MoC is effective in this role, being stable and computationally efficient. More importantly it allows contours optimised with respect to length to be produced, with characteristics at the nozzle throat as the only input. However, the technique is strictly limited to the supersonic, inviscid portion of the flow-field, and in fact the viscous region and its effects are entirely ignored in Rao's analysis.

Before the optimisation method may be used, the flow within the throat region of the nozzle must be modelled separately to allow purely supersonic characteristics to be extrapolated from this region, for use as a starting line for the MoC. The method described by Rao creates such a starting line via an analytical technique, based on power series expansions similar to the method due to Sauer [23] for conventional axial throats. Rao then states that having performed initial studies, it was found that a throat flow angle of ninety degrees allows a wide range of area ratios and optimised lengths to be produced. It should be noted, however, that the analytical scheme described is only applicable to throat angles very close to ninety degrees. It is probable therefore that Rao first examined a range of throat angles using a simple linear sonic line, but this would have been of questionable accuracy. It should also be noted that the Sauer starting profile is not an exact solution, and finally that Rao does not claim that a ninety degree throat always leads to the best results, merely that results are possible. A later study by Schorr [24] using similar methods noted a performance drop off for throat angles below 60 degrees, but no method for initial line generation is given, strongly implying a simple linear sonic line at the throat was used for all throat angles.

The primary deficiency in the analysis of both Rao and Schorr, however, lies in the treatment of the viscous region within the supersonic flow. For vacuum performance analysis and thrust prediction, the pintle base pressure is assumed to be zero. It may be argued that this therefore represents a worst case scenario, and in reality due to the entrapment of the base flow region during wake closure a small increase over predicted vacuum thrust is inevitable. However, this constitutes a level of uncertainty and inaccuracy in the analysis which may in turn effect the choice of optimum throat angle and geometry.

When calculating the variation of performance with ambient pressure, the problem is more serious. Again the actual flow processes are ignored, and a constant pressure boundary at atmospheric pressure is assumed for the inviscid-viscous flow interaction. Unfortunately, there is some evidence that this may not be the case in reality. It has been found by experiment that when the wake is in its closed position, this free jet boundary is not at constant pressure along its whole length [25]. It is therefore not unreasonable to assume that the pressure distribution along the wake also varies when open. The possibility that the high velocity supersonic flow surrounding the viscous wake may 'pump out' this region has already been mentioned, and is discussed in more detail in Chs. 4 and 6.

1.4.2 Mueller

Mueller, and those who worked with him, approached the problem from more or less the opposite direction. Whilst both ED [26], [27] and aerospike [11] nozzles were considered, attention was focused primarily on the latter. As such, the behaviour of the central viscous region was of great interest, particularly during wake closed mode (e.g. Refs. 25,28, and 29), for reasons outlined below. Attention focused almost entirely on the methods by which the flow and pressure distribution in this region could be predicted, and no attempt was made to demonstrate optimal nozzle design or calculate overall performance.

As has already been noted, the closed wake represents a system invariant with respect to atmospheric conditions. Combined with the fact that the viscous region is restricted to a finite volume, this considerably simplifies the analysis, and various mathematical models of the flow-fields around isolated bodies with a blunt base have been developed (e.g. Refs. 30, and 31). In both aerospike and ED nozzles, designing the contour to ensure that the wake behind the blunt base of the plug or pintle is closed over the entire range of operational ambient conditions allows this simplified analysis to be used.

This design strategy not only simplifies the analysis, but also provides some real benefits, particularly for aerospike nozzles. As the base pressure is approximately constant, the thrust provided will increase with altitude. Thus a low altitude wake closure will result in a higher base pressure (all other things being equal), and hence a greater thrust at altitude.

Further, if the wake is designed to close at or below sea level pressure ratios, the possibility of oscillatory or unsteady behaviour causing vibrations during wake closure is eliminated.

In an aerospike nozzle, the majority of the altitude compensation occurs upstream of the wake region, and hence is unaffected by wake closure. In an ED, however, the wake region provides the sole mechanism by which this is achieved, and hence if the wake is closed over the entire operating range, no altitude compensation is possible (this does not appear to have been noted by Mueller). Despite this, the (relative) simplicity of analysis and lesser risk of structural failure are attractive, and a nozzle so designed would still show a reduction in length compared to a bell. However, ensuring that the wake is always closed produces a nozzle flow that is underexpanded at all altitudes, and hence the energy of the flow is not fully utilised.

There is clearly a difference of philosophy apparent between the approach of Mueller and Rao, and this in turn lead to a series of design differences between the nozzles produced. Rao largely ignores the effects of the viscous flow, merely assuming a constant pressure boundary, and his work concentrates on the overall performance of the nozzle. From this, he suggests large throat angles, with as much operation in open wake mode as possible to provide maximum performance and altitude compensation. Mueller, however, models the viscous flow region with some apparent success, but only for small throat angles and closed wakes. He makes no attempt to provide overall performance comparisons, and makes use of ideal, rather than optimised, contours. It should also be noted that the flow at the throat region of such nozzles required experimental results to allow generation of starting lines for the MoC. A generic nozzle of each type is shown in Fig. 1.11.

Also shown in this figure is an approximation of the nozzle tested by Wasko [12]. Although not dimensionally accurate, this diagram shows the key features of the design, which clearly is most closely related to the Mueller school. There are, however, some important differences. The angle at pintle separation is even lower than those used by Mueller, only about 15 degrees. The throat is considerably upstream of the point of separation, and is in fact inclined inwards, towards the nozzle centreline. The reason for this strange arrangement is not given, and would result in a much higher Mach number at the separation point, in turn reducing open and closed wake base pressure. Examining Fig. 1.11, it is clear from the similarity with Mueller nozzles that it would be unlikely to exhibit significant altitude compensation, and due to the separation angle and peculiar throat angle, a low base pressure and poor overall performance would be expected. It is therefore unsurprising that this is indeed what Wasko found.

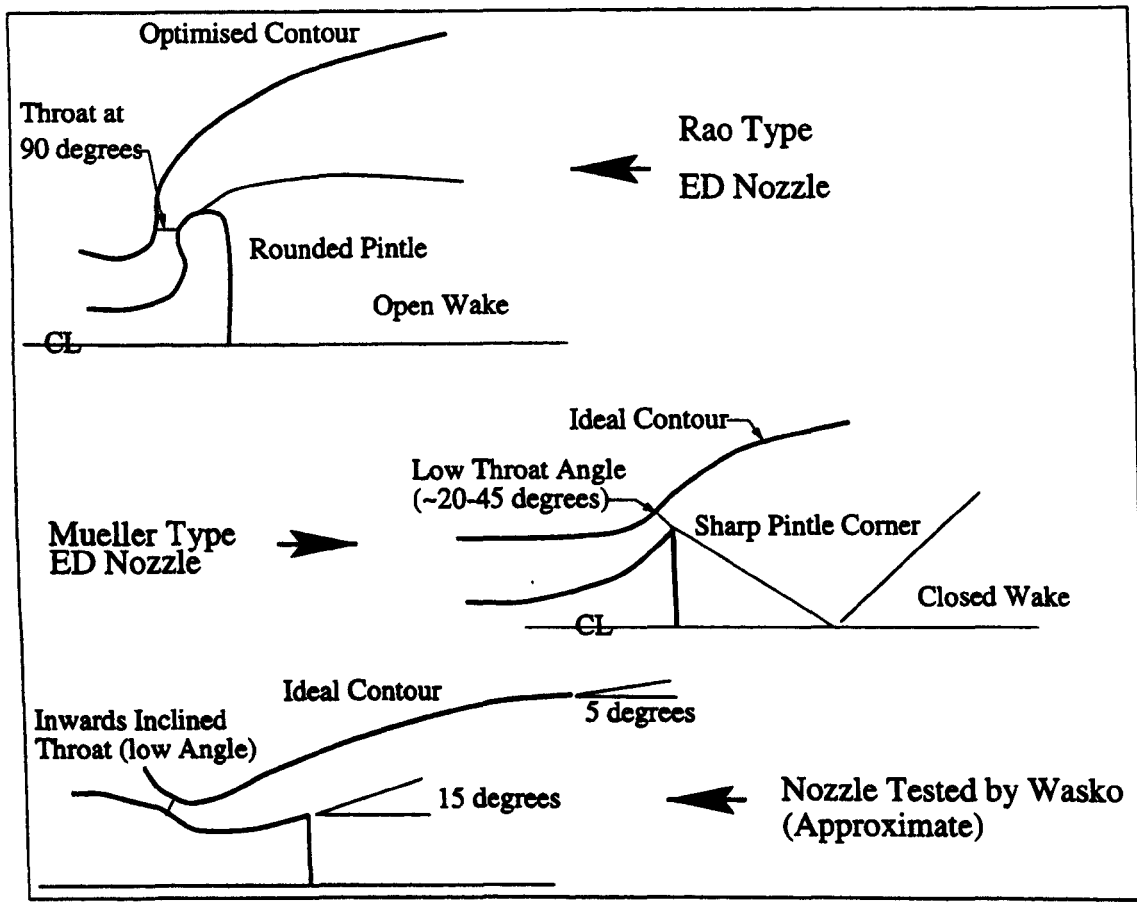

Figure 1.11: *Different ED Nozzle Concepts*

1.5 Aims and Objectives

The previous two sections have demonstrated that whilst the ED nozzle has its own advantages and disadvantages compared to other advanced nozzle concepts, it is from first principles at least as promising as any other type. However, it is equally clear that the current state of the art with respect to analysis of the type is insufficient to allow the necessary quantitative judgements to be made as to whether a developed version of this nozzle type is suitable for eventual application to space vehicles.

. The prime difficulty presented by the ED nozzle is the much greater complexity of the flow structures within the nozzle flow-field. The computational power and methods available in the early 60's when the initial research was carried out were insufficient to provide full analysis. Simplified models had to be used, which either considered only a part of the flow or a restricted operating regime, and were based on sometimes questionable assumptions. At this time, most proposed launch vehicles had multiple stages which reduced the potential gain provided by altitude compensation. Whilst the possible reductions in length benefit multiple stage designs, this would to some (unknown) extent be offset by an increase in the complexity and weight of the combustion chamber. The ED nozzle also suffered from competition in research resources by the plug nozzle, to which it was often deemed generally inferior. Finally, some experimental results brought into question whether the theoretical

performance could be realised in a real nozzle. Given all these problems, it is unsurprising that interest in the type waned, and in fact virtually no new work on the concept may be found in the literature since 1970.

In recent years, however, advances in computing power and methods have meant that the flow-fields of advanced nozzles, though still challenging, are no longer outside the bounds of possible solution. Further, it is widely expected that the next generation of launch vehicles will either be of Single Stage To Orbit (SSTO) type, or at least include a stage which operates a single propulsive unit over a very wide pressure range. Interest in advanced nozzle technology has therefore increased, particularly with respect to the linear aerospike, although nearly all the advanced types discussed in this chapter have been the subject of investigation in the last decade.

Interest in the ED nozzle, however, has been slow in reviving. This appears to be due to the highly influential paper by Wasko [12] previously discussed. For instance Hagemann *et al* in their recent review of advanced nozzle technology [8] state *'The ED nozzle concept has also been a subject of numerous analytical and experimental studies. Results from these studies show that the ED nozzle capabilities for altitude compensation are poor, and are in fact worse than those of plug nozzles, because of aspiration and over expansion losses'*. However, the list of 40 references provided by Hagemann *et al* has only a single entry directly relating to the ED nozzle, and that is Wasko's paper. It has already been seen that the ED nozzle examined by Wasko was unusual in several respects, and should not be used to discredit the entire ED concept alone. This topic relates to the anticipated evacuation of the viscous region by the supersonic flow, and is discussed in more detail in Ch. 4 of this dissertation.

It is therefore felt that the ED nozzle concept is ripe for re-analysis, using the modern techniques now available. Before the performance of the ED concept can be quantified, and a design procedure established, a series of issues require attention. First and foremost, a more accurate and flexible model of the throat region must be established. This will allow the two design philosophies of Rao and Mueller to be properly compared, as optimised contouring of the outer nozzle wall will be possible for any throat angle. The influence of throat angle and location on contour design may then be fully analysed for the first time. An accurate picture of the flow at the throat should also allow the influence of throat wall curvatures and pintle design to be examined. These factors may not only influence the contour design, but also the flow behaviour at separation and through this the viscous region.

The viscous region itself requires an improvement of analysis in both wake closed mode, and the much more difficult open wake mode (no previous work on the type even attempts to analyse the viscous region when the wake is open). Once both these modes are understood, the transition between the two must also be considered, as the stability of this process is

uncertain and could induce vibrations and thus structural damage. If this is the case, methods for the reduction and control of the vibrations must be found.

Only when all these issues are considered and accounted for may a design procedure be established. At this point, the flow-field in the region of the throat will be sufficiently well understood to allow an assessment of the difficulties posed by the increased heat flux, and if necessary, design solutions investigated. It would also then be possible to examine other postulated benefits of the nozzle, such as throttling using pintle displacement, and the influence of base bleeding (injection of gas into the base region) on both overall performance, and on active control of the wake transition behaviour.

This obviously represents a sizeable advance on the current state of analysis, requiring a considerable amount of theoretical and experimental work. This dissertation does not attempt to address all these issues, and instead emphasis is placed first and foremost on the throat region, and secondly on the modelling of both open and closed wake behaviour. Throughout, both linear and axisymmetric concepts are developed side by side, and emphasis is placed on complete nozzle performance.

Before attempting analysis of the ED nozzle behaviour, the flow regimes and methods of analysis for conventional nozzles are examined. This approach is required to ensure not only a firm basis for the extension of the techniques to the more complex nozzle, but also to provide a database for comparison of the ED with the lower performance types, allowing a quantitative assessment of the advantages provided. Ch. 2, therefore, details the analysis of the throat region of conventional nozzles, giving methods previously used, and comparing these with a computational technique derived primarily for the ED nozzle, but also applicable to these more simple geometries. Ch. 3 then describes the analysis and design of the complete conventional nozzle designs.

ED nozzle analysis begins in Ch. 4 where the throat flow model is detailed, and design methods and analysis for the vacuum performance of length optimised ED contours are presented. Results for these methods are presented in Ch. 5. Ch. 6 completes the analysis of the type by discussing methods for the calculation of performance variation with altitude and wake closure pressure ranges, with results for these methods being presented in Ch. 7. Finally, Ch. 8 provides conclusions derived and an assessment of the amount of progress made, whilst Ch. 9 discusses areas of possible future work.

Chapter 2

Throat Modelling Techniques

As mentioned in the introductory chapter, the Method of Characteristics (MoC) is extremely effective for the analysis of purely supersonic and inviscid flows, being both rapid and accurate. A detailed description of the method and its uses is provided in the following chapter, where analysis of the supersonic flow region is discussed. However, the MoC in its usual form is a space marching scheme, and the elliptical nature of the governing equations in transonic flow mean that the throat region of a rocket nozzle cannot be modelled by such techniques. A separate solution method must therefore be utilised to analyse the small region of flow within the vicinity of the nozzle throat. Results from this limited analysis are then used as input conditions for the MoC algorithms employed for the majority of the nozzle flow-field.

Two generic approaches to this task are possible, analytical methods and time marching techniques. The later make use of the hyperbolic nature of the unsteady flow equations, and solution methods belong within the realm of Computational Flow Dynamics (CFD). CFD schemes evolve an initial approximate flow-field forward in time by solving the unsteady flow equations until (hopefully) a steady state is achieved. In general, this is computationally intensive and time consuming. Analytical methods, however, provide solutions to the steady state equations. This means that they require no iterative procedures and are therefore much more rapid. For this reason they were considered first.

2.1 Analytical Throat Models

In 1944, Sauer produced a method based on a power series expansion of small velocity perturbations about the sonic line, for both two-dimensional and axisymmetric nozzles [23], and Hall extended the method in 1962 by considering higher order expansions [32]. Two-dimensional and axisymmetric methods were presented, each involving up to three terms in

the expansions. Unfortunately, both the Sauer and Hall solutions suffer from instability when applied to nozzles where $R_w^=$, the radius of curvature of the nozzle wall at the throat, is small ($R_w^= \sim\leq 1.5R_t$, depending on method type).

In an attempt to remove this limitation, Kliegel and Levine produced an alternative expansion [33], and also produced corrected third order axisymmetric solutions (Ref. 32 having been found to contain errors). However, a later paper by Levine and Coates [34] demonstrated that the governing flow equations were not satisfied within the transformed coordinate system created by this expansion. Fortunately, in 1981 Dutton and Addy finally produced an alternative method which obeys the equations correctly, and remains stable for nozzle throats with small $R_w^=$ [35].

An alternative to such power series methods was developed in the mid sixties by Hopkins and Hill [36]. However, the inverse nature of the solution technique renders matching of real and modelled nozzle contours difficult, and means that the throat geometry must be designed to suit the flow solution, restricting possible configurations. This undoubtedly accounts for the infrequent referencing of this technique in subsequent works, and these factors combined resulted in this method being discarded early on in this investigation. Therefore, the analytical phase was limited to power series expansion methods.

2.1.1 Derivation of Governing Equation

Whilst the full Navier-Stokes equations which govern the flow of a fluid are impossible to solve analytically, in certain circumstances sufficient assumptions may be made about the behaviour of a fluid to allow solution of a restricted form to accurately model the flow. In the throat region of a nozzle it is reasonable to assume that outside of a thin boundary layer attached to the nozzle wall, the effects of fluid viscosity may be neglected (inviscid flow). Under normal operating conditions there will be no shock waves in this region, resulting in irrotational flow. Further, the region may be modelled as a perfect gas in a steady state, with no heat transfer at the walls and negligible body forces, and hence the total enthalpy is constant.

Once these assumptions have been made, the Navier-Stokes equations reduce to

$$\frac{\partial u}{\partial x}(a^2 - u^2) + \frac{\partial v}{\partial y}(a^2 - v^2) - 2uv\frac{\partial u}{\partial y} + ka^2\frac{v}{y} = 0 \qquad (2.1)$$

where the coordinate system is as defined in Fig. 2.1, a is the local speed of sound, and k is a scalar (zero for two-dimensional flow, and one for axisymmetric).

As

$$a^2 = \frac{\gamma + 1}{2}a^{*2} - \frac{\gamma - 1}{2}(u^2 + v^2) \qquad (2.2)$$

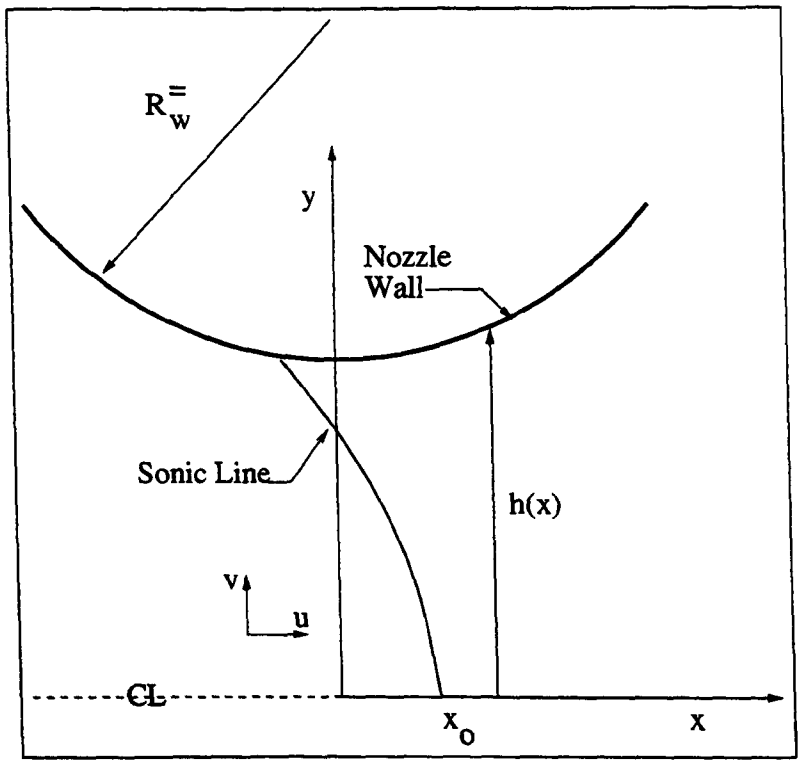

Figure 2.1: *Coordinate System*

where a^* is the critical velocity (i.e. the local speed of sound at $M = 1$), substituting the non dimensional velocities

$$\tilde{u} = \frac{u}{a^*}; \qquad \tilde{v} = \frac{v}{a^*} \tag{2.3}$$

into Eqn 2.1 results in

$$\frac{\partial \tilde{u}}{\partial x}\left(1 - \tilde{u}^2 - \frac{\gamma-1}{\gamma+1}\tilde{v}^2\right) + \frac{\partial \tilde{v}}{\partial y}\left(1 - \frac{\gamma-1}{\gamma+1}\tilde{u}^2 - \tilde{v}^2\right) - \frac{4}{\gamma+1}\frac{\partial \tilde{u}}{\partial y}\tilde{u}\tilde{v} + k\left[1 - \frac{\gamma-1}{\gamma+1}(\tilde{u}^2 + \tilde{v}^2)\right]\frac{\tilde{v}}{y} = 0 \tag{2.4}$$

This equation is exact, but has no analytical solution. However, as only flow in the region of the sonic line is being considered, small perturbation velocities $\hat{u}, \hat{v}$ may be introduced where

$$\hat{u} = \tilde{u} - 1; \qquad \hat{v} = \tilde{v} \tag{2.5}$$

As $\hat{u}$ and $\hat{v}$ are small quantities, their products may be neglected, and hence after substituting into Eqn. 2.4 and some manipulation, a much simpler governing equation is derived:

$$(\gamma+1)\hat{u}\frac{\partial \hat{u}}{\partial x} - \frac{\partial \hat{v}}{\partial y} - k\frac{\hat{v}}{y} = 0 \tag{2.6}$$

2.1.2 Boundary Conditions

Method of Sauer

In Ref. 23, Sauer proceeds by taking advantage of the flow symmetry about the centreline to express the stream function φ as the infinite power series

$$\varphi = f_0(x) + y^2 f_2(x) + y^4 f_4(x) + ... \tag{2.7}$$

and hence

$$\hat{u} = \frac{\partial \varphi}{\partial x} = f_0'(x) + y^2 f_2'(x) + y^4 f_4'(x) + ... \tag{2.8}$$

$$\hat{v} = \frac{\partial \varphi}{\partial y} = 2y f_2(x) + 4y^3 f_4(x) + ... \tag{2.9}$$

Substituting these equations into Eqn. 2.6, and equating coefficients of powers of y results in

$$2(1+k) f_2 = (\gamma+1) f_0' f_0'' \tag{2.10}$$

$$2(6+2k) f_4 = (\gamma+1)(f_0' f_2'' + f_0'' f_2') \tag{2.11}$$

Assuming the linear variation of velocity along the nozzle centreline

$$f_0'(x) = \hat{u}_0(x) = \alpha x \tag{2.12}$$

where α is the gradient of the velocity profile in turn means that f_0'' is unity. This allows calculation of f_2 and f_4, finally resulting in

$$\hat{u} = \alpha(x - x_0) + \alpha^2 y^2 \frac{\gamma+1}{2(k+1)} \tag{2.13}$$

$$\hat{v} = \alpha^2 y (x - x_0) \frac{\gamma+1}{k+1} + \alpha^3 y^3 \frac{(\gamma+1)^2}{6+10k} \tag{2.14}$$

where x_0 is the x coordinate of the intersection of the sonic line and the centreline (as shown in Fig. 2.1). By a lengthy consideration of various control points and streamline equations, Sauer was able to show that as a first approximation

$$\alpha = \sqrt{\frac{k+1}{(\gamma+1)R_w^=}} \tag{2.15}$$

and x_0 is given by

$$x_0 = \frac{1}{6+2k} \sqrt{\frac{(k+1)(\gamma+1)}{R_w^=}} \tag{2.16}$$

Method of Hall

In his work, Hall proceeds in slightly different fashion. First, as the flow is irrotational,

$$\frac{\partial \hat{v}}{\partial x} = \frac{\partial \hat{u}}{\partial y} \tag{2.17}$$

and this allows Eqn. 2.6 to be recast as

$$(1+\gamma)\frac{\partial}{\partial x}\Big(\hat{u}\frac{\partial \hat{u}}{\partial x}\Big) = \frac{\partial^2 \hat{v}}{\partial y^2} + \frac{k}{y}\frac{\partial \hat{u}}{\partial y} \tag{2.18}$$

Further, the radial distance of the nozzle wall from the centreline, $h(x)$, may be represented by

$$h(x) = 1 + \frac{x^2}{2R_w^=} + \frac{x^4}{8R_w^=} + 0(x^6) \tag{2.19}$$

As the flow must be tangential to the solid surface at the wall, and parallel to the longtitudional axis at the centreline, boundary conditions are provided by

$$\hat{v}(x,0) = 0 \tag{2.20}$$

$$\hat{v}\big(x,h(x)\big) = \Big[1+\hat{u}\big(x,h(x)\big)\Big]\frac{dh}{dx} \tag{2.21}$$

By considering the relative orders of the variables near the throat region, Hall was able to show that Eqn. 2.6 is only satisfied if x is of the order of $(R_w^=)^{-1/2}$. By transforming to a coordinate system (y,z), where z is a stretched longtitudional coordinate given by

$$z = \Big[\frac{(1+k)R_w^=}{\gamma+1}\Big]^{\frac{1}{2}} x \tag{2.22}$$

the non dimensionalised velocity components can be expressed in power series form as

$$\hat{u} = \frac{u_1(y,z)}{R_w^=} + \frac{u_2(y,z)}{(R_w^=)^2} + \frac{u_3(y,z)}{(R_w^=)^3} \tag{2.23}$$

$$\hat{v} = \Big[\frac{\gamma+1}{(1+k)R_w^=}\Big]^{\frac{1}{2}}\Big(\frac{v_1(y,z)}{R_w^=} + \frac{v_2(y,z)}{(R_w^=)^2} + \frac{v_3(y,z)}{(R_w^=)^3}\Big) \tag{2.24}$$

Substituting into Eqns. 2.17 and 2.18 results in

$$\frac{\partial v_n}{\partial z} = \frac{\partial u_n}{\partial y}; \quad n = 1,2,3,... \tag{2.25}$$

$$-u_1\frac{\partial u_1}{\partial z} + \frac{1}{1+k}\frac{\partial v_1}{\partial y} + \frac{k}{1+k}\frac{v_1}{y} = 0; \quad n = 1 \tag{2.26}$$

$$-u_1\frac{\partial u_n}{\partial z} - u_n\frac{\partial u_1}{\partial z} + \frac{1}{1+k}\frac{\partial u_n}{\partial y} + \frac{k}{1+k}\frac{v_n}{y} = \phi_{n-1}; \quad n = 2,3,... \tag{2.27}$$

where

$$\phi_{n-1} = f(u_1, v_1, ...u_{n-1}, v_{n-1}) \tag{2.28}$$

and are as listed in Ref. 32. It is possible to show that the Hall solution restricted to the first terms (i.e. $\hat{u}(u_1), \hat{v}(v_1)$) is mathematically identical to that of Sauer.

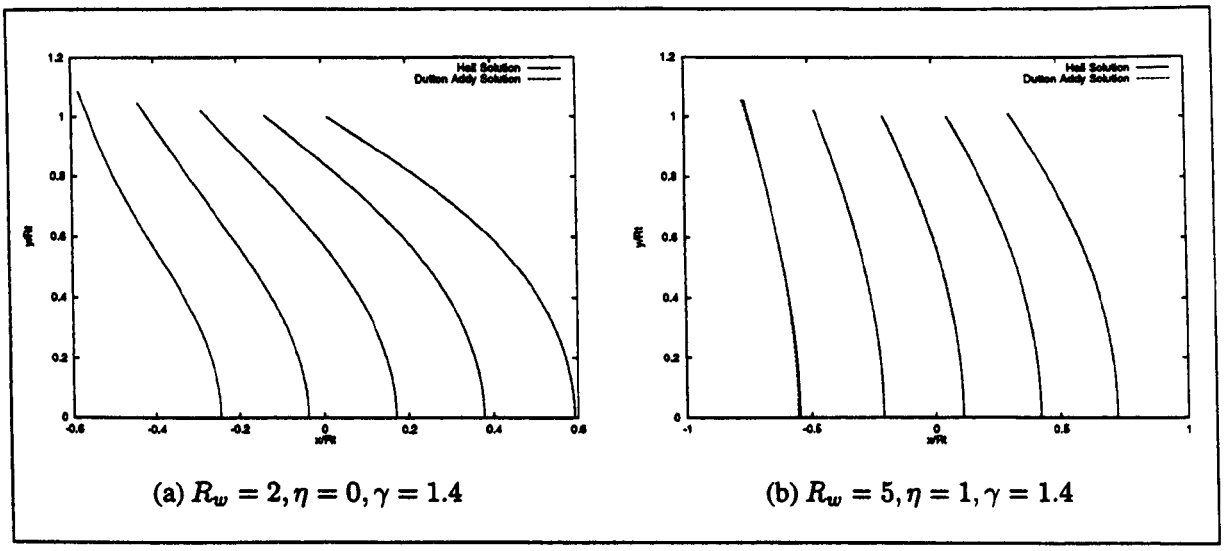

(a) $R_w = 2, \eta = 0, \gamma = 1.4$ (b) $R_w = 5, \eta = 1, \gamma = 1.4$

Figure 2.2: *Comparison of Three Term Hall and Dutton Addy Methods, Planar Flow*

Method of Dutton and Addy

However, Eqn. 2.22 implies that as $R_w^{=} \rightarrow 0$, $z \rightarrow 0$, and hence the solution process becomes unstable. To allow nozzles with small $R_w^{=}$ to be analysed, Dutton and Addy [35] introduced an arbitrary expansion variable, η, such that

$$\epsilon = (R_w^{=} + \eta) \tag{2.29}$$

Substitution of ϵ for $R_w^{=}$ into the above working and following a very similar derivation process results in equations for $\hat{u}$ and $\hat{v}$ which remain stable even for $R_w^{=} < 1$.

The original paper by Dutton and Addy concerned only axisymmetric flow, and hence a two-dimensional version of this method has been derived, using the same procedure as that for the axisymmetric case. The derivation process is long and involved and hence is not presented here. However, correct derivation and implementation of the equations within the computational algorithms may be demonstrated by comparison with the Hall solution. As either the throat radius tends to infinity or the expansion parameter (η) tends to zero, the Dutton Addy method should tend to the Hall solution. Fig. 2.2 shows the Mach contours produced by the two methods for zero η and large $R_w^{=}$. As expected, the contours are extremely similar (in fact identical for $\eta = 0$). The Hall solution itself was verified by comparing numerical values generated to data provided in Ref. 32.

The Dutton Addy equations used for the results presented in this chapter are given in App. A, for the full three term Dutton Addy solution, in both two-dimensional and axisymmetric form. The Hall solution may be found from these by setting η to zero, and the Sauer method by only including the first term of the Hall series.

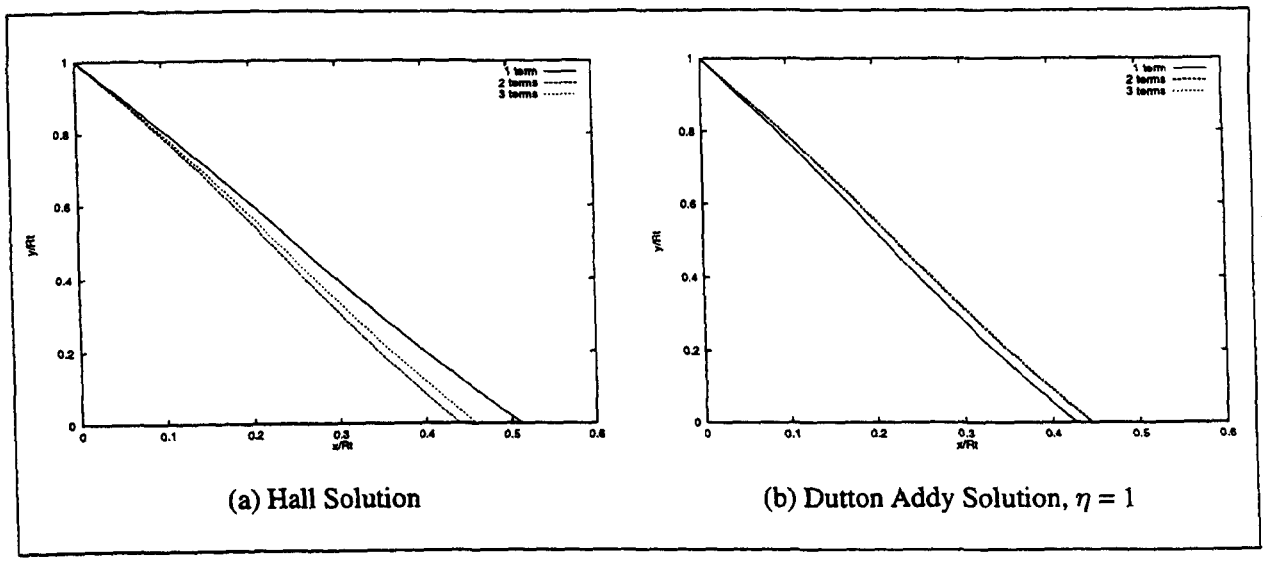

(a) Hall Solution

(b) Dutton Addy Solution, $\eta = 1$

Figure 2.3: *Convergence Properties,* $R_w^= = 3, \gamma = 1.4$, *Planar Flow*

2.1.3 Method Comparison

The improved stability and convergence properties of the Dutton Addy formulation compared to that of Hall may be inferred directly from the previously described derivation process. However, a brief demonstration is included here, with emphasis placed on the effect on the first Right Running Characteristic (RRC) of the nozzle flow. This characteristic originates at the intersection of the nozzle wall and geometric throat, and is the starting line used by all the nozzle design and analysis methods described in the following chapters. It is created by interpolation of points generated by the throat analysis.

Considering initially two-dimensional flows, Figs. 2.3 and 2.4 compare the convergence properties of the two techniques for two different nozzle throat conditions. Fig. 2.3 presents results for a nozzle with $R_w^= = 3$, representing a large wall radius. As may be seen, both the Hall and Dutton Addy solutions converge with increasing terms in the velocity expansions. The differences between the two techniques is very slight, although the Dutton Addy method does produce a more closely grouped set of characteristics, implying that the solution is less dependent on the number of terms approximating the perturbation velocities. The RRC produced for both the full three term Hall and Dutton Addy solutions are very nearly identical, as would be expected.

Fig. 2.4 shows the first RRC produced when $R_w^= = 1$, showing typical results for throats with small wall radii. As can be seen from this figure, the Hall solution produces the expected instability. This is demonstrated by Fig. 2.4 (a), where the variation in the number of terms causes a dramatic alteration in the location of the first RRC. Fig. 2.4 (b), however, clearly demonstrates the improved stability of the Dutton Addy technique, which still converges rapidly to a solution as the number of terms is increased.

For axisymmetric nozzles, the advantages of the Dutton Addy expansion is even more

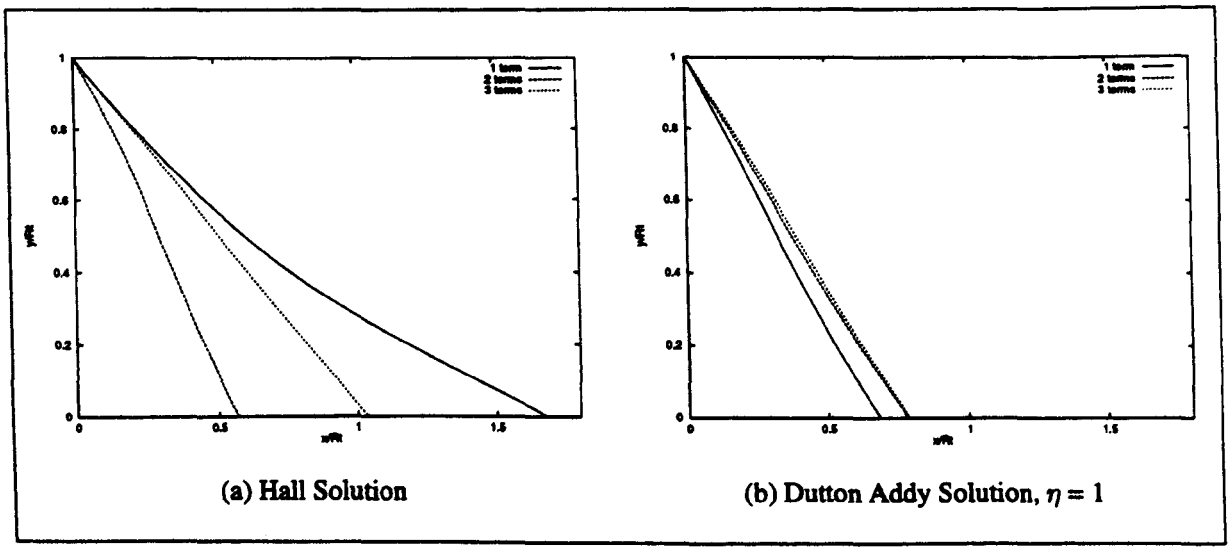

(a) Hall Solution

(b) Dutton Addy Solution, $\eta = 1$

Figure 2.4: *Convergence Properties,* $R_w^{=} = 1, \gamma = 1.4$, *Planar Flow*

pronounced. Figs. 2.5 and 2.6 show the same nozzles geometries as Figs. 2.3 and 2.4 respectively, but this time for an axisymmetric flow. As may be seen, even with relatively large $R_w^{=}$ (Fig. 2.5), there is a definite improvement in the convergence properties for the Dutton Addy solution, and when a throat with a small wall radius is considered, it is dramatic. In fact, no solution exists at all for the Hall method restricted to the first term (which, as has already been mentioned, is identical to the Sauer solution).

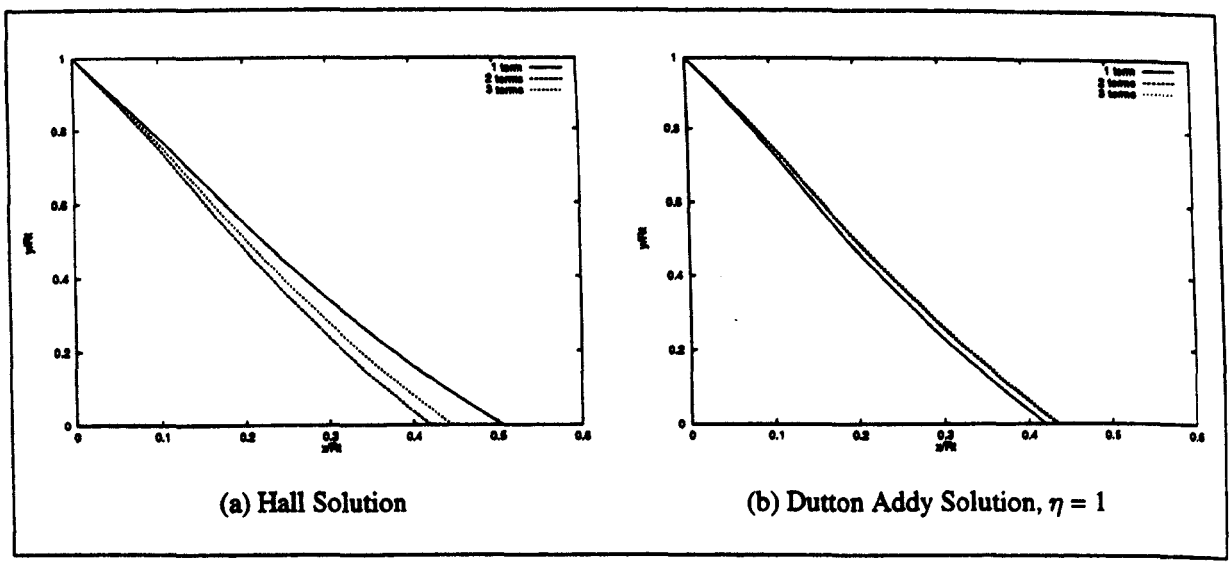

(a) Hall Solution

(b) Dutton Addy Solution, $\eta = 1$

Figure 2.5: *Convergence Properties,* $R_w^{=} = 3, \gamma = 1.4$, *Axisymmetric Flow*

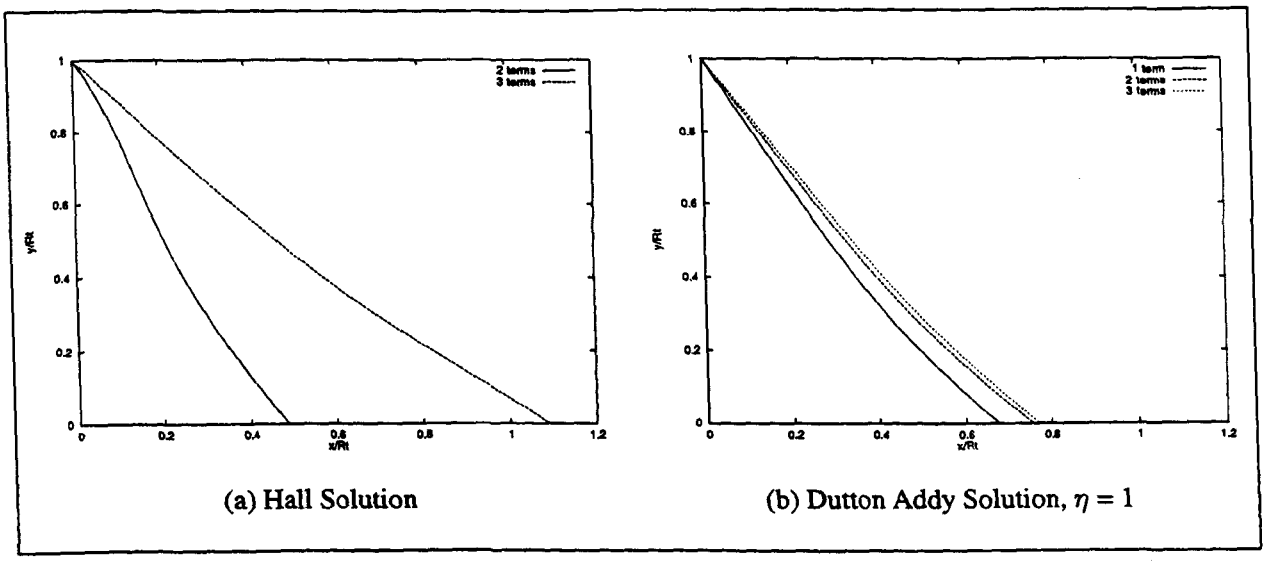

(a) Hall Solution

(b) Dutton Addy Solution, $\eta = 1$

Figure 2.6: *Convergence Properties,* $R_w^{=} = 1, \gamma = 1.4$, *Axisymmetric Flow*

The results presented here clearly show the superior convergence and stability of the Dutton Addy technique, and hence for the remainder of this thesis the term 'analytical solution' refers to results obtained from a three term Dutton Addy type expansion with η set to 1, unless otherwise stated.

2.2 The CFD Model

The analytical methods discussed in the previous section, once inserted into suitable computational algorithms, allow practically instantaneous generation of an initial characteristic for throat geometries located on the centreline with the nominal flow direction parallel to the nozzle axis of revolution, such as are found in conventional nozzles. However, a full analysis of the ED nozzle concept requires modelling of throat geometries at completely arbitrary inclinations and displacements from the centreline. Unfortunately, the derivation process of the analytical techniques discussed depend upon the assumption of small velocity perturbations from one-dimensional sonic flow. For ED nozzles, there is a large range of throat configurations where this assumption is invalid (this is discussed in more detail in Ch. 4). In contrast, computational methods are not restricted by this requirement, and hence are applicable to such flow regimes.

The need to analyse unconventional throat geometries was the primary motivation for the development of a CFD based transonic flow solution method. However, even for conventional nozzles, the assumption of small perturbations is in some circumstances questionable. As either $R_w^{=}$ is reduced, or the distance from the sonic line increases, the perturbation from sonic flow will grow. Therefore, a comparison of the CFD technique with the analytical method for conventional nozzle configurations serves two purposes. It allows the CFD method itself to be validated against solutions known to be accurate, and provides a method

by which an investigation into the range of applicability of the analytical solution may be achieved. The remainder of this chapter describes the CFD method selected and derivation, and compares results obtained by this method with those produced by the analytical scheme for conventional throat geometries.

2.2.1 Method Selection

Before choosing a suitable CFD coding scheme from the multitudes available, an assessment of the reasonable assumptions which may be made about the flow to be modelled is required. Many of these are the same as those already made in the derivation of the analytical solution. The flow is assumed to be inviscid (reducing the Navier-Stokes equations to the Euler equations), and either two-dimensional or axisymmetric (reducing the number of momentum equations from three to two). The flow is also assumed to be that of a perfect gas with constant total enthalpy, removing the need to calculate the energy equation. However, there are no assumptions of either small velocity perturbations, or irrotational flow.

Given these assumptions, the number of applicable algorithms is reduced. Whilst several alternatives were considered (for instance those presented in Refs. 37 and 38) the finite volume, cell centred differencing scheme developed in the late 1970's by Jameson was selected. This method is a well established technique known to be effective for examining the flow over transonic aerofoils, a problem sharing many of the key characteristics of nozzle throat flow.

2.2.2 Method Description

For two-dimensional flow, the Euler equations (in conservative form) are

$$\frac{\partial \underline{U}}{\partial t} + \frac{\partial \underline{F}}{\partial x} + \frac{\partial \underline{G}}{\partial y} = 0 \tag{2.30}$$

where

$$\underline{U} = \begin{pmatrix} \rho \\ \rho u \\ \rho v \\ \rho e_0 \end{pmatrix}; \quad \underline{F} = \begin{pmatrix} \rho u \\ \rho u^2 + P \\ \rho uv \\ \rho u h_0 \end{pmatrix}; \quad \underline{G} = \begin{pmatrix} \rho v \\ \rho uv \\ \rho v^2 + P \\ \rho v h_0 \end{pmatrix}; \tag{2.31}$$

and e_0 and h_0 are total energy and enthalpy respectively. The analytical solutions to the throat flow problem required the assumption of constant total enthalpy. This was justified on the grounds that there would be little heat transfer at the nozzle walls. As heat transfer at the throat is not a subject of the current investigation, this assumption is also included in the

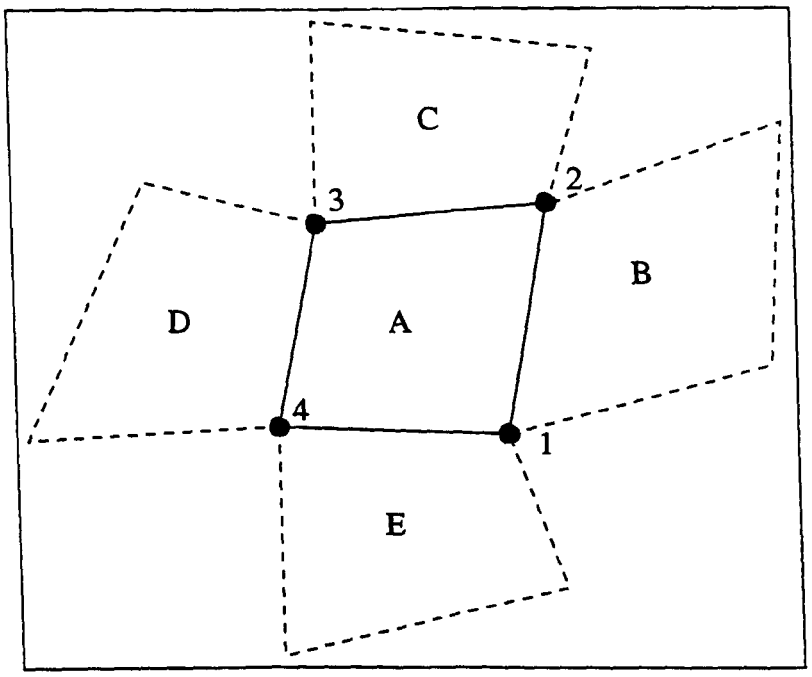

Figure 2.7: *Generalised Grid*

CFD method, and hence Eqn. 2.31 reduces to

$$\underline{U} = \begin{pmatrix} \rho \\ \rho u \\ \rho v \end{pmatrix}; \qquad \underline{F} = \begin{pmatrix} \rho u \\ \rho u^2 + P \\ \rho uv \end{pmatrix}; \qquad \underline{G} = \begin{pmatrix} \rho v \\ \rho uv \\ \rho v^2 + P \end{pmatrix}; \tag{2.32}$$

where

$$P = \rho \frac{\gamma - 1}{\gamma}(h_0 - (u^2 + v^2)) \tag{2.33}$$

It should be noted, however, that whilst this assumption reduces the number of equations solved and hence solution times, is not in itself a necessary step in the development of the Jameson method. Therefore, at a future date this assumption may be removed to allow for the effects of heat transfer at the walls on the flow produced in the throat of a rocket nozzle.

Over an arbitrary cell, A, (see Fig. 2.7) Eqn. 2.30 may be integrated via the Gauss divergence theorem to give

$$\iint_A \frac{\partial \underline{U}}{\partial t} dxdy + \int_S \underline{F} dy - \int_S \underline{G} dx = 0 \tag{2.34}$$

where S represents the cell boundary. As the flow properties (u, v, ρ) are stored at the cell centres, they may be made to represent the average values over the cell. Thus

$$\varpi \frac{d\underline{U}}{dt} + \int_S \underline{F} dy - \int_S \underline{G} dx = 0 \tag{2.35}$$

where ϖ is the area of cell A. By defining the flux velocity

$$W_k = (y_{k+1} - y_k)u_k - (x_{k+1} - x_k)v_k \tag{2.36}$$

Eqn. 2.35 may be approximated by

$$\varpi\frac{d\rho}{dt}+\sum_{k=1}^{k=4}(W_k\rho_k)=0$$

$$\varpi\frac{d\rho u}{dt}+\sum_{k=1}^{k=4}(W_k(\rho u)_k+\Delta y_k P_k)=0 \qquad (2.37)$$

$$\varpi\frac{d\rho v}{dt}+\sum_{k=1}^{k=4}(W_k(\rho v)_k-\Delta x_k P_k)=0$$

where k defines the cell vertex, numbered as shown in Fig. 2.7, and flow properties are averaged across suitable adjacent cells (i.e. u_1, is the average velocity for cells A and B, etc.). In theory, the integration forward in time of Eqn. 2.37 (denoted $P(\underline{U})$, the flux operator) should result in an accurate steady state solution. However, it is well known that in practise finite volume methods of central difference type are prone to instability, and hence require artificial dissipation.

2.2.3 Dissipation

In Ref. 39 Jameson outlines a combination of second and fourth order terms to provide the necessary damping. The fourth order terms damp oscillations over the entire computational domain, whereas the second order differences are only activated near shock waves, being turned off in areas of the flow in which such waves are not present. Whilst a well designed rocket nozzle throat under normal operating conditions should not develop shock waves, the calculation grid is extended a distance downstream of the throat, to form a short conical nozzle for reasons discussed in Sec. 2.2.7. Shock wave formation is a possibility within such nozzles (discussed in Sec. 3.2.2), and hence both the second and fourth order dissipation terms are included.

The dissipation is given by

$$\underline{D}(\underline{U})=\underline{D}_X(\underline{U})+\underline{D}_Y(\underline{U}) \qquad (2.38)$$

where

$$\underline{D}_X=d_{i+\frac{1}{2},j}-d_{i-\frac{1}{2},j} \qquad (2.39)$$

and

$$d_{i+\frac{1}{2},j}=\frac{\varpi_{i+\frac{1}{2},j}}{\Delta t^*_{i+\frac{1}{2},j}}\left[\kappa_{i+\frac{1}{2},j}(\underline{U}_{i+1,j}-\underline{U}_{i,j})-\xi_{i+\frac{1}{2},j}(\underline{U}_{i+2,j}-3\underline{U}_{i+1,j}+3\underline{U}_{i,j}-\underline{U}_{i-1,j})\right] \qquad (2.40)$$

$\varpi_{i+\frac{1}{2},j}$ is the average area of the two cells i,j and $i+1,j$, and $\Delta t^*_{i+\frac{1}{2},j}$ is the average over the same two cells of the time step that would achieve a local CFL of unity. $\kappa_{i+\frac{1}{2},j}$ is a second order damping function, given by

$$\kappa_{i+\frac{1}{2},j} = max(\Lambda_{i+1,j}, \Lambda_{i,j}) \tag{2.41}$$

where

$$\Lambda_{i,j} = K^{\kappa} \frac{|P_{i+1,j} - 2P_{i,j} + P_{i-1,j}|}{|P_{i+1,j}| + 2|P_{i,j}| + |P_{i-1,j}|} \tag{2.42}$$

and K^{κ} is a constant. As Λ is proportional to the second difference of pressure, it will tend to zero over the majority of the flow, where there are no shock waves. By defining the fourth order damping function $\xi_{i+\frac{1}{2},j}$ as

$$\xi_{i+\frac{1}{2},j} = max(0, (K^{\xi} - \kappa_{i+\frac{1}{2},j})) \tag{2.43}$$

(where K^{ξ} is another constant), the fourth order damping can be switched off near shock waves, to prevent it interfering with the second order terms. It should also be noted that Eqn. 2.40 is translated (not reflected) for the opposite side, i.e.

$$d_{i-\frac{1}{2},j} = \frac{\varpi_{i-\frac{1}{2},j}}{\Delta t^*_{i-\frac{1}{2},j}} \left[\kappa_{i-\frac{1}{2},j} (\underline{U}_{i,j} - \underline{U}_{i-1,j}) - \xi_{i-\frac{1}{2},j} (\underline{U}_{i+1,j} - 3\underline{U}_{i,j} + 3\underline{U}_{i-1,j} - \underline{U}_{i-2,j}) \right] \tag{2.44}$$

2.2.4 Time Stepping

Eqns. 2.37 and 2.38 may be combined to give

$$\underline{R}(\underline{U}) = \underline{P}(\underline{U}) + \underline{D}(\underline{U}) \tag{2.45}$$

Where $\underline{P}(\underline{U})$ is the flux operator, and $\underline{D}(\underline{U})$ the dissipation. Time integration is achieved via an explicit four stage Runge Kutta technique (as used in Ref. 40);

$$\begin{aligned}
\underline{U}^0 &= \underline{U}_{ij}^{t=t} \\
\underline{U}^1 &= \underline{U}^0 - \frac{1}{4}\frac{\Delta t}{\varpi_{ij}} \underline{R}(\underline{U}^0) \\
\underline{U}^2 &= \underline{U}^0 - \frac{1}{3}\frac{\Delta t}{\varpi_{ij}} \underline{R}(\underline{U}^1) \\
\underline{U}^3 &= \underline{U}^0 - \frac{1}{2}\frac{\Delta t}{\varpi_{ij}} \underline{R}(\underline{U}^2) \\
\underline{U}^4 &= \underline{U}^0 - \frac{\Delta t}{\varpi_{ij}} \underline{R}(\underline{U}^3) \\
\underline{U}_{ij}^{t=t+\Delta t} &= \underline{U}^4
\end{aligned} \tag{2.46}$$

and Δt is found using the method outlined in Ref. 37;

$$\Delta t = CFL \times min(\frac{\varpi}{\mid u\Delta y^l - v\Delta x^l \mid + a\Delta l}; \frac{\varpi}{\mid u\Delta y^m - v\delta x^m \mid + a\Delta m}) \tag{2.47}$$

in which

$$\begin{aligned}
\Delta l &= \sqrt{(\Delta x^l)^2 + (\Delta y^l)^2} \\
\Delta m &= \sqrt{(\Delta x^m)^2 + (\Delta y^m)^2} \\
\Delta x^l &= \frac{1}{2}(x_3 + x_2 - x_4 - x_1) \\
\Delta y^l &= \frac{1}{2}(y_3 + y_2 - y_4 - y_1) \\
\Delta x^m &= \frac{1}{2}(x_2 + x_1 - x_4 - x_3) \\
\Delta y^m &= \frac{1}{2}(y_2 + y_1 - y_4 - y_3)
\end{aligned} \tag{2.48}$$

Here subscripts refer to the cell vertices as defined in Fig. 2.7. The solution procedure is time accurate, (i.e. the time step used is the smallest Δt calculated over the entire flow domain).

2.2.5 Axisymmetric Flow

Transforming to cylindrical coordinates, where x, u are in the longitudinal direction (as before), and y, v are radial components, mass conservation requires

$$\frac{\partial \rho}{\partial t} + \nabla . \rho \underline{V} = 0 \tag{2.49}$$

where $\underline{V}$ is the velocity vector. In axisymmetric flow tangential velocities and gradients are zero, and hence the divergence reduces to

$$\nabla . \underline{V} = \frac{1}{y}\frac{\partial yv}{\partial y} + \frac{\partial u}{\partial x} \tag{2.50}$$

so Eqn. 2.49 becomes

$$\frac{\partial \rho}{\partial t} + \frac{1}{y}\frac{\partial \rho yv}{\partial y} + \frac{\partial \rho u}{\partial x} = 0 \tag{2.51}$$

$$\Rightarrow \frac{\partial \rho}{\partial t} + \frac{\partial \rho v}{\partial y} + \frac{\rho v}{y} + \frac{\partial \rho u}{\partial x} = 0 \tag{2.52}$$

Similar manipulation of x and y momentum equations results in

$$\begin{aligned}
\frac{\partial \rho u}{\partial t} + \frac{\partial \rho u^2 + p}{\partial x} + \frac{\partial \rho uv}{\partial y} + \frac{\rho uv}{y} &= 0 \\
\frac{\partial \rho v}{\partial t} + \frac{\partial \rho uv}{\partial x} + \frac{\partial \rho v^2 + p}{\partial y} + \frac{\rho v^2}{y} &= 0
\end{aligned} \tag{2.53}$$

Referring to Eqn. 2.30, we see that this becomes

$$\frac{\partial \underline{U}}{\partial t} + \frac{\partial \underline{F}}{\partial x} + \frac{\partial \underline{G}}{\partial y} + \frac{\underline{h}}{y} = 0 \tag{2.54}$$

where $\underline{U}, \underline{F}, \underline{G}$ are as defined in Eqn. 2.32, and

$$\underline{h} = \begin{pmatrix} \rho v \\ \rho uv \\ \rho v^2 \end{pmatrix} \tag{2.55}$$

As there are no derivatives in Eqn. 2.55, integrating w.r.t. dx and dy results in

$$\underline{H} = \varpi \underline{h} \tag{2.56}$$

Therefore, all that is required to transform the two-dimensional solution into that for axisymmetric flow is the addition of a source term $\underline{S}(\underline{U})$ s.t.

$$R(\underline{U}) = P(\underline{U}) + \underline{D}(\underline{U}) + \underline{S}(\underline{U}) \tag{2.57}$$

where

$$\underline{S}(\underline{U}) = \frac{\underline{H}}{y} \tag{2.58}$$

and y is measured to the midpoint of the cell.

2.2.6 Boundary Conditions

The boundary conditions at the centreline and nozzle wall are applied by requiring that the flux vector across these surfaces in the calculation of $P(\underline{U})$ is zero. The outflow boundary is supersonic and hence $\underline{U}_{ni,j}$ may be extrapolated from internal points. The inflow boundary, however, is subsonic, and whilst this allows one quantity to be extrapolated from internal points, two others must be imposed. This is achieved by assuming that the incoming flow is parallel to the nozzle centreline, and that total density is constant over the first two columns of cells.

The first of these assumptions results in the inflow velocity vector retaining merely the u component, which is extrapolated linearly from downstream cells. Eqn. 2.33 can then be re-arranged to give the local speed of sound, a, as

$$a = (h_0 - \frac{u^2}{2})(\gamma - 1) \tag{2.59}$$

and hence

$$M = \sqrt{\frac{u}{a}} \tag{2.60}$$

If total density is constant then

$$\rho = \frac{\rho_0}{(1 + \frac{\gamma-1}{2} M^2)^{\frac{1}{\gamma-1}}} \tag{2.61}$$

where ρ_0 is first calculated using ρ and M values from the immediate downstream cell. This provides enough information to calculate $\underline{U}_{1,j}$.

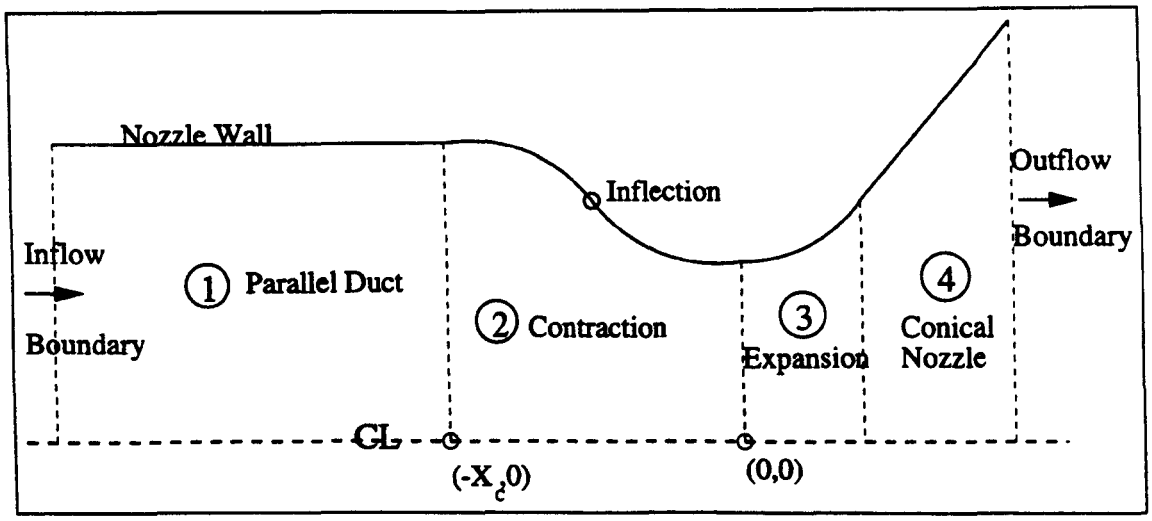

Figure 2.8: *Grid Regions*

2.2.7 Grid Generation

As with most CFD schemes, the generation of the computational grid is of critical importance, affecting the rate at which the solution converges, and even whether convergence occurs at all. Whilst for the purposes of the present analysis only the flow near to the throat is of significance, care must be taken with both inflow and outflow boundaries to ensure stability in these regions. The flow domain may therefore be considered to consist of four areas, as shown in Fig. 2.8. The coordinate system chosen is somewhat arbitrary, and is based around an origin at the intersection of the geometric throat and centreline to allow comparison with results produced by the power series techniques discussed in the previous section.

As previously mentioned, the flow properties at the inflow boundary are calculated assuming parallel onflow. To ensure sufficient distance to remove the effects of the contraction on the subsonic flow, the parallel duct (region 1 in Fig. 2.8) is extended upstream for a length of four times that of the contraction (X_C). The last column of cells in the parallel duct is equal in length to the first column of cells in the contraction to provide a smooth join between these two regions. However, to avoid excessive numbers of cells in an area of low gradients, the cell lengths are scaled linearly. Therefore the inflow boundary of the first column of cells lies at $-5X_C$, and the length of these and subsequent cells is given by

$$\Delta x = \overline{x} + (\frac{k-1}{2} - i)\frac{(\overline{x} - x_k)}{(\frac{k-1}{2})} \tag{2.62}$$

where i is incremented from 0 to $k-1$, x_k is the length of the final cell, and

$$\overline{x} = \frac{4X_C}{k}; \quad k = \frac{7}{32}n_i \tag{2.63}$$

n_i being the total number of cells in the x direction of the entire mesh.

The remainder of the cells are distributed approximately linearly across the contraction, expansion and conical sections (regions 2, 3, and 4 respectively). The exit plane of nozzle

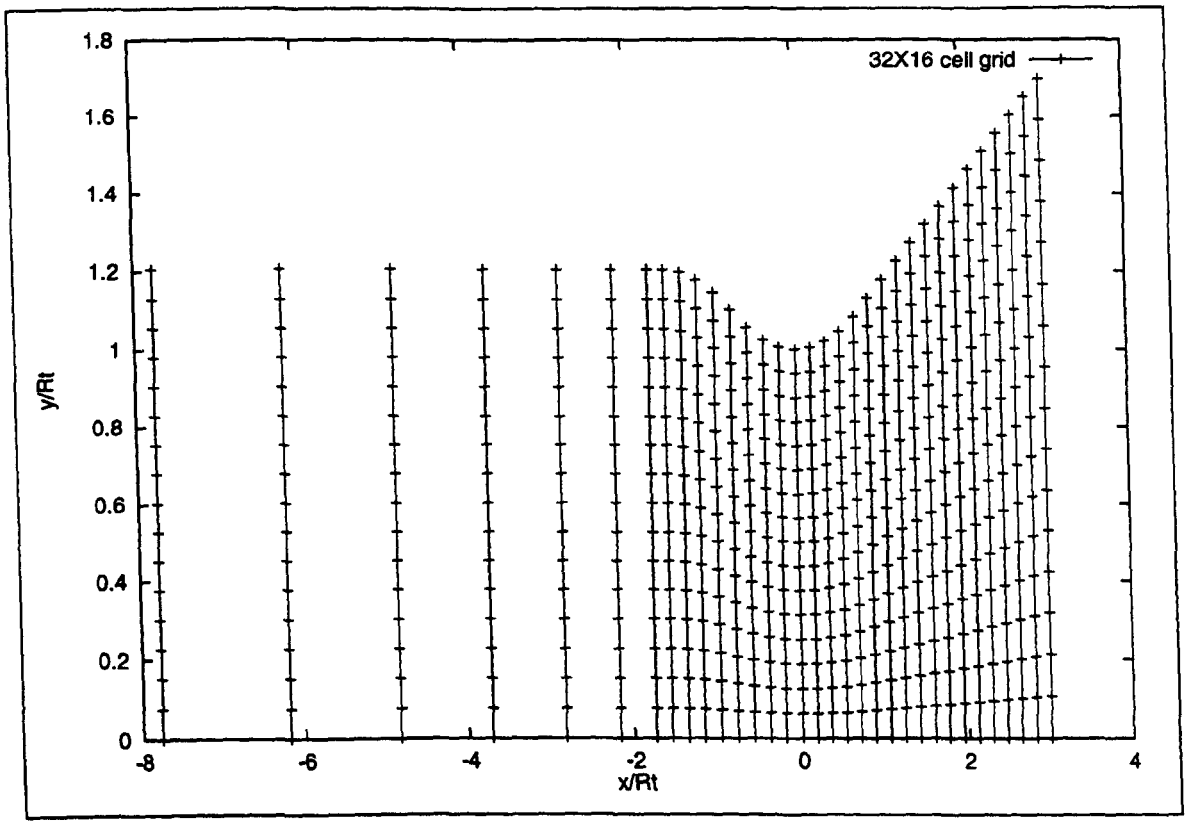

Figure 2.9: *Typical Mesh,* $R_w^{=} = 3$, *Circular Arc Walls*

is set at a user defined distance downstream from the geometric throat, x_{out}. This conical region of the nozzle ensures that the RRC emanating from the nozzle wall - geometric throat intersection will not cross the outflow boundary (a particular problem for nozzles with small $R_w^{=}$). Whilst flow derivatives in the conical region should be lower than at the throat and hence allow coarser grids, there is a possibility of shock waves developing within this region, especially for axisymmetric nozzles (see Sec. 3.2.2). The cell density therefore is maintained in this region.

The distribution of cells is only approximately linear, as a cell boundary is forced to coincide with the geometric throat of the nozzle (i.e. there exists a cell boundary at x = 0). This ensures that the radius of the nozzle throat is modelled accurately. However, all cells upstream of the throat are of equal length to each other, as are all cells downstream. The difference between the upstream and downstream cell length is minimised. All streamwise cell boundaries are vertical (radial in axisymmetric), and the flow domain is split uniformly in this direction. A typical (coarse) grid is shown in Fig. 2.9.

As was explained in the introduction to this section, one of the primary advantages of the computational technique compared to conventional perturbation methods is the ease with which unconventional throat configurations may be accommodated. As well as ED type throats, the CFD solutions process also allows non circular arcs, and indeed throat configurations of arbitrary character, to be considered for conventional nozzle designs. Only the grid generation need be altered, the solution process itself being unaffected. The grid generation

algorithm developed is based on elliptical wall curves, conventional circular arcs merely being a special case where the eccentricities of both the inflow and outflow ellipses arcs are zero. The wall contour before the point of inflection (see Fig. 2.8) is created by a 180 degree rotation of the elliptical wall between the point of inflection and the throat.

To reduce the time taken to convergence, an initial estimate of the flow properties throughout the computational domain is required. A simple approximation is provided by imposing one-dimensional flow properties. The Mach number at any point in a one-dimensional flow may be found from

$$\left(\frac{A}{A^*}\right) = \frac{1}{M^2}\left[\frac{2}{\gamma+1}(1+\frac{\gamma-1}{2}M^2)\right]^{\frac{\gamma+1}{\gamma-1}} \tag{2.64}$$

where the ratio A/A* is simply the vertical height of the channel in two-dimensional flow, and the square of this distance in axisymmetric. This process requires an iterative procedure, but once M is established, standard isentropic relationships may be used to provide the density and local speed of sound.

2.2.8 Multigrid Scheme

Multigrid schemes create a layering of the computational mesh, each cell of higher layers containing a number of those from the lower. This reduces solution times for a given flow problem by allowing high frequency corrections to occur on a fine grid, and lower frequency corrections on coarser meshes [41]. The CFD algorithm implemented incorporates a simple multigrid scheme which may operate as either a two or three grid 'V' cycle, and follows that presented in Ref. 42.

Eqn. 2.57 (or Eqn. 2.45 for two-dimensional flow) is repeated a number of times on the finest mesh, to perform an initial smoothing before the multigrid stage begins. The solution is then restricted to the next (coarser) mesh. As the Jameson scheme uses finite volume differencing in two dimensions, the coarser mesh contains four of the finer cells. The flow variables in a given coarse cell are therefore the average of these four fine cells, weighted to the area of each cell, i.e.

$$\underline{U}_N^R = \frac{\sum_1^4 \underline{U}_{N-1}^S \varpi_{N-1}}{\sum_1^4 \varpi_{N-1}} \tag{2.65}$$

where the subscript N refers to grid level, and superscripts R and S refer to restricted and smoothed solutions respectively. The second stage is to evaluate the forcing function, f_N

$$f_N = \sum_1^4 [R_{N-1}(\underline{U}_{N-1}^S) + f_{N-1}] - R_N(\underline{U}_N^S) \tag{2.66}$$

where $R(\underline{U})$ is as defined in Eqn. 2.57 or 2.45. Once the solution has been restricted, a series of iterations are performed before the solution is passed on to the next coarser mesh.

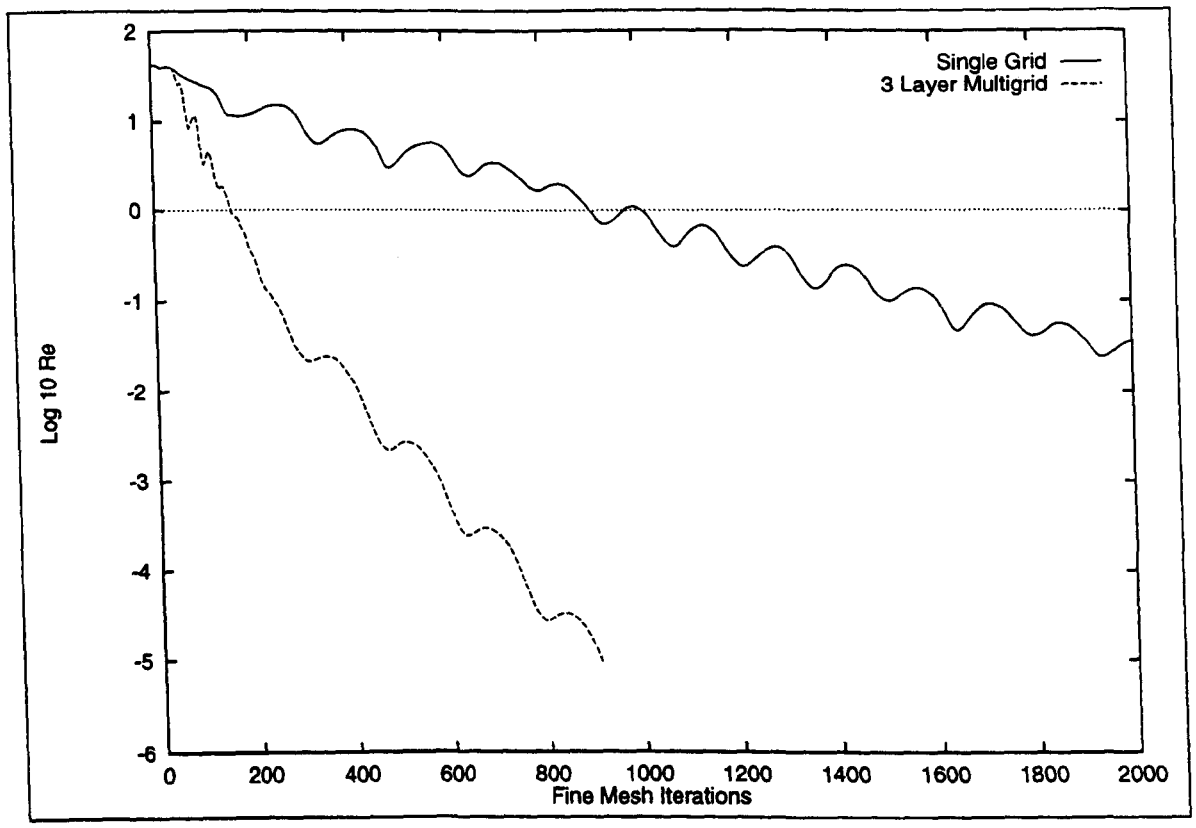

Figure 2.10: *Multigrid Speedup*

When the required number of iterations on the coarsest mesh have been performed, the solution must be prolonged back to the finest mesh. This is achieved one mesh at a time, passing on the change in the solution over the iterations, i.e.

$$\Delta \underline{U}_{N+1} = \underline{U}^S_{N+1} - \underline{U}^R_{N+1} \tag{2.67}$$

The corrections are then prolonged to the next finest grid, creating a new $\underline{U}^S_N$, which is used to generate a solution on the next finest grid, and so on. Prolongation is achieved via tri-linear interpolation.

Convergence of a computational scheme to the steady state is usually monitored by measuring the variation of the density residual. However, the purpose of this computational scheme is to provide input for a characteristics scheme, and the only outputs required are Mach number and flow angle. Convergence for this method is therefore determined by monitoring the Mach number residual, Re, defined by

$$Re = \frac{\sum_1^n |\Delta M|}{N \Delta t} \tag{2.68}$$

where n is the total number of cells is the mesh, and Δt is the global time step. The solution is considered to have converged when $Re < 10^{-5}$.

The effectiveness of the multigrid scheme is demonstrated in Fig. 2.10. Shown here is the convergence history for a two-dimensional flow case, specifically a circular arc nozzle with $R^{=}_w = 2, \gamma = 1.23$. The grid contains 320 cells in the flow direction, and 32 laterally.

The residual is shown against equivalent iterations of the finest mesh (i.e. four iterations on the second mesh are counted as equivalent to a single fine mesh iteration, as they require a similar number of calculations). As may be seen, the multigrid method dramatically reduces the time taken to convergence.

2.2.9 Validation of the Method

The Jameson technique has been widely used within the aerospace field for many years, and hence there is no need to validate the method itself, as this has already been achieved by many others for various applications. However, it is necessary to demonstrate that not only has the method been correctly implemented, but that it is suitable for this specific application, i.e. the transonic region of nozzle flows. Conventionally, the first stage of validation of the CFD technique is a comparison with an exact analytical solution. Whilst the power series methods outlined in the previous section are not exact, they will be extremely accurate where the perturbation assumption is most reasonable, as in the limit the perturbation equations tend to the exact equations. Therefore the solutions should be very nearly exact in the flow region near the sonic line in nozzles with large wall radii.

Fig 2.11 shows Mach contours and the mass flow through the throat region for the CFD and analytical methods, produced for a two-dimensional nozzle having circular arc throat walls, with $R_w^= = 5$, and $\gamma = 1.4$ (simulating air). The computational grid measured 128 by 32 cells. As may be seen from Fig. 2.11 (a), the Mach contours produced are very nearly

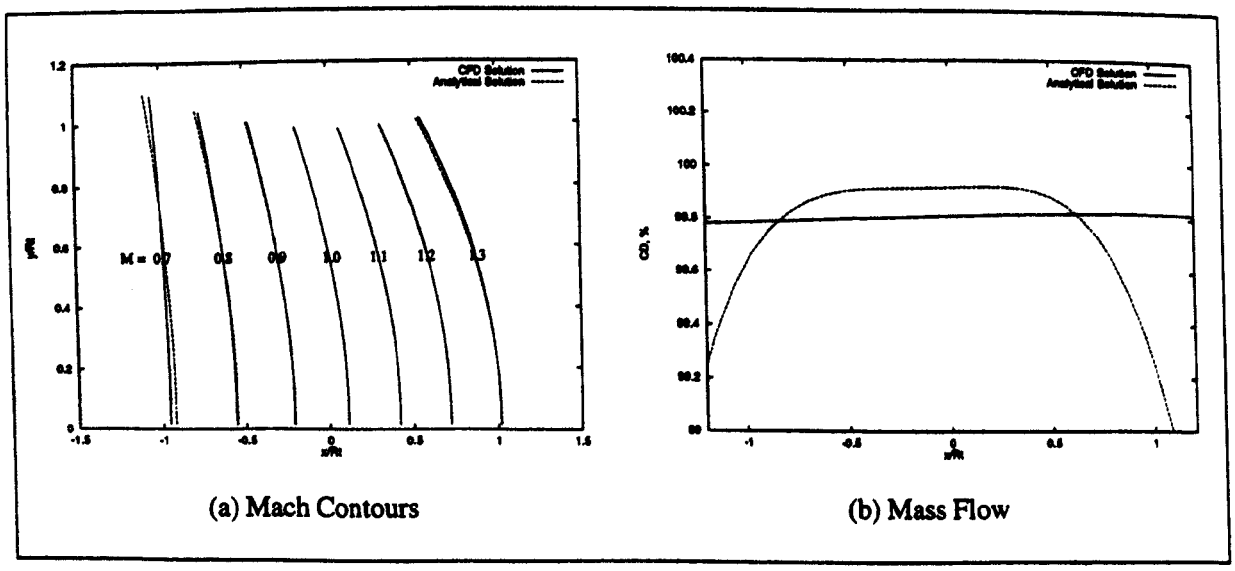

(a) Mach Contours (b) Mass Flow

Figure 2.11: *CFD and Analytical Methods* $R_w^= = 5R_t, \gamma = 1.4$, *Planar Flow*

identical for both methods; only at appreciable distances from the throat is any difference discernible. As the analytical solution is based on perturbations about the critical velocity, it is reasonable to ascribe these slight differences to the loss of accuracy of this assumption at large distances from the sonic line. This conclusion is supported by Fig. 2.11 (b), where the

improved conservation of mass produced by the computational method over this region is shown. The graph shows the mass flows produced by the two different methods, shown as a percentage of the one-dimensional mass flow rate of the nozzle (i.e. the discharge coefficient, C_D). The mass flow is calculated by integrating the mass flux along vertical grid lines.

Fig. 2.12 shows the Mach contours and mass flows for the same nozzle contours and specific heats, this time for axisymmetric flow. Very similar trends to the two-dimensional results are apparent. The Mach contours shown in Fig. 2.12 (a) are if anything even more similar than for the equivalent two-dimensional nozzle. This would be expected, as the Mach

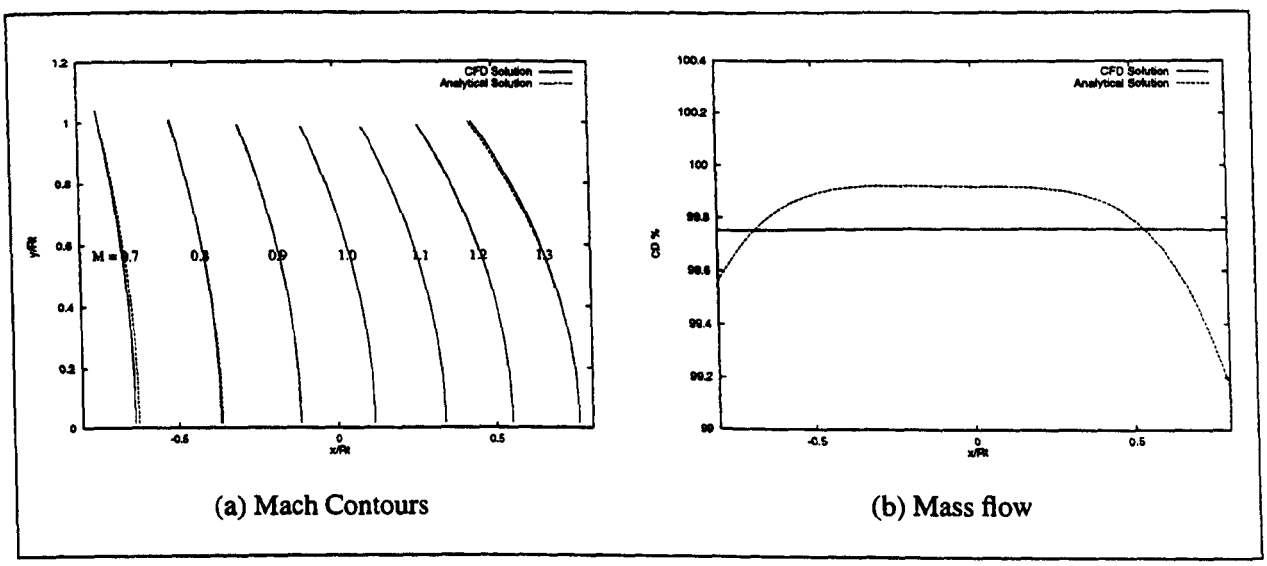

(a) Mach Contours

(b) Mass flow

Figure 2.12: *CFD and Analytical Methods* $R_w^{=} = 5R_t, \gamma = 1.4$, *Axisymmetric Flow*

contours in axisymmetric nozzles are closer together, due to the cross sectional area being proportional to the square of the local nozzle radius, and hence varying more rapidly in the throat region of an axisymmetric nozzle. As the Mach contours are therefore nearer the geometric throat, the perturbation scheme is more accurate.

2.3 Comparison of the Methods

The previous sections have outlined two different approaches which allow the flow of a gas through the throat region of a convergent divergent nozzle to be analysed, and a starting line for the Method of Characteristics produced. It has already been shown that both methods generate similar results for nozzles with large wall radii of curvature, and due to the nature of the analytical equations it may further be assumed that both methods are accurately modelling the inviscid flow-field. However, a more general comparison is necessary to determine the range of nozzle configurations for which the analytical method is accurate, as it is preferable to utilise the simpler and more rapid technique wherever good results may be expected.

2.3.1 Discontinuous Throat Curves

Before a presentation of the effect of wall curvature is given, the issue of discontinuous throat wall radii must be addressed. The derivation and description of both the computational and analytical schemes thus far have assumed a continuous wall radii of curvature in the throat region (i.e. $R_w^=$). However, this is not often the case in real rocket nozzle designs. The contraction before the throat generates an adverse pressure gradient along the wall, increasing boundary layer thickness and flow turbulence. These effects reduce with increasing R_w^-. In contrast, the expansion after the geometric throat produces a favourable pressure gradient, allowing the use of much smaller radii of curvature with no adverse effects. As a general rule, the smaller R_w^+, the shorter the overall nozzle, and hence R_w^+ is often considerably less than R_w^- (although taking this to the extreme of using a sharp corner, i.e. zero wall radius, will result in unwanted separation of the flow).

For the computational method this presents no particular problem, as the geometry of the throat region has no effect on the solution method, and hence throats with either a constant or variable wall radius may be modelled with equal ease. However, the analytical methods described require $R_w^=$ to ensure that the equations used to model the flow are accurate. This in turn means that a complete picture of the flow-field around the geometric throat cannot be produced.

Fortunately, the analytical schemes are required only to define the first RRC in the nozzle flow. As this characteristic originates at the intersection of the wall and geometric throat, it in effect marks the downstream boundary of the area of flow-field independent of the post throat curve, assuming that the flow is supersonic along the entire characteristic (see Fig 2.13). This means that once an RRC has been generated from a symmetric throat flow solution, it may be used as input for any alternative post throat radius. In fact, due to this flow phenomenon, a reduction in time consuming CFD program operations may be achieved by only solving for geometries where $R_w^=$, and using the resulting RRC for a range of post throat curve configurations.

For extremely large $R_w^=$, it is possible that the first RRC may intersect the sonic line, and thus become subsonic. This would require a characteristic emanating from a point further downstream to be used as input to the MoC algorithms, and the properties along such a characteristic would depend on R_w^+. However, the characteristic line produced for a $R_w^=$ of 5 was found to be entirely supersonic for both two-dimensional and axisymmetric flow-fields. As this is the largest wall radius used in any nozzle calculations in this thesis, and is considerably larger than the largest R_w^- that would be expected on any reasonably designed rocket nozzle, this possibility could safely be ignored.

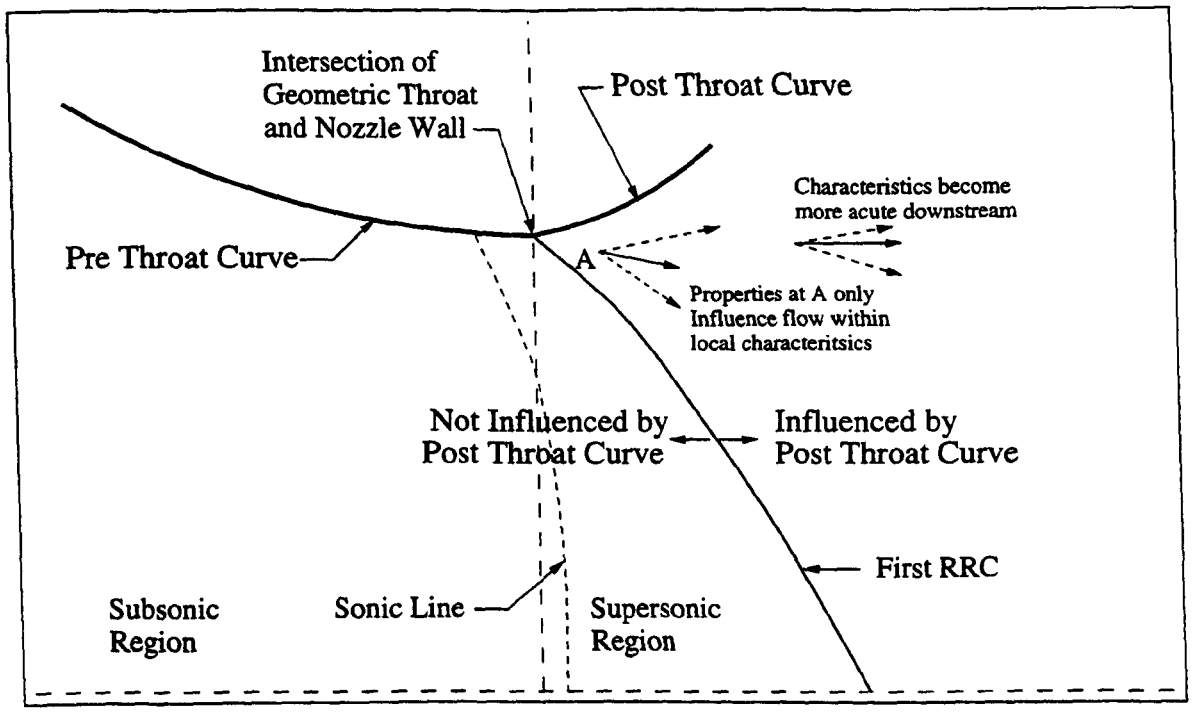

Figure 2.13: *First RRC in Nozzle Flow, Discontinuous Wall Radii*

2.3.2 Small Wall Radii

As has already been shown here and elsewhere [35], the Dutton Addy method remains stable down to small throat wall radii ($R_w^{=} < R_t$). However, the smaller the wall radius, the greater the perturbations of the velocity components near the geometric throat, and hence the less accurate the analytical method becomes. Whilst some experimental evidence exists to show that the results are accurate even for nozzles with wall radii of curvature equal to the throat radius (results for a nozzle with $R_w^{=} = R_t$ are compared to experimental results from Ref. 43 in Ref. 35), this concerns only a single test case. Therefore, a comparison of results obtained by the two techniques for nozzles having continuous throat wall radii of various sizes is presented.

The figures on the following four pages show the effect on the predicted properties of the first RRC in the nozzle flow (as defined in Fig. 2.13) generated by the computational and analytical methods for a range of $R_w^{=}$ values, flow dimensions, and ratio of specific heats. For each configuration, the spatial location of the this RRC is shown, along with the variation of Mach number along the length of this characteristic. In all cases, the computational mesh contained 128 and 32 cells in the longitudional and lateral directions respectively.

Figs. 2.14 and 2.15 show results for a nozzle with a planar throat, with $\gamma = 1.4$. As may be seen, for nozzles with wall radii of 2 and 3 times the nozzle throat half height, the computational and analytical methods produce very similar results. However, as $R_w^{=}$ is further reduced, the two methods begin to diverge, with the analytical method predicting higher Mach numbers and a corresponding downstream shift in the location of the characteristic

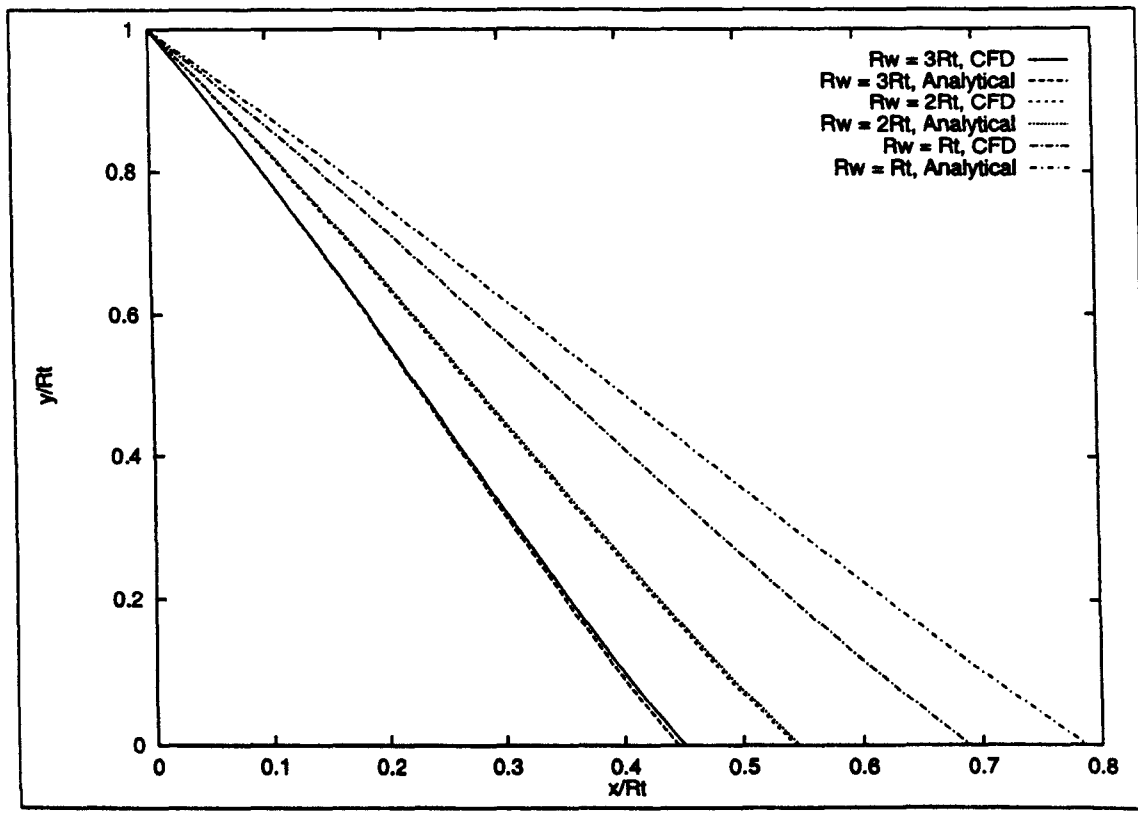

Figure 2.14: *First RRC's, $\gamma = 1.4$, Planar Flow*

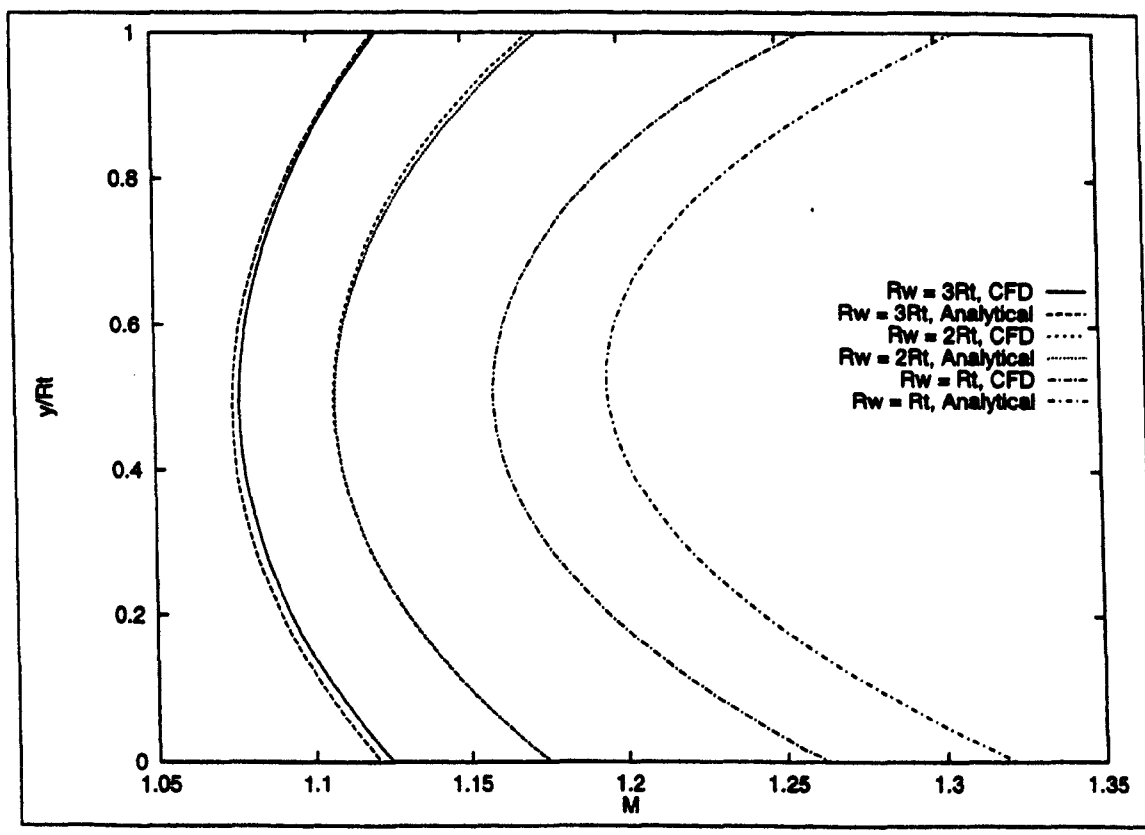

Figure 2.15: *Mach Number Along First RRC's, $\gamma = 1.4$, Planar Flow*

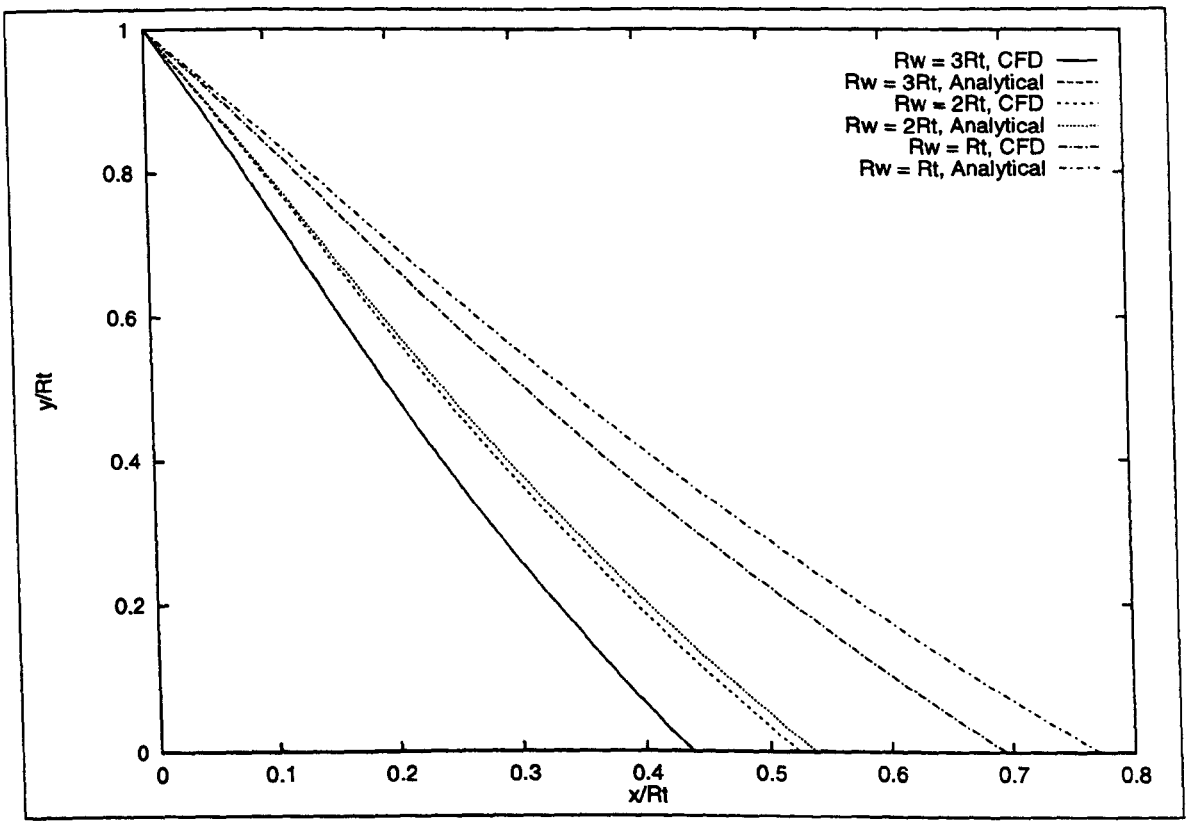

Figure 2.16: *First RRC's, $\gamma = 1.4$, Axisymmetric Flow*

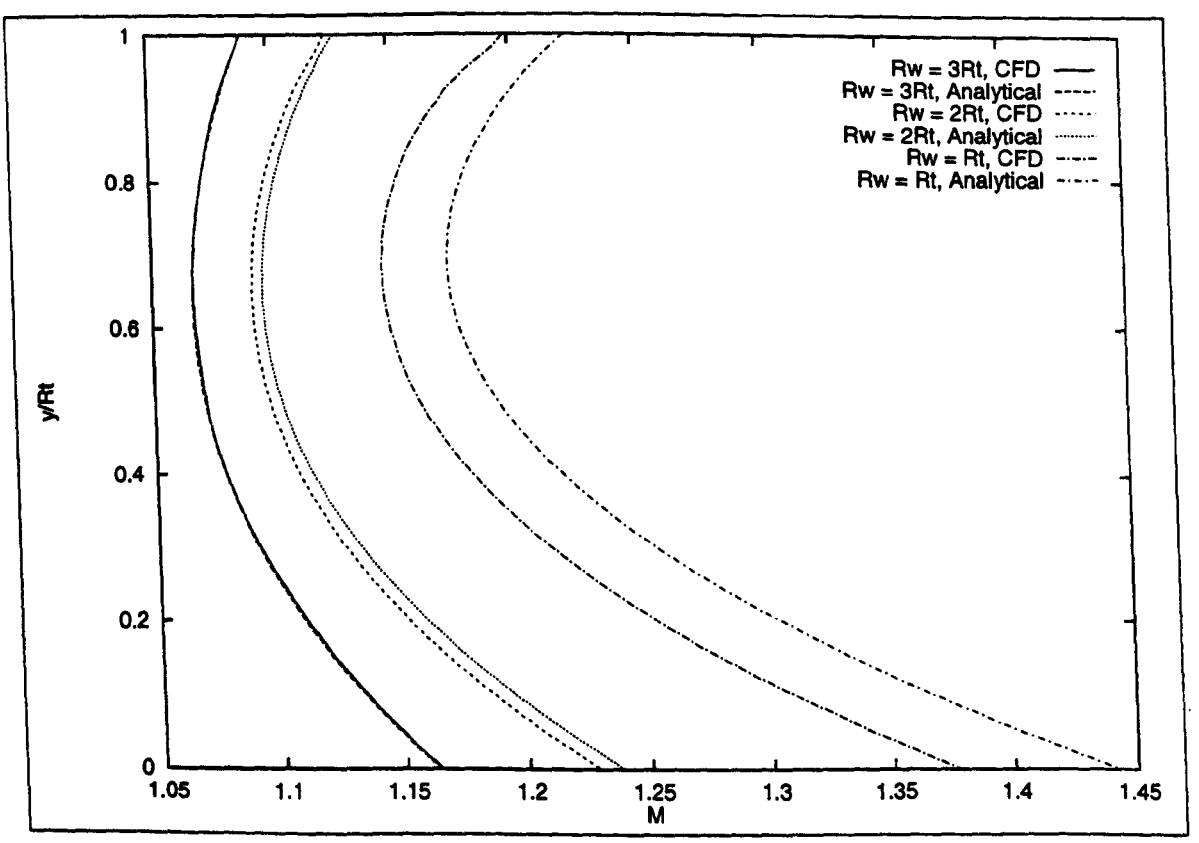

Figure 2.17: *Mach Number Along First RRC's, $\gamma = 1.4$, Axisymmetric Flow*

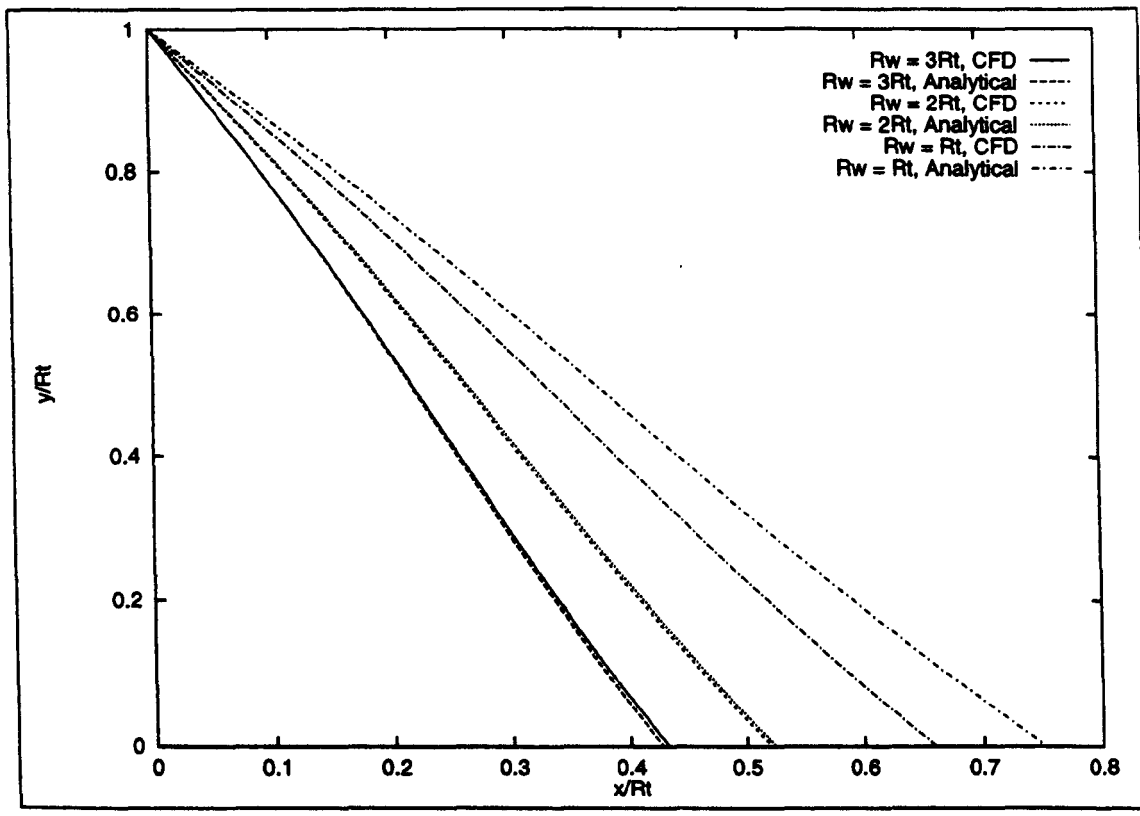

Figure 2.18: *First RRC's, $\gamma = 1.23$, Planar Flow*

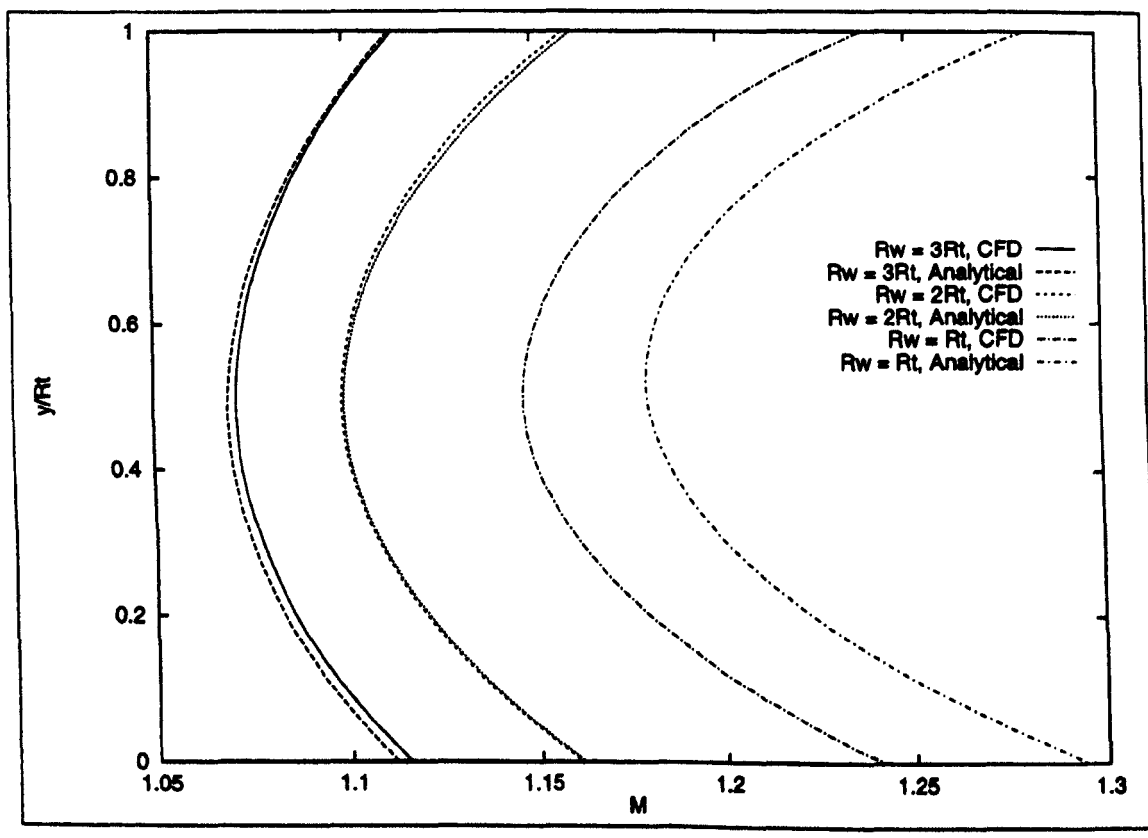

Figure 2.19: *Mach Number Along First RRC's, $\gamma = 1.23$, Planar Flow*

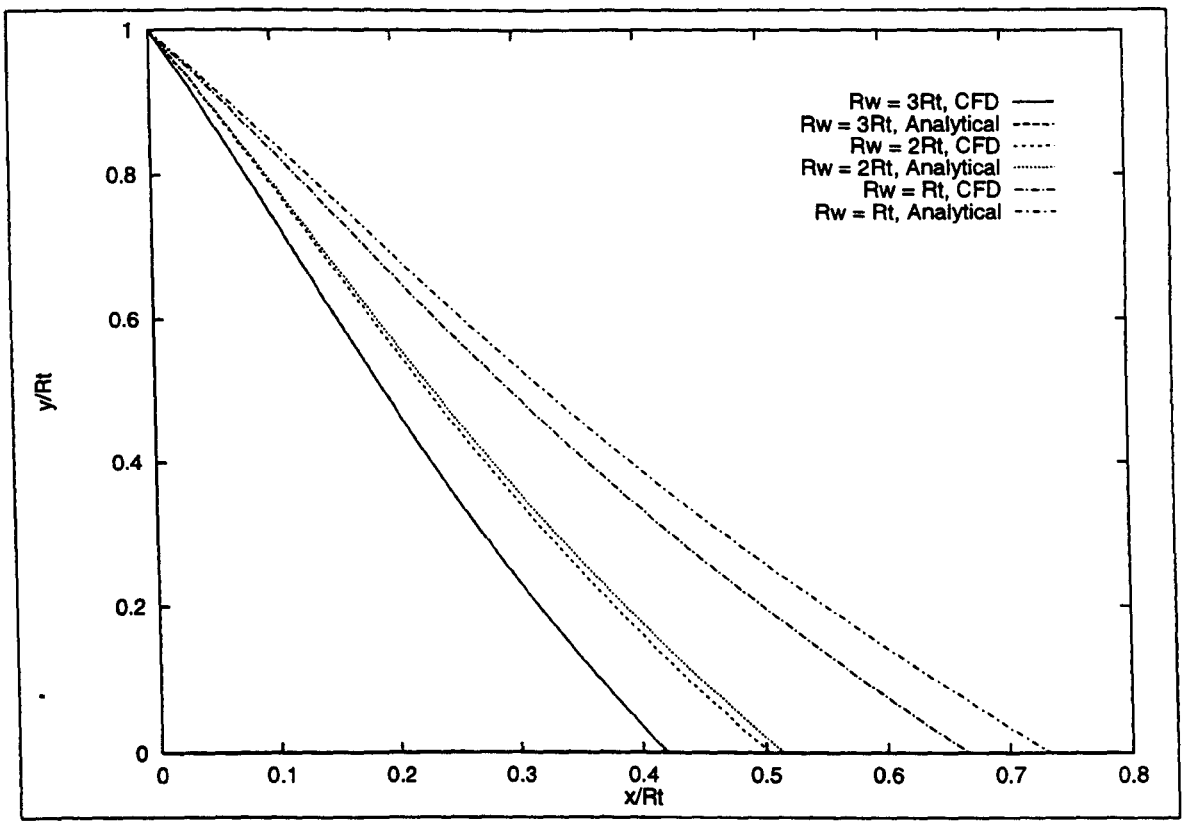

Figure 2.20: *First RRC's, $\gamma = 1.23$, Axisymmetric Flow*

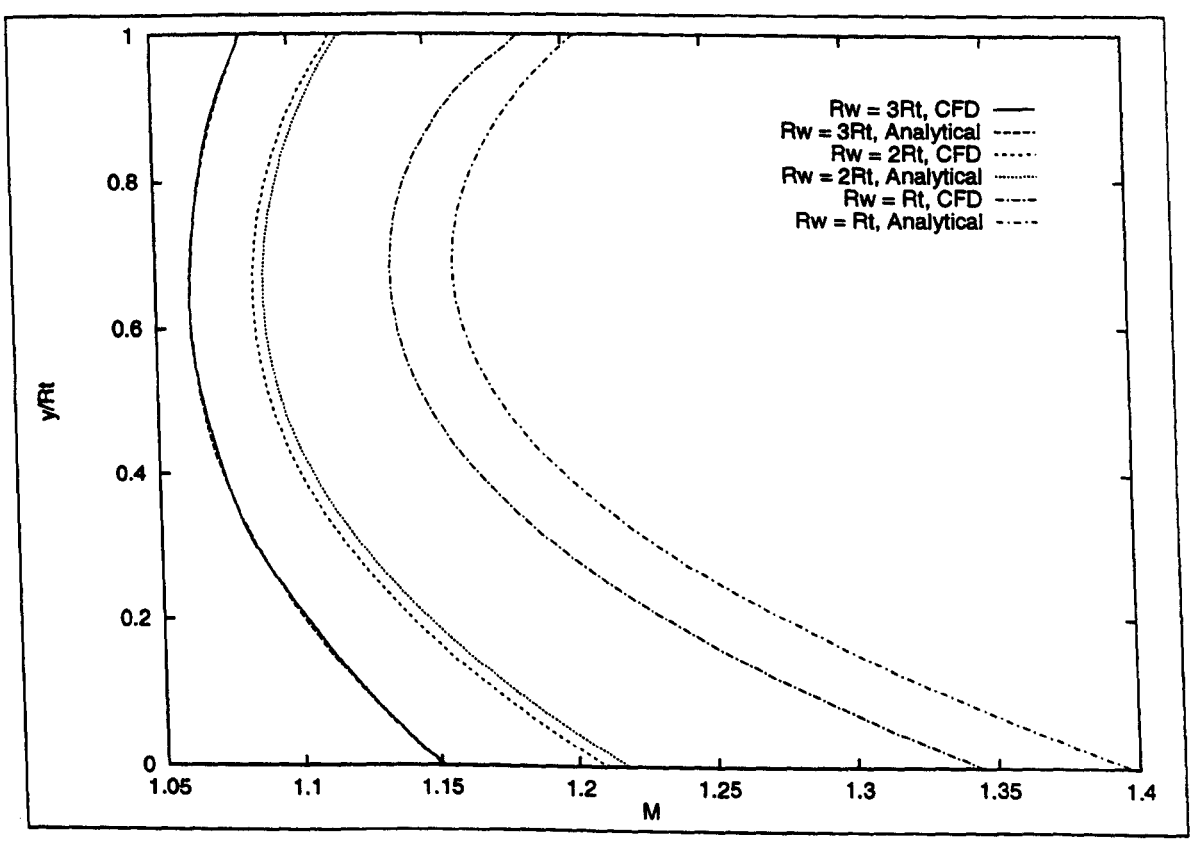

Figure 2.21: *Mach Number Along First RRC's, $\gamma = 1.23$, Axisymmetric Flow*

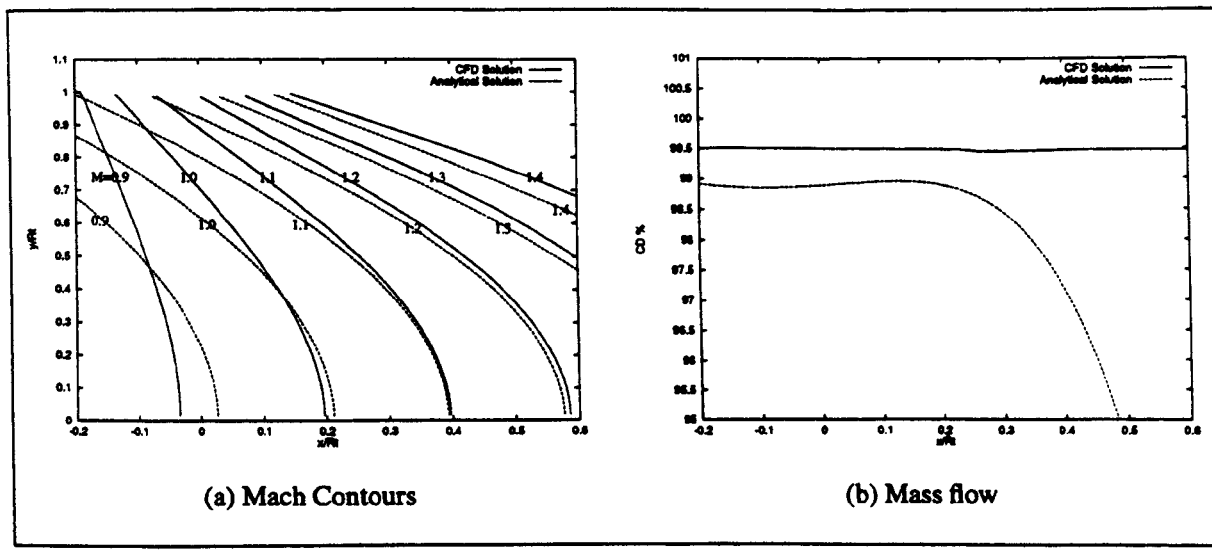

(a) Mach Contours

(b) Mass flow

Figure 2.22: *CFD and Analytical Methods* $R_w^= = R_t, \gamma = 1.23$, *Planar Flow*

near the nozzle centreline.

A similar picture emerges in the axisymmetric case (Figs. 2.16 and 2.17), although the differences between the two techniques is slightly less pronounced.

To simulate the behaviour with a fluid flow more representative of the products of rocket propellant combustion, the same nozzle configurations were analysed with $\gamma = 1.23$, an approximation of LOx/LH exhaust products. Figs. 2.18 and 2.19 present results for the planar nozzle, and Figs. 2.20 and 2.21 for the axisymmetric. Similar trends are evident for this propellant combination.

Whilst these results show where differences arise between the techniques, they do not provide conclusive evidence demonstrating which is more accurately modelling the flow. To allow such an assessment to be made, a more complete analysis of the flow predicted by each technique in this region is required. Figs. 2.22 and 2.23 show Mach contours and mass flows over the entire throat region produced by the computational and analytical methods, for a nozzle wall radius equal to the throat radius (the smallest considered in both planar and axisymmetric flow).

These figures reveal that the analytical method is still producing generally good results in the region near to the throat, especially for the axisymmetric case. Large variations between the methods occur upstream of the throat, but this is due to the influence of the shape of the contraction on the CFD produced solution, not included in the analytical model. In the supersonic region just downstream of the throat (of primary interest as it is from here that the first RRC is extracted), the contours match quite well. However the analytically derived results show slightly higher wall Mach numbers for a given streamwise location. This is in agreement with available experimental data [35], where the method was found to match with experimental results extremely well along the nozzle centreline, but slightly over predict

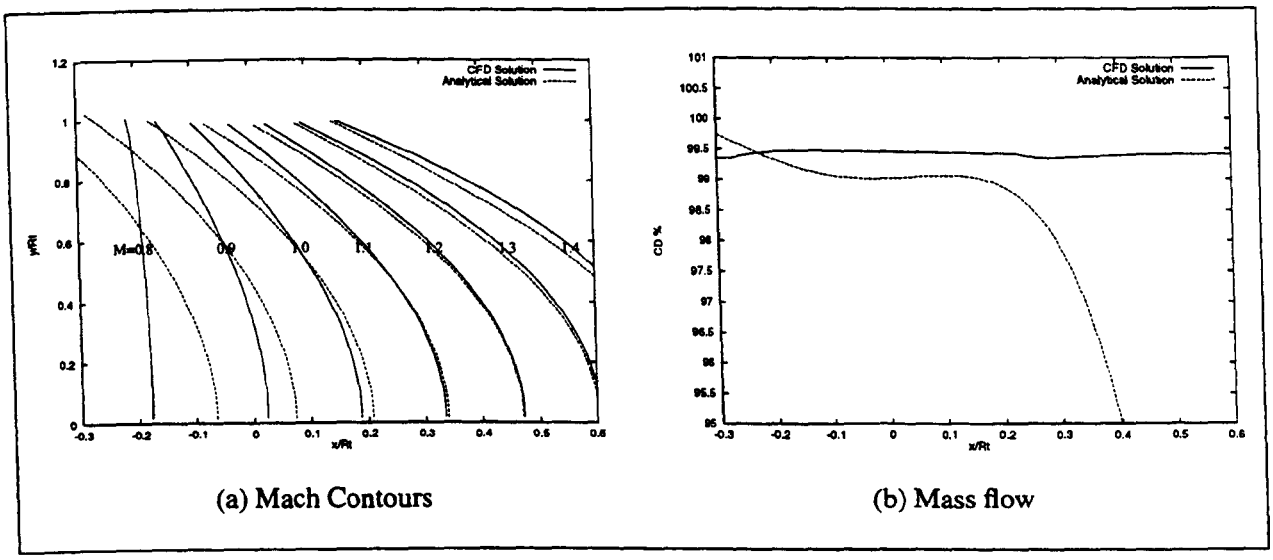

(a) Mach Contours

(b) Mass flow

Figure 2.23: *CFD and Analytical Methods* $R_w^{=} = R_t, \gamma = 1.23$, *Axisymmetric Flow*

Mach numbers on the nozzle wall.

The mass flows predicted by the two techniques are also presented, and once again it is clear that the computational technique obeys the continuity equation more accurately. Moreover, the error produced by the analytical technique at distances from the throat is considerably more pronounced than for nozzles with large $R_w^{=}$ (Figs. 2.11 and 2.12). This is as expected, as the reduced wall radius increases the importance of the higher order terms.

In conclusion, it may be surmised that the Dutton Addy method produces a good model of the flow over most $R_w^{=}$, but for very small throat radii it has a tendency to over predict the Mach number at the wall near the throat, and this in turn results in a first RRC that is further downstream than it actually occurs in a real flow. The computational method, however, does not suffer from this weakness. How this effects the design and analysis of the complete nozzle is discussed in the next chapter.

Chapter 3

Conventional Nozzle Analysis

Under normal operating conditions, the majority of the flow in a conventional nozzle is supersonic downstream of the throat. As the equations governing the flow of such a fluid are spatially hyperbolic, the flow variables at a point are dependent solely upon the upstream flow-field. This means that the properties of a flow may be found by marching downstream from a set of known conditions. By further assuming that the effects of the viscosity of the fluid are negligible outside thin and attached boundary layers, the Navier Stokes equations may be reduced to the Euler equations. The Method of Characteristics (MoC) provides a suitable analytical method for modelling such inviscid, supersonic flow, and many previous authors have used the technique for the analysis and design of both conventional and ED nozzles.

As the MoC is an analytical method, it allows much more rapid analysis of flows than is possible with numerically based CFD techniques widely used in many fields of aerodynamics (such as the Jameson method described in the previous chapter). Further, storage of large grids is not required, as grid formation is a part of the solution process. However, it is strictly limited to purely supersonic and inviscid flows, and control of the mesh in areas of rapid variable change or particular interest is difficult. Neither of these limitations effect the ability of the method to model the entirety of the supersonic flow within conventional nozzles.

The previous chapter considered in detail the methods by which the transonic throat region may be analysed, and described how the first Right Running Characteristic (RRC) in a nozzle flow may be obtained. This chapter describes how the remainder of the supersonic nozzle flow-field may then be modelled using the MoC, and how, in combination with the calculus of variations, length optimised nozzle contours designed. Comparisons of the performance of various conventional nozzles are included, demonstrating not only the improved performance of optimised contours, but also providing data to allow comparison with the ED

nozzles described in subsequent chapters. An analysis of the sensitivity of this performance data to input variables (particularly throat wall radius) is also considered. To begin, however, a brief overview of the MoC is provided, as this forms the core of all the nozzle flow calculation algorithms subsequently discussed.

3.1 The Method of Characteristics

Characteristic lines in a flow-field are defined as the directions in which flow variables (P, ρ, u, v etc.) are continuous, but flow variable derivatives are indeterminate (or even discontinuous). Along these lines, and only these lines, it is possible to transform the partial differential conservation equations that govern the flow into ordinary differential equations, called compatibility equations. As these ordinary differential equations are integrable, this allows the flow-field variables to be calculated along the characteristics if boundary conditions and an input characteristic are known. These compatibility equations differ depending on whether the flow-field under consideration is rotational or irrotational, and whether it is two-dimensional or axisymmetric (full three-dimensional analysis, with some restrictions, is also possible but not relevant to the nozzle analysis considered in the present investigation).

As only full flowing conventional nozzles operating at or near their design points are to be considered, it is assumed that the flow-field will not contain shock waves or areas of separated flow. This in turn means that the flow may be treated as irrotational, reducing the complexity of the derivation and resulting equations. As the MoC has been in widespread use for many years, derivation of the equations may be found in several textbooks (for instance Refs. 44 and 45 for two-dimensional and axisymmetric irrotational flow respectively), and hence is not reproduced here. However, the resulting equations are outlined, along with a description of how these basic equations may be implemented into a computational algorithm.

The derivation process reveals that the directions of the characteristics lines are the same in both two-dimensional and axisymmetric flow, and are given by

$$\frac{dy}{dx} = \tan(\theta \mp \mu) \tag{3.1}$$

where θ and μ are flow and Mach angles respectively. The characteristic lying at the Mach angle above the flow direction is known as a Left Running Characteristic (LRC), and that below a Right Running Characteristic (RRC).

If an arbitrary point in space (denoted 3 in Fig. 3.1) is joined by a RRC to point 1 and by a LRC to a second point 2, both of which are upstream of 3 and have known flow properties,

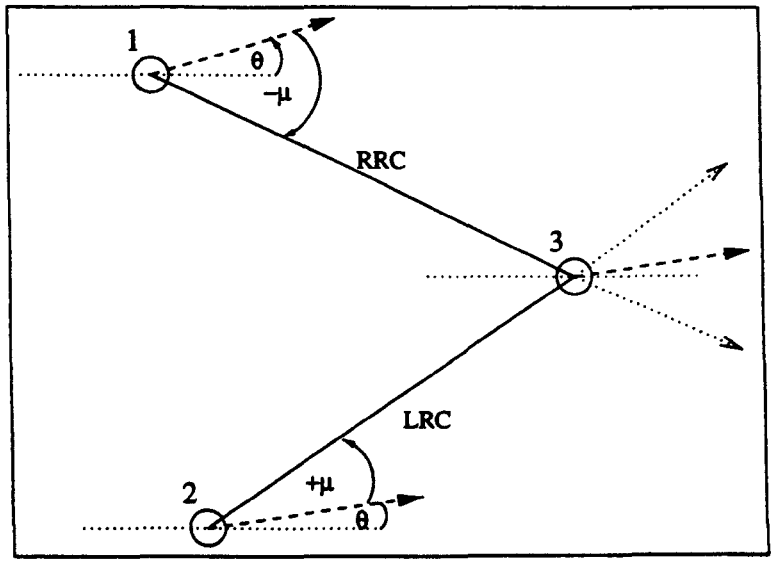

Figure 3.1: *Characteristic Lines*

then

$$\nu_3 = \frac{1}{2}(F1 + F2 + F1i + F2i) \tag{3.2}$$

$$\theta_3 = \frac{1}{2}(F1 - F2 + F1i - F2i) \tag{3.3}$$

where

$$F1 = (\nu_1 + \theta_1); \qquad F2 = (\nu_2 - \theta_2) \tag{3.4}$$

and ν is the Prandtle-Meyer function

$$\nu = \int_{M=1}^{M} (M^2 - 1)^{\frac{1}{2}} \frac{dV}{V} \tag{3.5}$$

The only difference between two-dimensional and axisymmetric flow lies in the functions $F1i$ and $F2i$. For irrotational flow, the two-dimensional form is

$$F1i = F2i = 0 \tag{3.6}$$

and that for axisymmetric (expressed as a finite difference approximation) is

$$F1i = \frac{1}{\sqrt{M^2 - 1} - \cot\theta} \frac{\Delta y_{13}}{y}; \quad F2i = \frac{1}{\sqrt{M^2 - 1} + \cot\theta} \frac{\Delta y_{23}}{y} \tag{3.7}$$

where

$$\Delta y_{13} = y_3 - y_1; \quad \Delta y_{23} = y_3 - y_2 \tag{3.8}$$

and flow variables (M, θ, y) are averages between the appropriate two points. Once ν_3 is known, M_3 and μ_3 follow from

$$\nu = \sqrt{\frac{\gamma+1}{\gamma-1}} \tan^{-1} \sqrt{\frac{\gamma-1}{\gamma+1}(M^2 - 1)} - \tan^{-1} \sqrt{M^2 - 1} \tag{3.9}$$

(the integrated form of Eqn. 3.5), and

$$\mu = \sin^{-1}\frac{1}{M} \tag{3.10}$$

Next, the slope of the LRC is found by approximating the curve between points 2 and 3 as a straight line

$$\phi_L = \frac{1}{2}[\theta_3 + \mu_3 + \theta_2 + \mu_2] \tag{3.11}$$

and similarly that of the RRC is

$$\phi_R = \frac{1}{2}[\theta_3 - \mu_3 + \theta_1 - \mu_1] \tag{3.12}$$

The position of the new point is located at the point of intersection of these two lines, i.e.

$$x_3 = \frac{y_2 - y_1 - x_2 \tan\phi_L + x_1 \tan\phi_R}{\tan\phi_R - \tan\phi_L} \tag{3.13}$$

and

$$y_3 = y_2 + [x_3 - x_2]\tan\phi_L \tag{3.14}$$

In axisymmetric flows, the values of the functions $F1i$ and $F2i$ are dependent upon the properties of the flow at point 3, and hence an iterative process is required.

3.2 Conical Nozzle Flows

The simplest form of nozzle in common use is the conical nozzle. This type has the advantage of easy and cheap construction without significant performance loss, and hence provides a bench mark against which more complex higher performance nozzles may be compared. Both two-dimensional (or planar) and axisymmetric conical nozzles may be analysed using the MoC.

3.2.1 Planar Conical Nozzles

Whilst by definition planar nozzles are never actually conical, the name is used due to the similarities between this nozzle type and true (axisymmetric) conical nozzles. In a planar conical nozzle the flow is first expanded around the post throat arc (generally circular) until the required wall angle is reached. The remainder of the nozzle is then formed by a linear nozzle wall contour at this angle, which is equivalent to the cone half angle of true conical designs.

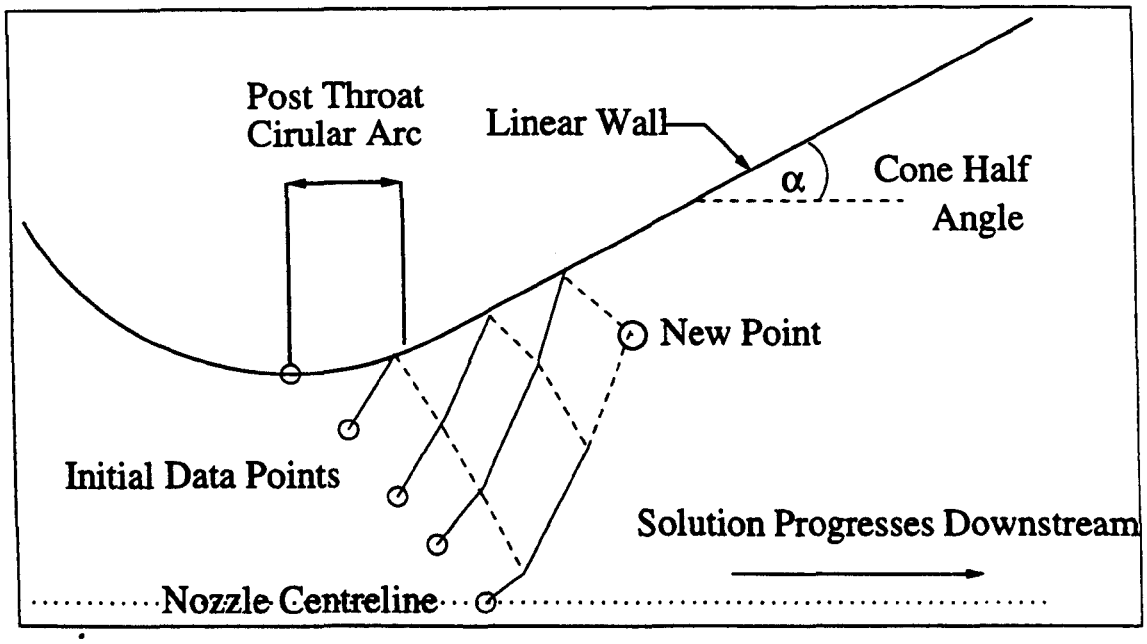

Figure 3.2: *Planar Conical Nozzle Analysis*

This reduces the analysis of such nozzles to the simple task of marching downstream, generating successive characteristics of a family. Either RRC's or LRC's may serve this purpose, although utilising LRC's reduces the area of flow analysed, and hence the solution is arrived at more rapidly. Calculation of points along each characteristic follows the method described in the previous section. Points on the nozzle wall have a known flow angle (equal to the cone half angle), and the flow along the centreline is axial. This leaves only a single unknown (ν), allowing solution at the flow boundaries. Fig. 3.2 demonstrates the flow solution process graphically.

3.2.2 Axisymmetric Conical Nozzles

Analysis of axisymmetric conical nozzles presents a greater problem. Characteristic lines in axisymmetric flow tend to be more highly curved than in an equivalent planar geometry. This in turn leads to difficulties when analysing conical nozzles using the method described previously for planar flows. If the post throat curve terminates abruptly at the cone half angle, a step change in the flow angle derivative occurs at this point. This leads to a convergence of the characteristics emanating from the nozzle wall in this region, which in turn leads to the formation of a shock wave within the flow. This is undesirable, as the assumption of irrotational flow made in the derivation of the MoC is violated.

Whilst it is possible to derive a set of compatibility equations that do not require this assumption (the so called rotational MoC), they too are invalid through a shock wave. Solution of the flow therefore requires an iterative procedure based on the oblique shock wave equations to find flow properties beyond the shock wave, from where the rotational MoC may proceed. However, this greatly increases the complexity of the solution method, and hence

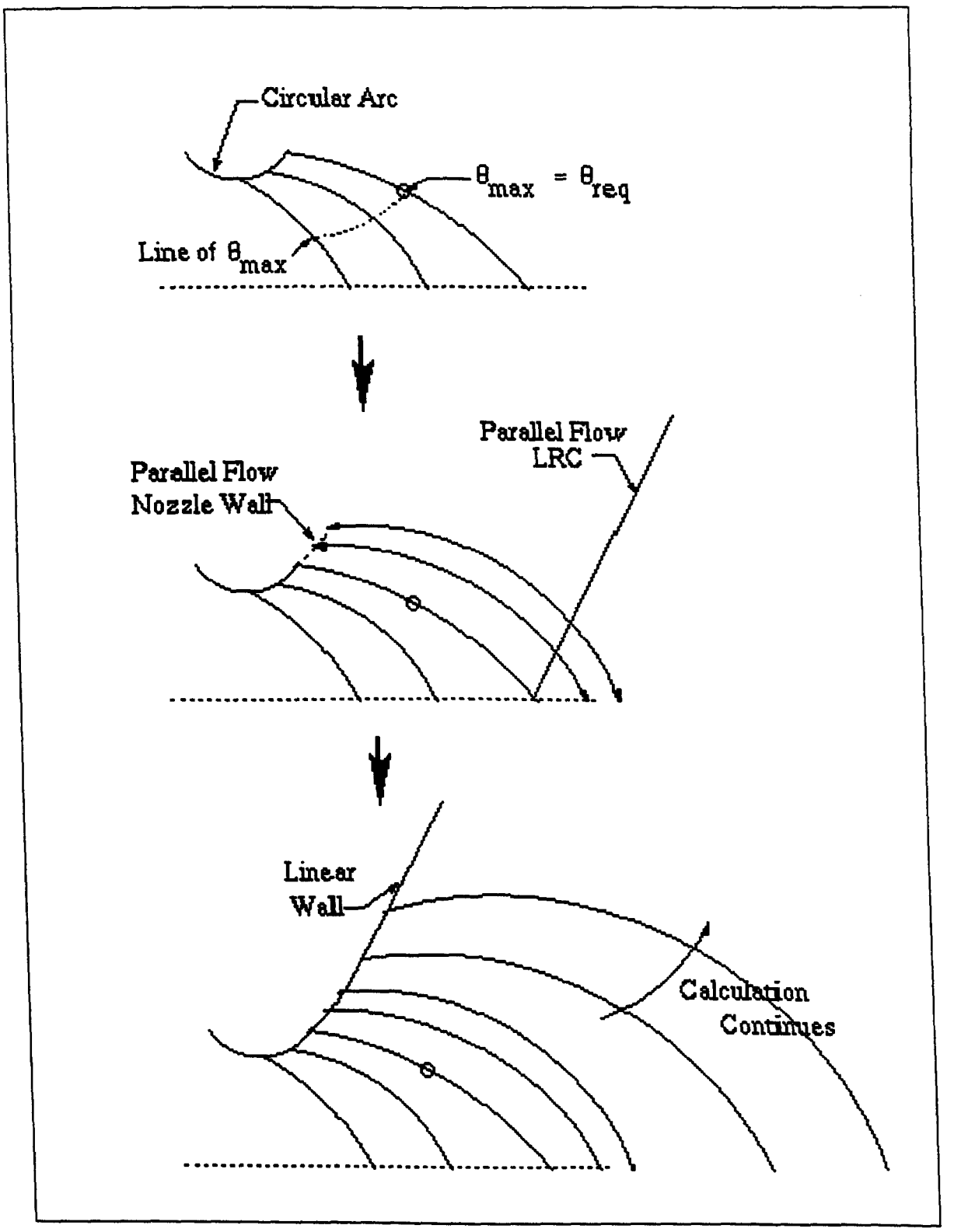

maximum

Figure 3.3: *Shock- Free Conical Nozzle Generation*

the time required for a flow solution to be generated.

A simpler and more elegant approach is to design the nozzle contour in such a way that this shock wave does not form. This has the further advantage of removing performance losses associated with this non isentropic flow process. The phenomena of shock formation within conical nozzles was analysed by Darwell and Badham [46], and a method devised by which shock free axisymmetric conical nozzles could be designed was devised.

This is achieved by the insertion of a short section of a parallel flow contour between the post throat curve and linear wall sections of the nozzle. A parallel flow nozzle is designed to produce uniform and axial flow at the exit plane, which results in a nozzle of considerable length. However, as only a relatively short section of the final conical nozzle is created in this manner, the effect on overall length is negligible, whilst the step change in wall angle gradient (and thus the shock wave) is removed.

Figure 3.3 shows the process by which such nozzles may be created. Initially, the flow is expanded around the post throat arc in the usual manner, and flow properties are calculated along successive RRC's. The maximum angle on each RRC is found, and the expansion continues until this angle reaches a user defined value (θ_{req}), which will be approximately the cone half angle of the final nozzle. A LRC with a constant and axial flow angle is then created from the intersection of this RRC and the centreline. Examination of Eqn. 3.7 reveals that if θ is zero, $F1i$ and $F2i$ must also be zero, as $\cot\theta$ will be infinite. As this is the case, it follows that ν and therefore M and μ are also constant, resulting in the LRC being a straight line, all properties along which are constant. The region between this LRC and the nozzle wall may be backfilled (in the directions of the arrows in the figure) using the MoC, with the equations suitably adjusted. The wall contour follows the streamline originating at the post throat arc, and this process continues until a maximum wall angle is reached. At this point, the wall angle is maintained at this maximum for all downstream coordinates, and a conical nozzle is formed.

3.3 Optimised Contours

The method outlined here for the generation of contours optimised for minimum length for a given thrust was first presented by Rao in axisymmetric form in Ref. 3. That which follows is a summary of that paper, combined with a description of the techniques required for implementation within computational algorithms.

Fig. 3.4 shows the intersection of the nozzle contour with the meridional plane. Initially the flow is expanded around a post throat curve formed by a suitable circular arc (line AB'). The expansion terminates at some point B, the exact location of which is unknown *a priori*.

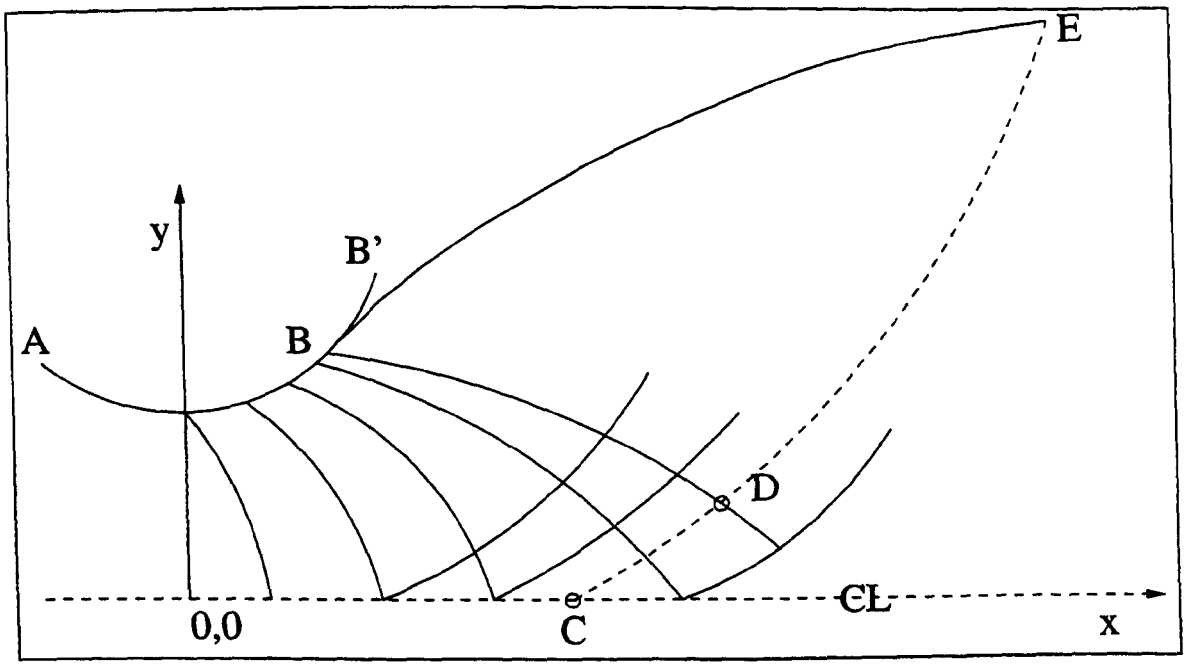

Figure 3.4: *Optimum Thrust Nozzle Construction*

The remainder of the nozzle from B to E consists of a contour designed to smoothly turn the flow back towards (although not reaching) axial flow. The aim of the following process is to describe the shape of the contour which will give optimum thrust for a proscribed nozzle length, x_E.

3.3.1 Formulation of the Problem

Let the line CE in Fig. 3.4 represent the intersection of the meridional plane with a control surface passing through the exit of the nozzle, where the inclination of the surface to the nozzle axis is a function of y (the radial distance), $\phi(y)$. The location of C, and the function $\phi(y)$ then completely define the control surface. By considering an elemental length of CE, ds, and by noting that the elemental area generated by this length is

$$dA = \frac{2}{\pi y ds} \tag{3.15}$$

and that

$$ds = \frac{dy}{\sin\phi} \tag{3.16}$$

it is possible to derive the following

$$\dot{m} = \rho u \frac{\sin(\phi - \theta)}{\sin\phi} 2\pi y dy \tag{3.17}$$

$$mom_x = \rho u^2 \frac{\sin(\phi - \theta)\cos\theta}{\sin\phi} 2\pi y dy \tag{3.18}$$

By integrating from C to E, the mass flow and thrust of the nozzle may be obtained

$$\dot{m} = \int_C^E \rho u \frac{\sin(\phi - \theta)}{\sin\phi} 2\pi y dy \tag{3.19}$$

$$Thrust = \int_C^E [(P - P_a) + \rho u^2 \frac{\sin(\phi - \theta)\cos\theta}{\sin\phi}] 2\pi y dy \tag{3.20}$$

where P_a is the ambient pressure. The axial distance between C and E is given by

$$x_E - x_C = \int_C^E \cot\phi dy \tag{3.21}$$

hence

$$length = x_C + \int_C^E \cot\phi dy \tag{3.22}$$

Any variation in the nozzle contour will involve a variation in the control surface. As this may be achieved by varying ϕ, point C may be treated as fixed. This means that the integrand on the RHS of Eqn. 3.22 must be a constant, as the contour variations are subject to constant length (x_E). As the mass flow is also a constant determined by initial conditions, the optimum contour is achieved via the maximisation of Eqn. 3.20, given that Eqns. 3.19 and 3.22 are constant. Using the Lagrangian multiplier method, this problem may be reduced to maximising the integral

$$I = \int_C^E (f_1 + \lambda_2 f_2 + \lambda_3 f_3) dy \tag{3.23}$$

where

$$\begin{aligned} f_1 &= [(P - P_a) + \rho u^2 \frac{\sin(\phi - \theta)\cos\theta}{\sin\phi}] y \\ f_2 &= \rho u \frac{\sin(\phi - \theta)}{\sin\phi} y \\ f_3 &= \cot\phi \end{aligned} \tag{3.24}$$

3.3.2 The Solution

The solution of Eqn.3.23 is described in detail in App. B. However, the important results are:

$$\phi = \theta + \mu \quad \text{along DE} \tag{3.25}$$

$$-\lambda_2 = \frac{u\cos(\theta - \mu)}{\cos\mu} \tag{3.26}$$

$$-\lambda_3 = y\rho u^2 \sin^2\theta \tan\mu \tag{3.27}$$

$$\sin 2\theta = \frac{2(P - P_a)}{\rho u^2} \cot\mu \quad \text{at E} \tag{3.28}$$

$$\frac{d\theta}{dy} - \frac{\sqrt{M^2 - 1}}{M(1 + \frac{\gamma - 1}{2} M^2)} \frac{dM}{dy} + \frac{\sin\mu \sin\theta}{y \sin(\theta + \mu)} = 0 \tag{3.29}$$

Eqn. 3.25 implies that the control surface CE coincides physically with the last LRC in the nozzle. Fortunately, Eqn. 3.29 proves that the irrotational, axisymmetric characteristic compatibility equation of the LRC is satisfied. If the compatibility criteria were not met, the solution would be a limiting line, and hence represent a physically impossible flow.

3.3.3 Contour Construction

Whilst the derivation of the equations required for the design of a nozzle of optimum thrust assumed a required length as input, the contour generation process is simplified if an exit Mach number (M_E) is specified instead. The solution will be unique, each combination of M_E and chamber to ambient ratio having an associated optimum nozzle contour, which will of course have a specific length. If a nozzle producing maximum thrust for a given length is desired, the Mach number corresponding to this length may found by interpolation, and the related optimised contour generated.

Once the pressure ratio and exit Mach number have been specified, μ_E and ν_E follow directly from Eqns. 3.9 and 3.10. Eqn. 3.28 may then be used to find the wall angle at the exit, θ_E. From Eqn. 3.26 we have

$$Ma\frac{\cos(\theta-\mu)}{\cos\mu} = -\lambda_2 \tag{3.30}$$

where a is the local speed of sound, given by

$$a = \sqrt{\gamma R\frac{T_c}{1+\frac{\gamma-1}{2}M^2}} \tag{3.31}$$

and for a given contour construction problem γ, R, and T_c are constants, related to the combustion process.

Eqns. 3.30 and 3.31 may be combined to give

$$\sqrt{\frac{M^2}{1+\frac{\gamma-1}{2}M^2}}\frac{\cos(\theta-\mu)}{\cos\mu} = \frac{-\lambda_2}{\sqrt{\gamma RT_c}} \tag{3.32}$$

Multiplying the top and bottom of the fraction within the root by $\frac{2}{M^2}$ results in

$$\sqrt{\frac{1}{\gamma-1+\frac{2}{M^2}}}\frac{\cos(\theta-\mu)}{\cos\mu} = \frac{-\lambda_2}{\sqrt{2\gamma RT_c}} \tag{3.33}$$

The RHS of Eqn. 3.33 is a constant, denoted K_1. By substituting the exit values of M, θ, and μ into Eqn. 3.33, the value of K_1 for the required control surface is obtained.

Once the above calculation has been performed, the initial characteristic provided by the transonic flow solution may be used to begin an expansion of the flow around the post throat

curve, to calculate the kernel. Successive RRC's are generated, and at each point on the RRC, the LHS of Eqn. 3.33 is evaluated using local flow properties. Initially, this quantity will be smaller than K_1 for the entire length of the RRC, and the RRC reaches the nozzle centreline, where it is terminated assuming axial flow.

As the expansion around the post throat circular arc continues, an RRC will eventually be generated containing a point where substitution of local flow properties into the LHS of Eqn. 3.33 produces K_1. However, there will be several such points in the flow, only one of which will result in a physically possible flow. Selection of the correct point is ensured by application of the continuity equation. Referring to Fig. 3.4, it may be seen that the nozzle contour and the two characteristic lines BD and DE form an enclosed area. As the nozzle contour is a streamline, the mass flow entering the enclosed region by crossing the RRC BD must leave by crossing the LRC DE. Denoting the candidate point D', this constraint on the mass flow results in

$$2\pi\rho_t u_t \int_B^{D'} \frac{\rho u y \sin\mu}{\rho_t u_t \cos(\theta-\mu)} dx = 2\pi y_E^2 \rho_t u_t \int_1^{D'} \frac{\rho u \sin\mu}{\rho_t u_t \sin(\theta+\mu)} \frac{y}{y_E} d(\frac{y}{y_E}) \qquad (3.34)$$

where all dimensions are non dimensionalised with respect to the throat radius. As

$$\frac{\rho}{\rho_t} = \frac{\rho}{\rho_0}\frac{\rho_0}{\rho_t} = \frac{(1+\frac{\gamma-1}{2}M_t^2)^{\frac{1}{\gamma-1}}}{(1+\frac{\gamma-1}{2}M^2)^{\frac{1}{\gamma-1}}} = (\frac{1+\frac{\gamma-1}{2}}{1+\frac{\gamma-1}{2}M^2})^{\frac{1}{\gamma-1}} \qquad (3.35)$$

and

$$\frac{u}{u_t} = \frac{M}{M_t}\frac{a}{a_t} = M\sqrt{\frac{\gamma RT}{\gamma RT_t}} = M\sqrt{\frac{T}{T_c}\frac{T_c}{T_t}} = M\sqrt{\frac{1+\frac{\gamma-1}{2}}{1+\frac{\gamma-1}{2}M^2}} \qquad (3.36)$$

the mass flows may be calculated entirely from local flow properties. The LHS of Eqn. 3.34 is the mass flow crossing the RRC joining B to D', and may be approximated by totalling the mass flux entering this outer region between each pair of points on the RRC. To evaluate the RHS, however, the radial distance of the exit point y_E must be known, as well as the flow properties along the LRC DE.

These variables may be calculated by referring again to the governing equations derived in Sec. 3.3.2. From Eqn. 3.27, using Eqn. 3.31 for the speed of sound, and expressing ρ in terms of its throat value and Mach number, we have

$$y\frac{\rho_c}{(1+\frac{\gamma-1}{2}M^2)^{\frac{1}{\gamma-1}}} M^2\gamma RT_c \frac{1}{1+\frac{\gamma-1}{2}M^2}\sin^2\theta\tan\mu = -\lambda_3 \qquad (3.37)$$

Rearranging this equation gives

$$yM^2(1+\frac{\gamma-1}{2}M^2)^{\frac{-\gamma}{\gamma-1}}\sin^2\theta\tan\mu = \frac{-\lambda_3}{\gamma RT_c\rho_c} \qquad (3.38)$$

The RHS of Eqn. 3.38 is a constant, denoted K_2. However, it is not possible to use flow properties at E to generate an absolute value of K_2, as y_E is not known. Instead, the ratio

of K_2 to y_E is found, which then allows an associated value of y_E to be evaluated for any other point in the flow for which all properties (including y) are known. The RHS of Eqn. 3.34 may be approximated by using Eqns. 3.38 and 3.33 to find a series of points along the LRC from D' to E. Both equations must be valid at each point on the LRC, and Eqn. 3.38 also provides the ratio $\frac{y}{y_E}$ at each point, allowing the LRC to be located in the physical plane. This provides sufficient information for the mass flow to be evaluated. If Eqn. 3.34 is not satisfied, the next RRC in the flow is calculated, and a new D' created.

By the above process, a pair of characteristics BD and DE will eventually be defined which satisfy both the equations derived by Rao and conservation of mass. The position and flow properties along both of these characteristics will be known. The next stage is to solve for the flow in the outer region, allowing the generation of the nozzle contour. This may be achieved by using points on the LRC DE as the last point on an RRC from the nozzle wall. As the RRC BD is known, the remainder of this new RRC can be calculated backwards to the nozzle wall.

The contour is formed from the streamline joining points B and E. This may be represented by a series of points, located at the intersection of the streamline and each RRC. The streamline between points two points r (known) and s (new) is approximated as a straight line, and hence

$$y_s = y_r + (x_s - x_r)\tan(\frac{\theta_r + \theta_s}{2}) \tag{3.39}$$

Assuming that the intersection of this line and the RRC occurs between point p and $p+1$ on the RRC, we also have

$$y_s = y_p + (x_s - x_p)\tan(\frac{\theta_p - \mu_p + \theta_{p+1} - \mu_{p+1}}{2}) \tag{3.40}$$

From Eqns. 3.39 and 3.40, the coordinates of point s may be found. The flow angle at s may be approximated using the flow angles on the RRC, via linear interpolation. This value will vary with any change in the coordinates of point s, hence the solution must be calculated by an iterative process, which is monitored to ensure that point s lies between p and $p+1$.

3.3.4 Planar Optimised Nozzles

The previous discussion considered only axisymmetric flows. However, the majority of the assumptions and equations are equally valid for two-dimensional flows, the only difference is the removal of terms involving y, the radial distance. By following through the equations

provided in App. B, but removing this variable, it is possible to derive

$$\phi = \theta + \mu \quad \text{along DE} \tag{3.41}$$

$$-\lambda_2 = \frac{u\cos(\theta - \mu)}{\cos\mu} \tag{3.42}$$

$$-\lambda_3 = \rho u^2 \sin^2\theta \tan\mu \tag{3.43}$$

$$\sin 2\theta = \frac{2(P - P_a)}{\rho u^2}\cot\mu \quad \text{at E} \tag{3.44}$$

The only equation that differs from the axisymmetric case is Eqn. 3.43 which is now independent of y.

As both Eqns. 3.42 and 3.43 are constant along the control surface, it follows that M, μ, θ and ϕ must all be constant along CE. This results in a reduction in the complexity of the solution process, as instead of points satisfying both a K_1 value and continuity, all that is required is for a point in the flow to be located with local Mach number and flow angle of M_E and θ_E. As the flow variables along CE are constant, they are of course also known, and hence the flow in the outer region may be calculated (in fact, as the line CE is straight, all other characteristics in this region are also), and the streamline defining the nozzle wall may be found as before.

3.4 Calculation of Thrust Coefficients

The thrust produced by a rocket engine is equal to the integral of the axial momentum and pressure forces acting on the exit plane of the nozzle. In Fig. 3.5, this plane is represented by the line AB. However, the flow-field along AB is not calculated by the methods so far discussed, as this would require extending the flow-field downstream for this purpose alone. Instead, it is more convenient to consider the forces acting in the remainder of the control volume ABCD.

The forces acting on the other three surfaces must be equal and opposite to the thrust force acting across AB. As inviscid flow is assumed, no forces act along the centreline (DA), and hence the thrust may be found by calculating the combined momentum and pressure forces acting across the input RRC (CD), and the pressure forces acting along the nozzle wall (CB). This is true for both conical and optimised nozzle types, in two-dimensional and axisymmetric flows.

The vacuum thrust coefficient, C_F^∞, follows from the standard definition

$$C_F^\infty = \frac{\text{Vacuum Thrust}}{P_c A_t} \tag{3.45}$$

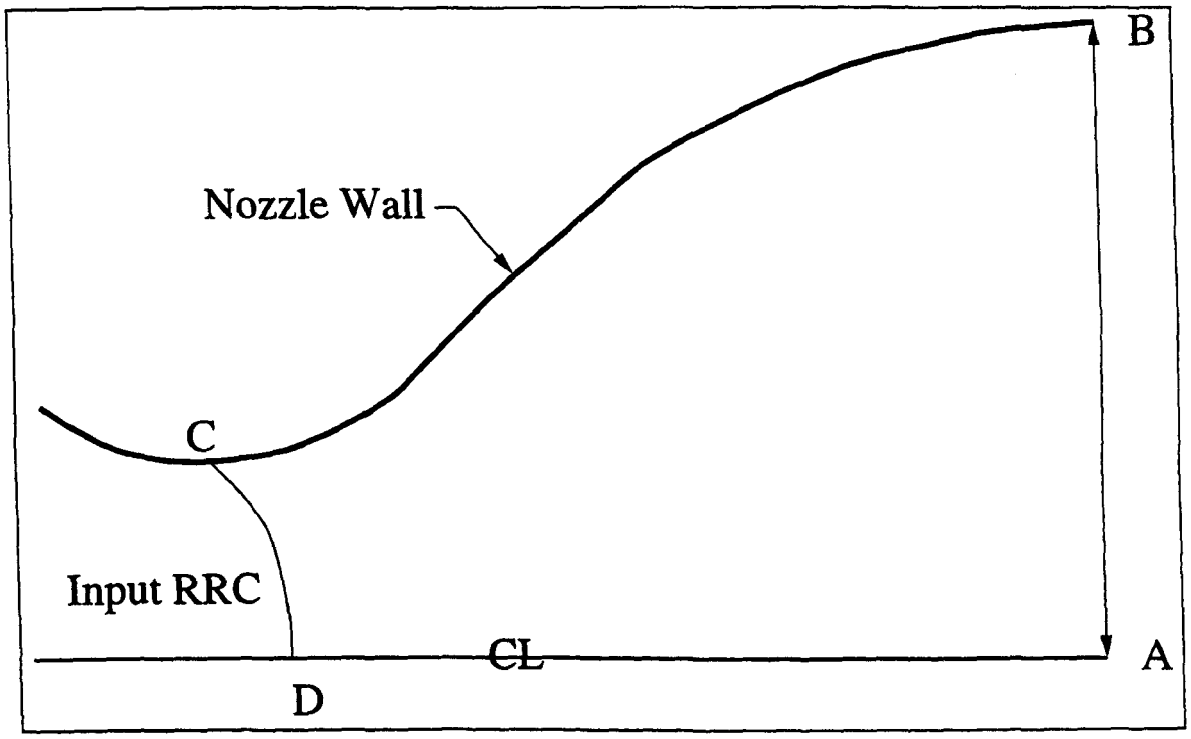

Figure 3.5: *Nozzle Control Volume*

As the coordinate system is non dimensionalised with respect to the throat radius R_t, the throat area is $2R_t$ per unit depth for planar nozzles, and πR_t^2 for axisymmetric. The momentum flux is found from the approximate discrete form of Eqn. 3.20 applied along the input characteristic, resulting in

$$C_{Fc}^{\infty} = \sum_{2}^{nc} [\bar{P} + \bar{\rho}\bar{u}^2 \frac{\sin(-\bar{\mu})\cos(\bar{\theta})}{\sin(\bar{\theta} - \bar{\mu})}] Y \tag{3.46}$$

where barred quantities are the average of points i and $i-1$, and

$$Y = \begin{cases} \frac{(y_i^2 - y_{i-1}^2)}{P_c} & \text{in axisymmetric flow,} \\ \frac{y_i - y_{i-1}}{P_c} & \text{for two-dimensional.} \end{cases} \tag{3.47}$$

Pressure is found assuming constant total pressure, i.e.

$$\frac{P_0}{P} = (\frac{T_0}{T})^{\frac{\gamma}{\gamma-1}} = (1 + \frac{\gamma - 1}{2} M^2)^{\frac{\gamma}{\gamma-1}} \tag{3.48}$$

Generally, P_0 is assumed to be identical to the chamber pressure P_c, although this need not be the case if known losses must be accommodated. For irrotational flow, the total pressure is constant.

The pressure force exerted by the flow on a nozzle contour (containing nw points) is found from

$$C_{Fw}^{\infty} = \sum_{2}^{nw} \bar{P} Y \tag{3.49}$$

Again barred quantities are averaged between points i and $i-1$ on the nozzle contour, and Y is as defined before. The total thrust coefficient of the nozzle is then simply the sum of Eqns. 3.46 and 3.49.

Finally, assuming that the flow does not separate within this control volume, the thrust coefficient may be calculated for any altitude from

$$C_F = C_F^{\infty} - \frac{P_a}{P_c}\frac{A_E}{A_t} \tag{3.50}$$

3.5 Results

The purpose of the results presented in this section is primarily to demonstrate the techniques outlined in this chapter, and utilise them to conduct a comprehensive survey of the performance characteristics produced by conventional nozzles against which the ED nozzle type discussed in the following chapters may be compared. Each of the four principle types of conventional nozzles already discussed is examined, these being planar and axisymmetric conical nozzles, and the planar and axisymmetric variants of the optimised contour.

As a secondary objective, it is possible to assess the effect on overall nozzle behaviour produced by the two different approaches to the modelling of the throat flow described in the previous chapter. This allows the range of throat configurations for which the more simple and rapid analytical technique is applicable to be determined, and also the size of error that might be expected when the analytical method is applied to nozzles outside its optimum range.

The performance of a nozzle design is usually assessed on the relation between the thrust coefficient produced and nozzle length. Except for unusual circumstances (e.g. wind tunnels), the aim is to achieve the minimum length for a given thrust (or conversely the maximum thrust given a specified length). This minimum length requirement forms the basis of the optimisation process derived by Rao (described in Sec. 3.3), and is the historically accepted criteria by which advanced nozzle designs are judged. As there is a high correlation between the length and mass of a nozzle, minimising length directly reduces mass. Vehicles which possess nozzles that are stored internally for any part of the flight trajectory also benefit from a reduction in inter-staging length. As the mass of the primary structure per unit length will be larger than that of the nozzle, nozzle length has a disproportionate impact on overall system mass.

Vacuum thrust performance alone is considered, as for typical launch vehicle trajectories (especially upper stages, but also to a lesser degree lower stages and single stage vehicles) altitude is gained rapidly to avoid losses due to atmospheric drag. This means that low ambient

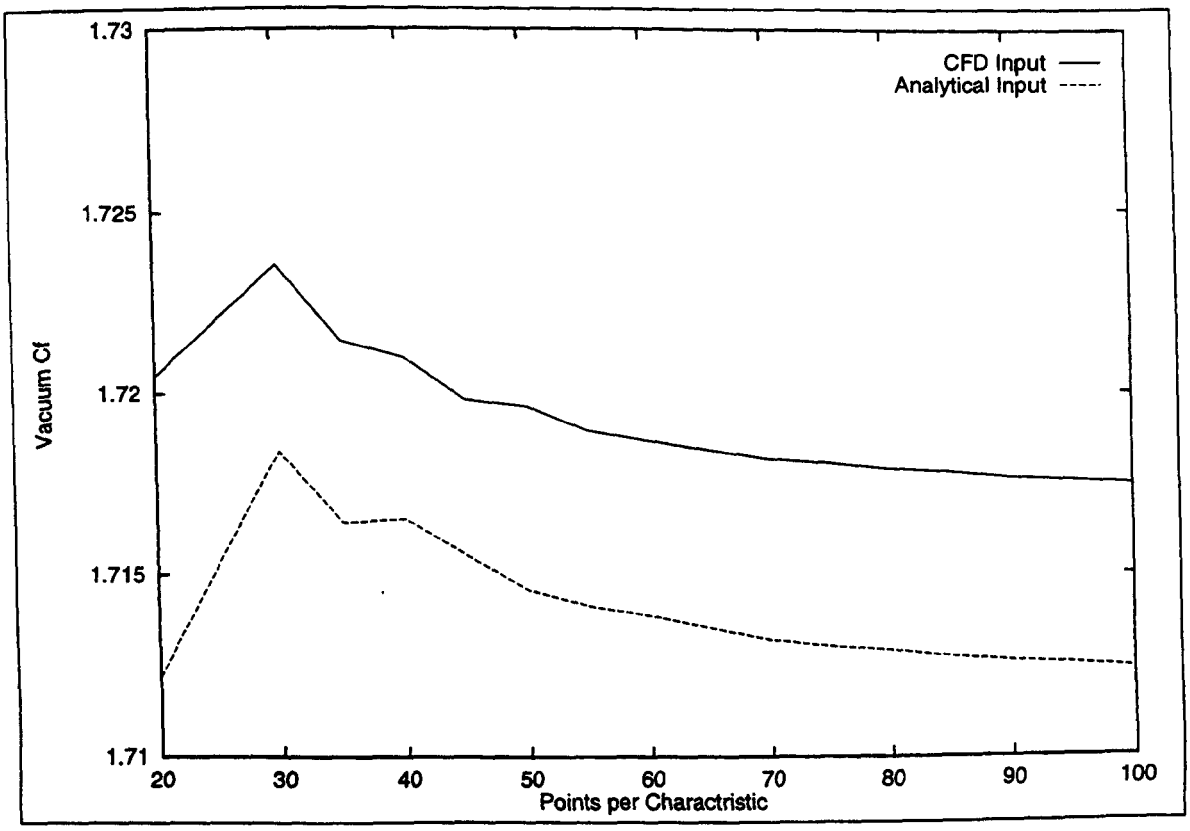

Figure 3.6: C_F^{∞} *vs.n, Planar Conical Nozzle,* $R_w^{=} = R_t, \theta_w = 35, L = 40R_t$

and high chamber pressures combine to form a dominance of extremely high pressure ratios, and hence nearly all nozzle designs assume vacuum conditions at the design point. In the results presented in this chapter, therefore, the possibility of overexpansion and separation within the nozzle is ignored.

A constant ratio of specific heats is assumed, and is equal to 1.23 (approximating that typical of the combustion products from a LOx/LH engine) unless otherwise stated. Each nozzle flow calculation requires an input characteristic. This characteristic is created by linear interpolation of results obtained for the throat region of the flow from either the analytical or CFD based methods. Grids used for the CFD code follow the general layout described in Ch. 2, and contain 256 by 64 cells. Increasing the number of points on this input characteristic increases the accuracy of the results, but obviously also increases run time. To determine the minimum number of points necessary to still produce reliable results, the effects of three primary variables determining mesh density were considered, these being $R_w^{=}$, nozzle length, and wall angle.

From the results presented in the previous chapter, it is clear that reducing $R_w^{=}$ produces an increase in the Mach numbers along an initial characteristic, and a greater deviation of this line from the vertical. This causes the initial point of subsequent RRC's to occur at a higher wall Mach number, increasing the spacing between characteristics of the same family. Characteristics are also spread out by an expansion in the flow, and hence increasing the cone half angle and overall nozzle length increases the coarseness of the mesh. Therefore,

the effect of the number of points on the input characteristic on the overall thrust coefficient produced was examined using a planar conical nozzle of half angle 35 degrees, $R_w^= = R_t$, and length 40 R_t, representing the worst case of these values. Figure 3.6 shows the thrust coefficients produced by both the analytical and computational methods for a varying number of points on the input characteristic. As can be seen, very little change in results occurs above about 80 points, and hence this value was used for all subsequent results presented.

3.5.1 Planar Conical Nozzles

The first step of the investigation involved an assessment of the impact of the choice of throat modelling technique on overall nozzle performance. Fig. 3.7 shows the variation of thrust coefficient with length for planar conical nozzles for the two methods, for three different values of $R_w^=$. The half angle was allowed to vary with total nozzle length by interpolating between results produced for a range of half angles. This process ensures that the maximum possible thrust coefficient for such nozzles is available for comparison with planar optimised and ED nozzles.

This figure shows that for nozzles with wall radii twice the throat half height, the analytical throat flow method produces nearly identical results for the overall nozzle thrust as the computational model. However, as $R_w^=$ is reduced, slight differences between the two occur. For $R_w^= = 1.5R_t$, this is extremely small, but just visible. As the wall radius is reduced further to $R_w^= = R_t$, the analytical method predicts a significantly lower thrust coefficient for a given nozzle length.

	Nozzle length, $C_F^\infty = 1.6$			Nozzle Length, $C_F^\infty = 1.7$		
$R_w^=$	Analytical	CFD	Percent	Analytical	CFD	Percent
5	10.685364	10.692711	100.07	25.681521	25.708774	100.12
3	10.148156	10.171108	100.22	26.025476	26.121421	100.37
2	9.977574	9.986581	100.09	26.780907	26.828010	100.18
1.5	10.000754	9.929012	99.28	27.681631	27.386635	98.93
1	10.267567	9.865864	96.09	29.741827	27.921978	93.88

Table 3.1: *Nozzle Lengths for Specified C_F^∞, Planar Conical Nozzles*

This effect is emphasised by the results shown in Table 3.1. This table shows the length of nozzle (in terms of throat half height, R_t) required to produce two different thrust coefficients for a range of wall throat radii, for both the analytical and computationally derived input conditions. The values presented are given to a far higher degree of accuracy than is reasonable if a design exercise were actually being undertaken, but as the level of error is

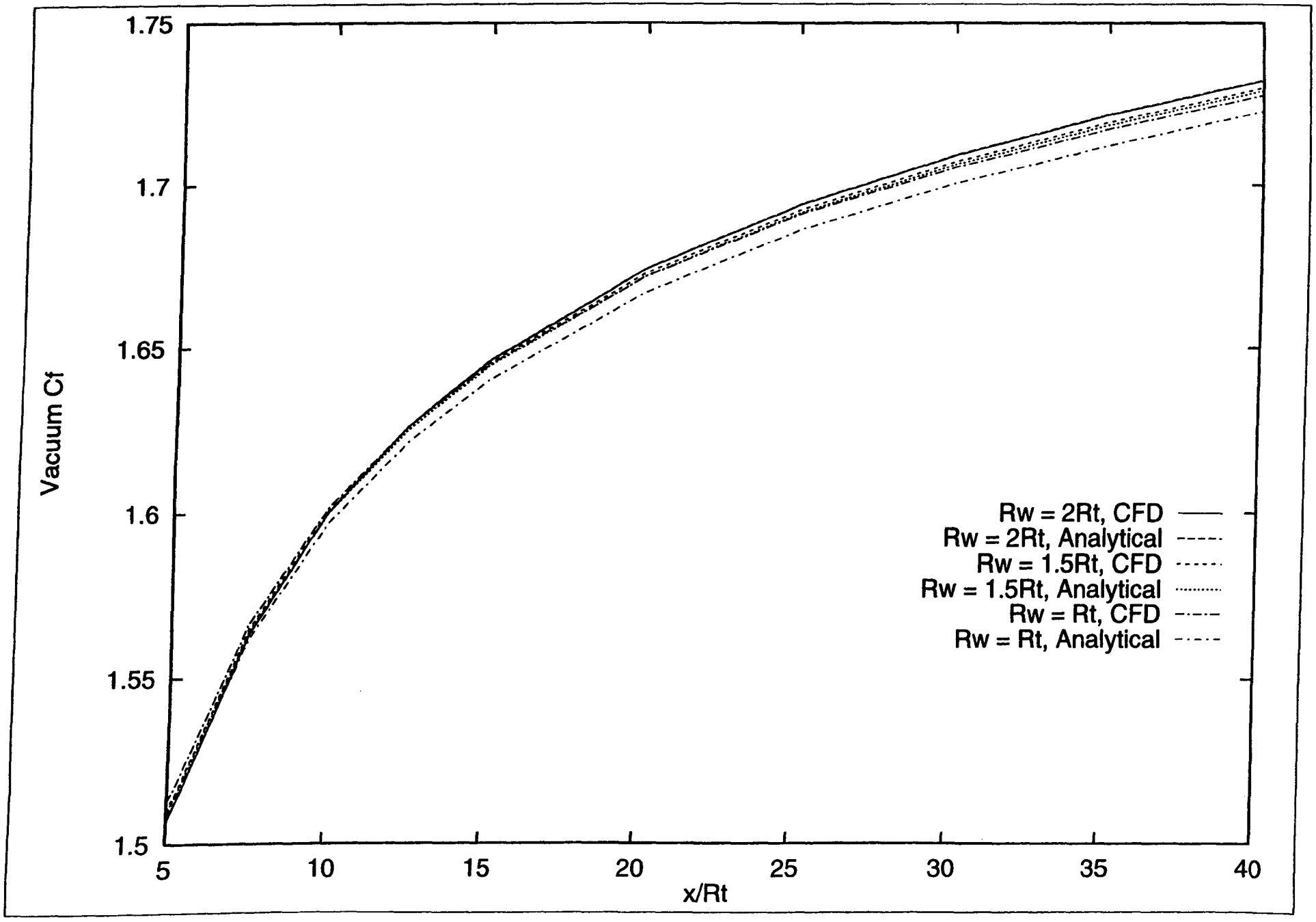

Figure 3.7: *Effect of Throat Model Type, Planar Conical Nozzle*

very similar for each case, the high number of decimal places are included to give a more detailed comparison of the methods.

As expected there is very little difference between the results for the two throat prediction techniques for nozzles with $R_w^=$ above $2R_t$. However, below this, the CFD technique predicts shorter nozzles for a given thrust (up to 6 percent for a $R_w^=$ of R_t). Further, it is clear that for a continuous wall radii at the throat, the optimum radius for minimum length is dependent on the desired C_F^∞. For the larger nozzles, minimum lengths are produced by large $R_w^=$, whereas lower thrust nozzles benefit from smaller $R_w^=$. The exact value of $R_w^=$ that offers minimum length varies (apparently gradually, see Fig. 3.7) with required thrust.

These trends are as expected. As was shown in the previous chapter, the analytical and computational methods produce virtually identical results for nozzles with $R_w^=$ of approximately $2R_t$ and above, but below this the analytical technique predicts wall Mach numbers that are slightly higher, and a lower mass flow through the throat region. This in turn leads to a loss in the predicted momentum flux across the throat, and hence a corresponding drop in the overall thrust predicted for a given nozzle.

Whilst from Fig. 3.7 this loss in predicted thrust would seem to be relatively small, its effect grows with nozzle length. This is because the gradient of the thrust curve reduces with increasing length, and therefore for a constant thrust deficit, the difference in length for a given thrust coefficient rises. Therefore a slight reduction in predicted thrust leads to a noticeable increase in the predicted length (i.e. 6 percent for a $C_F^\infty = 1.7$ nozzle with $R_w = R_t$) between the two initial lines. This in turn leads to the possibility of the design of a nozzle longer than necessary, and hence of slightly greater performance than expected.

In a real nozzle design process this effect would be obscured by semi empirical calculations required to allow for combustion losses and boundary layer effects. Of greater significance is the possibility that a nozzle design may erroneously be optimised with a higher than needed $R_w^=$, again leading to a longer than necessary nozzle. The results presented in Table 3.1 for the lower thrust coefficient nozzle ($C_F^\infty = 1.6$) show that if the analytical throat method were used, a wall radius of approximately $3R_t$ would be selected. The computational simulation, however, suggests that reducing this to R_t would actually save 1 percent of nozzle length.

The previous discussion has shown that for nozzles with radii of curvature at the throat greater than twice the nozzle half height, identical results are produced whichever method is used to model the throat region, and therefore the analytical scheme could be used to reduce solution time. However, the remainder of the results presented here were calculated using computationally derived input conditions regardless of $R_w^=$, to ensure commonality.

Fig. 3.8 shows the effect of varying $R_w^=$, for a wider range than that shown in Fig.

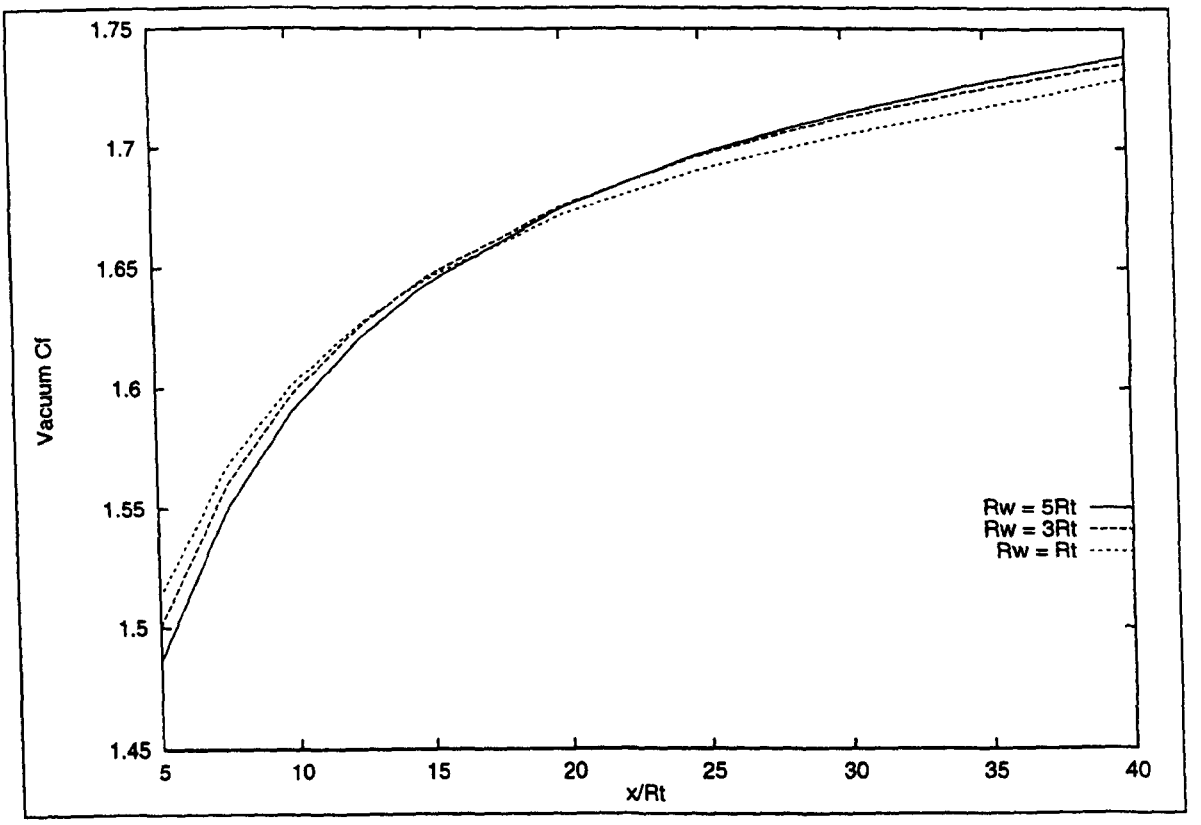

Figure 3.8: *Effect of $R_w^=$ on C_F^∞, Planar Conical Nozzle*

3.7. The variation produced in thrust coefficient is quite small, but as was demonstrated by the results in Table 3.1, the effect on predicted nozzle length for a specified C_F^∞ is more significant due to the low gradient of the thrust curve (particularly for long nozzles). Fig. 3.8 also graphically demonstrates the already noted relation of optimum $R_w^=$ and total nozzle

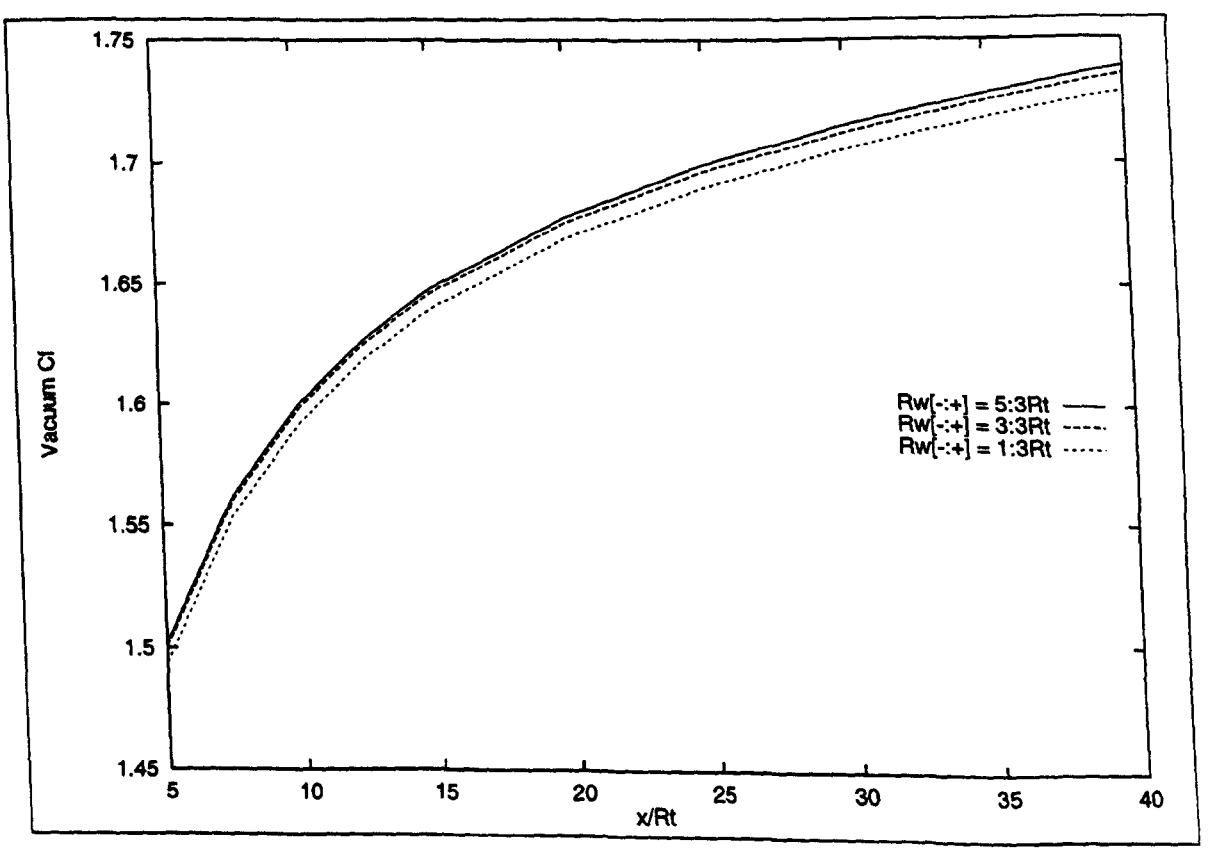

Figure 3.9: *Effect of R_w^- on C_F^∞, Planar Conical Nozzle*

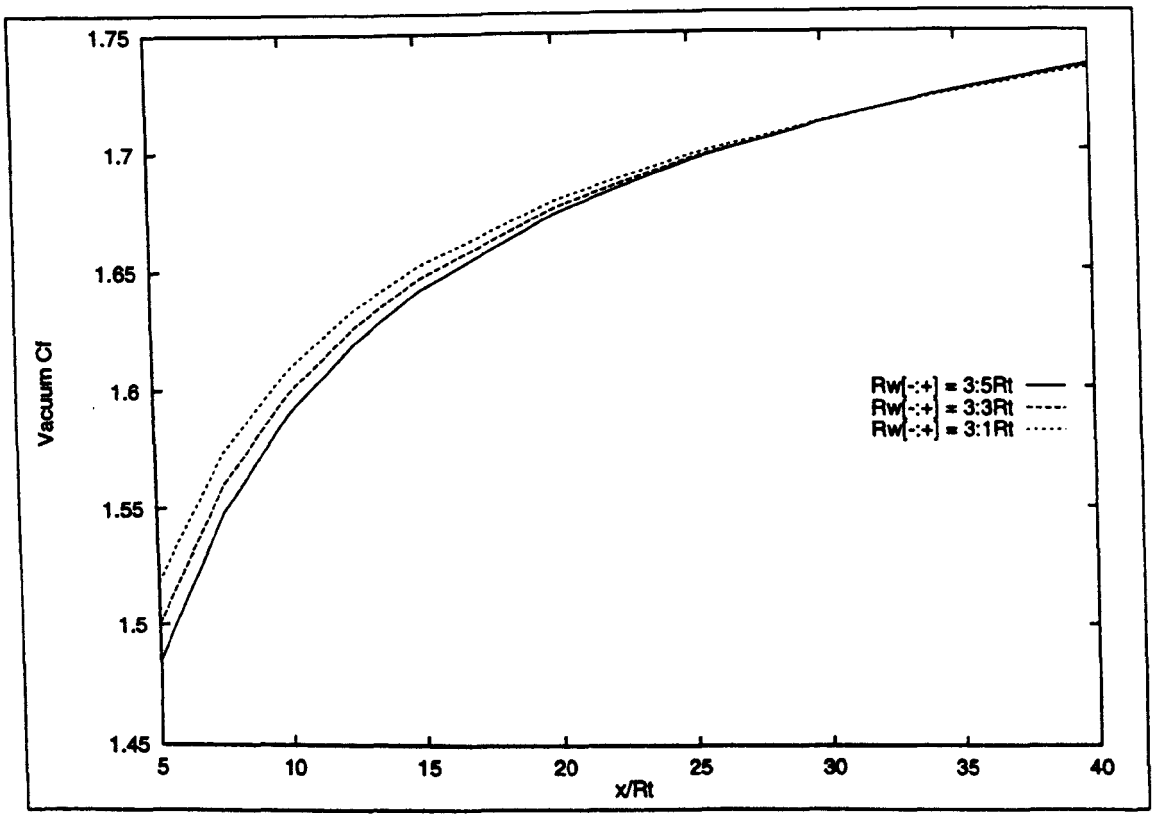

Figure 3.10: *Effect of R_w^+ on C_F^∞, Planar Conical Nozzle*

length, the thrust curves for the three values of $R_w^=$ clearly crossing.

It was noted at the end of the last chapter that the value of R_w^+ may be varied independently of R_w^-, creating a discontinuity in radius at the throat. This is possible as the RRC

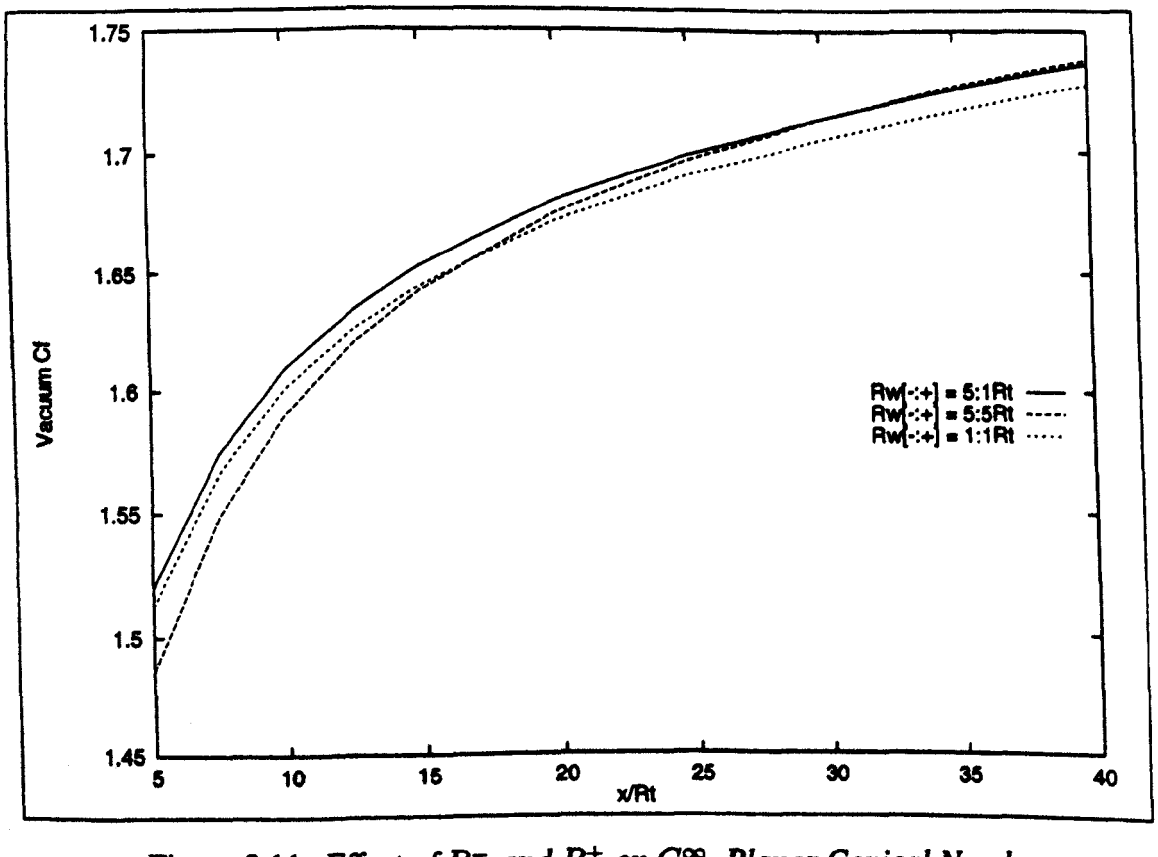

Figure 3.11: *Effect of R_w^- and R_w^+ on C_f^∞, Planar Conical Nozzle*

generated from the computational results (or analytical if this method is preferred) initiates at the intersection of the geometric throat and nozzle wall. As this characteristic is entirely supersonic, the flow properties along it are unaffected by any downstream wall geometry, including the post throat curvature. It is therefore possible to separate the effects of the pre and post throat radii, shown in Figs. 3.9 and 3.10.

These figures reveal that the pre and post throat radii produce opposing effects with respect to C_F^∞. Increasing R_w^-, independently of R_w^+ (as shown in Fig. 3.9) has little effect on short nozzles. However, as the length of the nozzle increases, the C_F^∞ curves diverge, and a larger pre throat curve produces a greater overall thrust. Conversely, Fig. 3.10 shows that varying R_w^+ has little effect on long nozzles, but reducing this radius results in increased thrusts for short nozzles.

Obviously these effects may be combined, and Fig. 3.11 reveals the anticipated result that in general maximum thrust is achieved by increasing R_w^- and minimising R_w^+. A fuller description of the implications of this result is included in the final section of this chapter.

3.5.2 Planar Optimised Contours

The method chosen for production of the initial characteristic would also be expected to have some effect on the performance of planar nozzles with length optimised contours. Fig. 3.12 presents thrust coefficients generated by planar optimised nozzles for the same three values of $R_w^=$ shown for planar conical nozzles in Fig. 3.7. As was the case for the simpler nozzle, the effect of throat model choice on overall thrusts is negligible for $R_w^=$ of $2R_t$, barely discernible for $R_w^=$ of $1.5R_t$, but of some small significance for $R_w^=$ equal to R_t.

	Nozzle length, $C_F^\infty = 1.6$			Nozzle Length, $C_F^\infty = 1.7$		
$R_w^=$	Analytical	CFD	Percent	Analytical	CFD	Percent
5	10.388252	10.395792	100.07	22.660564	22.679658	100.08
3	9.764827	9.777504	100.13	21.834515	21.889502	100.25
2	9.465911	9.471760	100.06	21.702017	21.736702	100.16
1.5	9.415701	9.352699	99.33	21.922329	21.728273	99.11
1	9.564252	9.234951	96.56	22.707235	21.672149	95.44

Table 3.2: *Nozzle Lengths for Specified C_F^∞, Planar Optimised Nozzles*

Table 3.2 shows the lengths required for the optimised nozzles to deliver the same two thrust coefficients demanded from planar conical nozzles in Table 3.1, again comparing the prescribed nozzle length produced from analytically derived starting lines to those from the computational technique (the same comments with respect to the accuracy implied apply).

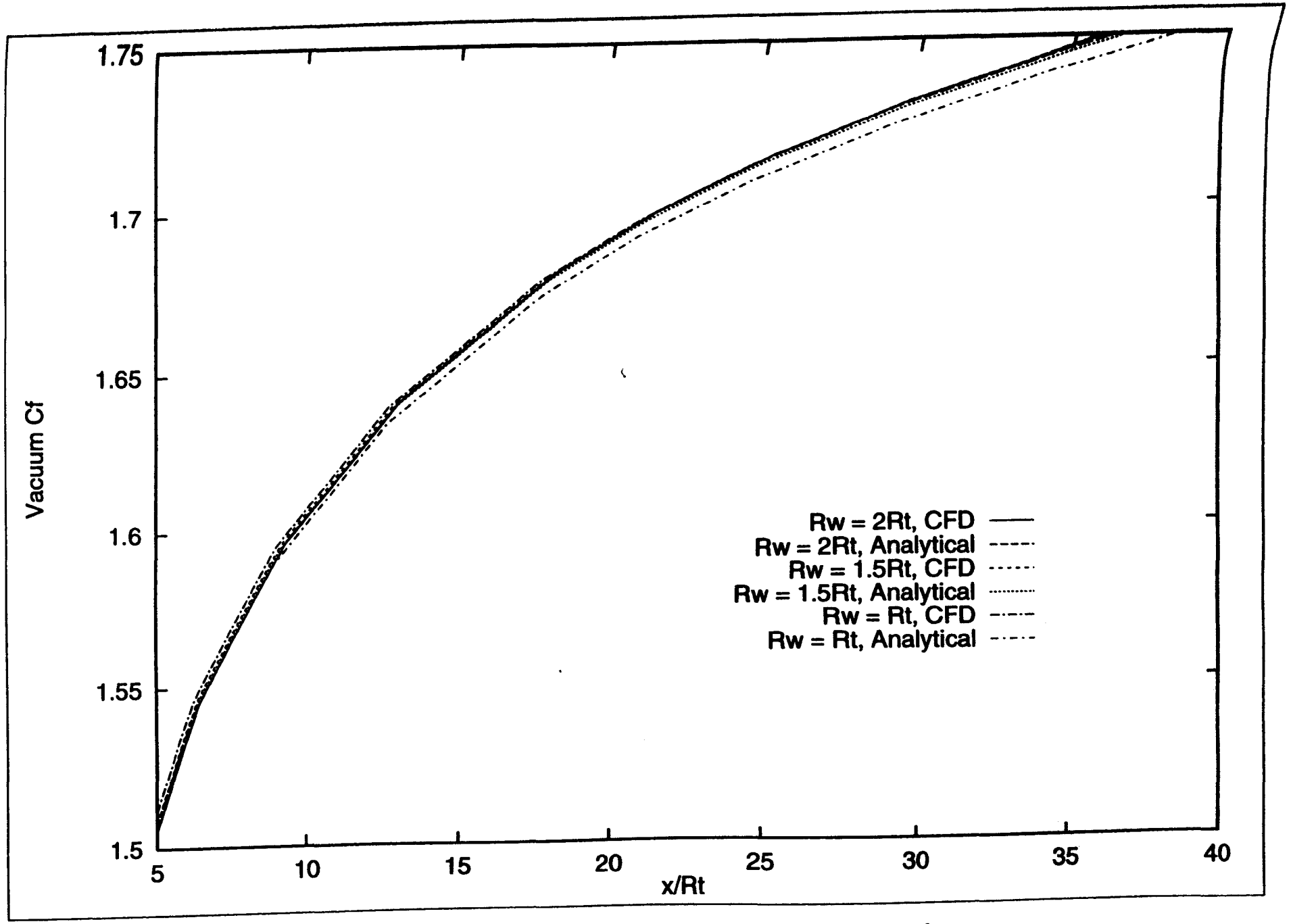

Figure 3.12: *Effect of Throat Model Type, Planar Optimised Nozzles*

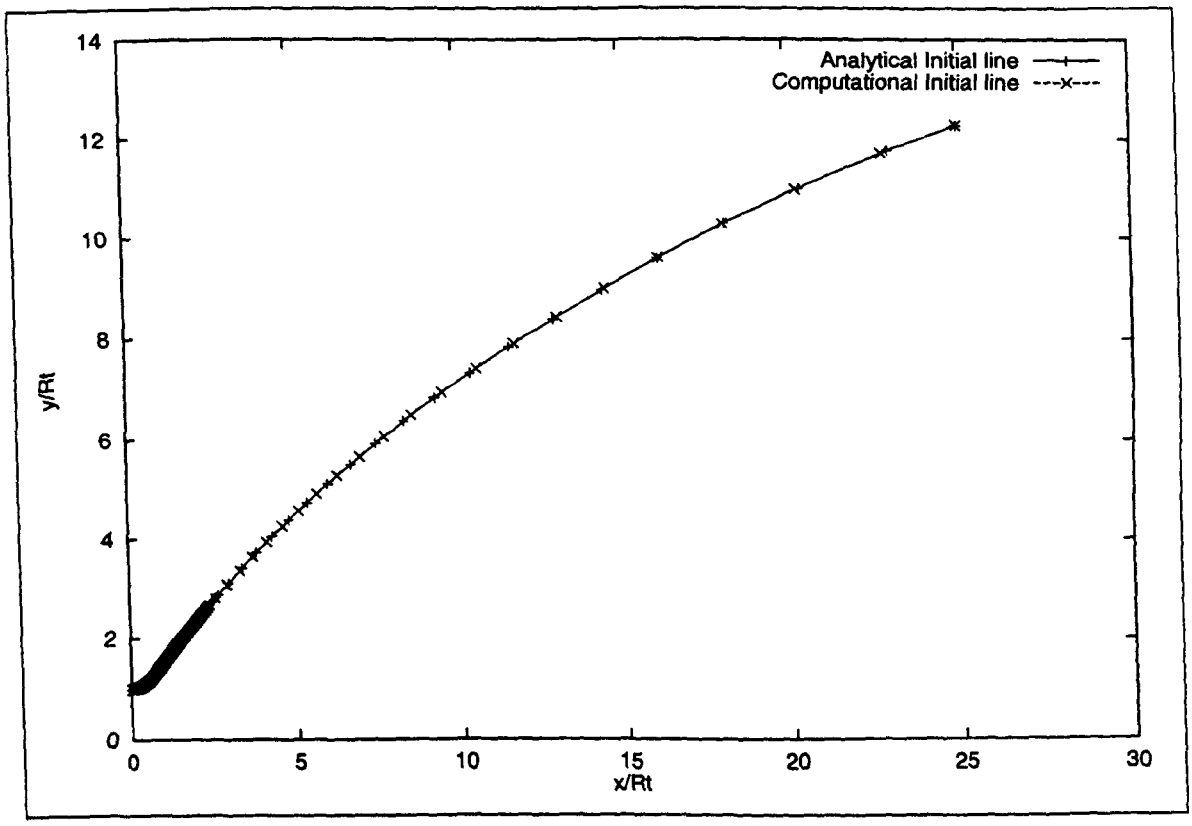

Figure 3.13: *Comparison of Contours, Length 25 R_t*

As before, very little difference is produced by the different input characteristics, unless $R_w^=$ is reduced below $2R_t$. In fact these results suggest that optimised nozzles are slightly less effected by throat wall radii variation than the planar conical type.

As was the case for planar conical nozzles, the use of the analytical rather than computational throat model leads to a possibility of over estimating the nozzle length required if the throat wall radius is small, and the optimum wall radius may be missed due to the under prediction of thrust coefficient for small $R_w^=$ (note that for the $C_F^\infty = 1.6$ nozzle in Table 3.2 the analytical method again favours a $R_w^=$ of $3R_t$, whilst the computational suggests R_t). Further to these concerns, there is an extra problem not applicable to the planar conical type, which could have more serious implications for nozzle design.

The contour geometry of optimised nozzles is formed as a part of the flow solution process, and if this geometry is effected there would be the possibility that contours produced from the analytically derived initial line would not actually be of optimum design for small $R_w^=$. To examine this possibility, the input Mach number was varied to produce a contour of length 25 R_t, for a nozzle with an $R_w^=$ of R_t. Fig. 3.13 shows the contours produced, and as may be seen, they are identical. This means that even if an incorrect thrust is predicted, the contour itself is still optimum.

A more detailed comparison of Tables 3.1 and 3.2 reveals two further features. Most importantly, the optimised contours are indeed shorter for a given thrust, as would be expected. A less obvious trend is that the change in C_F^∞ produced by reducing $R_w^=$ below $3R_t$ for the

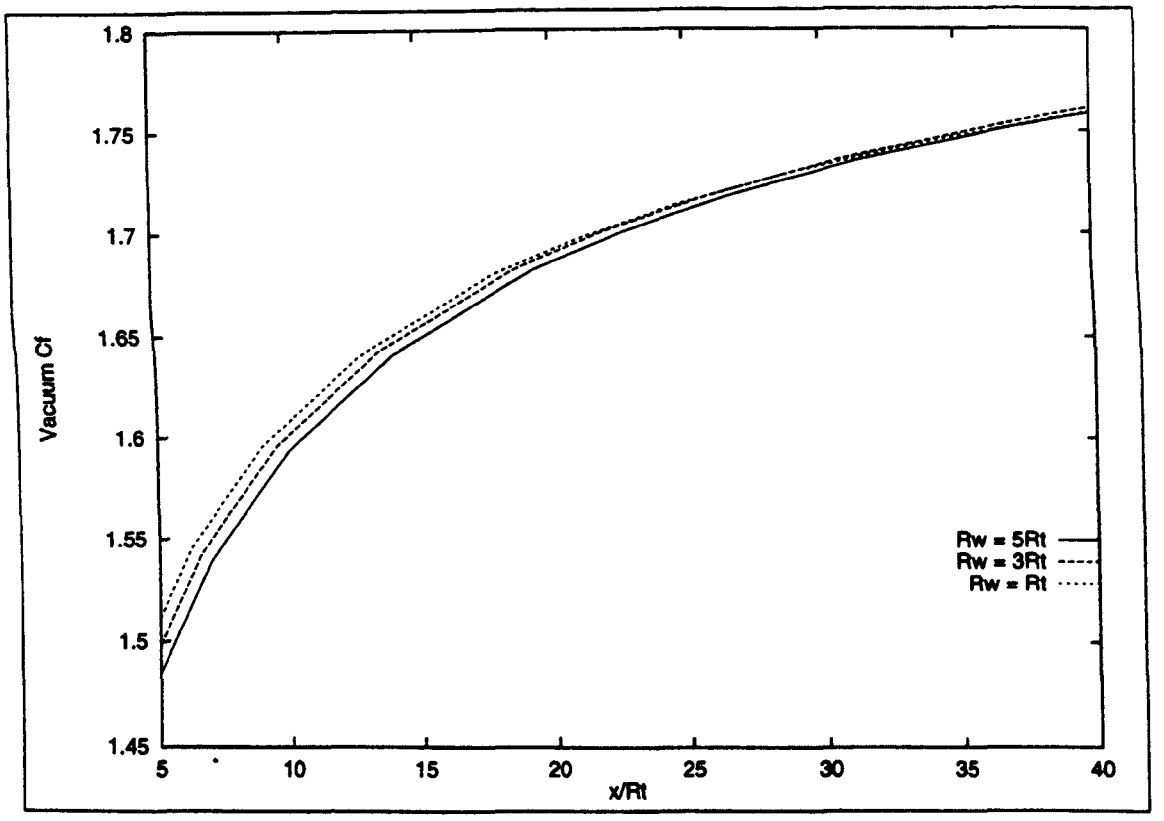

Figure 3.14: *Effect of $R_w^=$ on C_F^∞, Planar Optimised Nozzle,*

optimised nozzles is less pronounced than that of the planar conical type. It may also be seen that for the planar optimised nozzle, the smallest value of $R_w^=$ produces a shorter nozzle for both thrust coefficients investigated, whereas the higher thrust planar conical type required an $R_w^=$ of $5R_t$ for optimum. This might suggest that reducing $R_w^=$ is always advantageous for

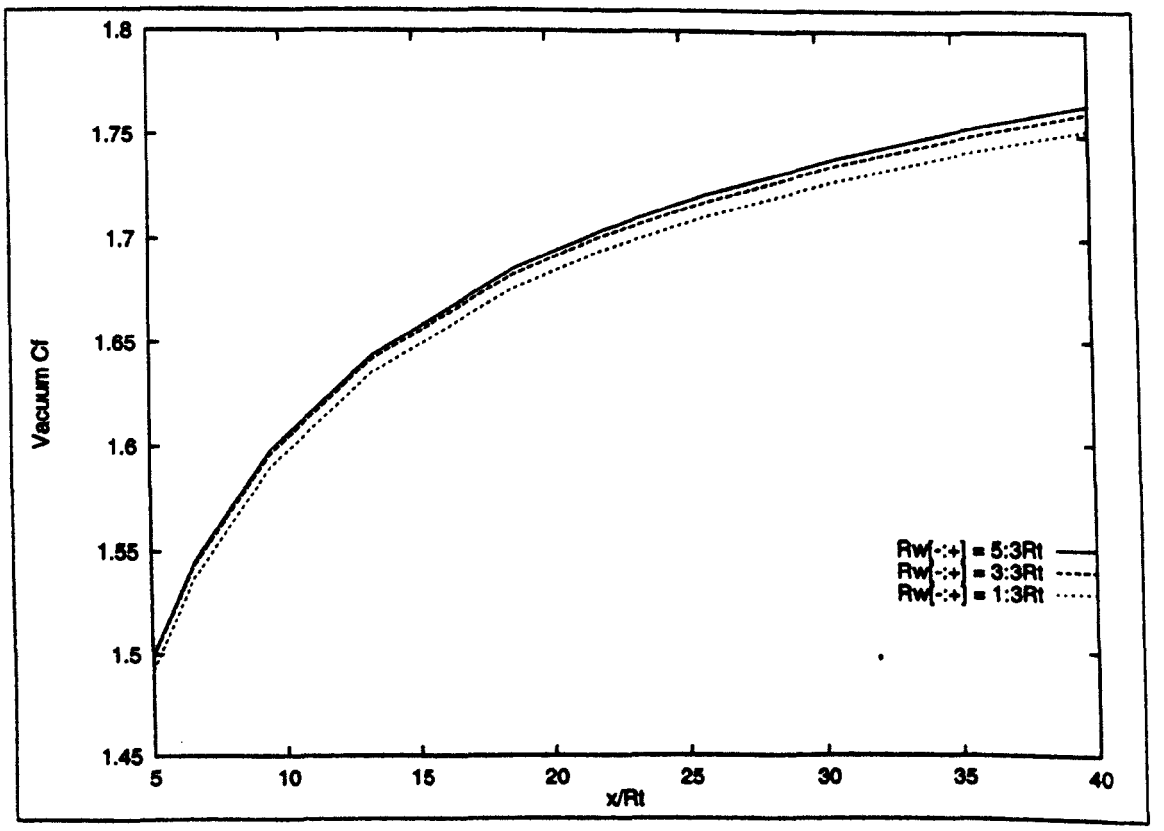

Figure 3.15: *Effect of R_w^- on C_F^∞, Planar Optimised Nozzles*

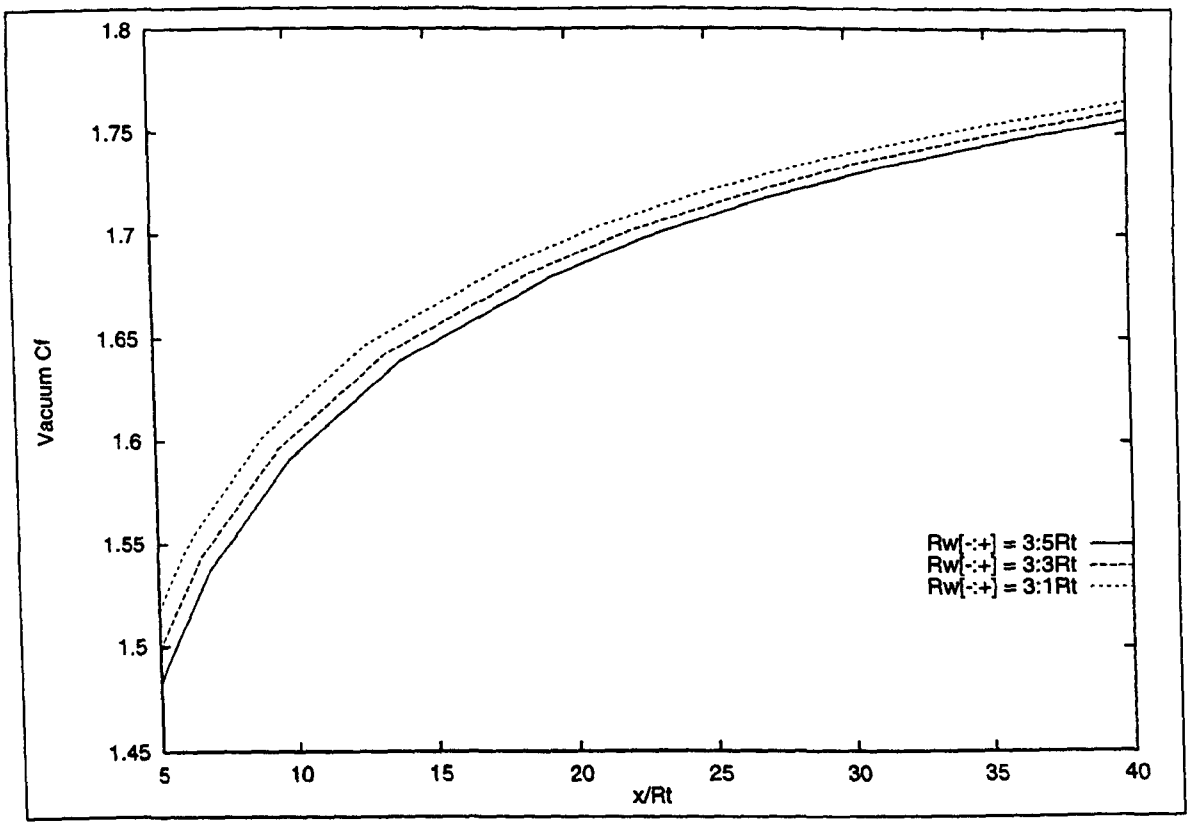

Figure 3.16: *Effect of R_w^+ on C_F^∞, Planar Optimised Nozzles*

optimised nozzles. However, Fig. 3.14 shows the variation of C_F^∞ with length over a wider range (and is comparable to Fig. 3.8), and clearly demonstrates that the optimum wall radius remains a function of required length, but that the total nozzle length at which any give value of $R_w^=$ becomes optimal has increased substantially.

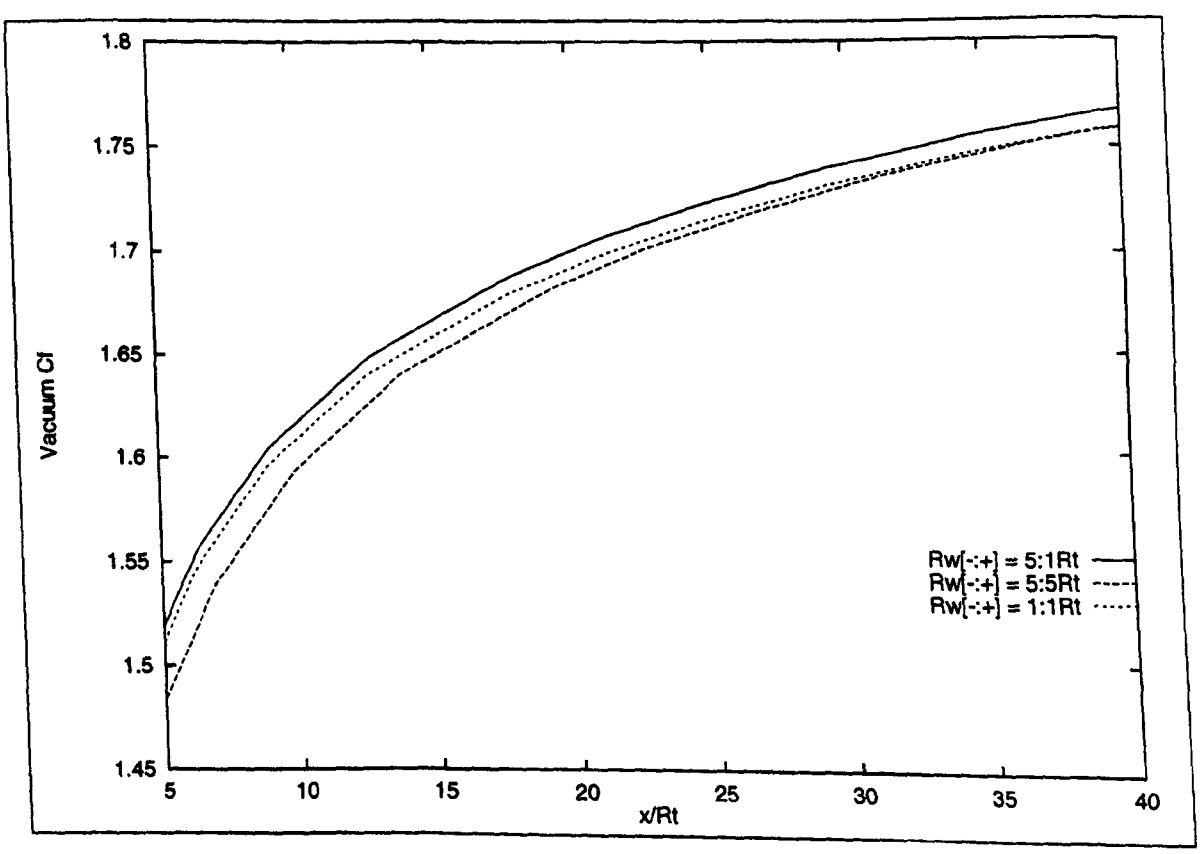

Figure 3.17: *Effect of R_w^- and R_w^+ on C_F^∞, Planar Optimised Nozzles*

As was the case for the previous nozzle type, it is possible to separate the effects of R_w^- and R_w^+, and these are shown in Figs. 3.15 and 3.16. The effect of R_w^- on thrust coefficient is similar to that for planar conical nozzles, having little effect on short nozzles but producing reduced thrusts for reduced R_w^- in longer nozzles. The post throat curve however has a more general effect, as reducing R_w^+ improves performance for all lengths. This undoubtedly explains the increase in length (relative to the conical type) at which a given $R_w^=$ becomes optimum observed in Fig. 3.14 and discussed earlier. To finish, Fig. 3.17 demonstrates the combined effect of varying R_w^- and R_w^+, with the expected result that as with planar conical nozzles, optimum results are obtained by increasing pre throat and reducing post throat radii.

3.5.3 Conical Nozzles

Turning to true conical nozzles (designed using the shock free formulation described previously), Fig. 3.18 demonstrates the effect on thrust coefficient of small $R_w^=$ nozzles produced by selection of throat modelling technique. Results from the previous chapter suggested that the axisymmetric flow case was less effected by throat model choice, the initial characteristics being more similar than their two-dimensional equivalents, particularly near the nozzle wall. Compared to Fig. 3.7, the thrust coefficient plots for axisymmetric flows do indeed appear to be more similar, effected less by both throat model choice and $R_w^=$. It should be noted, however, that the thrust coefficient range of Fig. 3.18 is greater than that in Fig. 3.7 (due to the higher thrusts obtained by the conical design for a given length), and hence a definitive comparison is difficult from these figures.

	Nozzle length, $C_F^\infty = 1.75$			Nozzle Length, $C_F^\infty = 1.85$		
$R_w^=$	Analytical	CFD	Percent	Analytical	CFD	Percent
5	10.571381	10.580534	100.09	23.390542	23.478288	100.38
3	10.167118	10.173430	100.06	23.970138	24.026850	100.24
2	10.077728	10.053593	99.76	24.801026	24.739371	99.75
1.5	10.149445	10.039104	98.91	25.785178	25.331381	98.24
1	10.454464	10.000152	95.65	27.321305	25.704488	94.08

Table 3.3: *Nozzle Lengths for Specified C_F^∞, Conical Nozzles*

Table 3.3 gives a numeric analysis of the the effect of reducing the wall throat radius (again to a deliberately unrealistic accuracy). The thrust coefficients demanded have been raised compared to the planar nozzles in Tables 3.1 and 3.2 to ensure that the resulting nozzle length is approximately similar. By comparing these results with those contained within Table 3.1 it would seem that almost identical conclusions may be drawn about the effect of throat model selection of both planar and axisymmetric conical nozzles, i.e. only significant

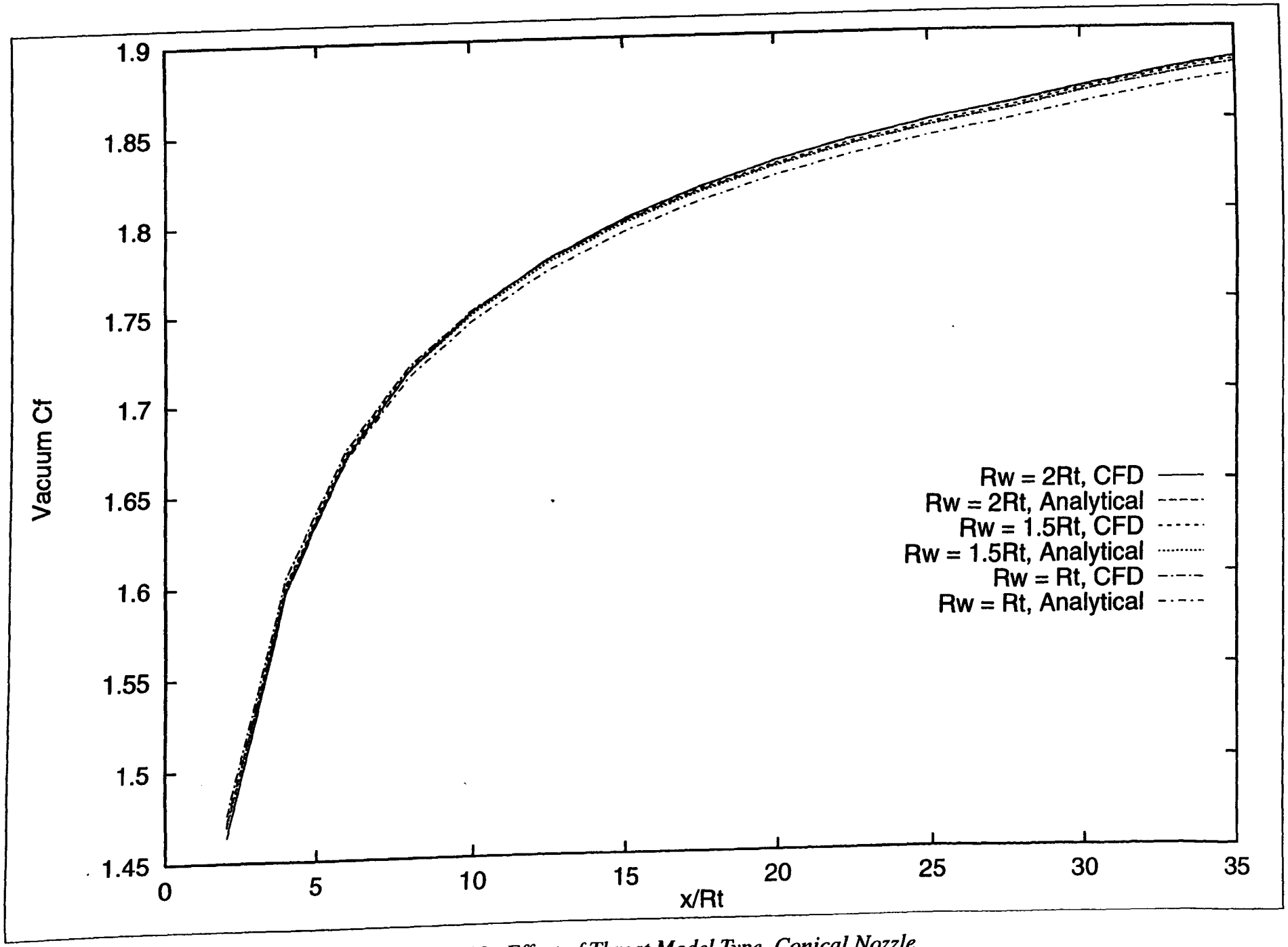

Figure 3.18: *Effect of Throat Model Type, Conical Nozzle*

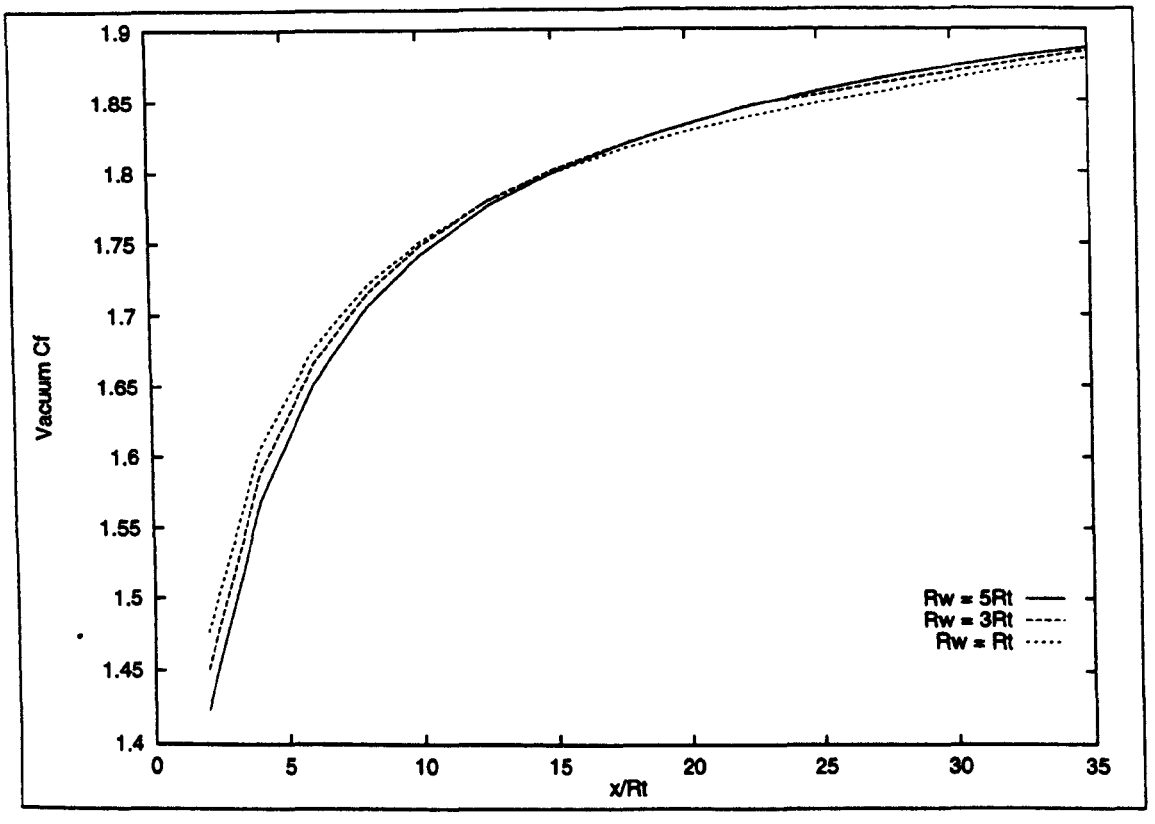

Figure 3.19: *Effect of $R_w^=$ on C_F^∞, Conical Nozzles*

deviation occurs for $R_w^=$ below $2Rt$, the optimum throat wall radius is a function of the desired length, and using the analytical method for input characteristics could conceivably lead to the selection of a non optimum value of $R_w^=$, particularly for short nozzles. It would further appear that the percentage change in predicted length caused by the choice of throat

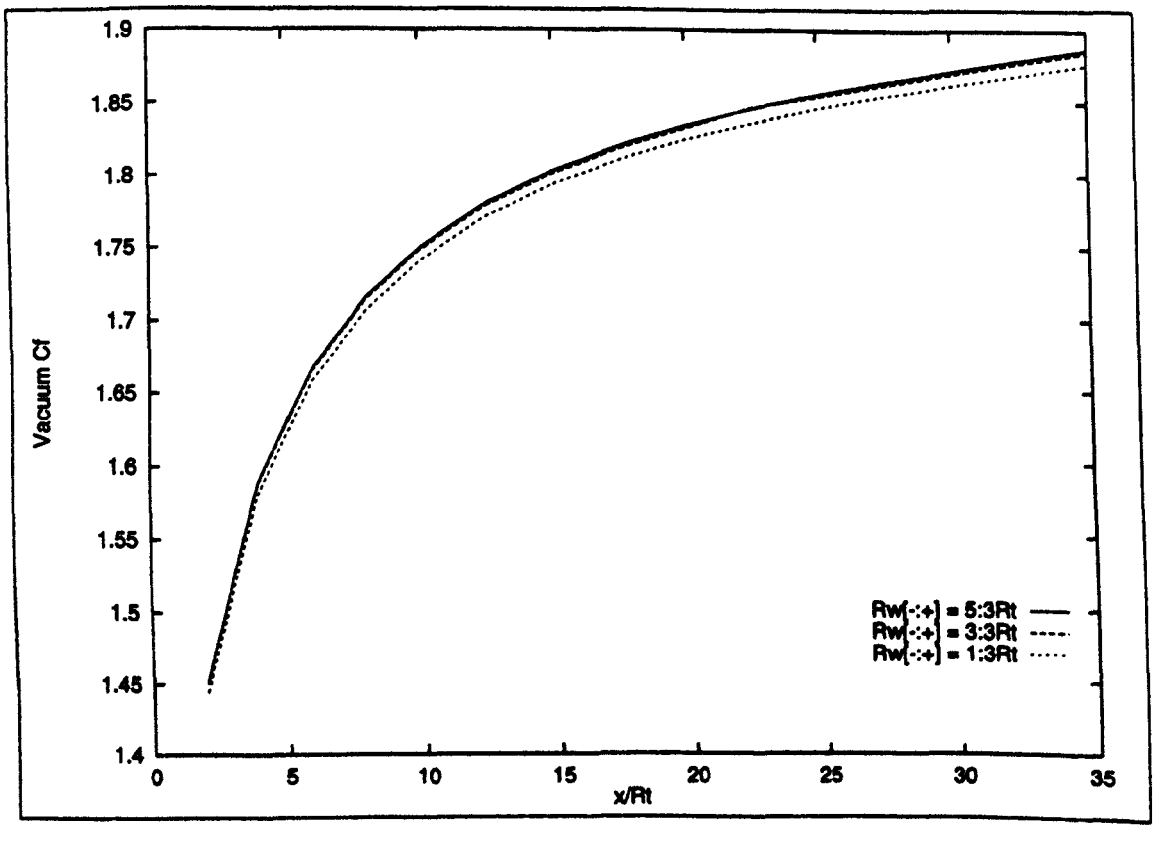

Figure 3.20: *Effect of R_w^- on C_F^∞, Conical Nozzles*

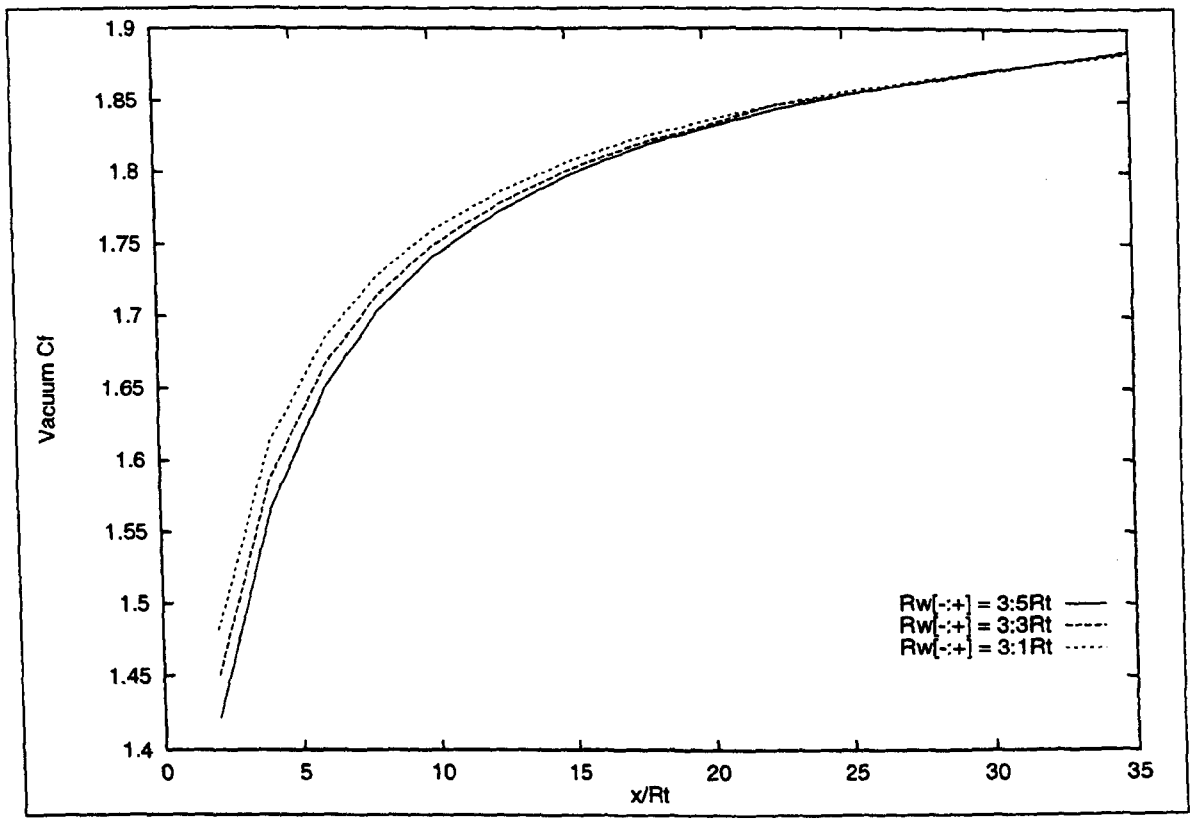

Figure 3.21: *Effect of R_w^+ on C_F^∞, Conical Nozzles*

model is actually very similar between planar and axisymmetric conical nozzles, although there is a small reduction in this effect in axisymmetric flow.

A graphical illustration of the effect of $R_w^=$ on conical nozzles is provided in Fig. 3.19 (as for the other nozzle types described, this figure and all following results are produced from input characteristics derived from the computational throat model). This figure reveals that the primary effects of $R_w^=$ on axisymmetric conical nozzles closely resemble those induced on the planar variant (Fig. 3.7). Again, optimum $R_w^=$ increases with total nozzle length, and the lengths at which the thrust coefficient plots cross (i.e. the length at which a $R_w^= = 3R_t$ nozzle produces more thrust than an $R_w^= = R_t$ nozzle, etc.) occur at very similar lengths in both the planar and axisymmetric nozzles.

Figs 3.20 and 3.21 isolate the effects of the pre and post throat wall radius on the vacuum thrust coefficient. As was the case for planar conical nozzles, increasing R_w^- has little effect on short nozzles, but offers increased performance for longer designs. Conversely, reducing R_w^+ increases performance of shorter nozzle, but this effect lessens with increased nozzle length. Performance is therefore increased for all nozzles by increasing R_w^+ and reducing R_w^-.

3.5.4 Axisymmetric Optimised Contours

The final category of nozzle examined is that most often used on launch vehicles, and is the highest performance conventional type. This is the minimum length axisymmetric nozzle, otherwise known as a 'bell' or optimum contoured nozzle. Fig. 3.22 shows the effect of throat modelling method on the thrust coefficient estimate produced for such nozzles, for a range of (small) values of $R_w^=$. This figure shows the now familiar trends; in general little difference emerges regardless of throat model type until $R_w^=$ reduces to approximately $1.5R_t$ or below, and then the analytically derived input conditions produce a small drop in the total thrust estimated.

The length of nozzle required to generate two values of C_F^∞ are shown in Table 3.4, and demonstrate this effect. Comparison with the two-dimensional optimised nozzles provided in Table 3.2 show that the level of under prediction of thrust is very similar for the planar and axisymmetric cases. Comparison with Table 3.3 produces the expected result that optimised contours are indeed considerably shorter for a given thrust than equivalent conical nozzles.

	Nozzle length, $C_F^\infty = 1.75$			Nozzle Length, $C_F^\infty = 1.85$		
$R_w^=$	Analytical	CFD	Percent	Analytical	CFD	Percent
5	9.964158	9.975557	100.14	19.618979	19.650198	100.16
3	9.369212	9.374948	100.06	18.895685	18.912221	100.09
2	9.130654	9.111178	99.79	18.775312	18.724244	99.73
1.5	9.102128	9.017760	99.07	19.013857	18.757906	98.65
1	9.289114	8.954013	96.39	19.939907	18.904780	94.81

Table 3.4: *Nozzle Lengths for Specified C_F^∞, Axisymmetric Optimised Nozzles*

As was the case for the planar optimised nozzle, the effect of method choice on thrust coefficient is small, even for low $R_w^=$, and hence is likely to be swallowed by other empirical corrections required for actual nozzle design. However, there is again the more significant possibility that error could occur in the contour design process if the input characteristics result in contour designs that are not truly optimum. The effect of initial line on contour construction was therefore examined for the $R_w^= = R_t$ case, using a constant length requirement (in this case a nozzle of 15 R_t). The resulting contours are shown in Fig. 3.23, and as may be seen, are identical.

The effect of the wall radii at the throat on C_F^∞ is shown in Figs. 3.24 to 3.26, for computationally derived input conditions. The general trends are very similar to those produced by planar optimised nozzles, the pre throat wall radius having very little effect except for long nozzles, but a reduction in post throat causing an increase in thrust for all lengths.

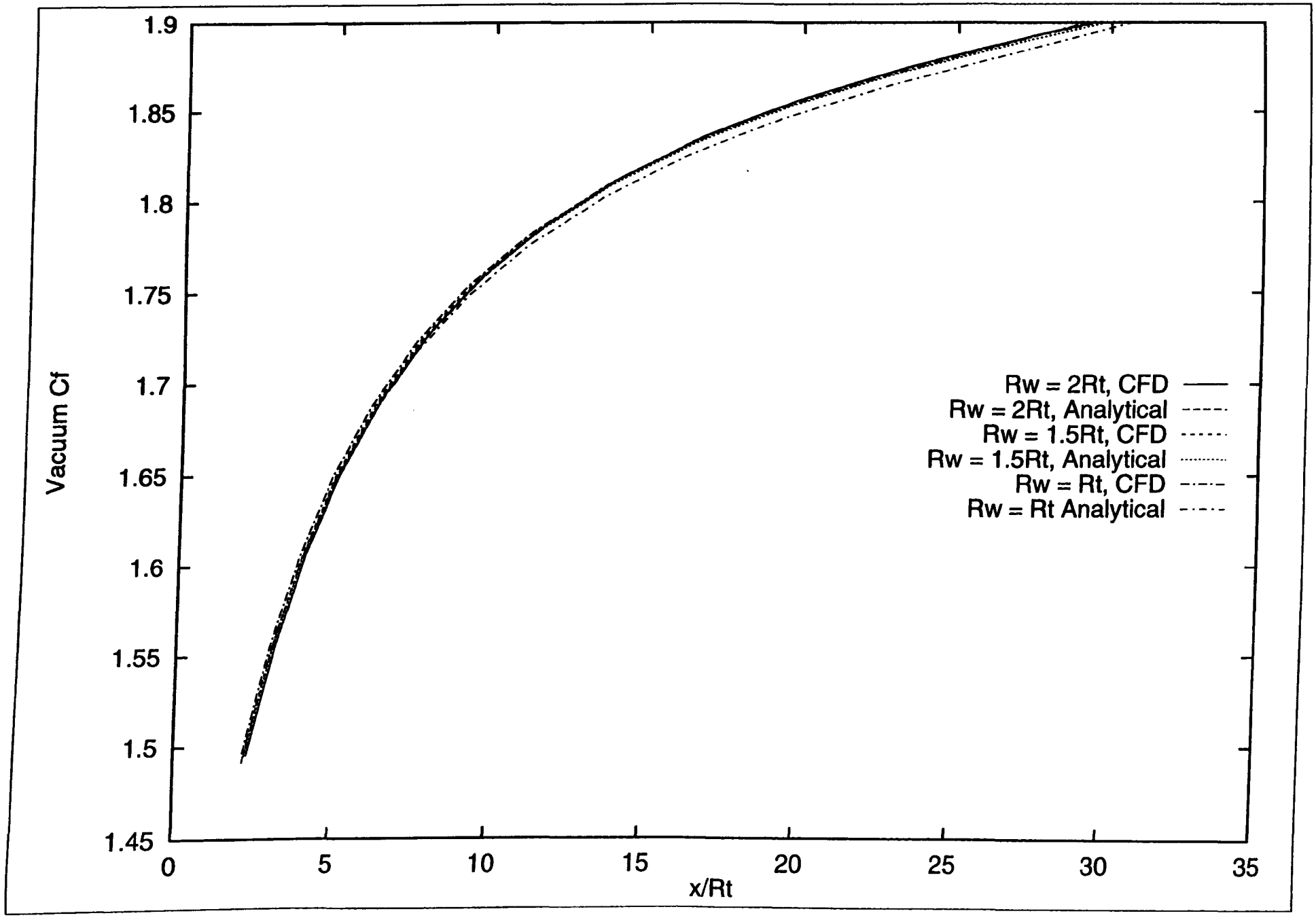

Figure 3.22: *Effect of Throat Model Type, Optimised Axisymmetric Nozzle*

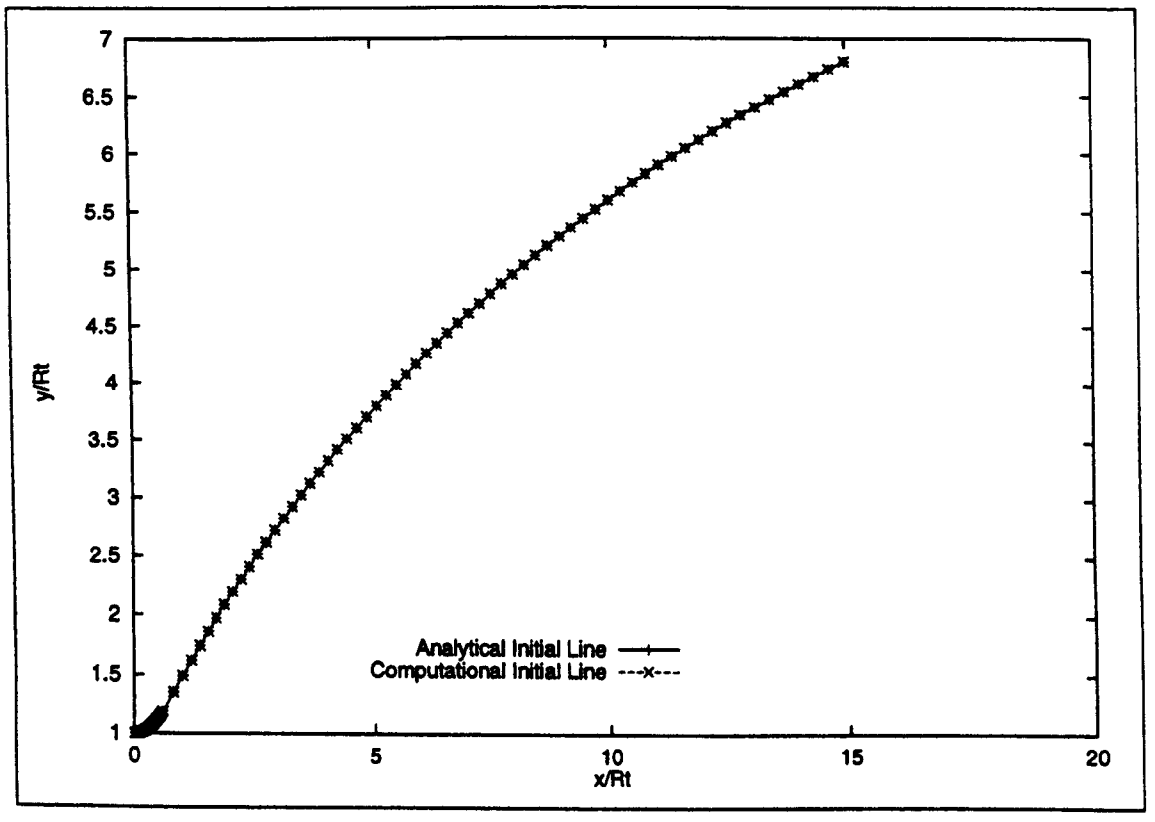

Figure 3.23: *Comparison of Contours, Length 15 R_t*

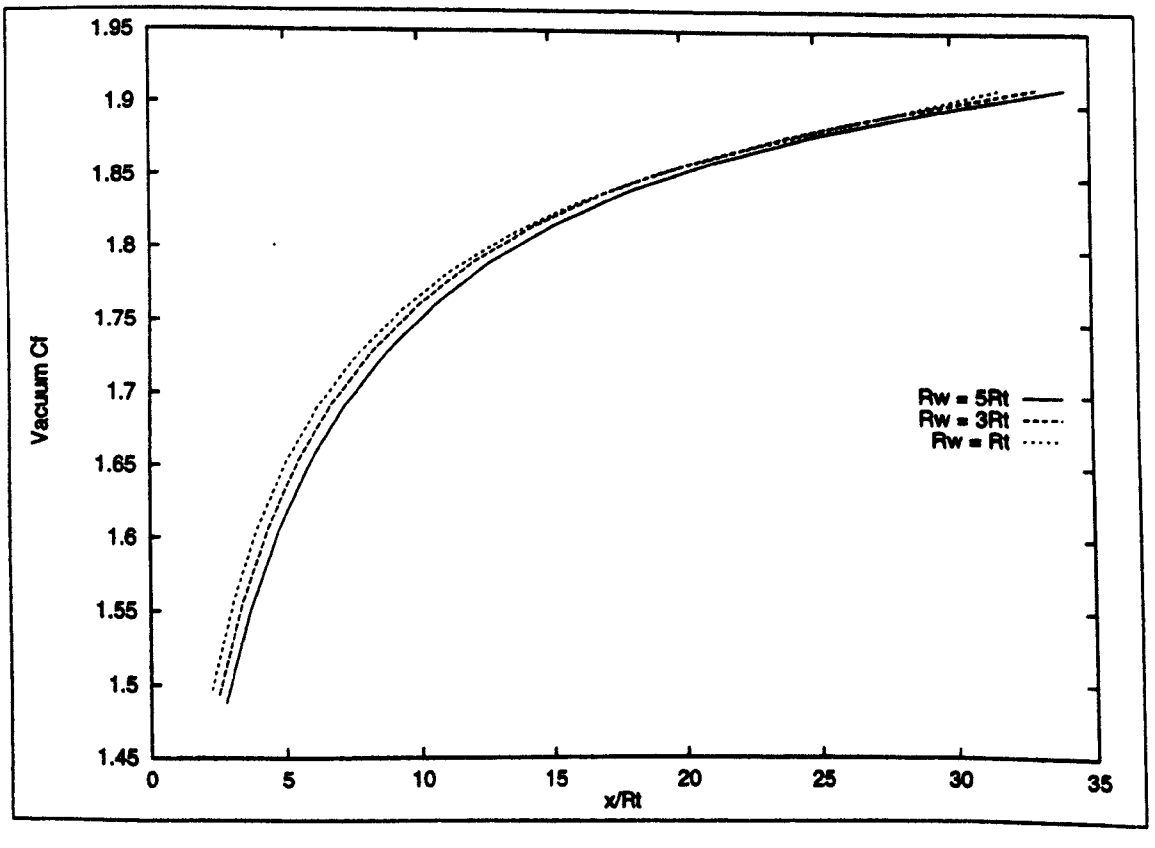

Figure 3.24: *Effect of $R_w^=$ on C_F^∞, Axisymmetric Optimised Nozzle*

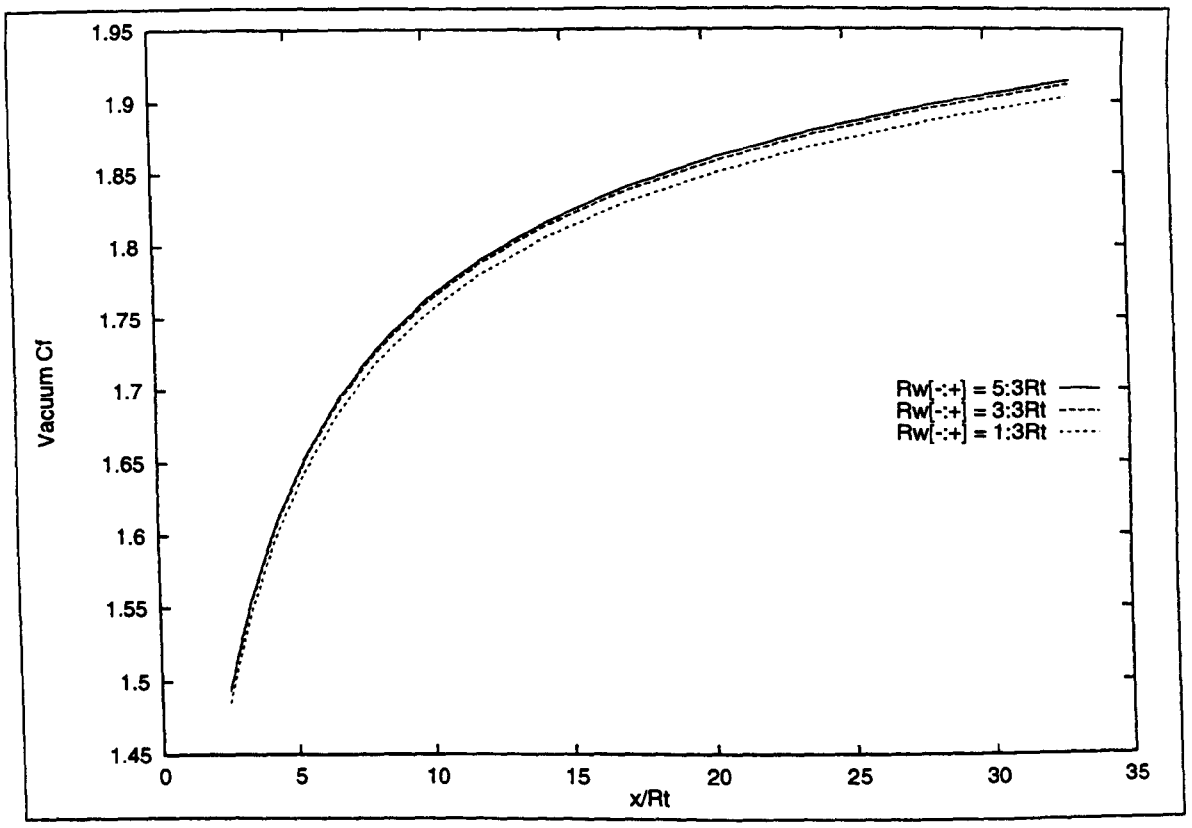

Figure 3.25: *Effect of R_w^- on C_F^∞, Planar Optimised Nozzle*

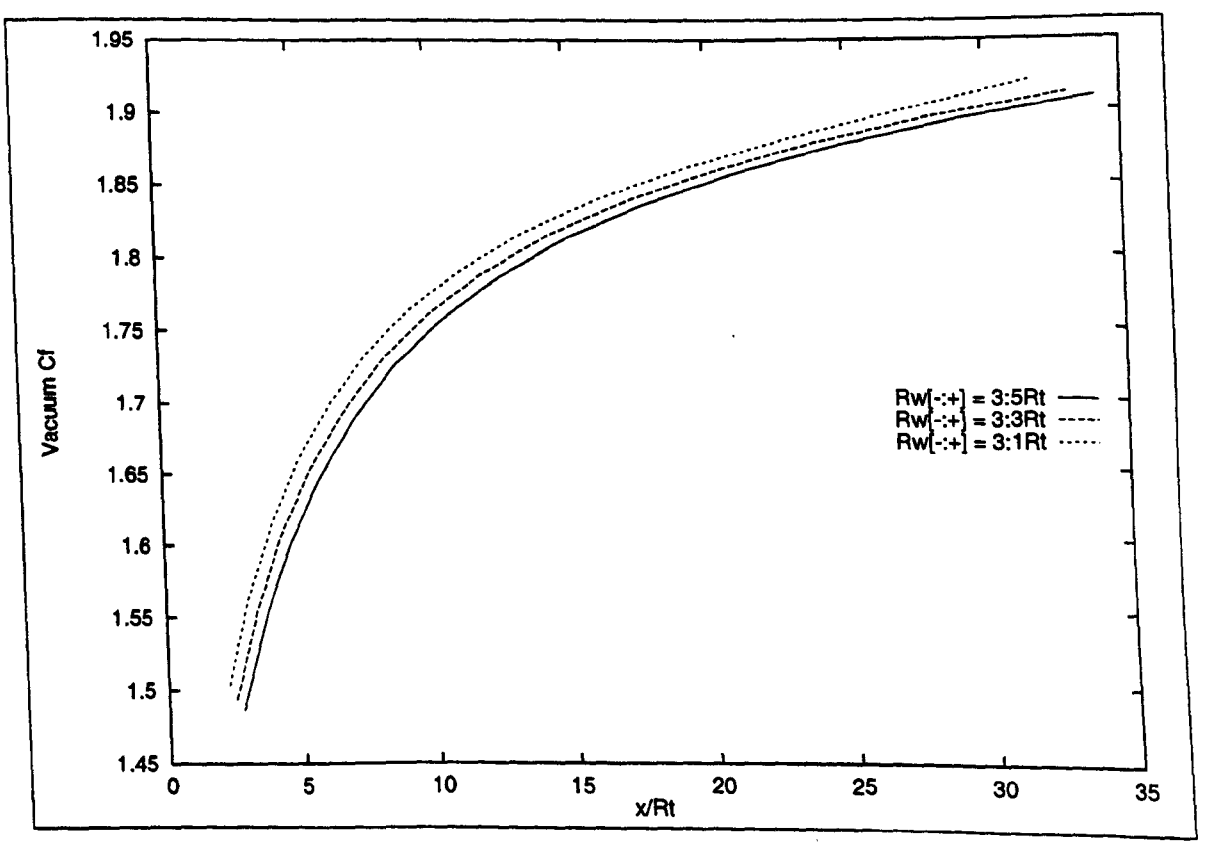

Figure 3.26: *Effect of R_w^+ on C_F^∞, Planar Optimised Nozzle*

3.6 Summary of Results

3.6.1 Initial Line Generation

Two different methods by which the input flow conditions for the MoC were described in Ch. 2. These were an analytical scheme, available in the literature, and a computational scheme, unique to this investigation. Initial conditions were generated using both methods, and used to predict thrust coefficient and nozzle flow-fields for a range of conventional nozzle types. The thrust coefficients produced by the two methods were then compared, to determine what effect, if any, the choice of throat model has on the complete nozzle analysis process.

It was found that for nozzles with a wall radius of curvature more than twice the throat radius (or half height in planar nozzles), the differences between the two methods were negligible. This result was expected, as little difference in initial characteristic for such throat configurations had been found in the investigation presented at the end of the previous chapter. It demonstrates that the computational model (developed primarily for ED throats) is accurately modelling the flow in the throat region of convergent - divergent nozzles. However, the computational method requires a far greater solution time, and therefore in the design of nozzles with relatively large wall radii of curvature at the throat, the analytical method is superior for all of the conventional nozzle types examined.

As $R_w^=$ is reduced below $2R_t$, there is a growing discrepancy in the results produced by the two techniques. In the previous chapter, the conservation of mass of the two methods in the throat region was used to demonstrate the superiority of the computational scheme for such configurations. The effect of the lessening accuracy of the analytical scheme produces similar trends for all the nozzle types investigated, this being a slight reduction in estimated thrust coefficient. Whilst this underestimation of thrust is very small for a nozzle of a given length, the low gradient of the thrust curve means that larger differences occur in the predicted nozzle length for a given thrust level, particularly if high thrust coefficients, and hence long nozzles, are required (differences of up to 5 percent occur for nozzles where $R_w^= = R_t$). This could result in an incorrect selection of optimal throat wall radius for a particular nozzle design. It has been demonstrated, however, that no errors occur in the contour produced by optimising routines.

3.6.2 Relation of C_F^∞ to the Wall Radii of Curvature at the Throat

It is clear from the results presented in this chapter that the thrust coefficient produced by a nozzle design is dependent upon the radii of curvatures of both the pre and post throat walls, each of which have different effects depending on nozzle type. Whilst the resulting variance

in thrust produced is relatively small, as has been discussed in the previous section the impact is increased by the low gradient of the thrust curve, especially for long nozzles. Table 3.5 shows the effect of reducing R_w^+ for a variety of nozzles. As can be seen, the saving in length achieved by this simple method ranges from 1 to 12 percent. It is also clear that nozzles of optimised contour design benefit to a greater degree from this effect, compared to the simpler conical types. Variations in R_w^- are not included here, as the length of the connecting duct to the combustion chamber will be effected. As the possible impact of combustion chamber design produced by this is not included in the present analysis, the effect of R_w^- on the total length of the rocket motor is more difficult to ascertain.

	Planar Nozzles, $C_F^\infty = 1.7$		Axisymmetric Nozzles, $C_F^\infty = 1.85$	
$R_w[- : +], R_t$	Conical	Optimised	Conical	Optimised
5:5	26.21	22.68	23.48	19.65
5:3	25.29	21.37	23.58	18.51
5:1	25.13	20.03	23.18	17.34
percent change	4.12	11.68	1.27	11.77

Table 3.5: *Nozzle Lengths in R_t for Specified C_F^∞*

The implication derived from the results presented is that the optimal combination is an infinite pre throat radius leading to a sharp corner at the throat. In practise, however, the pre throat radius is limited by the combustion chamber geometry (a larger pre throat radius will require a longer channel between the combustion chamber and the throat), and a sharp corner at the throat would be subject to aerodynamic losses, such as separation and other viscous effects ignored in the present analysis. Any sharp corner would also suffer structurally, due to high stress concentrations.

A common compromise is a R_w^- of about $1.5R_t$ and R_w^+ near $0.5R_t$ respectively (e.g. Skylon, and the nozzles examined by Rao [3]. It is interesting to note that from the results produced by the analytical scheme, the optimum R_w^- is about $1.5R_t$; increasing R_w^- above this has little effect, but decreasing causing a noticeable drop in performance. The results derived from the computational initial line, however, imply that this variable could in fact be reduced further without undue losses. Unfortunately, testing of this hypothesis is difficult, as experimental evidence for the effect of R_w^- on overall nozzle performance does not exist within the literature. It must also be remembered that other factors ignored by the present analysis, such as boundary layer thickness and other viscous effects, are likely to produce increasingly significant effects on the throat flow as R_w^- is reduced.

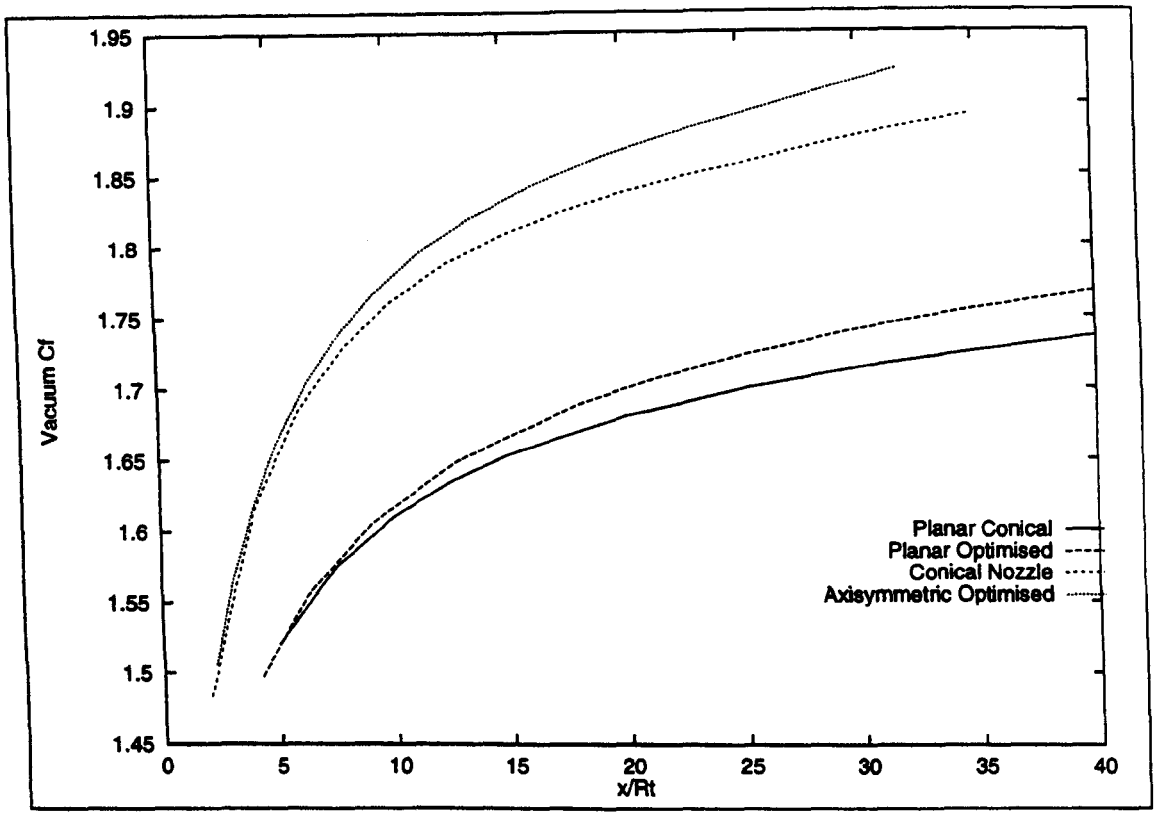

Figure 3.27: *Comparison of Nozzle Performance,* $R_w^- = 5R_t, R_w^+ = R_t$

3.6.3 Performance Summary

To complete this chapter, a comparison of vacuum thrust coefficients produced for each of the four nozzle types is shown in Fig. 3.27 (for R_w^- and R_w^+ of $5R_t$ and R_t respectively) and

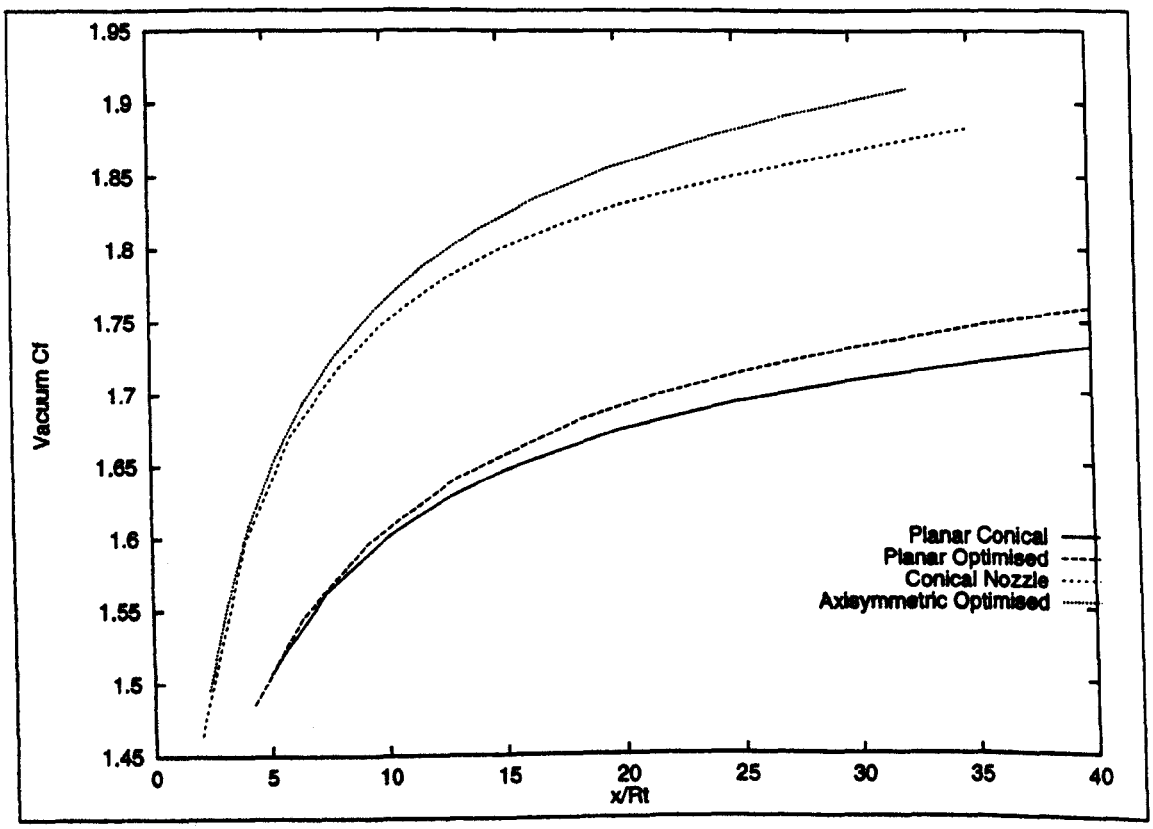

Figure 3.28: *Comparison of Nozzle Performance,* $R_w^- = 2R_t, R_w^+ = 2R_t$

Fig. 3.28 (for R_w^- and R_w^+ both of $2R_t$). As may be seen, the optimisation of the contour clearly reduces length for a given C_F^∞ in both planar and axisymmetric flows. The figures already presented in Table 3.5 show that for a nozzle with wall radii of $R_w[- : +] = 5 : 1$, the saving on length for an axisymmetric nozzle of C_F^∞ of 1.85 is just over 25 percent, and for the planar case with a C_F^∞ of 1.7, it is slightly above 20 percent. These savings increase with increasing C_F^∞.

Chapter 4

ED Nozzle Design and Closed Wake Mode Analysis

The previous two chapters dealt with conventional nozzles, and have demonstrated the techniques by which effective design and performance analysis of conical and bell nozzle types may be achieved. The aim of this chapter is to extend the design methodology to allow generation of length optimised ED nozzle contours, and the analysis process to include the closed wake flow-field and performance characteristics of this nozzle type.

It was noted in the introductory chapter that the primary flow present within an ED nozzle is similar to that of a conventional nozzle, in that it may be described as an inviscid fluid accelerating through a transonic region to a supersonic exit plane. However, the ED nozzle flow-field is further complicated in two ways; it contains a recirculating region entrapped within the primary supersonic inviscid flow, and the throat geometries of such nozzles are formed by nozzle walls displaced radially from, and inclined at an angle to, the nozzle centreline. The first of these factors considerably complicates the analysis of the flow-field within the nozzle, particularly with respect to the effects produced by variations in ambient conditions, and the second complicates the analysis of the transonic region.

The first part of this chapter discusses the alterations made to the standard throat model presented in Ch. 2 to allow analysis of the flow through ED nozzle throat geometries. The results of this CFD analysis then define a set of input conditions for a characteristics based algorithm allowing optimised contour design, and a discussion of this technique is presented.

In the optimisation process, only the inviscid flow need be considered. However, to allow the thrust of such nozzles operating in a vacuum to be predicted, the effect of the interaction of the inviscid and viscous flow regimes behind the central pintle must be included. As the wake behind the pintle will be closed under these conditions, this flow regime represents a simplification of the analysis problem. Prediction of the detail of the flow-field is not

necessary, as it will have no effect on wall pressures. This means that the vacuum thrust of an ED nozzle may be estimated if only the pressure acting on the base of the pintle is known, and the method by which this is achieved is presented to end the chapter.

4.1 Throat Analysis

As with more conventional nozzle types, the flow conditions around the sonic line may be analysed using either analytical or computational methods. In two-dimensional flow, a reasonable approximation to the conditions at the throat may be achieved by rotating and translating results produced for an equivalent axial throat. In axisymmetric flow, however, this method is inapplicable, as the cross sectional area between the nozzle walls (perpendicular to the local flow direction) is a function of the radial distance of these walls. This results in a distortion of the Mach contours by both the radial location and inclination of the throat.

Analytical methods have been developed that attempt to allow for these effects on the flow through unconventional axisymmetric throats. These methods are appropriate either for annular, but approximately axial throats [47], or throats of arbitrary, but large inclination [48] (Hopkins and Hill also extended their technique to include such throat configurations [49], but this method was discarded for the same reasons as their method for axial throats, i.e. the indirect nature of the solution). For small perturbation techniques to be applicable, there must be a dominant flow direction, and hence the flow must be either predominantly axial or radial. Unfortunately, this means that a large range of axisymmetric nozzle configurations containing intermediate throat angles have no analytical solution, as the basic assumptions are violated.

Preliminary results from an analysis of two-dimensional nozzles demonstrated that a unique throat angle exists for optimum thrust performance for a specified total nozzle length. It was found that this angle was dependent on nozzle length, increasing as the required nozzle length grew. It was therefore necessary to predict the flow in the throat regions of a wide variety of nozzles configurations, in both two-dimensional and axisymmetric flows. Of particular concern is the fact that the small to medium sized nozzles likely to be the first step in an experimental program examining the effectiveness of the ED concept required throat angles in the range of 30 to 60 degrees, precisely the region in which the analytical technique is inapplicable. This being the case, the analytical methods were discarded, and effort concentrated on the computational technique described in Ch. 2.

4.1.1 ED Throat Geometry Generation

The CFD scheme described in Ch. 2 makes no assumptions of small perturbations, and hence is unaffected by the local flow direction and Mach number. This being the case, it is only at the generation of the computational mesh that differences between solution procedures for conventional axial and totally arbitrary ED throat configurations arise. This process is complicated, however, by an increase in the number of input variables used to define the geometry of the throat region.

For a conventional nozzle, prescribing $R_w^=$ combined with a simple rule for creating a parallel flow duct to ensure reliable inflow boundary conditions is sufficient to define the entire mesh. In the case of an ED nozzle, however, the location and inclination of the geometrical minimum between the outer (contour) and inner (pintle) walls must be specified, along with the radii of curvature of these walls. From this information, a mesh must be created that not only matches these geometric requirements, but will also result is a smoothly accelerating flow without any discontinuities or localised high velocity gradients.

To provide similarity with conventional combustion chambers, it is likely that a parallel flow region leading up to the contraction before the throat will be required. This is also necessary to allow the computational method to retain the simple inflow boundary conditions described in Ch. 2. This too increases the number of variables, as the radial locations of the inner and outer wall of this duct must be defined. To produce consistent results with smooth Mach isobars in the region on the geometric throat, it is helpful if the wall surfaces connecting the parallel duct to the throat curves have continuous gradients. It is also desirable to keep this region as short and compact as possible, to reduce mass.

There are several methods by which nozzle throat geometries satisfying these requirements could be created, and the technique described in this section is but one of these. In the case of a specific nozzle design, a more unique set of construction rules may lead to a more efficient and compact throat region. However, the following process has been found to produce a mesh allowing convergence of the CFD method for a wide range of input parameters. This quality is of particular importance in a generic study of the ED nozzle concept, where an attempt is made to evaluate the impact of a variety of parameters on general nozzle design and performance.

To provide an easy comparison with conventional nozzles, the geometric parameters in the ED nozzle throat region are non dimensionalised with respect to the length of the shortest perpendicular connecting the two walls forming the nozzle, denoted G_t. In two-dimensional flow this distance forms the equivalent of the throat half height (R_t) of conventional nozzles. The remainder of this subsection will deal with the generation of planar throat geometries whilst the added complications involved with axisymmetric grids are considered in more

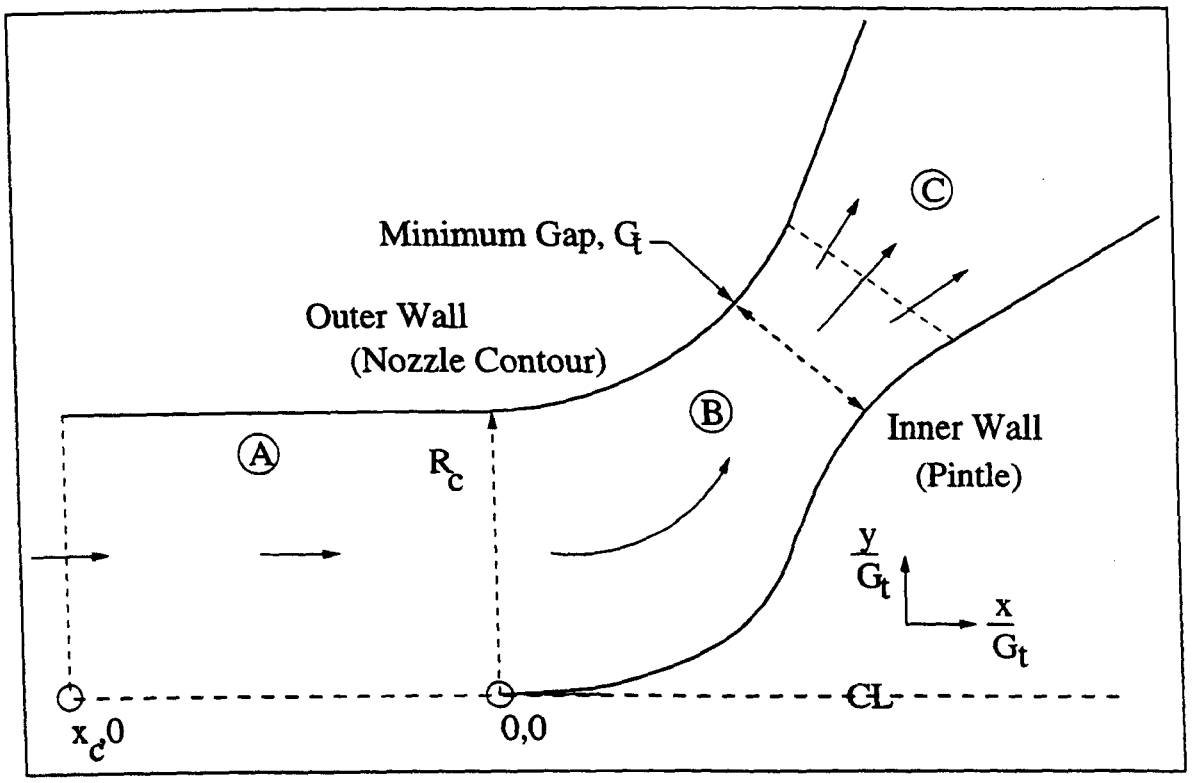

Figure 4.1: *ED Nozzle Throat, General Configuration*

detail in the that following. subsection.

Fig. 4.1 shows the three main regions of flow in a typical ED nozzle throat. Region A is the parallel flow duct. This has a similar function to the parallel duct generated by the axial throat geometry definition routine, in that it allows the inflow boundary, x_c, to be located at a sufficient distance upstream of the sonic line that the assumption of parallel flow necessary at this boundary is reasonable. The inflow boundary is set at a distance of $2R_c$ upstream, where R_c is the separation of the duct walls. The nozzle contour in this region is therefore formed by the line $y = R_c$, and the pintle wall by $y = 0$. A similar scaling technique is used as outlined in Sec. 2.2.7 to allow concentration and rarefication of cells where appropriate. This region of the flow contains $\frac{10}{32}ni$ cells, ni being the total number of cells in the i (flow) direction.

The outflow region (area C in Fig. 4.1) serves a similar purpose to the short conical section at the end of conventional throat geometries. It allows the outflow boundary to be sufficiently downstream of the throat that the characteristics originating from the intersection of the geometric minima and the throat walls are contained within the flow-field without the need for large exit wall angles, and associated high velocity gradients at the outflow boundary. It is formed by simple linear extensions of both the contour and pintle walls and extends a short distance downstream. Cell spacing is linear, and of the same magnitude in the flow direction as the final column of cells in the throat region (B). The number of cells in this outflow region is $\frac{8}{32}ni$ cells

Generation of the inclined throat region (B) is more complicated. As well as the nominal

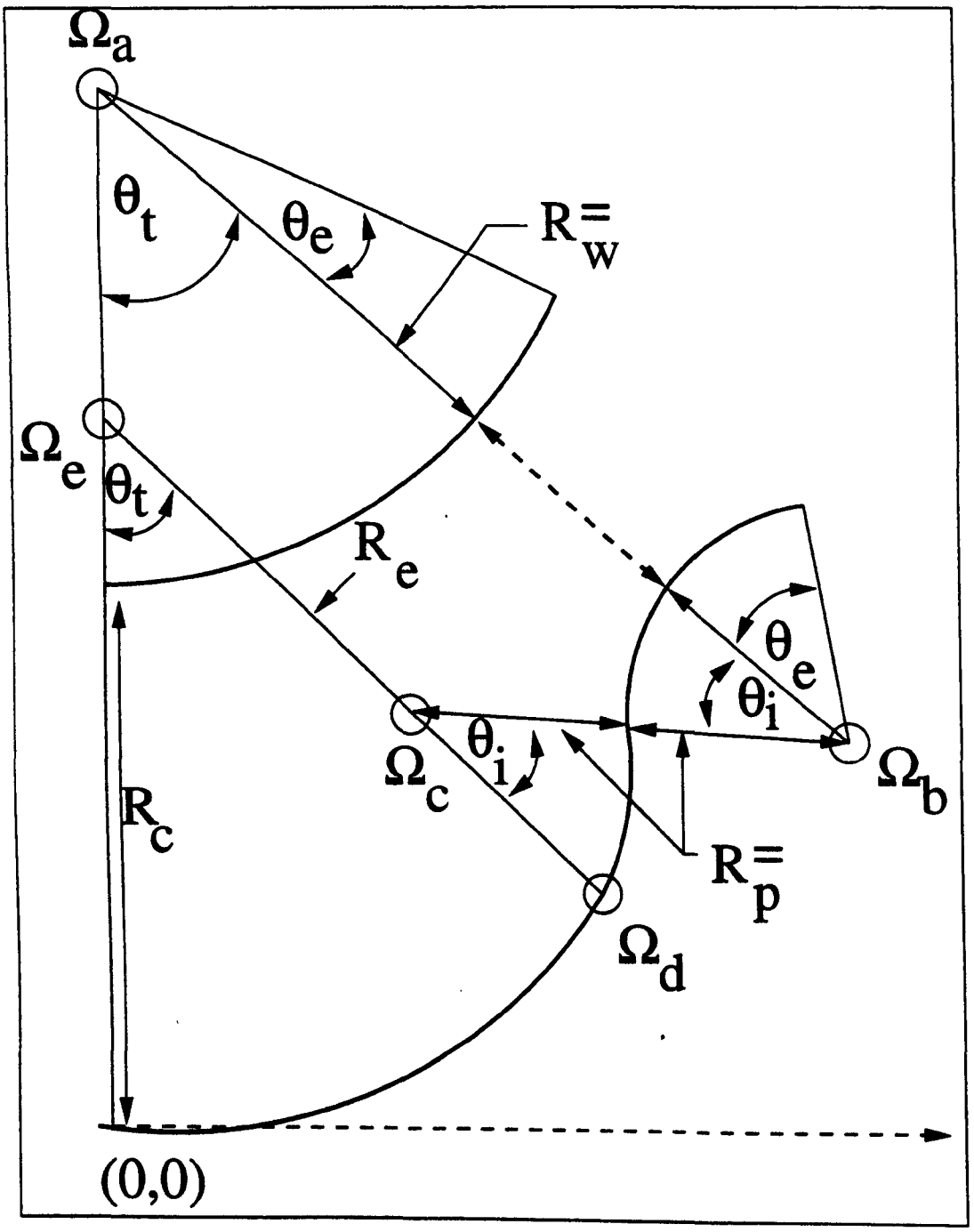

Figure 4.2: *ED Nozzle Throat, Construction*

throat angle (the angle subtended between the line forming the minimum wall gap and the vertical, θ_t), four further quantities are required as input to allow the equations defining the nozzle walls to be derived. These are the outer and pintle wall radii of curvature ($R_w^=$ and $R_p^=$), the maximum angle of the wall curvatures beyond the nominal throat angle (θ_e) and an inflection angle (θ_i). From this data, the wall contours are constructed using a method outlined graphically in Fig. 4.2, and as explained below. Centres of curvature are denoted by the symbol Ω.

R_c is unknown before the calculation initiates, and hence the wall contours are determined in terms of the relative positions of the centres of curvature. The pintle wall consists of a circular arc centred at Ω_e, of unspecified radius R_e, followed by two smaller arcs of

radius $R_p^=$ and included angle θ_i, centred at Ω_c and Ω_b. As the radii and subtended angles of these two back to back arcs are the identical, the angles subtended from centres Ω_a and Ω_e are equal to each other, and to the throat angle θ_t. The final section of the pintle is the circular arc wall after the throat of radius $R_p^=$ and subtended angle θ_e. The outer nozzle wall is simply formed by a circular arc, radius $R_w^=$ and subtended angle $\theta_t + \theta_e$.

Ω_b lies on a radial from Ω_a at the throat angle. Therefore

$$(\Omega_b)_x = (\Omega_a)_x + (R_p^= + R_w^= + 1)\sin(\theta_t) \tag{4.1}$$

and as by arbitrary convention $(\Omega_a)_x$ is 0, $(\Omega_b)_x$ is located. $(\Omega_c)_x$ then follows

$$(\Omega_c)_x = (\Omega_b)_x - 2R_p^= \sin(\theta_t + \theta_i) \tag{4.2}$$

and as the arcs centred on Ω_b and Ω_c are of known radius and subtended angle, consideration of the geometry results in

$$(\Omega_d)_x = (R_w^= + 1)\sin(\theta_t) - 2R_p^=(\sin(\theta_t + \theta_i) - \sin(\theta_t)) \tag{4.3}$$

The location of $(\Omega_d)_x$ allows the radius of curvature of the initial section of pintle wall centred at Ω_e to be found, as this curve is constrained to pass through the origin of the coordinate system, and hence

$$R_e = \frac{(\Omega_d)_x}{\sin(\theta_t)} \tag{4.4}$$

It follows that the centre Ω_e is located at $(0, R_e)$.

All the centres now have known x coordinates. In order to locate their positions in the radial direction, a pair of equations for the y coordinate of point Ω_d are derived, again from consideration of geometrical constraints:

$$(\Omega_d)_y = (R_e)(1 - \cos(\theta_t)) \tag{4.5}$$

$$(\Omega_d)_y = (\Omega_a)_y - (R_w^= + 1)\cos(\theta_t) - 2R_p^=(\cos(\theta_t) - \cos(\theta_t + \theta_i)) \tag{4.6}$$

Equating and rearranging the above results in

$$(\Omega_a)_y = (R_e)(1 - \cos(\theta_t)) + (R_w^= + 1)\cos(\theta_t) + 2R_p^=(\cos(\theta_t) - \cos(\theta_t + \theta_i)) \tag{4.7}$$

and as all quantities on the RHS of Eqn. 4.7 are known, $(\Omega_a)_y$ may be calculated. Once known, this value may then be substituted into

$$R_c = (\Omega_a)_y - R_w^= \tag{4.8}$$

to produce R_c. Once $(\Omega_a)_y$ is known, the radial location of all the other centres follow in a similar manner as outlined above, except radials are resolved in the y rather than x direction.

As the outer wall is simply an arc centred on (Ω_a) with radius R_w^+, the equations defining each wall are known, and attention may turn to the spacing of cell boundaries along these walls.

Cell vertices along the outer boundary are as evenly spaced as possible with respect to wall length along the throat and outflow regions, although again a cell boundary is created at the minimum wall gap to ensure that this minima actually occurs in the flow. This means that the number of cells before this minima, nb_1, is

$$nb_1 = \frac{14}{32} ni \frac{R_w^=(\theta_t)}{R_w^=(\theta_t + \theta_e) + \frac{x_c}{\sin(\theta_e)}} \tag{4.9}$$

and that after, nb_2, is

$$nb_2 = \frac{14}{32} ni \frac{R_w^=(\theta_e)}{R_w^=(\theta_t + \theta_e) + \frac{x_c}{\sin(\theta_e)}} \tag{4.10}$$

Considering initially cell boundaries before the geometric minima, the angle subtended about centre Ω_a between the vertical and cell boundary i on the outer wall, θ_w, is

$$\theta_w = \frac{i}{nb_1} \theta_t \tag{4.11}$$

and hence the coordinates of this boundary point on the outer nozzle wall are

$$x_o^i = R_w^= \sin\theta_w \tag{4.12}$$

$$y_o^i = 1 + R_w^=(1 - \cos\theta_w) \tag{4.13}$$

The equations used to define points on the inner (pintle) wall are dependent upon the value of θ_w. If $\theta_w < \theta_1$

$$x_p^i = R_e \sin(\frac{\theta_w \theta_t}{\theta_1}) \tag{4.14}$$

$$y_p^i = R_e(1 - \cos(\frac{\theta_w \theta_t}{\theta_1})) \tag{4.15}$$

where

$$\theta_1 = \tan^{-1} \frac{(\Omega_d)_x}{(\Omega_a)y - (\Omega_d)_y} \tag{4.16}$$

If θ_w lies between θ_1 and θ_2 then

$$x_p^i = (\Omega_c)_x + R_e \sin(\theta) \tag{4.17}$$

$$y_p^i = (\Omega_c)_y - R_e \cos(\theta) \tag{4.18}$$

where

$$\theta = \theta_t + \frac{(\theta_w - \theta_1)\theta_i}{\theta_2 - \theta_1} \tag{4.19}$$

$$\theta_2 = \tan^{-1} \frac{(\Omega_b)_x + (\Omega_c)_x}{2(\Omega_a)_y - ((\Omega_b)_y + (\Omega_c)_y)} \tag{4.20}$$

and if θ_w is greater than θ_2 but less than θ_t then

$$x_p^i = (\Omega_b)_x - R_e \cos(\theta) \tag{4.21}$$

$$y_p^i = (\Omega_b)_y + R_e \sin(\theta) \tag{4.22}$$

where

$$\theta = \frac{\pi}{2} - \theta_t - \theta_i + \frac{(\theta_w - \theta_2)\theta_i}{\theta_t - \theta_2} \tag{4.23}$$

For the walls beyond the geometric minima,

$$\theta_w = \frac{i - nb_1}{nb_2}\theta_e \tag{4.24}$$

and substitution of this value into Eqns. 4.12 and 4.13 allows the outer wall point to be found. The pintle wall point may be located from Eqns. 4.21 and 4.22 with

$$\theta = 2\theta_t - \theta_w \tag{4.25}$$

Once points on the inner and outer contours for each value of i have been created, the local cross sectional area is simply the length of the line joining each pair of points. Eqn. 2.64 may then be used to determine an equivalent one-dimensional velocity, which is assumed to act perpendicular to this cross section. This allows a reasonable approximation to the flow to be used as input to the computational algorithms, reducing solution time (although it should be noted that this approximation is less realistic than was the case for conventional nozzles, particularly in axisymmetric mode). Cells are distributed evenly in the j direction.

Fig. 4.3 displays a typical coarse grid produced by this method. The throat geometry shown has both wall radii set to 1.5 G_t, a throat angle of 45 degrees, and θ_i and θ_e are 15 degrees. As may be seen, the cells are generally evenly distributed, and rectangular about the local flow direction. Some cells on the lower boundary just before the geometric minima are somewhat skewed, but this region of flow will generally be subject to low velocity gradients, and hence this does not pose a serious difficulty.

The solution of the flow for the nozzle geometry defined in Fig. 4.3 is presented in Fig. 4.4, with air as the working fluid and a finest grid measuring 192 cells in the i direction, and 48 in the j. The resulting Mach contours are smooth and continuous in the region of the geometric throat. Solution times are greater than for conventional nozzle geometry, due to the more complex flow-field, the less realistic initial conditions, and the presence of high velocity gradients at the exit boundary (this is unavoidable, as the geometry downstream of the throat is unknown).

Fig. 4.5 shows a comparison between Mach contours produced by the computational method for the same ED throat geometry, and results obtained by rotating, translating and

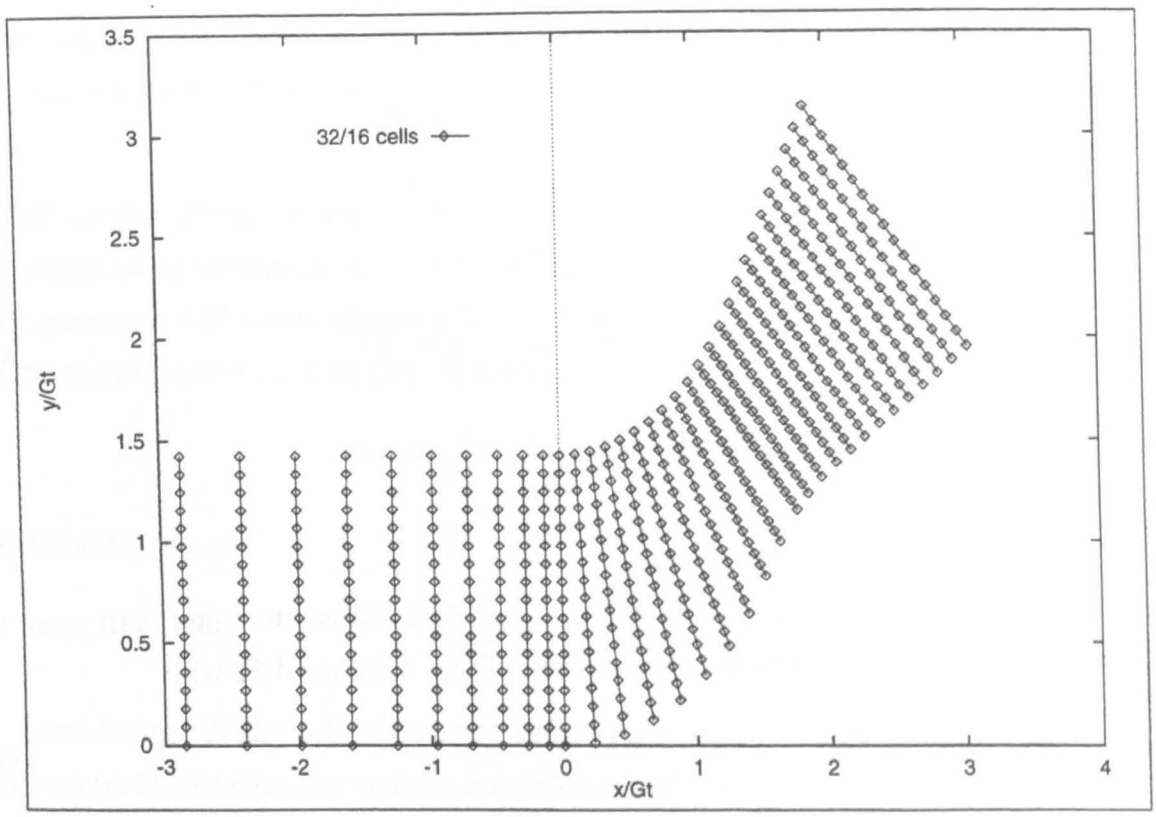

Figure 4.3: *Typical Mesh*

rescaling an analytical solution for a conventional nozzle. To ensure flow similarity, the wall radii of the conventional throat $R_w^=$ is 3 R_t. This is because the throat region of a planar ED nozzle is split into two equal halves, each with a centreline of (approximate) symmetry. Locally, therefore, each half of the flow will pass through the equivalent of a conventional

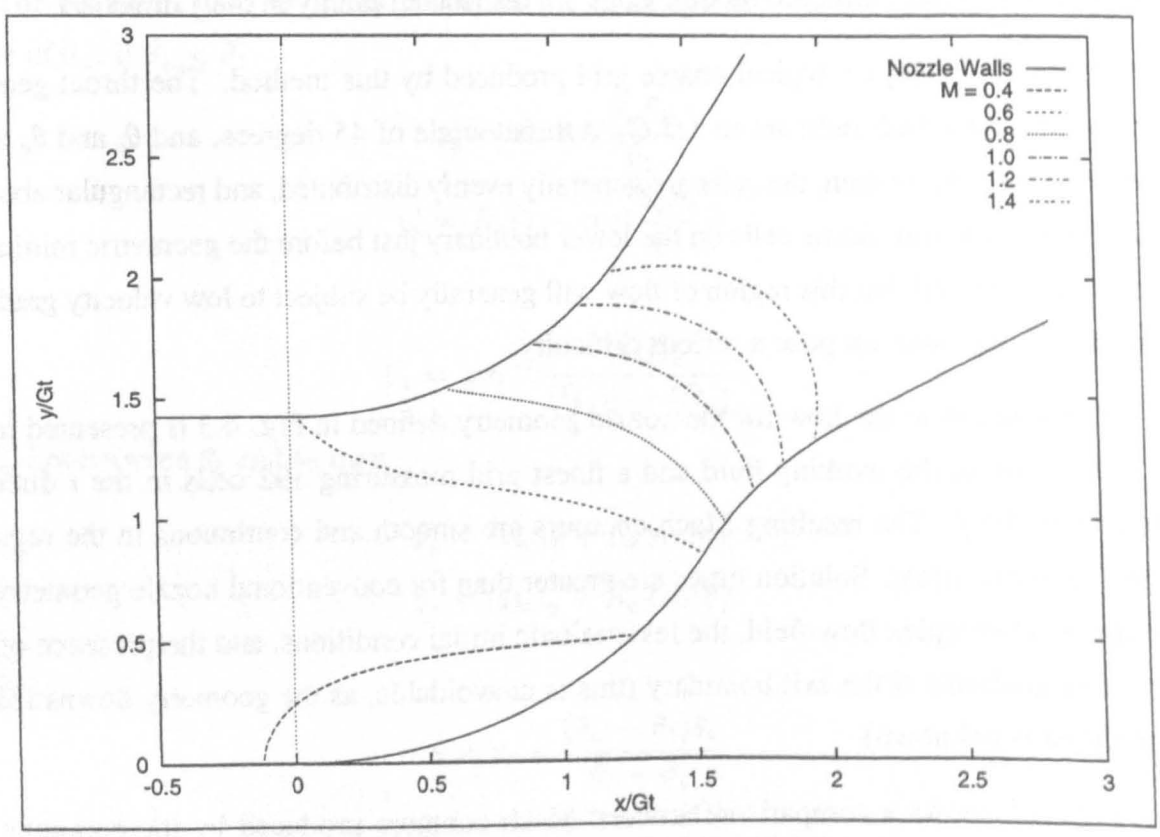

Figure 4.4: *Mach Contours, Planar ED Throat*

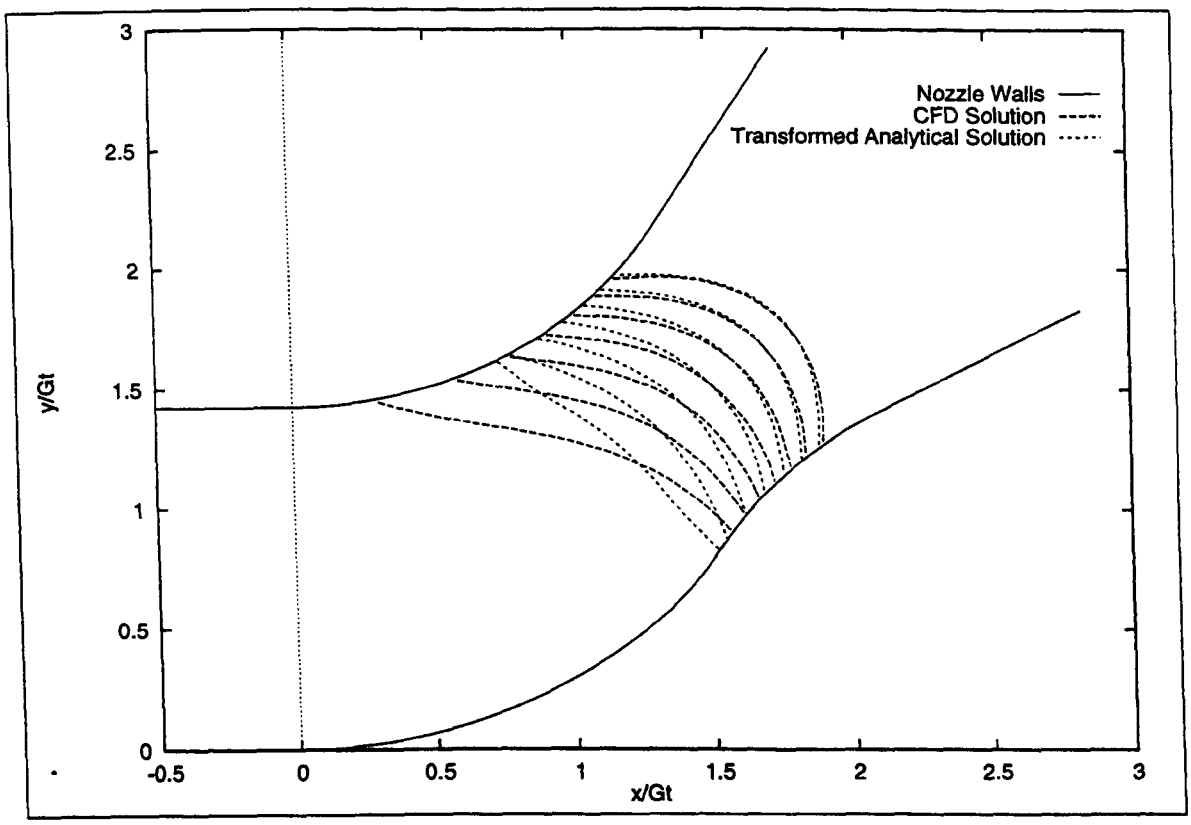

Figure 4.5: *Comparison of Mach Contours*

throat with an R_t of 0.5 G_t. Therefore, whilst the radii of curvature is still defined in terms of G_t (as this will result in equal mass flows), the flow-field will behave as if the radius were twice this value. As was demonstrated in the previous chapter, the larger the wall radius, the smoother the flow and the greater the final thrust of the nozzle. This effect therefore provides a slight inherent advantage for the ED nozzle with respect to conventional types, as smaller wall radii of curvature may be used without risk of associated performance losses.

Returning to the results presented in Fig. 4.5, the contours shown range from M = 0.7 to 1.3, with 0.1 separation. Generally, the supersonic Mach contours (from which the input characteristics for the nozzle optimisation routines are extracted) predicted by the two methods are similar. This demonstrates the expected result that no significant distorting effect due to radial distance is present in planar throat flows. There is a slight tendency for the analytical method to over predict the wall Mach numbers, as was found to be the case for conventional nozzle throats with small $R_w^=$.

The grid generation technique described here does not allow for nozzle geometries with discontinuous wall radii of curvature at the geometric throat, for either the outer contour or the pintle. However, as was the case for conventional nozzle throats, the characteristics extracted from the computational method will be entirely supersonic and originate at the respective intersections of the contour and pintle walls with the geometric minimum. This means that the post throat radii have no effect on these contours, and hence the same computational results may be used for a range of arbitrary post throat configurations. This reduces

the number of time consuming computational solutions required.

4.1.2 Axisymmetric Throats

The equations governing the flow within axisymmetric throat geometries contain a radial component, and hence the flow variables at any location in the throat region will be affected by its radial position. This means that if a specific radial position is required for the throat, the mesh must be displaced before the CFD solution initiates, rather than merely translating the results produced at the end of the process as is possible for two-dimensional geometries. This is achieved by generating a mesh using the method outlined for the two-dimensional flow regime, and then translating this mesh using a radial step y_d.

The magnitude and location of the minimum cross sectional area of the nozzle, A_t, will be effected by both the throat geometry, and the magnitude of the selected radial step. The value of A_t is required to allow calculation of the thrust coefficient from the wall pressures and momentum flux integrals. The throat area of a conventional nozzle is defined as the minimum cross sectional area of the flow perpendicular to the nominal (axial) flow direction. Following this convention, A_t for an ED nozzle is defined as the minimum surface area generated by rotating each constant i mesh line about the centreline of the nozzle. Therefore

$$A_t = min_1^{ni}(2\pi\zeta_i\Delta\zeta_i) \tag{4.26}$$

where

$$\Delta\zeta_i = \sqrt{(x_{i,1} - x_{i,nj})^2 + y_{i,1} - y_{i,nj})^2} \tag{4.27}$$

and

$$\zeta_i = \frac{y_{i,1} + y_{i,nj}}{2} \tag{4.28}$$

This is a slight simplification, as the cell vertices are not precisely perpendicular to the one dimensional flow direction. However, this deviation is minimal, and is reduced near to the geometric minima and with increased mesh density. It should be noted that the location of this minimal cross sectional area is not necessarily coincident with the location of the minimum wall separation, as is the case for conventional axial throat geometries.

Unlike two-dimensional flows, the radial displacement of the throat influences the shape and location of the Mach contours produced. Figs. 4.6 and 4.7 show results for two different displacements of the same initial mesh used for the two-dimensional results presented earlier, again with air as the working fluid. The first is displaced by 0.5 G_t, the second by 4.0 G_t. The flow variables are then solved using the axisymmetric version of the CFD code, and Mach contours displayed.

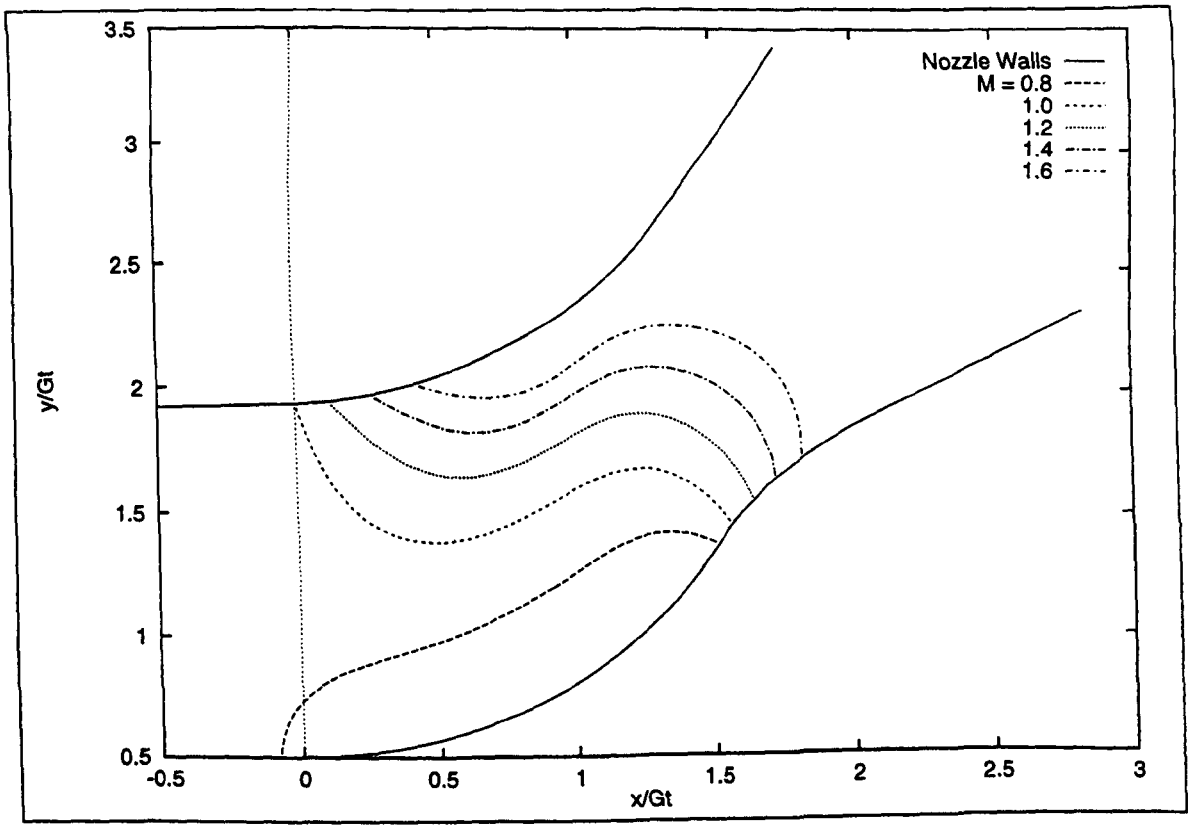

Figure 4.6: *Mach Contours,* $y_d = 0.5G_t$

The effect of this on the radial displacement may be clearly seen. With only a minimal y_d, the Mach contours are highly distorted from the usual parabolic shape. This occurs primarily because the minimum cross section of this geometry is considerably upstream of the minimum wall gap. As the flow will turn supersonic at approximately this minimum

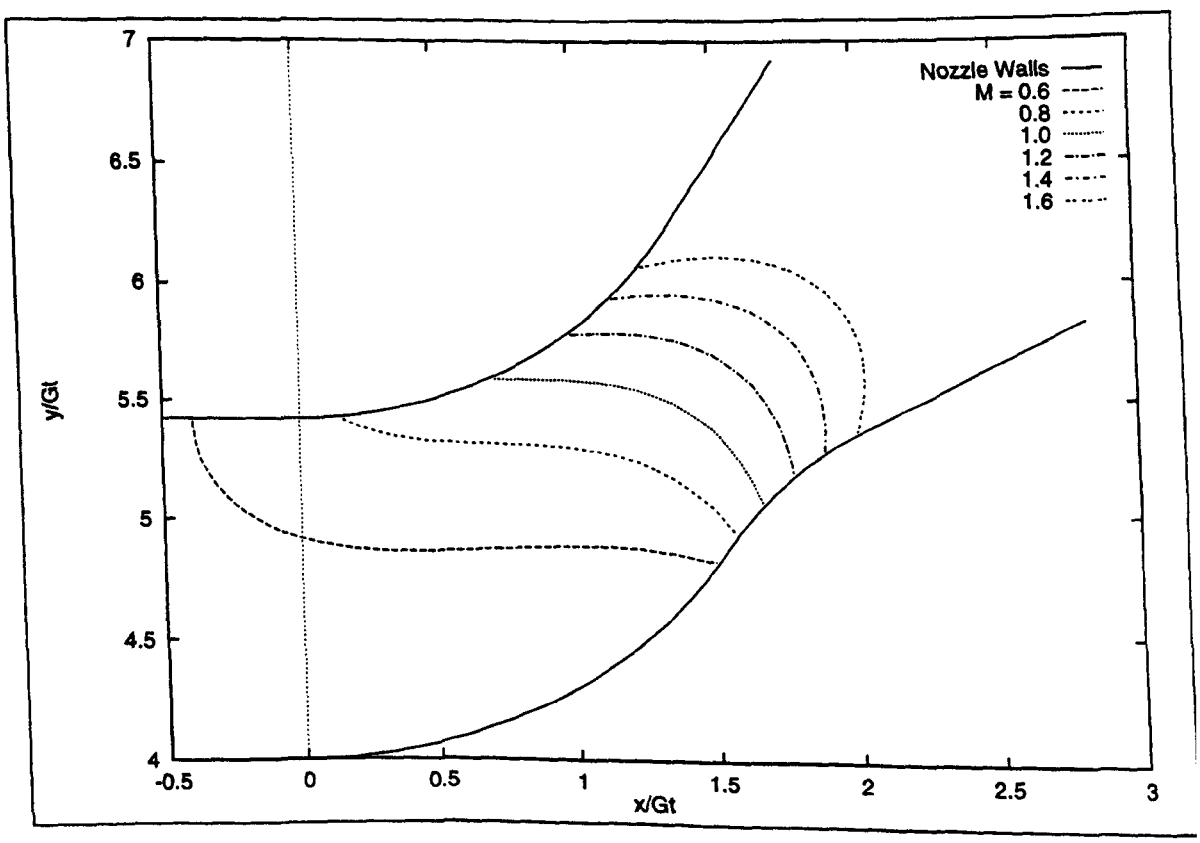

Figure 4.7: *Mach Contours,* $y_d = 4.0G_t$

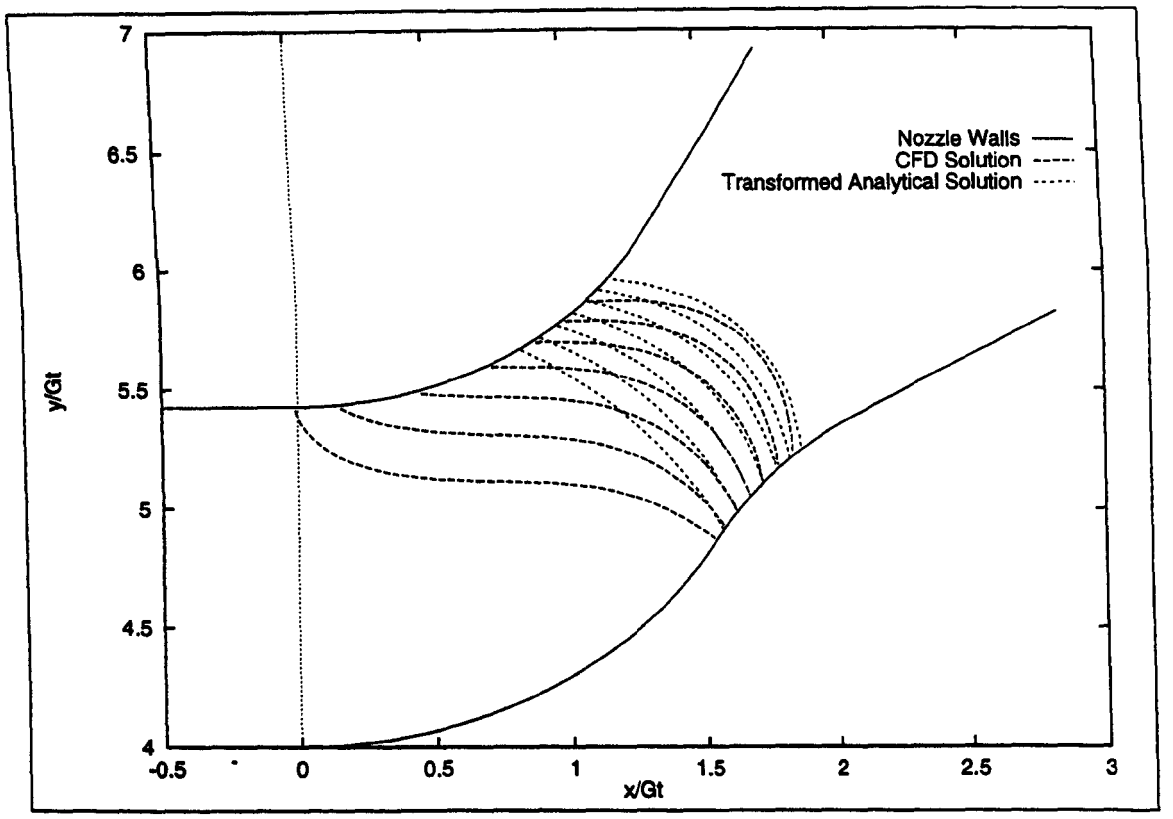

Figure 4.8: *Mach Contours, yd = 1.5*

area, the velocities at the location of G_t are considerably supersonic. A larger displacement of the initial mesh (Fig. 4.7) causes the location of the minimum area to shift downstream, reducing the velocities at the geometric minima, and creating Mach contours which resemble the usual parabolic form.

The magnitudes of the minimum areas are approximately 11 and 34 G_t^2 respectively. This means that the second nozzle will have over three times the mass flow, despite being formed by essentially the same pair of nozzle walls. It should also be remembered that if $G_t = R_t$, all conventional axial axisymmetric throats will have A_t equal to πG_t^2, and hence it is clear that an axisymmetric ED nozzle will actually have a far greater mass flow than a conventional nozzle should this be the case. This factor must be allowed for when making comparisons between bell and ED nozzles, and the method by which this is achieved is discussed in detail in Ch. 5.

Finally, Fig. 4.8 presents a comparison of the computationally derived solution with an approximation based on rotated and transformed Mach contours generated by the analytical method for an equivalent axial throat. The ED nozzle throat in question is the same as that shown in Fig. 4.7, and the analytical solution has been obtained by the same method described for planar throat flows, and again ranging from 0.7 t0 1.3 in intervals of 0.1. As can be seen, the Mach contours have little resemblance in shape or location. In contrast to the two-dimensional case (Fig. 4.5), it is apparent that such a technique is inadequate for the analysis of inclined and displaced axisymmetric throat configurations.

4.2 Contour Generation

In an ED nozzle operating under vacuum conditions, the forces acting on the outer nozzle wall are assumed to dominate the forces acting on the pintle. It is also likely that the force generated on the pintle will be relatively independent of nozzle length, and that at the design point the primary inviscid flow will extend from the throat to the exit of the nozzle without any interference effects from the viscous mixing region. This in effect restricts the length optimising process to defining the contour which produces the maximum thrust from the inviscid flow within the nozzle for a given length, and hence the viscous flow region and associated pressures on the pintle are ignored in the design of ED nozzles. Whilst this approach allows length optimised nozzles to be designed, it will be to some extent an approximation, dependent upon the accuracy of the preceding assumptions. These assumptions are evaluated in the light of results provided in Ch. 5.

Once the CFD model has achieved convergence, the results may be used as input for the MoC to produce a solution for the remainder of the inviscid flow within the ED nozzle, in a similar manner as outlined previously for conventional nozzles. This allows contours optimised for length to be created using the same calculus of variations technique previously described for the design of bell nozzles, with minor adaptations.

A graphical representation of the optimisation process is shown in Fig. 4.9. The LRC CDE is equivalent to that shown in Fig. 3.4, and is the last LRC in the nozzle flow-field. The same derivation process may be applied to show that not only must the characteristics equations be obeyed between D and E, but that the set of governing equations used to form optimised contours (Eqns. 3.25 to 3.29) must also hold if a maximisation of thrust for a specified length is desired. There are, however, some differences in the way that the equations are applied. This is because there is now an extra degree of freedom, as the flow may be expanded around the post throat curve of not only the outer nozzle wall, but also that of the inner pintle.

4.2.1 Two-Dimensional Nozzles

Considering first the simpler case of two-dimensional flow, it is again possible to show that the only difference between planar and axisymmetric flow optimisation equations is the removal of terms involving y, the radial distance, and hence the flow is governed by Eqns. 3.41 to 3.44.

This means that once an exit Mach number and overall design pressure ratio have been selected, the exit flow angle may be calculated directly. The nozzle generation algorithm then extracts from the computational results the two characteristics originating at either side of

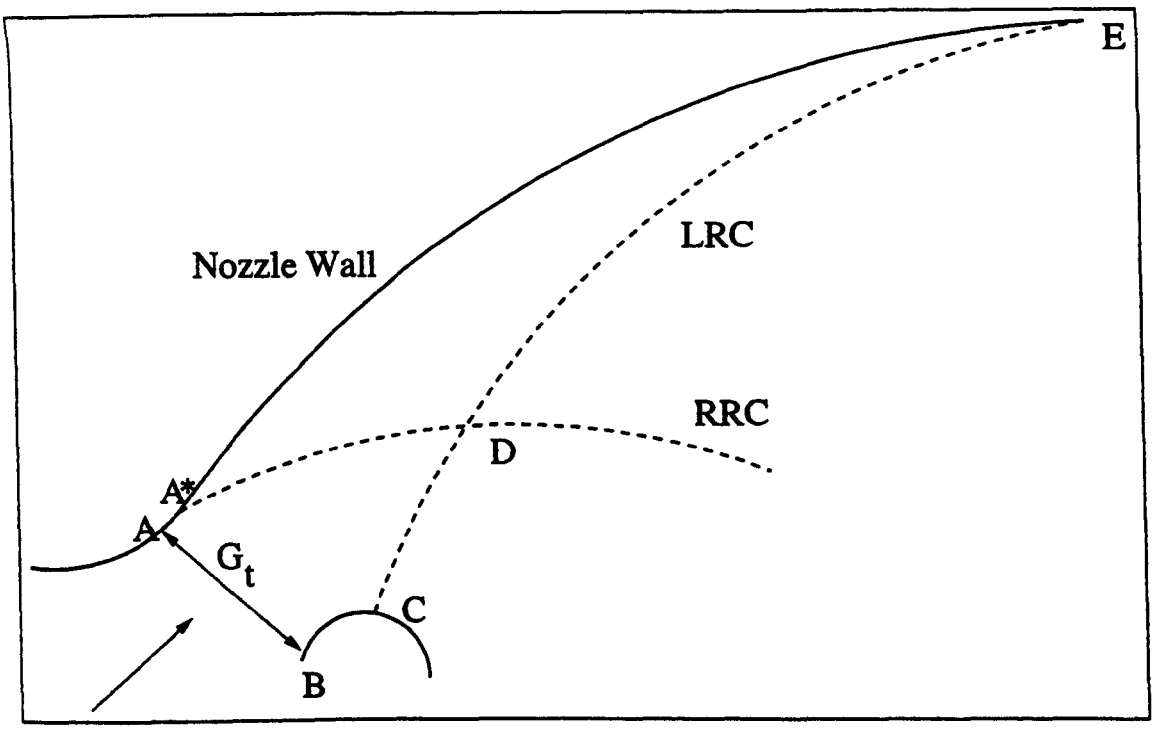

Figure 4.9: *ED Nozzle, General Configuration*

the geometric throat minima (points A and B on Fig. 4.9). That from A is an RRC, and from B an LRC. The mass flow crossing the RRC into the outer region is calculated and stored. This RRC is then extended downstream by calculating the points formed by the intersection LRC's generated by expanding the flow around the post throat curve on the pintle.

This process is continued until either the Mach number on the RRC exceeds the exit value, in which case the point where $M = M_E$ and its associated flow angle are found, or the RRC intersects the pintle wall. The next RRC is then generated by expanding the flow around the outer wall post throat curve. This expansion ends when the flow angle associated with the point $M = M_E$ is greater than the earlier computed exit angle. The location of point D (where M and θ will be equal to the exit values) may then be determined by interpolation. Once this has been achieved, the characteristics mesh in the outer region is calculated in the same manner as for planar optimised bell nozzles, as the characteristics in this region will be straight lines. The contour is found by computing the streamline from A* to E.

If the exit Mach number required is reduced sufficiently, the initial RRC originating from the geometric minimum and outer contour intersection may contain a point where $M = M_E$, but with an associated flow angle greater than the exit angle. If this is the case, it is not possible to create an optimised ED nozzle that will obey the governing flow equations. This defines a minimum nozzle size (as reducing M_E reduces nozzle length) for a particular throat geometry. The significance of this restriction is examined in more detail in Ch. 5.

In the discussion at the end of the previous chapter, it was noted that for conventional nozzles of all types, reducing the post throat radius improved the thrust to length ratio. It

was inferred from this that optimum performance would be achieved using a zero throat radius, i.e. a sharp corner. This was deemed impractical, as it would result in flow separation from the nozzle shroud, undesirable in conventional nozzle operation. In the case of the ED nozzle however, whilst separation from the outer shroud remains undesirable, separation of the flow from the pintle is not only inevitable, but a requirement for altitude compensating behaviour. Therefore, a sharp corner on the pintle (i.e. $R_p^{=} = 0$) at the geometric throat represents a possible nozzle design case, and such nozzles require analysis.

If $R_p^{=} = 0$, the nozzle may be designed using the same methods as described above, with a minor alteration to the routine used for finding the initial point on the LRC's emanating from the pintle. Rather than reflecting a point on a previous characteristic off the post throat pintle arc, a Prandtle-Meyer expansion fan, centred on the point of separation, is assumed. This results in the location of the initial point of a new LRC being coincident with that of the previous. A user defined arbitrary expansion step, $\delta\nu$, is applied to the flow variables such that

$$\nu_{i,1} = \nu_{i-1,1} + \delta\nu; \quad \theta_{i,1} = \theta_{i-1,1} - \delta\nu \tag{4.29}$$

and M, μ, P follow from ν in the usual manner. From this point, an LRC within the expansion fan can be generated using the previous LRC and the characteristic equations in the usual manner. As with ED nozzles of non zero radii of curvature, this LRC is continued until it intersects the initial RRC in the post throat flow, and the expansion fan is extended until the Mach number on the RRC exceeds the exit value.

4.2.2 Axisymmetric Nozzles

The optimisation process for axisymmetric flows is very similar. Again, the fundamental physical aspects of the flow-field are unchanged with respect to conventional nozzles, and hence the control volume analysis presented in Sec. 3.3.2 may be applied to produce the same calculus of variations optimisation problem described in Eqns. 3.23 and 3.24. Note that Eqn. 3.22 still holds, as although the point C moves in two-dimensional space, for a given nozzle geometry it is constrained to lie on the post throat pintle arc, and is thus reduced to a one dimensional variable. This means that the same equations hold as for the simpler, conventional bell nozzle, and hence the same optimisation process may be used, as described in the previous chapter.

It should be noted that as was the case for two-dimensional ED nozzles, there are restrictions on the allowable range of exit Mach numbers which will produce an optimised contour meeting both mass conservation and the optimisation equations. As the wall angle at the exit plane of the nozzle, θ_E, is independent of the throat angle, a small M_E combined with

a large θ_t will require a rapid change in flow angle along the wall without a corresponding rapid increase in M. This may not be possible, and hence there is a minimum permissible M_E for a given throat angle. Large M_E produces a corresponding large nozzle, but there is a limit to the maximum amount of mass flow that may enter the outer region across RRC A*D, and if the demanded M_E is too high, no solution to the optimisation equations exists that satisfies continuity, setting a maximum on M_E. Again, the impact of these limitations is discussed in greater detail in Ch. 5.

4.3 Closed Wake Thrust Prediction

When operating in a vacuum, the ED nozzle flow-field will assume general characteristics as shown in Fig. 4.10. Whilst the majority of the flow is supersonic, at a certain point on the pintle the flow separates (E), and a viscous recirculating region forms behind the pintle. A distance downstream this region contracts to the centreline (G), and a shock wave is formed as the supersonic flow is turned parallel. As the viscous region is entirely enclosed within supersonic flow, it is unaffected by ambient pressure variations, and the nozzle may be described as operating in 'closed wake' mode.

The calculation of vacuum thrust coefficients for ED nozzles is similar to that employed in the previous chapter for conventional nozzles. For both types, the thrust is equal to the sum of the axial momentum flux and pressure forces acting at the exit plane of the nozzle. However, the rather than calculate the flow properties at this plane (which would require the entire flow-field within the nozzle to be calculated, shock waves and viscous regions included), consideration of a control volume provides a simpler approach.

In Fig. 4.10 line AH represents the exit plane of the nozzle. The force acting on this exit plane will be equal and opposite to the sum of the forces on all the other surfaces bounded by AH, irrespective of whether the viscous region extends sufficiently downstream that the recompression point (G) is downstream of the exit plane, or is as shown.

The force acting along the shroud contour between points A and B may be calculated by integration of the wall pressures generated by the flow via Eqn. 3.49. The thrust acting across the input characteristics (between points B and C) is equal to the combination of pressure and axial momentum forces, and is calculated from Eqn. 3.46. Between points C and E, wall pressure forces may also be calculated from Eqn. 3.49, noting however that as the pintle faces in the opposite direction to the shroud, the sign of Y must likewise be reversed.

As along the centerline between F and H there are no surface forces, the calculation of the thrust of the nozzle may be completed if the force acting on the base of the pintle is known. Prediction of this base pressure may be attempted by considering the similar problem of

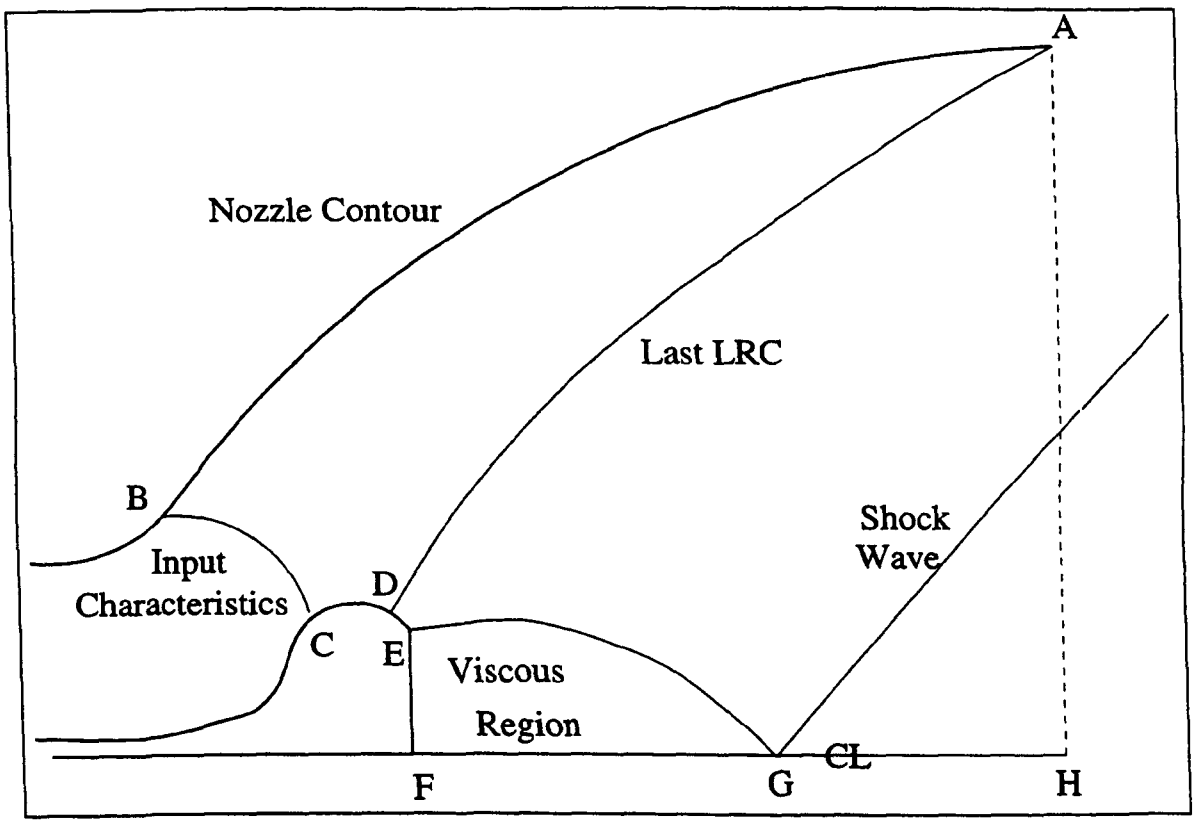

Figure 4.10: *ED Nozzle, Vacuum Operation*

wedges and rearward facing steps immersed in supersonic flow-fields.

4.3.1 Rear Facing Steps, an Overview

From the fifties onwards, the growing number of blunt based supersonic aerodynamic vehicles (e.g. re-entry vehicles, missiles after burn out, supersonic aerofoils with blunt trailing edges) encouraged the development of a number of techniques for the prediction of the pressures acting on the rear faces of such objects, this being necessary for an accurate prediction of overall drag. The majority of these methods are based on a constant pressure mixing technique derived independently by Korst [30] and Chapman [50].

4.3.2 Method of Korst

The flow past a rearward facing step is shown schematically in Fig. 4.11. Uniform onflow (M_1, P_1) expands through a Prandtle-Meyer expansion fan at point A, the corner of the step. There then follows a wake region containing a turbulent mixing layer, originating at the point of separation (A), and terminating at the point of reattachement (R). Within this layer, there is a dividing stream line (D) which marks the boundary between flow that is forced to recirculate within the wake, and flow that escapes downstream.

If the thickness of the dissipative region remains small compared to any significant length

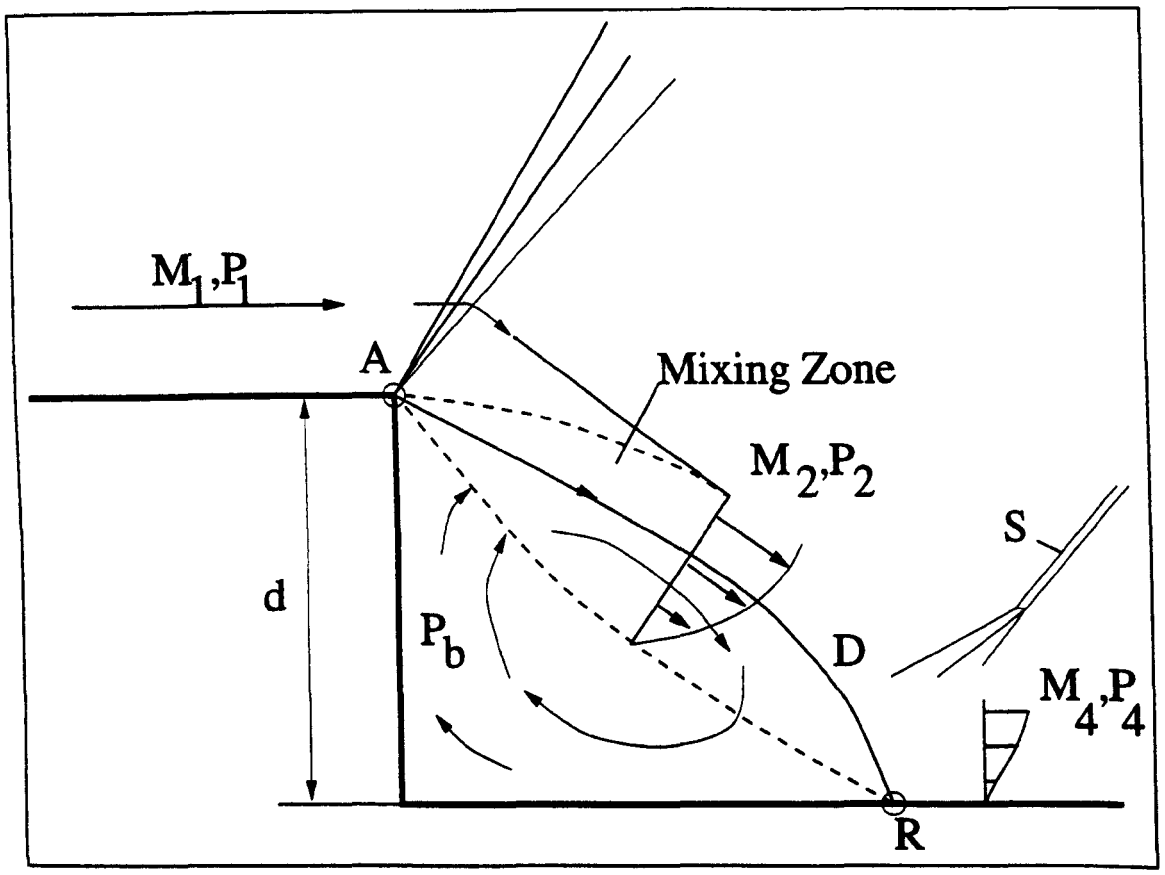

Figure 4.11: *Two-Dimensional Supersonic Flow past a rearward Facing Step*

in the wake (e.g. the step height (d), or the radius of curvature related to the jet boundary), the processes within the mixing layer may be considered to occur at constant pressure, and hence the pressure acting on the supersonic boundary, P_2, is constant from A to R. It is further assumed that the total pressure is constant along the dividing streamline, D. This has been confirmed experimentally to be generally the case [51], and results in

$$\frac{P_b}{P_1} = \left[\frac{1+\frac{\gamma-1}{2}M_4^2}{1+\frac{\gamma-1}{2}\frac{M_4^2}{1-\phi_D^2}}\right]^{\frac{\gamma}{\gamma-1}} \tag{4.30}$$

where ϕ is the non dimensional velocity profile through the shear layer, and hence

$$\phi_D = \frac{U_D}{U_2} \tag{4.31}$$

This equation was first derived by Chapman [50], but is equally applicable to Korst's method. Note that due to the above assumptions velocity similarity is ensured, and hence ϕ is independent of stream-wise position within the mixing layer.

Obviously the primary difficulty is the evaluation of ϕ_D. Korst solves this problem for an asymptotic jet mixing problem ('restricted theory'), which assumes that the boundary layer approaching the rearward step is thin compared to the wake length. This represents the lowest limiting values of base pressure as Reynolds number increases for a given Mach number and step configuration. To further reduce the complexity of the resulting equations, only two-dimensional isoenergetic wakes were considered.

Given these assumptions, by translating the equations of motion into an orthogonal generally curvilinear coordinate system which follow the hypothetical equivalent inviscid flow boundary, it is possible to derive

$$\phi = \frac{1}{2}(1 + \text{erf}\,\eta) \tag{4.32}$$

where the error function follows the standard formula

$$\text{erf}\,\eta = \frac{2}{\sqrt{\pi}} \int_0^{\eta} e^{-\eta^2} d\eta \tag{4.33}$$

and η is a non dimensional distance through the shear layer, perpendicular to the flow direction. If no fluid can enter or leave the recirculating region (i.e. an approaching boundary layer of zero thickness, and no bleed through the rearward facing wall) then it may be shown that

$$\int_{\eta_D}^{\eta} \frac{\phi d\eta}{1 - C_2^2\phi^2} = \int_{\eta R}^{-\infty} \frac{\pi^2 d\eta}{1 - C_2^2\phi^2} \tag{4.34}$$

where η_R is a reference value large enough to ensure that ϕ_D calculated is asymptotic, and C is the Crocco number, a non dimensionalised velocity given by

$$C = \left[1 + \frac{2}{(\gamma - 1)M^2}\right]^{-1/2} \tag{4.35}$$

Although such a flow condition is not physically possible, it represents the asymptotic limit for flows where the oncoming boundary layer is very thin compared to the step height. Korst also provides equations for so called 'open wakes' (wakes where mass flow may enter and leave the wake region. This is not the same as the open wake flow regime of the ED nozzle, discussed in the following chapter, where there is no reattachement of the supersonic flow). Solution for such flows requires an additional empirical quantity, σ, which is a similarity parameter (often referred to as the jet spread parameter). A semi-empirical formulae for this quantity has been produced, and is given by

$$\sigma = \left[R'(1 + \beta(1 - C^2))\right]^{-1} \sigma_{inc} \tag{4.36}$$

where σ_{inc} is the incompressible jet spread parameter, found empirically to be 12, β is the ratio of the total temperature in the jet to that in the still air region (unity for isoenergetic mixing), and R' is an empirical compressible divergence function based solely on Crocco number, presented (graphically) by Channapragada in Ref. 52.

A comparison of this theory with experimental results is provided in Ref. 30, and appear to have a strong correlation. However, the number of experimental data points is small, and later experimental results show some disagreement, especially for low onflow Mach numbers (primarily in the range M = 1 to M =1 .5) [31].

A weakness in the theory which would explain the discrepancies found between experimental and theoretical results is the assumption contained within that the static pressure P_4 behind the shock is equal to the pressure at reattachement point (P_r). Experimental evidence has shown that this is not the case, and hence several authors have attempted to improve the accuracy of the method by including a recompression factor

$$N = \frac{P_r - P_b}{P_1 - P_b} \tag{4.37}$$

where N is determined empirically (e.g. Nash) or from a simplified analysis of the recovery region (e.g. Fox [51]). Other authors have examined this problem, including McDonald and Roberts, and their work is summarised in Ref. 53.

4.3.3 Application to ED Nozzles and Similar Flows

The Method of Mueller

Whilst the above identified weakness inherent with the technique has been recognised for a considerable period of time, the method still provides an attractive way of modelling the flow in the wake region behind a rearward facing vertical face in a supersonic flow. This semi-empirical method represents the main alternative to computing the flow via numerical simulation through the Navier-Stokes Equations. The latter is still a difficult and extremely lengthy process using modern computers, and was totally impractical 20 to 30 years ago, when the majority of work on the ED concept occurred. In fact it is only relatively recently that such solutions have been attempted for even simple back step flow-fields (e.g. Refs. 54 and 55).

In their work on the axisymmetric base pressure problem in the late 60's and early 70's Mueller *et al* devised a solution procedure based on a combination of the MoC for inviscid flow modelling, and a variation on the Korst flow model for the wake region [25]. This method had obvious applications for flow-field analysis of both ED and Plug nozzle types [29], [25]. The basic method requires supersonic input conditions at the throat of the nozzle, from which the rotational MoC is used to calculate the inviscid flow-field downstream. These input conditions were determined experimentally after model results had shown high sensitivity to them (initially an assumption of either a linear or simple parabolic initial sonic line had been used). The boundary with the mixing region is assumed to lie along a cone tail, which allows the generation of a pressure profile, removing the assumption of constant P_2. This is necessary to allow analysis of nozzle flows where Mach waves reflected from the nozzle contour will impinge on the wake region, and also appears to better represent the actual flow-field present in flow visualisation results.

The boundary layer leading up to the separation point is ignored, and the pressure normal to the 'corresponding inviscid jet boundary', produced by the MoC, is assumed constant through and near the mixing layer. Velocity profile similarity is assumed within the mixing region, and the same coordinate transformation and error function as used by Korst is included. Recompression is assumed to result through an oblique shock at an empirically determined trailing wake radius ratio, R_w/R_b. Here, R_w is the radial location of the initial point of the shock wave S in Fig. 4.11, and R_b the radius of the pintle at the separation corner.

The resulting analysis generated a series of equations, which although complex and requiring several integral evaluations similar to Eqn. 4.34, are dependent solely on the calculated pressure distribution along the inviscid jet boundary. This is achieved through Crocco number relations, and two empirical parameters; σ as defined in Eqn. 4.36, and R_w/R_b, mentioned above. Use of a recompression coefficient, N, discussed in the previous section was considered, but due to contradictory experimental evidence available at the time with regards to the necessity of incorporating it, was ignored in the interests of removing an empirical quantity.

The basic model was extended to allow non-isoenergetic mixing, base bleed and an initial boundary layer profile. Whilst these factors obviously increased the complexity of the model, particularly with respect to velocity profile integrations, the overall method remains the same, and may be summarised as follows:

1. An initial estimate of the base pressure ratio ($\frac{P_b}{P_c}$) is made. This is assumed equal to the static pressure in the inviscid free stream after passing through the expansion fan centred on the point of separation (i.e. there is no variation of base pressure in the radial direction. This has been demonstrated experimentally in Ref. 56 and elsewhere).

2. A value of wake radius ratio is then selected corresponding to the base pressure chosen, and this allows the MoC to be used to calculate the entire external inviscid flow-field.

3. This provides enough parameters to calculate the location of the dividing streamline D, and this in turn can be used to calculate a base pressure.

4. If this is the same as that initially estimated, the solution is found, if not, the loop repeats.

This procedure is highly iterative, and requires a complete recalculation of the inviscid flow-field with each iteration.

The technique described above does indeed provide a method by which the base pressure, and thus the thrust, of an ED nozzle operating in vacuum conditions may be predicted.

However, there are a number of problems inherent within the scheme. As has already been discussed, a series of empirical inputs are required, and there is insufficient experimental data to allow an assessment of the universal nature of the assumptions involved. Further, there is the previously discussed flaw in the underlying flow model with respect to recompression, acknowledged by Mueller. Finally, that the free jet boundary follows a cone tail is an assumption. Whilst some schlieren pictures are presented in the various references, the evidence is not conclusive, and it should be noted that a comparison between the theory and experimental results presented in Ref. 25 clearly shows a greater agreement with results produced assuming a constant pressure boundary, as originally postulated by Korst. In general, comparison of experimental to theoretical results is sparse, and restricted to small throat angles and relatively low overall pressure ratios.

Sudden Expansion from a Conical Convergent Nozzle

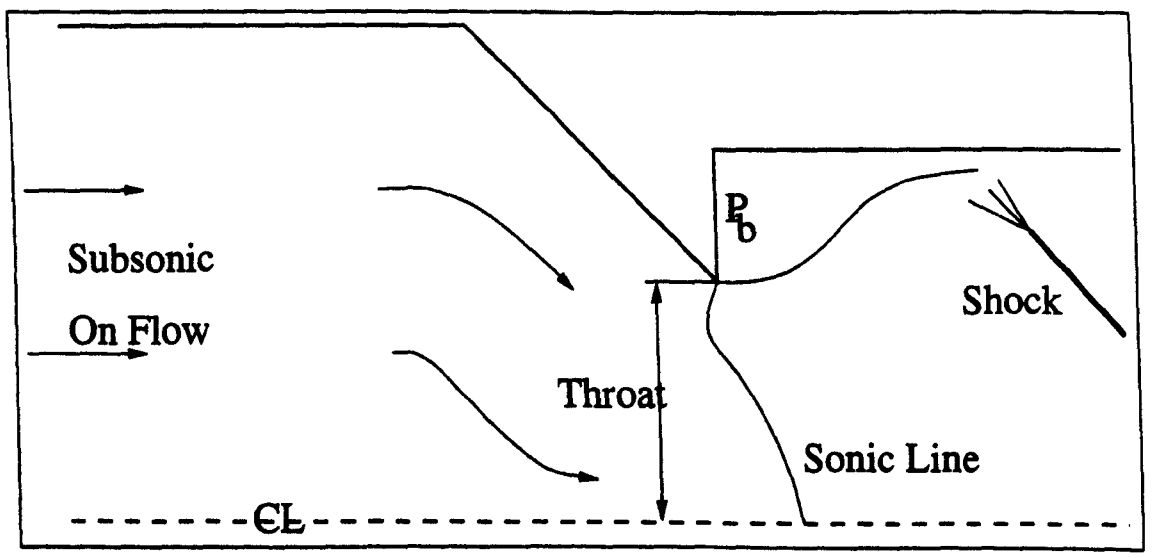

Figure 4.12: *Flow Past a Convergent Conical Nozzle with Sudden Enlargement*

More recently, an attempt has been made to analyse the back pressure on a sudden expansion from a conical converging nozzle using a similar flow model [57]. The flow-field, shown graphically in Fig. 4.12, contains a subsonic onflow boundary, a sonic line distorted by radial effects (although located on the axis of revolution), and a recirculating region (requiring calculation of the base pressure) which terminates in a shear flow, coupled with a recompression shock wave.

The solution method is similar in many respects to that employed by Mueller, and followed an evolution from previous work on axisymmetric bodies by one of the authors [58] which is similar to the method of Ref. 25. The main differences include the use of the unsteady MoC to calculate the inviscid flow-field, which allow both the subsonic and supersonic regions to be solved at the same time, and thus incorporate the effect of the base flow on the sonic line automatically (although this increases solution times, as convergence to a

stable steady state is required), and the use of a momentum balance across a control volume to ensure a physically possible solution. It should be noted however, that all the basic assumptions of the Korst base pressure method are retained, including σ, the empirical jet spread parameter. The solution procedure is highly iterative in nature. It is claimed that good results are obtained, however the experimental evidence presented in Ref. 58 is limited, and inconclusive.

4.3.4 The Method of Tanner

Due to the limitations of the previously described techniques, and particularly the difficulties related to predicting the recompression coefficient, Tanner evolved a method for the prediction of base pressures from an alternative perspective. It is a development of his previous work on base pressure prediction in subsonic flows, and has several advantages for application to ED nozzles. There is also a considerable body of experimental evidence showing good agreement with theory for a range of shapes and Mach numbers.

The basic model assumes constant pressure mixing, and therefore does not require calculation of entire flow-field, the base pressure being a unique solution obtainable from onflow conditions. Whilst it is likely that if desired a similar iterative interaction with the inviscid flow-field as used by Mueller to adapt Korsts model to non-constant pressure boundaries could be developed, due to the lack of experimental evidence that a cone tail is a better approximation than constant pressure mixing, this has not been attempted. A brief overview of the general theory is presented here, followed by a description of the adaption made to allow prediction of ED base pressures for planar and axisymmetric nozzles.

The Origin of Base Drag

The foundation of Tanner's method is the relationship between the base drag (and thus base pressure) of an object, and the increase in entropy of the fluid. Oswatitsch has shown that

$$\iint_{f_k} (\tilde{s} - \tilde{s}_\infty)\rho V_n df = D\frac{U_\infty}{T_\infty} \tag{4.38}$$

where the LHS of the equation is the entropy increase in a control volume containing the body, V_n the local velocity component normal to the element of the control surface f_k and D is the pressure drag of a body. This may be expressed as

$$\Delta S = D\frac{U_\infty}{T_\infty} \tag{4.39}$$

The solution procedure is derived from a comparison of two flow-fields, first that due to a hypothetical inviscid flow, followed by the actual viscous regime. These flows are shown

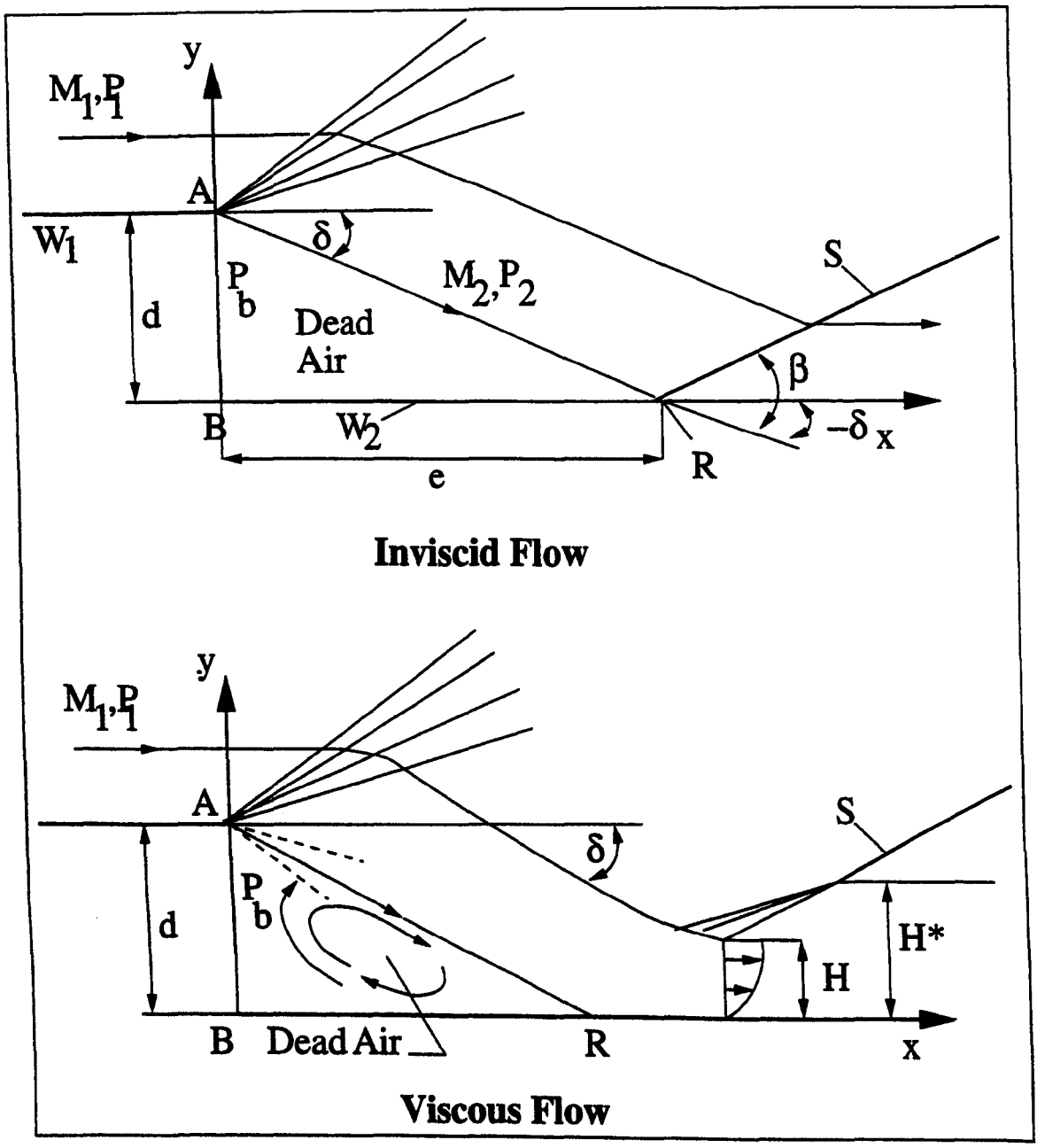

Figure 4.13: *Two Flow Models*

in Fig. 4.13. It is assumed that parallel flow exits upstream of the object under consideration, which will be satisfied in a generalised flow past an isolated body.

Next, it is assumed that the contribution to drag made by skin friction is negligible, i.e. the boundary layer approaching the rearward facing step is thin compared to the step height (this is the same assumption made in the restricted theory of Korst), and this reduces the total drag to merely the base drag in both flow cases. As this is the case, it may further be assumed that the drag in both cases is equal, and hence the entropy rise is also the same for both flow regimes, as a direct consequence of Eqn. 4.39.

In the inviscid flow, this increase in entropy is generated purely by the shock wave S. This wave extends for a finite distance due to interference from the expansion fan centred at A, and hence results in a finite drag. In the viscous case, the entropy is created by two

processes, the shock wave, and the mixing processes in the shear layer. The base drag is found by constructing a flow regime where the entropy generated within the shear layer is equal to that lost by the displacement of the shock wave from the solid surface, thus ensuring that the entropy increase in both flow regimes is equal. The equations providing the solution are developed fully in Ref. 53, and hence are only summarised here.

It may be shown that the rate of entropy increase in the shear layer at the shock wave is given by

$$\frac{\Delta S}{R} = K_1(M_1) H \frac{\gamma}{2} M_1^2 \rho_1 \underline{V_1} \tag{4.40}$$

where H is the height of the shear layer (see Fig. 4.13), a subscript of 1 represents onflow conditions, and

$$K_1(M_1) = 2 \int_0^H \frac{\rho}{\rho_1} \frac{\underline{V}}{\underline{V_1}} \left(1 - \frac{\underline{V}}{\underline{V_1}}\right) \frac{dy}{H} \tag{4.41}$$

The velocity distribution is calculated from

$$\frac{\underline{V}}{\underline{V_1}} = 0.16 + 0.42\left(1 + \sin\left(\frac{\pi y}{H} - \frac{\pi}{2}\right)\right) \tag{4.42}$$

Reasons for the selection of this approximation are discussed in some detail in Ref. 53, but it is essentially a semi empirical velocity distribution shown to match well with experimental observations of real shear layer flows. The density profile follows from

$$\frac{\rho_1}{\rho} = \frac{T}{T_1} = 1 + r \frac{\gamma - 1}{2} M_1^2 \left[1 - \left(\frac{\underline{V}}{\underline{V_1}}\right)^2\right] \tag{4.43}$$

where r is the recovery factor. This is a standard boundary layer approximation, sufficiently well known as to be included in textbooks (e.g. Ref. 59). In his work Tanner assumes a turbulent Prandtle number of 0.5, resulting in a thermal boundary layer of

$$\frac{\delta_T}{\delta} = \frac{1}{\sqrt{Pr_t}} = 1.41 \tag{4.44}$$

and provides experimental evidence to justify this. The recovery factor is set to 0.80, and this matches very closely the common approximation (again, see Ref. 59)

$$r = Pr_t^{\frac{1}{3}} \tag{4.45}$$

The rate of increase through an oblique shock wave is given by

$$\frac{\Delta S}{R} = ln\left[\frac{\left(1 + \frac{2\gamma}{\gamma+1}(M_2^2 \sin^2\beta - 1)\right)^{\frac{1}{\gamma-1}}}{\left(\frac{(\gamma+1)M_2^2 \sin^2\beta}{(\gamma-1)M_2^2 \sin^2\beta + 2}\right)^{\frac{\gamma}{\gamma-1}}}\right] H^* \rho_1 V_1 \tag{4.46}$$

If the entropy lost due to the displacement of the shock wave is to be replaced by that produced in the shear layer, then

$$K_1(M_1) \frac{\gamma}{2} M_1^2 = \frac{H^*}{H} B(M_2, \beta) \tag{4.47}$$

where $B(M_2, \beta)$ is the natural logarithm in the RHS of Eqn. 4.46. Solving this equation requires a value for H^*/H. This is determined entirely empirically, but is assumed to be constant regardless of flow details. Early work refers to a value of 6.498 [31], but later this was changed to 7.37 to match the theory to extended experimental results presented in Ref. 60. The assumption that this value was independent of on flow Mach number and object dimensions was justified by a considerable amount of experimental data. The LHS of Eqn. 4.47 is solely dependent of free stream conditions, and as through a shock wave

$$\tan\delta = 2\cot\beta\frac{M_2^2\sin^2\beta - 1}{M_2^2(\gamma + \cos 2\beta) + 2} \tag{4.48}$$

and δ may be determined directly from M_1 and M_2 (as it is equal to the expansion angle between these Mach numbers) the RHS depends only on the onflow conditions and a selected M_2. A solution may therefore be found by iterating M_2 until Eqn. 4.47 is satisfied. Once M_2 has been found, the base pressure coefficient c_{pb} will follow directly, as the static pressure at the point of separation is constant through the viscid/inviscid boundary (i.e. $P_b = P_2$), and hence

$$c_{pb} = \frac{2}{\gamma M_1^2}\left[\frac{P_b/P_0}{P_1/P_0} - 1\right] \tag{4.49}$$

Once the basic theory is developed, other factors such as the boundary layer profile at separation, boat tail and wedge angles may be considered.

Including Other factors

As mentioned above, the value of the constant H^*/H was selected to provide good agreement to a specific set of experimental results. The experimentally derived boundary layer momentum thickness at the point of separation for these results was found to be $\delta_2/d = 0.003$. By considering the entropy flux that the boundary layer momentum thickness will cause at the shock wave, a boundary layer of arbitrary thickness may be allowed for by replacing Eqn. 4.47 with

$$\frac{-c_{pb}}{-c_{pb} + 2\frac{\delta_2}{d} - 0.006}K_1(M_1)\frac{\gamma}{2}M_1^2 = \frac{H^*}{H}B(M_2, \beta) \tag{4.50}$$

(note that the RHS is unaffected as it merely describes the entropy increase due to an oblique shock wave).

The influence of the shape of the body is accounted for by considering its effect on the total drag of the object. If the object is boat tailed (see Fig. 4.14), the base pressure solution is found by comparing the inviscid-viscous flows over the actual boat tail to those over a rearward facing step of equal height. Considering first the inviscid flow-fields, if the onflow Mach number and the constant pressure boundary Mach number (M_2) are the same in both

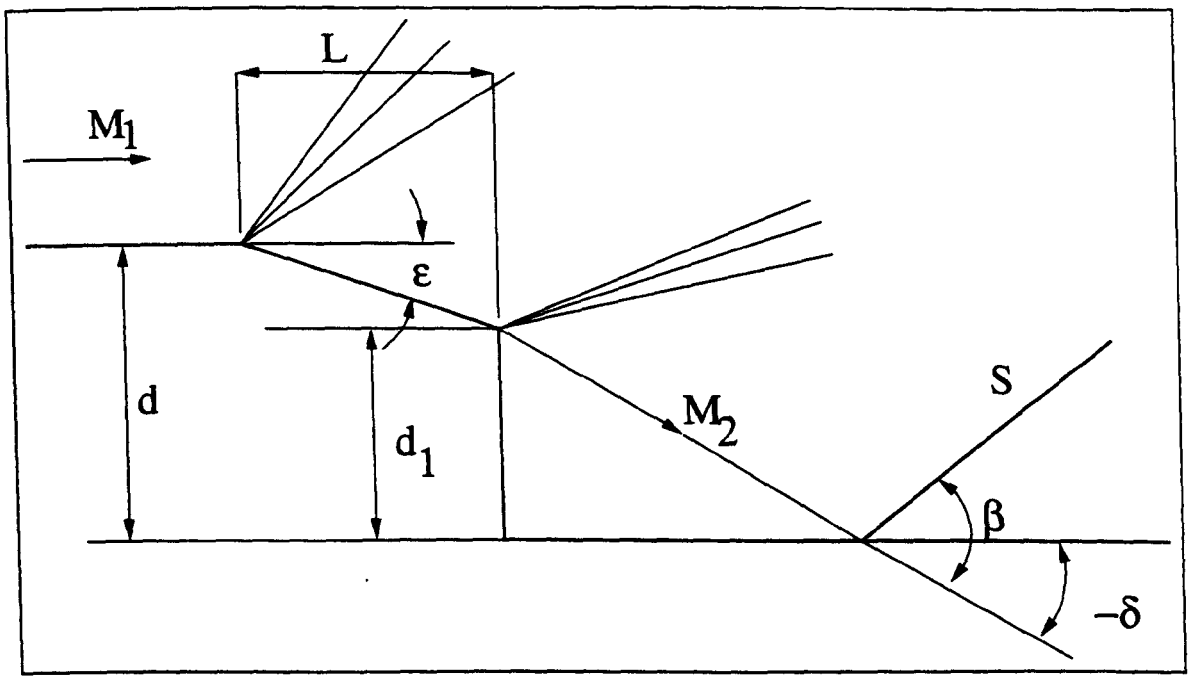

Figure 4.14: *Boat Tail Configuration*

cases, then the base pressure will be equal for both also. If this is the case, then in the region of interaction of the shear layer with the shock wave will generate the same increase in entropy per unit height. The total entropy increase, and hence drag, of the boat tailed object will actually be less, but this reduction in drag is due to earlier interference of the expansion waves originating from the edge of the boat tail, and hence the shock wave is reduced in strength nearer to the body. However, this effect does not occur until the first expansion waves reach the shock wave, a considerable radial distance from the centreline.

In terms of the viscous flows, the equality of drag between viscous and postulated inviscid flows requires that the loss in entropy due to the viscous shear layer (per unit height) is equal in either case, and the form of the RHS of Eqn. 4.47 remains. It should be remembered that the proposed flow over the backward step is hypothetical, and the constant pressure boundary Mach number (M_2) postulated will not in fact be equal to that which does occur in the real flow for such a geometry.

The entropy production due to the shear layer will differ between the boat tailed and simple step objects. If profile similarity is assumed,

$$H_B = \frac{d_1}{d} H \tag{4.51}$$

H_B being the height of the shear layer at the shock interaction, then the entropy flux may be expressed as

$$\Delta S = \frac{d_1}{d} K_1(M_1) \frac{\gamma}{2} M_1^2 R H \rho_1 u_1 \tag{4.52}$$

per unit step width. As the RHS of Eqn. 4.47 is again unaffected, the equation that must be

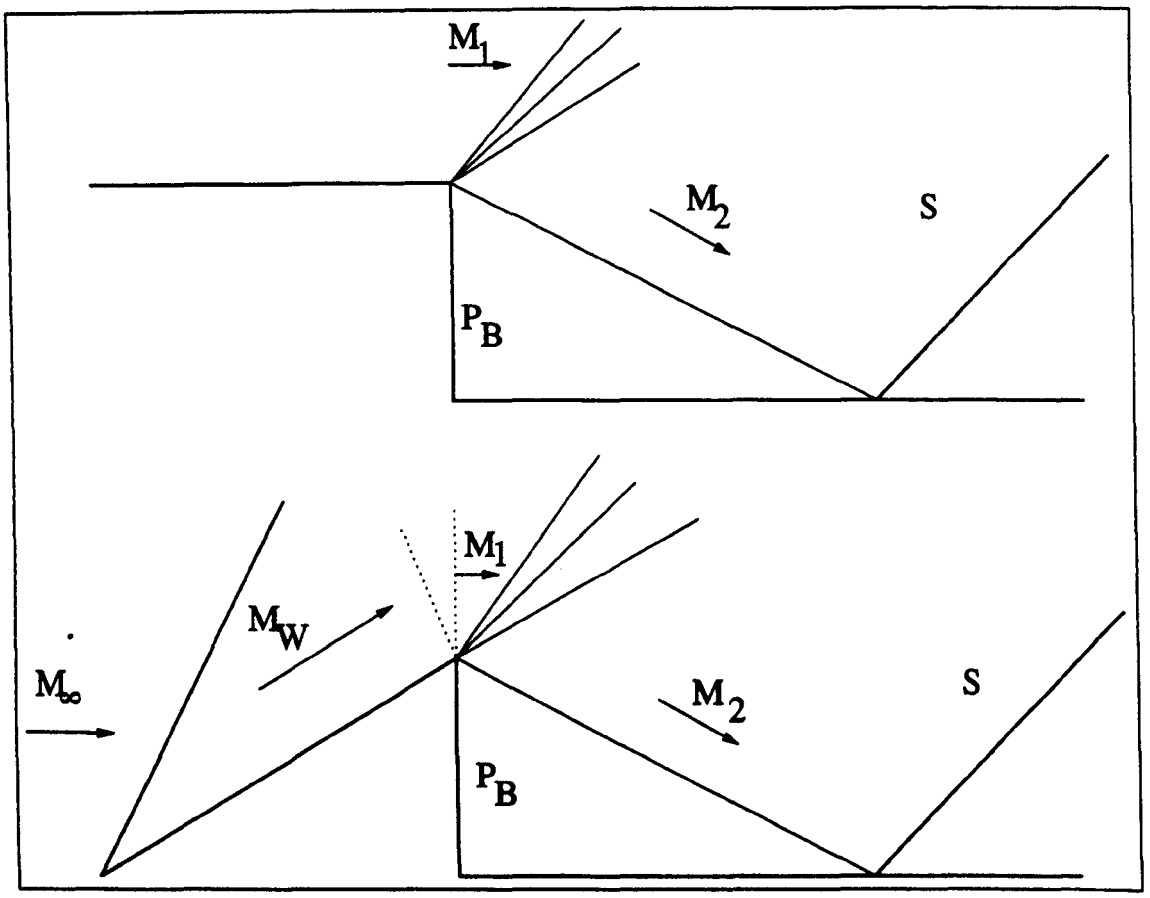

Figure 4.15: *Wedge and Rearward Step, Inviscid Flow Patterns*

satisfied is

$$\frac{d_1}{d}K_1(M_1)\frac{\gamma}{2}M_1^2 = \frac{H^*}{H}B(M_2,\beta) \tag{4.53}$$

The effect of a forebody may also be allowed for by a similar consideration of two flow geometries, that over a backward facing step and that over a body with a forebody (the simplest case is a wedge, as shown in Fig. 4.15). Using exactly the same arguments as for the boat tail, if an equivalent flow is hypothesised where the parallel flow Mach number before the separation corner (M_1 in Fig. 4.15) and M_2 in both cases are identical, then the entropy generated by the shock wave near the shear layer is the same regardless of the total drag of the body, and the RHS of Eqn. 4.47 is unaffected. For a simple wedge, M_1 may be calculated from standard shock wave relations (assuming the shock remains attached to the wedge at the nose) to find M_W, the Mach number along the wedge surface, and an expansion from M_W to M_1 equal to the wedge half angle.

The entropy increase in the shear layer is found from consideration of the total drag of the body. For the backward facing step, the entropy increase in the shear layer is proportional to the base pressure coefficient, as the base pressure generates the total drag of the body. For the flow with forebody, however, the total drag includes that due to the forebody drag coefficient, c_{df}. To retain the equivalence of the two geometries, this drag coefficient must be related to the parallel flow Mach number M_1. The calculation of the shear layer function

(K_1) is also conducted for this Mach number, but is valid for a wedge flow immersed in a free stream of M_∞. Therefore the governing equation becomes

$$\frac{c_{df} - c_{pb}}{-c_{pb}} K_1(M_1) \frac{\gamma}{2} M_1^2 = \frac{H^*}{H} B(M_2, \beta) \tag{4.54}$$

For simple wedges, c_{df} may be calculated directly from

$$c_{df} = \frac{2}{\gamma M_1^2} \left[\frac{P_W}{P_\infty} - 1 \right] \tag{4.55}$$

where P_W is the pressure acting on the wedge flank, and follows directly from M_∞ and the shock angle β (again assuming that the shock wave remains attached). Comparisons of the theory with experimental results for wedge flows show good agreement [31].

By combining all the above effects, it is possible to derive the general equation of the Tanner method for supersonic flows past two-dimensional objects :

$$\frac{c_{df} - c_{pb}}{-c_{pb} + 2\frac{\delta_2}{d} - 0.006} \frac{d_1}{d} K_1(M_1) \frac{\gamma}{2} M_1^2 = \frac{H^*}{H} B(M_2, \beta) \tag{4.56}$$

Axisymmetric Flows

For bodies of revolution, a very similar process to that for planar flows results in a general equation

$$\frac{c_{df} - c_{pb}}{-c_{pb} + 8\frac{\delta_2}{D} - 0.008} \frac{F_H}{F} K_{1R}(M_1) \frac{\gamma}{2} M_1^2 = \left(\frac{H^*}{H}\right)^2 B(M_2, \beta) \tag{4.57}$$

where D is the body diameter, F_H is the base area and F the cross sectional area of the body at the widest part (for bodies with boat tailing) and

$$K_{1R}(M_1) = 4 \int_0^1 \frac{\rho}{\rho_1} \frac{V}{V_1} \left(1 - \frac{V}{V_1}\right) \frac{y dy}{H^2} \tag{4.58}$$

where the same velocity and pressure distributions, Prandtle number and recovery factor are used as for two-dimensional flow. $B(M_2, \beta)$ is identical to that for two-dimensional flow (Eqn. 4.46). Whilst the ratio of radius of the initial shock point to the shear layer is still determined empirically, it is found to vary with Mach number, and is given by

$$\left(\frac{H^*}{H}\right)^2 = 2\left[1 + \frac{1}{0.00387 M_2^{3.2}}\right] \tag{4.59}$$

Some experimental evidence is provided, but is fairly limited. Agreement does, however seem reasonable [60].

Effects of the Lip Shock

Whilst the theory of Tanner is less well known than the derivative theories of Korst and Chapman, it has existed for some time. During this period it has been discussed, and on one occasion serious objections were raised to its validity. The primary concern is the lack of any inclusion of the effects of the lip shock in the theoretical model of Tanner. Obviously, before the method could be considered for application to ED nozzle thrust prediction, an assessment of the validity and impact of this complaint is warranted.

The phenomena of the lip shock was extensively experimentally analysed by Hama in Ref. [61]. The lip shock wave originates at the point of separation (or more precisely from the vertical face of the step or wedge, just beyond the separation corner), and is caused by the recompression of the flow, which tends to over expand around the separation point. This shock wave was found to have significant strength, which varied with respect to Mach number and Reynolds number. Magie *et al* [62] conceded that the experimental results provided by Tanner provided good agreement with his theory, but questioned the assumption that the ratio H^*/H could be considered a constant.

Experimental estimations of this quantity were presented, and found to vary considerably with Mach number. Further, extrapolations from Nash's results for such flows were used to calculate the variation of H^*/H with Mach number. This value was found to vary widely, and tend towards unity for hypersonic free stream Mach numbers. The seemingly good agreement of experimental results and theory was explained by an implicit allowance for the lip shock effects related to the specific experimental data which had been used for the calculation of the numeric value of H^*/H, and hence this value could and should not be considered universal.

In response to this criticism, Tanner defended his methodology on two fronts [60]. The concept that the lip shock is significant was accepted, however, the experimental evidence of H^*/H was rejected as inconclusive and difficult to interpret. Further the extrapolated values used to calculate this quantity were dismissed as unrealistic (evidence for this came from the very paper from which the values were taken).

To supplement these assertions, a wide range of experimental results, both from Nash, and various other sources were presented, showing a good agreement between the theory (including the assumption of constant H^*/H) and experimental results up to Mach numbers of 7. Tanner therefore concludes that although the lip shock can be shown to be significant, its effects are allowed for within the empirical factor H^*/H, which is valid for all Mach numbers.

With respect to the current project, it is felt that the criticisms have been adequately

addressed. Although the theory does not explain in detail how the lip shock effects the flow, the good agreement with experiment over a wide range of Mach numbers is undeniable. As the method chosen to model the base pressures of the pintle must of necessity be at least partially empirical, the detailed agreement between model and actual flow-fields is far less important than the accuracy of the final result. It is also noted that the experiments of Mueller on ED and other altitude compensating types showed that in many cases the lip shock was in fact very weak [29]. However, it is conceded that this area would be benefit from further research.

4.3.5 Adapting to ED Nozzles

Once Tanner's method had been selected for its ease of use and generally superior performance for the flows for which it was designed, some alterations were required to adapt it to ED nozzle flow-fields. One of the basic premises of both the theory of Korst, and specifically stated by Tanner, is that the problem under consideration is that of an isolated body immersed within a supersonic flow-field that is uniform at both up- and downstream infinity. Obviously, in an ED nozzle this assumption is violated. Not only is the pintle immersed within a non uniform flow-field, but there is a second body, the nozzle contour, in close proximity.

This will have a detrimental effect on the accuracy of either method. The influence of the accelerating (although steady) flow up to the point of separation will undoubtedly effect the shape of the Mach isobars at this point (i.e. velocity will no longer be constant in magnitude and direction at the initiation of the expansion fans), and the nozzle contour will interfere with the expansion fan originating at the point of separation. Note however that the important consequence of the assumption of expansion fan interference with the shock wave on Tanners theory remains, in that the shock wave will be of finite strength. Further, the increase in entropy within the viscous flow shear layer should equal that lost by the missing section of shock wave from the equivalent inviscid flow, provided that the expansion waves reflected from the contour do not interfere with the shock wave below this height (H^*). This is generally a reasonable assumption when considering ED nozzles, as long as the shroud is not truncated, or the pintle translated to off design conditions (due to throttling).

These considerations imply a limitation to the accuracy of the method, and hence is understood here to be only a first approximation. It is also noted that the method of Mueller, in assuming a cone tail free jet boundary, attempts to take these issues into consideration on a solely empirical basis, and in fact results from experiments tended to show that a constant pressure boundary (i.e. M_2 constant, as in the standard Tanner model) provides a better approximation. Hence the Tanner method retains the advantages of more accurate prediction

of simple flows, and also allows direct calculation of the base pressure from the input flow data and MoC solution up to the throat without any major disadvantages compared to the iterative methods outlined in Sec. 4.3.3.

To allow as accurate an approximation as possible, the effects of the interference of the outer contour, and both the shape of the pintle, and the boundary layer generated along it must be considered. The distortion of the parallel flow due to the effect of the ED contour is allowed for by the substitution of an average Mach number for the flow variables along the last LRC in the nozzle flow, weighted for the distance along which these occur. Between each pair of calculation points, i and $i-1$, on the last LRC in the nozzle flow, the average Mach number is expanded through the average flow direction to generate an effective parallel flow (i.e. $\theta = 0$) value, M_{eff}. The distance along which this Mach number acts is given by

$$ds = \sqrt{(x_i - x_{i-1})^2 + (y_i - y_{i-1})^2} \tag{4.60}$$

and hence

$$M_1 = \frac{\sum M_{eff} ds}{\sum ds} \tag{4.61}$$

The onflow conditions P_∞ and M_∞ are provided by the average pressure and Mach number across the first row of cells from the converged CFD solution. This represents parallel, undisturbed flow, although it should be noted that this is a subsonic boundary, and hence is not directly equivalent to the onflow conditions required for the standard Tanner model. With reference to Eqn. 4.49 it may be seen that the base pressure coefficient is given by

$$c_{pb} = \frac{2}{\gamma M_\infty^2}\left[\frac{P_b}{P_\infty} - 1\right] \tag{4.62}$$

For the forebody, the wall pressure force P_W may be found by integrating the pressure forces predicted at the wall by the CFD throat model up to the minimum geometric gap, and by the MoC from the geometric minima to the point of separation. The forebody drag coefficient is then calculated from

$$c_{df} = \frac{2}{\gamma h M_1^2}\left[\frac{P_W}{P_\infty} - 1\right] \tag{4.63}$$

where h is the difference in height between the separation point and lowest point in the CFD flow-field in two-dimensional flows, and the difference in the respective areas of revolution of these points in axisymmetric. P_W is the sum of the pressure forces acting in the axial direction integrated along the surface of the pintle (i.e. represents a force, not a pressure).

The boundary layer thickness is at present ignored. Once these values have been calculated, they are substituted into Eqn. 4.56 and the base pressure for the pintle at vacuum conditions estimated.

4.3.6 Comparison with Experimental Results

Whilst experimentally derived base pressures for flows past isolated bodies and simple rearward steps are fairly common in the literature, and used by both Tanner and the Korst school for verifications of their respective methods, the specific problem of the pressure behind the pintle in an ED nozzle has received very little attention. In fact, the only published data for axisymmetric nozzles uncovered is given by Mueller [25]. The data is presented in Fig. 11 of that reference as a plot of the variation in base pressure with M_1, the parallel flow Mach number. Unfortunately, the experimental conditions are not fully disclosed, and the dimensions of the pintle are not given. Despite this, it is still possible to provide a comparison of at least the prevalent trends.

The nozzles produced by Mueller make use of sharp edged pintles (i.e. $R_p^+ = 0$). The contours are of ideal type, and hence the last characteristic in the flow is a parallel flow expansion fan. Therefore the onflow Mach number is a function primarily of throat angle, assuming a constant upstream geometry. The base area and height are unfortunately not given, although this has a relatively minor effect on the base pressure (demonstrated in Ch. 5). To provide a qualitative comparison between the method described here and these experimental results, the base pressure behind various ED nozzles with sharp cornered pintles were found. The base height was maintained at 1 R_t, and the expansion fan was assumed to begin immediately after the throat. The pre throat curves on both outer and pintle contours were set to 2 G_t. Mesh size was 256 by 64 cells, and γ was set to 1.403 to simulate air (the working fluid used by Mueller in his experiments).

Fig. 4.16 shows a comparison between the experimental data of Mueller, and that produced by the above procedure with the current model. As can be seen, the general trends are similar, although the current model seems to over predict base pressure by approximately 20 percent. Whilst this is a significant error, it should be remembered that the current model is effected by the forebody shape of the pintle, which is unknown in the experimental results, that boundary layers are ignored (no data is available for the boundary layer thickness present in the experimental results), and that the shape of the Mach contours in the experimental model is unknown. Further, the exact data produced by Mueller is not available, the points shown in Fig. 4.16 being taken from measurements from the figure alluded to earlier. Finally, no assessment of possible experimental error is available.

The results presented in this figure demonstrate that the throat angle has no effect on the relationship of M_1 to P_b/P_1 predicted by the Tanner style analysis. It may also be seen that the current model more closely estimates the experimental results for small M_1. As large M_1 values will be associated with larger nozzles, and hence a greater dominance of the outer wall forces in the overall thrust prediction, the increased error in pressure prediction will

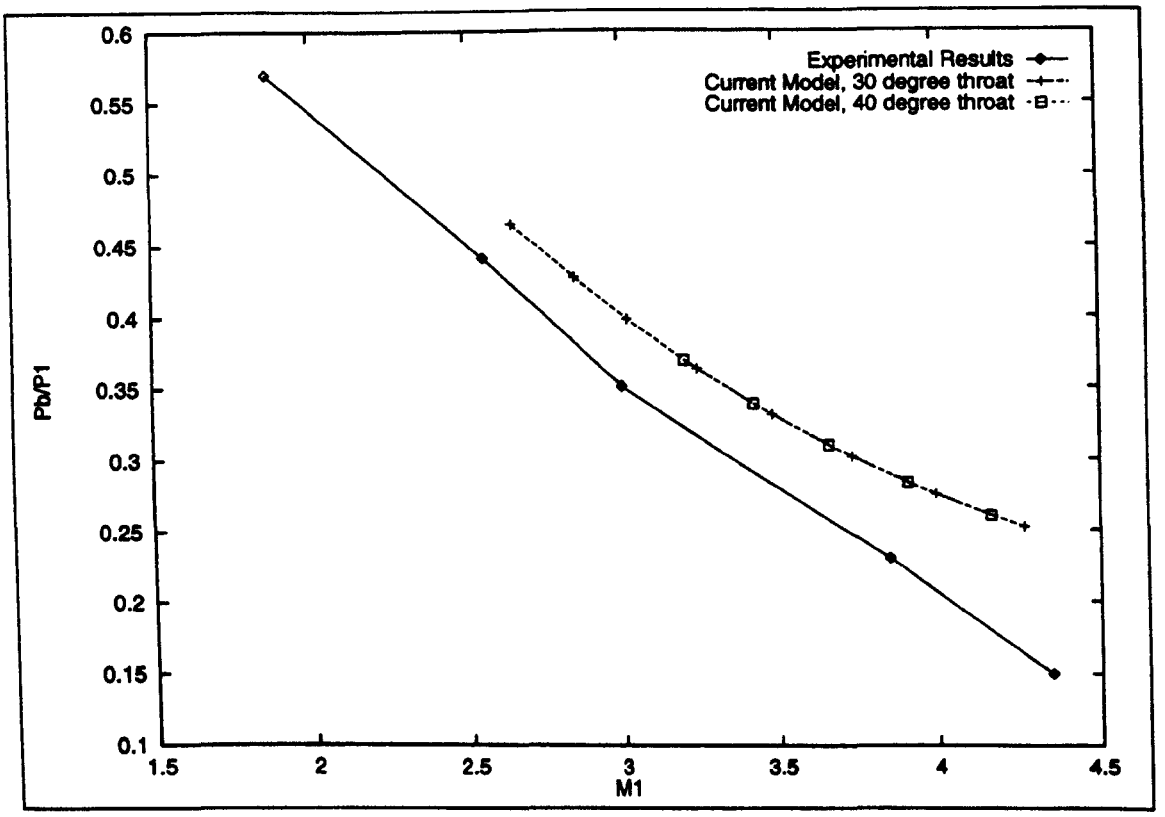

Figure 4.16: *Base Pressure Comparison*

have a much lesser impact in the accuracy of the final thrust prediction. However, the base pressure prediction method described in this section must be acknowledged to be little more than a framework which will allow a much more accurate solution method to be developed when a greater amount of experimental data becomes available. This topic is re-addressed in the final chapter.

4.3.7 Thrust Calculation

The three stage process of calculating the vacuum performance of an ED nozzle may be summarised as follows. The thrust due to the wall pressures acting on the shroud and pintle is estimated from

$$C_{Fw}^{\infty} = \sum_{2}^{nw} \frac{\bar{P}}{P_c}(y_i - y_{i-1}) \tag{4.64}$$

The contribution of the momentum flux across the throat is then calculated from

$$C_{Fc}^{\infty} = \sum_{2}^{nc} [\bar{P} + \bar{\rho}\bar{u}^2 \frac{\sin(-\bar{\mu})\cos(\bar{\theta})}{\sin(\bar{\theta} - \bar{\mu})}]Y \tag{4.65}$$

where barred quantities are the average between points i and $i-1$. Finally that due to the base pressure is

$$C_{Fb}^{\infty} = \frac{P_b}{P_c}\frac{A_b}{A_t} \tag{4.66}$$

where A_b is the base area associated with the height of the pintle at separation. The total vacuum thrust coefficient is therefore

$$C_F^\infty = C_{Fw}^\infty + C_{Fc}^\infty + C_{Fb}^\infty \tag{4.67}$$

Chapter 5

ED Nozzle Vacuum Performance

In some circumstances (e.g. propulsion systems for satellites, apogee kick motors etc), a knowledge of vacuum performance alone is sufficient for nozzle design, as this represents the entirety of operating conditions. Even when considering launch systems and other vehicles where a portion of the trajectory includes atmospheric flight, the performance in vacuum or near vacuum conditions will still tend to dominate the design, as high altitudes are achieved as rapidly as possible to reduce losses due to atmospheric drag. Therefore, the C_F^{∞} of a nozzle is an important indicator of performance.

The methods discussed in the previous chapter allow an assessment of the vacuum thrust performance of the ED nozzle type to be conducted, alongside a comparison with the conventional nozzle results presented at the end of Ch. 3. To achieve this, the effect of the variables used in the construction of the throat region on the thrust produced by the nozzle must be examined.

The design of the throat geometry of an ED nozzle requires a greater number of parameters to be defined than is the case for conventional configurations. These include R_w^+ and R_w^-, the pre and post throat radii of the outer nozzle wall, R_p^+ and R_p^-, the pre and post throat radii of the pintle wall, and θ_t and y_d, the throat angle and displacement. All of these may be independently varied, and hence influence the overall contour shape and performance of length optimised ED nozzles.

To conduct a comprehensive assessment of the influences of all these variables is at present an unrealistic objective, not least due to time and space constraints. Therefore, the ED nozzles examined and results presented in this chapter represent a restricted set of possible nozzle configurations, involving small variations in only some of these parameters. As with the results for conventional nozzles discussed in Ch. 3, the simpler case of planar flow nozzles are considered first, then followed by nozzles of axisymmetric type. The length of an ED contour is taken to be the distance between the intersection of the minimum throat

gap and the outer wall contour, and the exit plane of the nozzle. This is effectively precisely the same definition of nozzle length used for conventional nozzles.

5.1 Planar Nozzles

Very few real nozzles are of planar type, although the 'linear aerospike' is a notable exception. The reasons for preferring the linear variant of the aerospike nozzle to its axisymmetric counterpart relate primarily to specific and unusual difficulties associated with the large radial location of the throat. This causes the axisymmetric aerospike nozzle to suffer from a very narrow throat gap, increasing heat fluxes and producing a large base area, among other difficulties. These problems are reduced by the use of a planar aerospike contour.

A planar ED nozzle, however, would be unlikely to out-perform an axisymmetric variant under any circumstances. The location of the throat much closer to the axis of revolution means that it is unlikely that the throat gap will be increased, or base drag reduced, by switching from axisymmetric to planar flows. Despite this, results for the planar version are presented here, primarily to allow a more direct comparison of nozzle performance with results produced for linear aerospike nozzles when they become available (note that no comprehensive survey of the performance of the linear aerospike has yet appeared in the literature, results being limited to flow-field analysis and not including thrust coefficients, etc.). The flow is also simpler to analyse, and hence as many of the characteristics of the type will be similar between planar and axisymmetric flows, planar modelling represents a more efficient approach in the attempt to define design methodology.

Within the results presented, two different non dimensional lengths are used. This is an unfortunate but inevitable consequence of the grid definition process used for the ED nozzle throat region. The first, R_t, represents the throat half height of a conventional nozzle of equivalent mass flow, and is necessary to allow easy performance comparison between ED and conventional nozzles. Overall dimensions (i.e. nozzle lengths and area ratios) are referenced to this quantity. However, dimensions used to define the throat parameters are referenced to G_t, introduced in the previous chapter. For planar nozzles, equivalent mass flow between ED and conventional nozzle types is achieved if R_t and G_t are equal, and hence it could be argued that there is no need for this possibly confusing double dimensioning. Unfortunately, this is not the case in axisymmetric flow, and therefore this system is introduced for planar nozzles to maintain similarity in conventions for planar and axisymmetric ED nozzles.

Two-dimensional flow decouples the mass flow rate between the walls of the throat from its radial location, considerably reducing the impact of variation in y_d on the overall nozzle

performance. However, a displacement of the throat geometries produced by the techniques described in Ch. 4 is still required, to provide a thickness to the pintle stem. An arbitrary value of y_d equal to G_t has been used for all nozzle geometries unless otherwise stated. All the CFD grids used for generation of the initial starting line for the MoC based methods measured 256 by 64 cells, γ was 1.23 to simulate LOx/LH products of combustion, and both R_p^- and R_w^- were set (again arbitrarily) to $2G_t$.

The thrust coefficient predicted for a given throat configuration and M_E will be dependent upon n, the number of points in the initial characteristic derived from the CFD model. Increasing n increases the accuracy of the solution, but also raises run time and memory requirements. The sensitivity C_F^∞ to n reduces with increasing n, as the solution converges towards the exact value of C_F^∞ for an inviscid flow. However, the rate of this convergence is itself effected by the throat geometry, and will also reduce with the larger M_E necessary for long (and hence high thrust) nozzles. The value of n used for results associated with a particular throat geometry was therefore selected by examining the effect of increasing n on the vacuum thrust coefficient produced by a nozzle with a mid range M_E. Sufficient points in the starting line are deemed present when

$$\left|\frac{\partial C_F^\infty}{\partial n}\right| < 0.0001 \tag{5.1}$$

In general it was found that between 70 and 90 points were sufficient (n being only incremented in units of 10), depending on the range of nozzle lengths examined. However, for nozzles where R_w^+ and R_p^+ were 1 and 2 G_t respectively appeared to be especially sensitive to n, and required between 100 and 120 points to satisfy Eqn. 5.1. Reasons for this are as yet unknown.

The variation of thrust coefficient produced with overall nozzle length for optimised planar ED nozzles are displayed over the next two pages. Figs. 5.1 to 5.4 each show plots for a different throat angle, ranging from 30 to 75 degrees. Within each figure, results for a range of post throat wall radii curvatures are presented, reducing from continuous ($R_=^+ = 2G_t$) to a sharp expansion corner on the pintle ($R_p^+ = 0G_t$). These results include the contribution to vacuum thrust provided by the base pressure prediction technique. Although only a limited range of post throat radii are considered, examination of these results produces evidence of several general trends.

In all cases, an increment in C_F^∞ for a particular total nozzle length may be achieved by reducing R_w^+. A similar effect was observed to occur when R_w^+ was reduced in both conical and bell nozzles (see Ch. 3, particularly Figs 3.9 and 3.15), although it appears to be more pronounced in ED nozzles, particularly for small throat angles.

The effect of variations in R_p^+, is more complex. In general, reducing this radius reduces

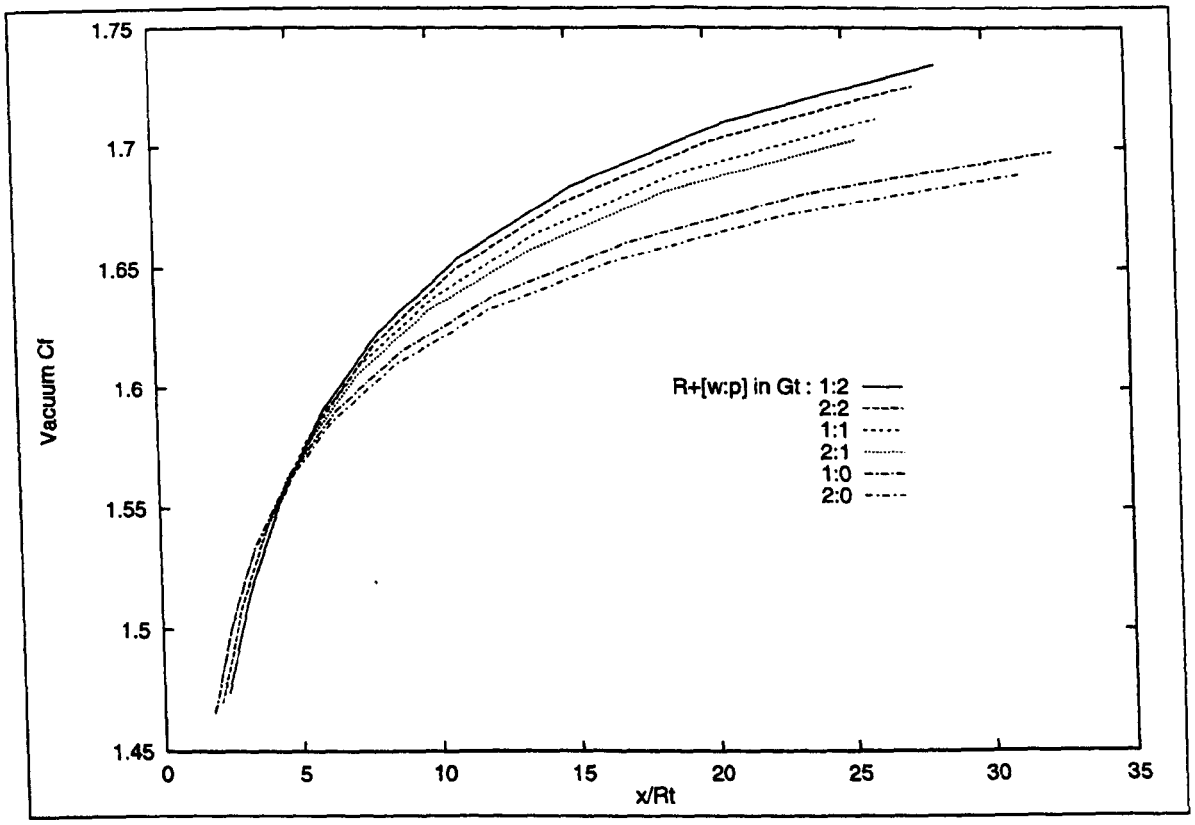

Figure 5.1: *Effect of R_w^+ and R_p^+ on C_F^∞, Planar ED Nozzles, $R_=^- = 2G_t$, $\theta_t = 30^0$*

thrust for a given length (markedly so for the sharp separation corner, $R_p^+ = 0$). However, for some very short nozzles, reducing the radius increases the thrust, and hence there is a point at which the plots cross. At this specific length, unique to each throat configuration, varying

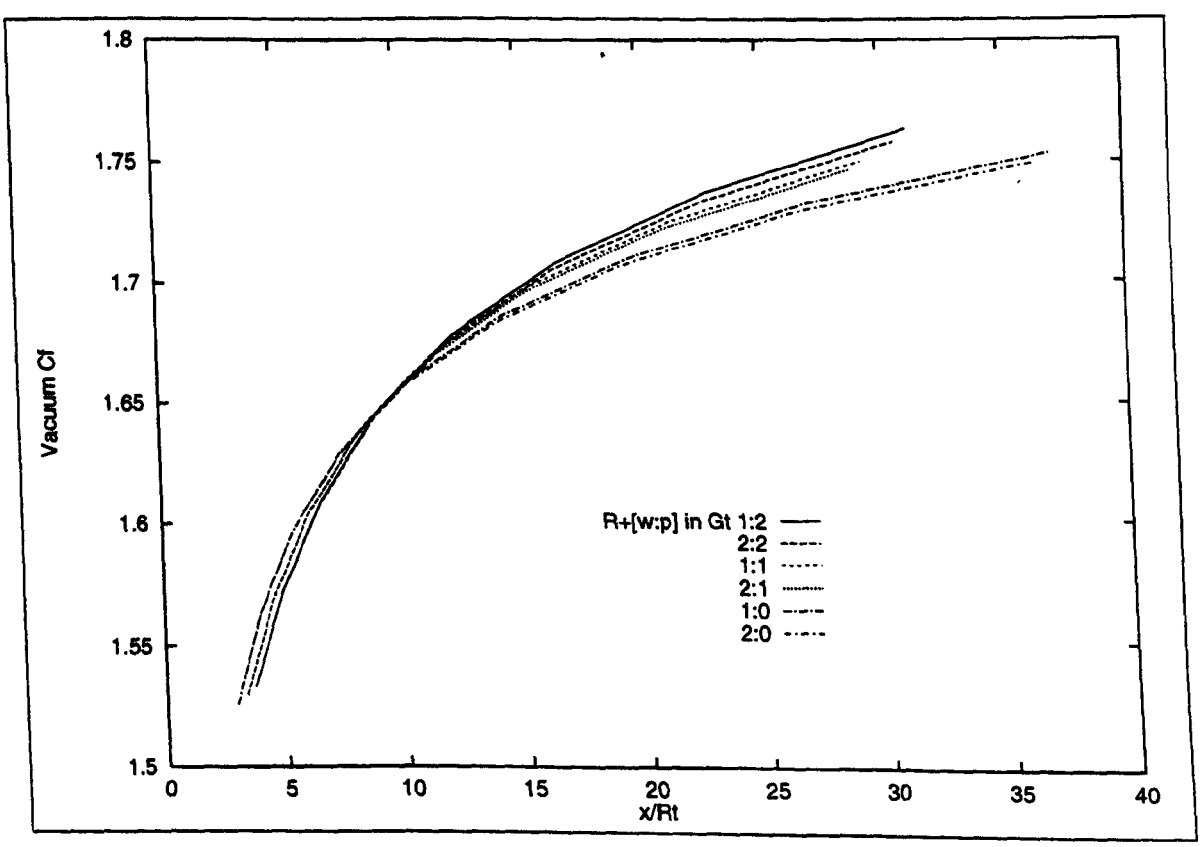

Figure 5.2: *Effect of R_w^+ and R_p^+ on C_F^∞, Planar ED Nozzles, $R_=^- = 2G_t$, $\theta_t = 45^0$*

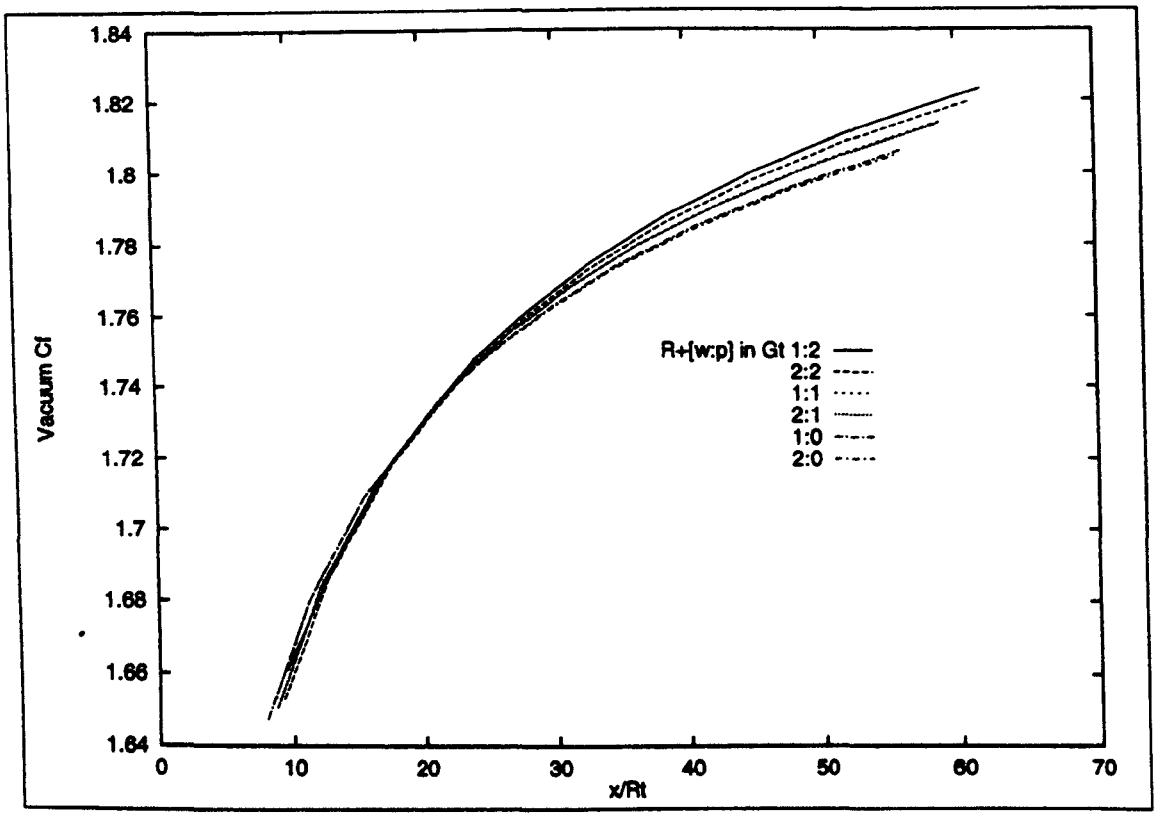

Figure 5.3: *Effect of R_w^+ and R_p^+ on C_F^∞, Planar ED Nozzles, $R_=^- = 2G_t$, $\theta_t = 60^0$*

R_p^+ has no effect on C_F^∞. The length at which this occurs increases with throat angle, being roughly 5, 10, 20 and 40 R_t respectively for throat angles of 30, 45, 60 and 75 degrees.

The influence of the post throat curves on C_F^∞ are most apparent for the smallest throat

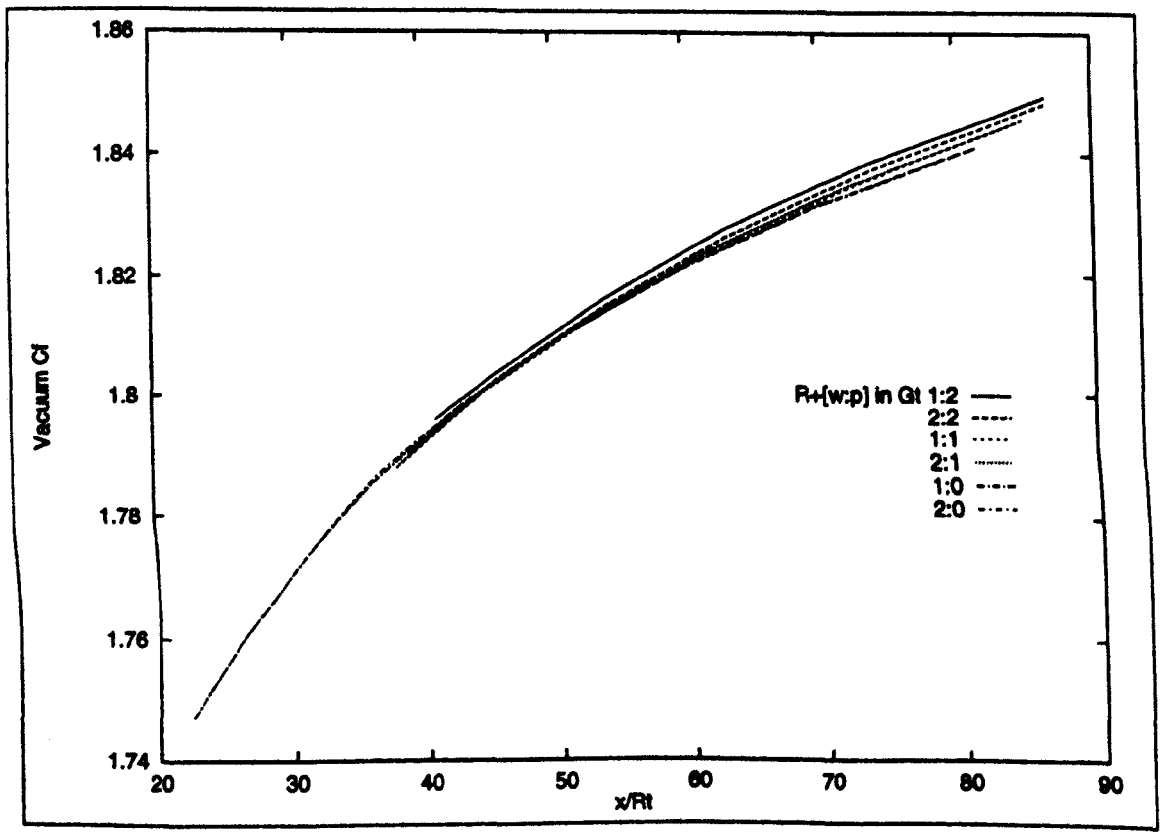

Figure 5.4: *Effect of R_w^+ and R_p^+ on C_F^∞, Planar ED Nozzles, $R_=^- = 2G_t$, $\theta_t = 75^0$*

angle (30^0, Fig. 5.1), but reduce in relative terms as the throat angle increases. In fact for the largest throat angle (75^0, displayed in Fig. 5.4), the difference in thrust produced by varying either R_w^+ or R_p^+ is extremely small over the length range considered. It should also be noted that the vertical scales are not of constant magnitude across all figures, and in fact the reduced separation between plots apparent in the later figures coincides with a reduced magnitude range of thrust coefficients, which would tend to increase the visibility of any effect caused.

However, as was the case with conventional nozzles, even a relatively small increase in C_F^∞ for a given length may have a significant effect if a nozzle is designed for a specified thrust. This is due to the low gradient of the thrust curves at greater nozzle lengths, and hence a relatively small increase in C_F^∞ can result in a considerable reduction in total nozzle length for a specified C_F^∞.

Whilst the maximum length considered in each figure is somewhat arbitrary, the minimum length is enforced due to the physical limitations of the nozzle itself, with the exception of the 30 degree throat. As was noted in Sec. 4.2.1, the equations used to derive the optimised contour may have no solution that allows sufficient mass flow to enter the outer region of the nozzle to produce a flow which obeys continuity. This effect becomes more severe for large throat angles, as the exit angle produced by Eqn. 3.28 is independent of the throat angle, and hence for a small M_E, the nozzle contour must turn the flow through a large angle without a significant increase in the wall Mach number. This may prove impossible, and hence the minimum lengths shown in Figs. 5.2 to 5.4 in fact represent the shortest nozzle possible of optimised contour design for each throat configuration. This minimum length is also effected by the various wall radii of curvature, and in particular use of a sharp expansion corner nozzle type invariably allows a shorter minimum nozzle length.

The relationship between throat angle and the pressure acting on the rear face of the pintle (assuming termination of the pintle with a sharp corner at the origin of the last LRC in the nozzle, causing separation) is shown in Fig. 5.5 for nozzles with R_w^+ and R_p^+ set to 1 and 2 G_t respectively. Fig. 5.6 shows the same quantities for nozzles with R_w^+ and R_p^+ set to 1 and 0 G_t. From these figures it is clear that the base pressure predicted is essentially independent of throat angle. Whilst it is true that nozzles with large throat angles will tend to have lower base pressures, this is primarily due to an associated increase in nozzle length. Comparing these two figures also reveals that the magnitude of pintle radius after the nozzle throat has very little impact upon the base pressure, although a very slight increment when R_p^+ is reduced is just visible.

Figs. 5.7 and 5.8 demonstrate the effect of throat angle on the ratio of pintle base to nozzle exit area. As may be seen, a larger throat angle results in an increase in the pintle cross sectional area at the base relative to that of the nozzle at the exit plane. Comparison between

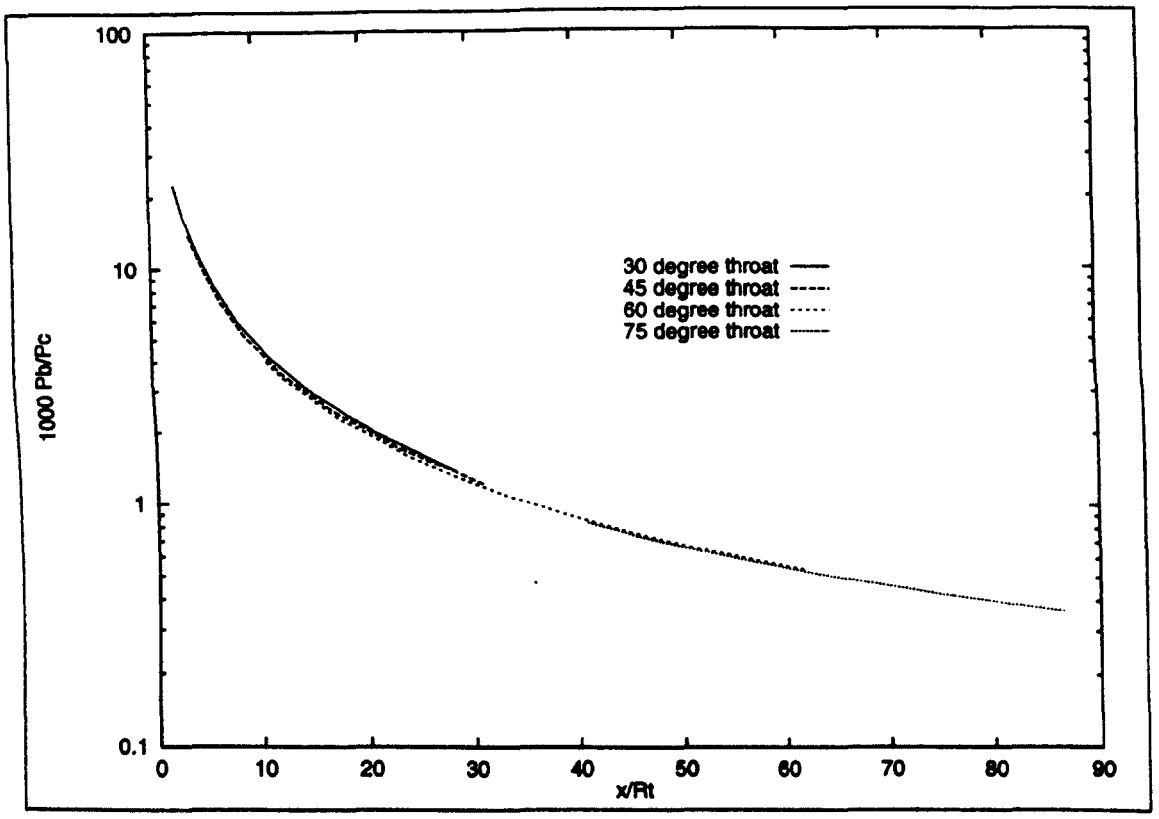

Figure 5.5: *Effect of θ_t on P_b, Planar ED Nozzles, $R_w^+ = 1, R_p^+ = 2, R_=^- = 2G_t$*

the two figures also reveals a reduction of this area ratio for pintles with a sharp expansion corner. However, both these effects are relatively small compared to the dominant factor of nozzle length, an increase of which reduces the relative base area. This is as expected, for if only M_E is varied and all other variables remain constant, the actual base area is maintained

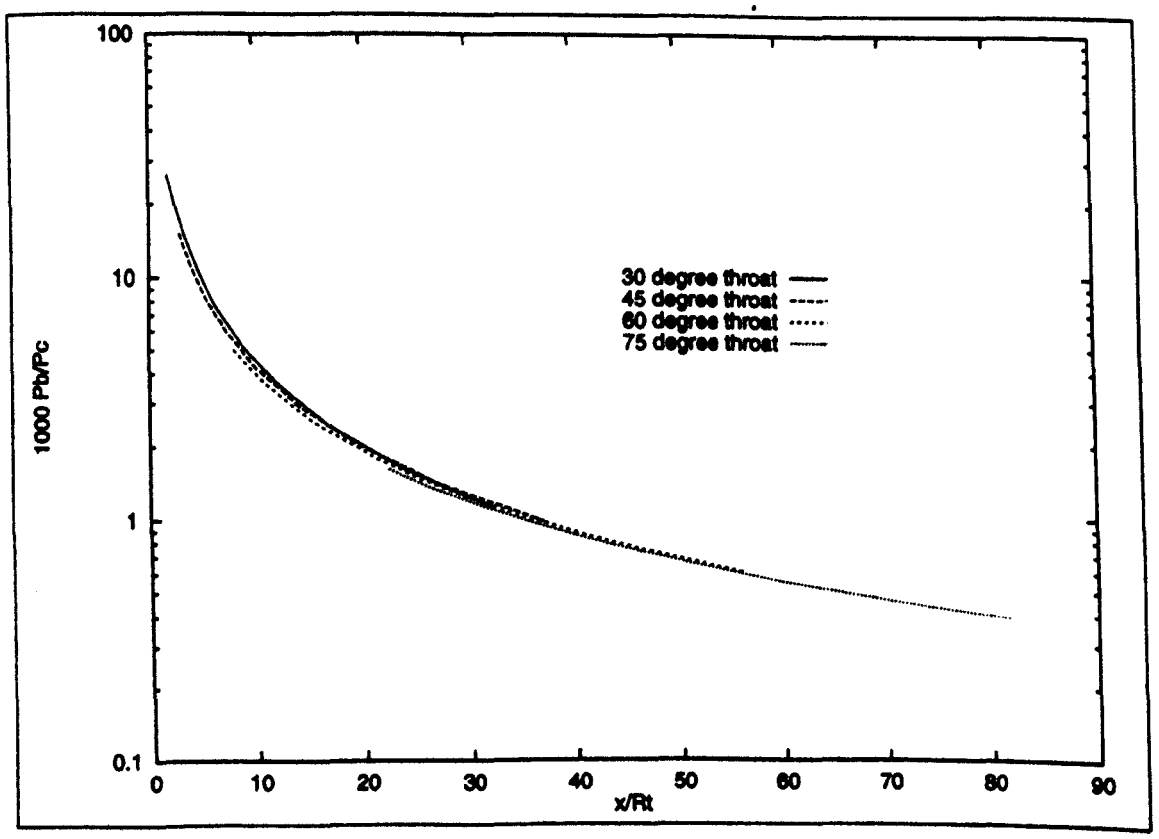

Figure 5.6: *Effect of θ_t on P_b, Planar ED Nozzles, $R_w^+ = 1, R_p^+ = 0, R_=^- = 2G_t$*

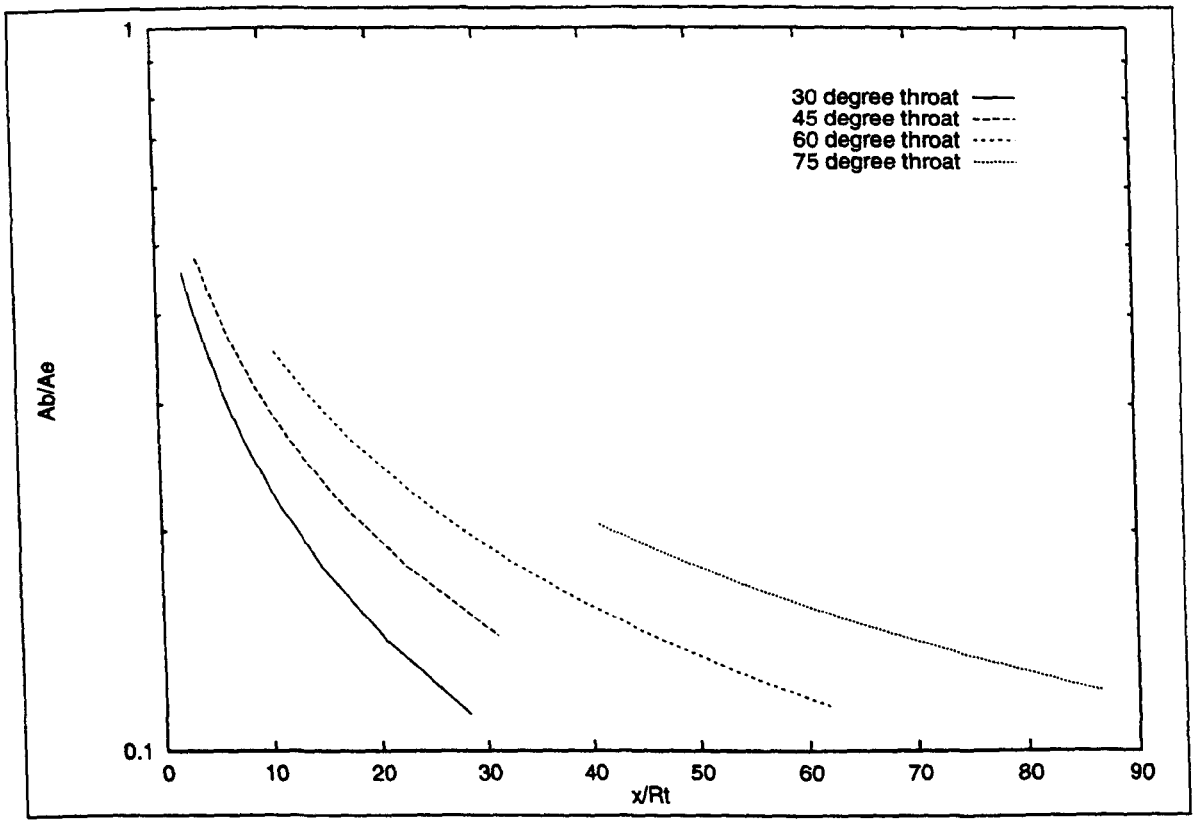

Figure 5.7: *Effect of θ_t on A_b, Planar ED Nozzles, $R_w^+ = 1, R_p^+ = 2, R_=^- = 2G_t$*

relatively constant in size. However, increasing M_E increases total nozzle length, and hence the exit area of the nozzle.

From the previously described figures, it may be concluded that the effect of the base

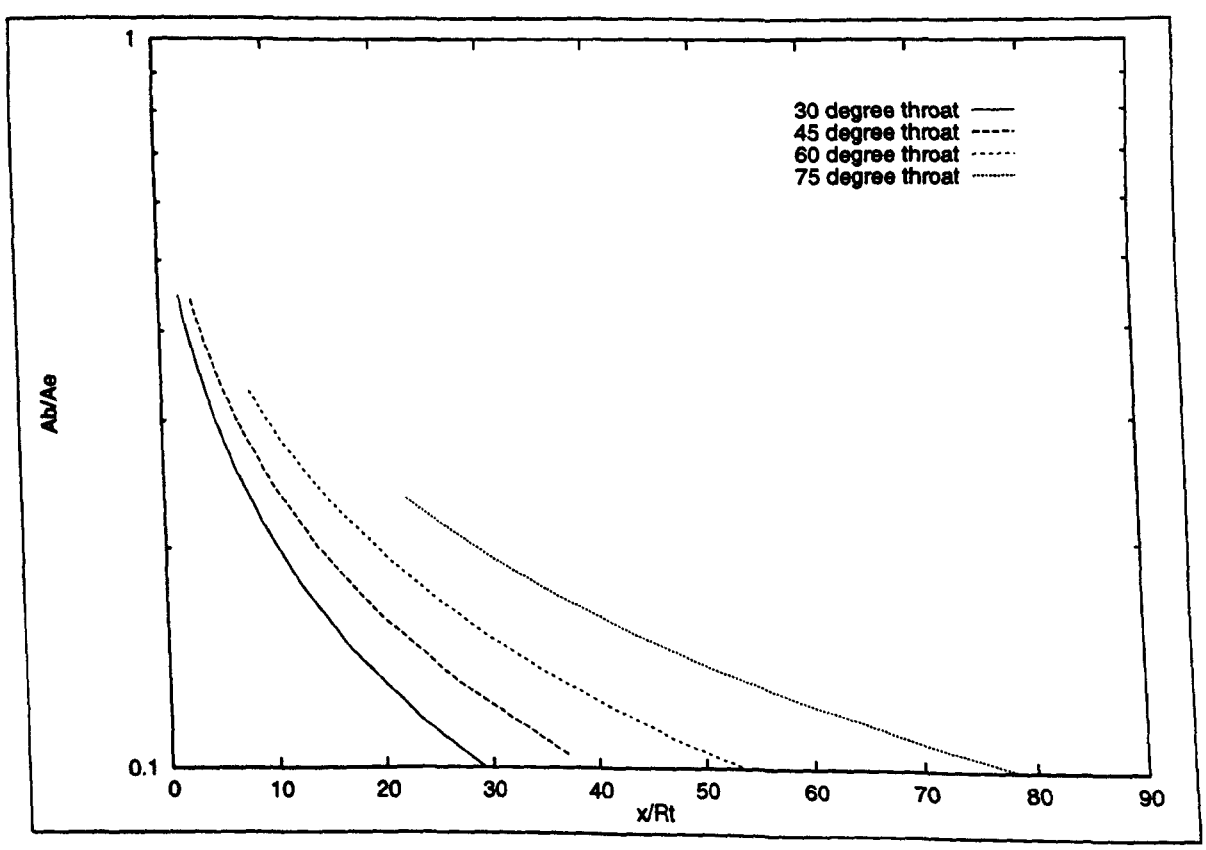

Figure 5.8: *Effect of θ_t on A_b, Planar ED Nozzles, $R_w^+ = 1, R_p^+ = 0, R_=^- = 2G_t$*

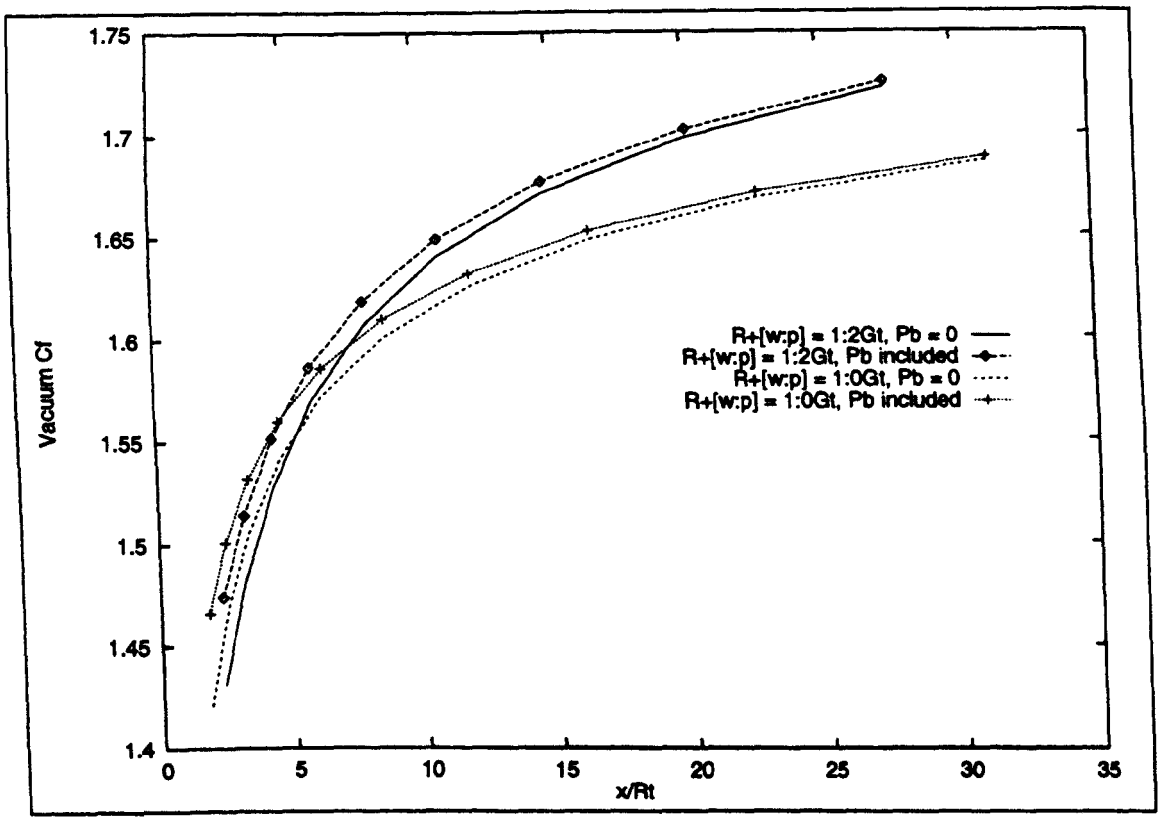

Figure 5.9: *Contribution of P_b to Total Thrust, Planar ED Nozzles, $\theta_t = 30$*

pressure on overall nozzle thrust will be greatest for relatively short nozzles, and reduce dramatically as the overall nozzle length increases. Fig. 5.9 shows the consequence of removing the contribution to thrust provided by the base pressure on nozzles with a 30 degree throat. Two sets of curves are shown, the first produced from a throat configuration with R_w^+ and R_p^+ of 1 and 2 G_t respectively, and in the second these variables are 1 and 0 G_t. Fig. 5.10 provides results for nozzles of the same wall radii, but with a throat angle of 75 degrees. These figures demonstrate that as expected, the impact of the base pressure does indeed reduce considerably with length, and generally provides only a minimal contribution to thrust.

Finally, Fig. 5.11 shows the effect on total thrust produced by varying the throat angle. R_w^+ and R_p^+ are 1 and 2 G_t, as this generally produced the maximum thrust of all configurations considered, and the contribution due to the base pressure is included. This figure clearly demonstrates the variation of optimum throat angle with desired nozzle thrust; as nozzle length (and hence thrust coefficient) increases, the angle of the throat which gives maximum C_F^∞ also rises.

This in turn means that the restriction on minimum length for large throat angles imposed by the physics of the flow noted earlier does not pose a serious problem, as the length at which a particular throat angle becomes optimum is greater than this minimum (although there is a slight gap between the thrust curves for 60 and 75 degree throats, there is a fifteen degree gap in throat angle. If a continuous variation of θ_t were shown, the jump between

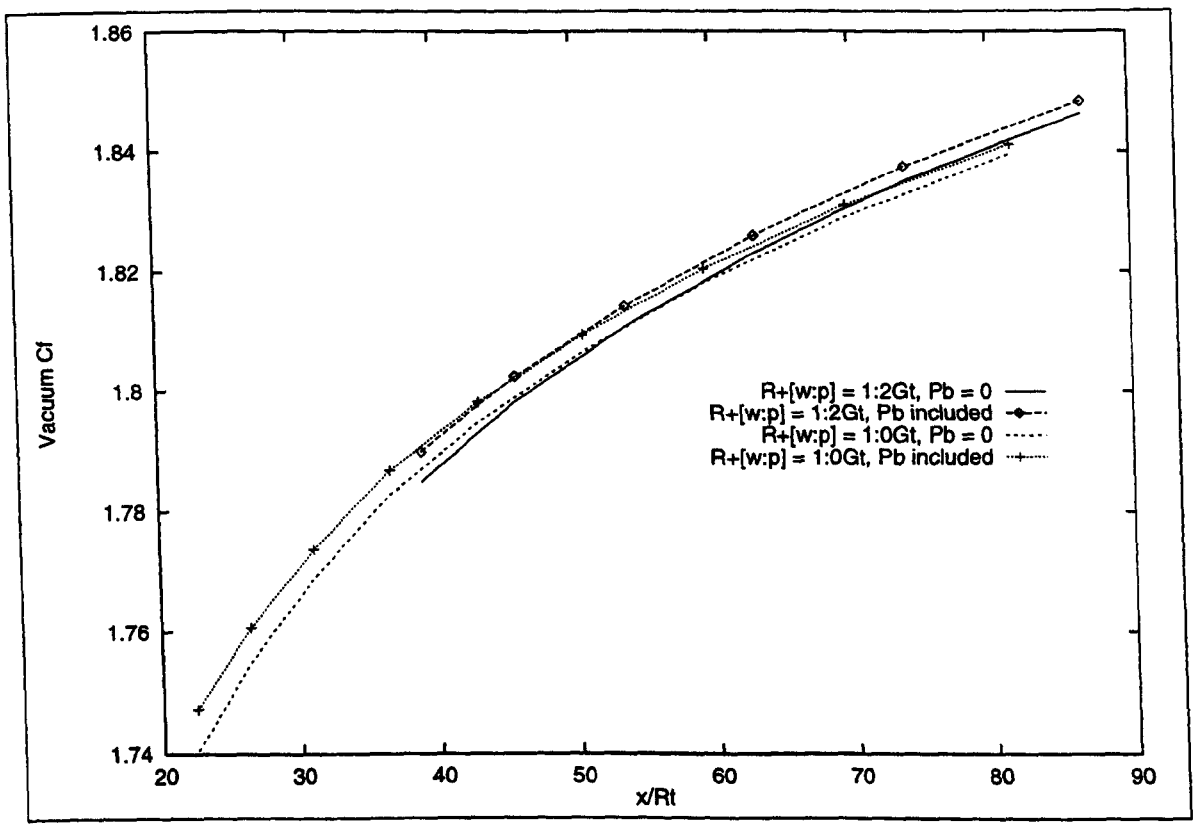

Figure 5.10: *Contribution of P_b to Total Thrust, Planar ED Nozzles, $\theta_t = 75$*

these plots would vanish). As this is the case, if a nozzle length were desired that was shorter than the minimum allowable for a given throat angle, reducing θ_t would not only allow a contour to be obtained, but would also increase the C_F^∞ obtained for that particular nozzle length.

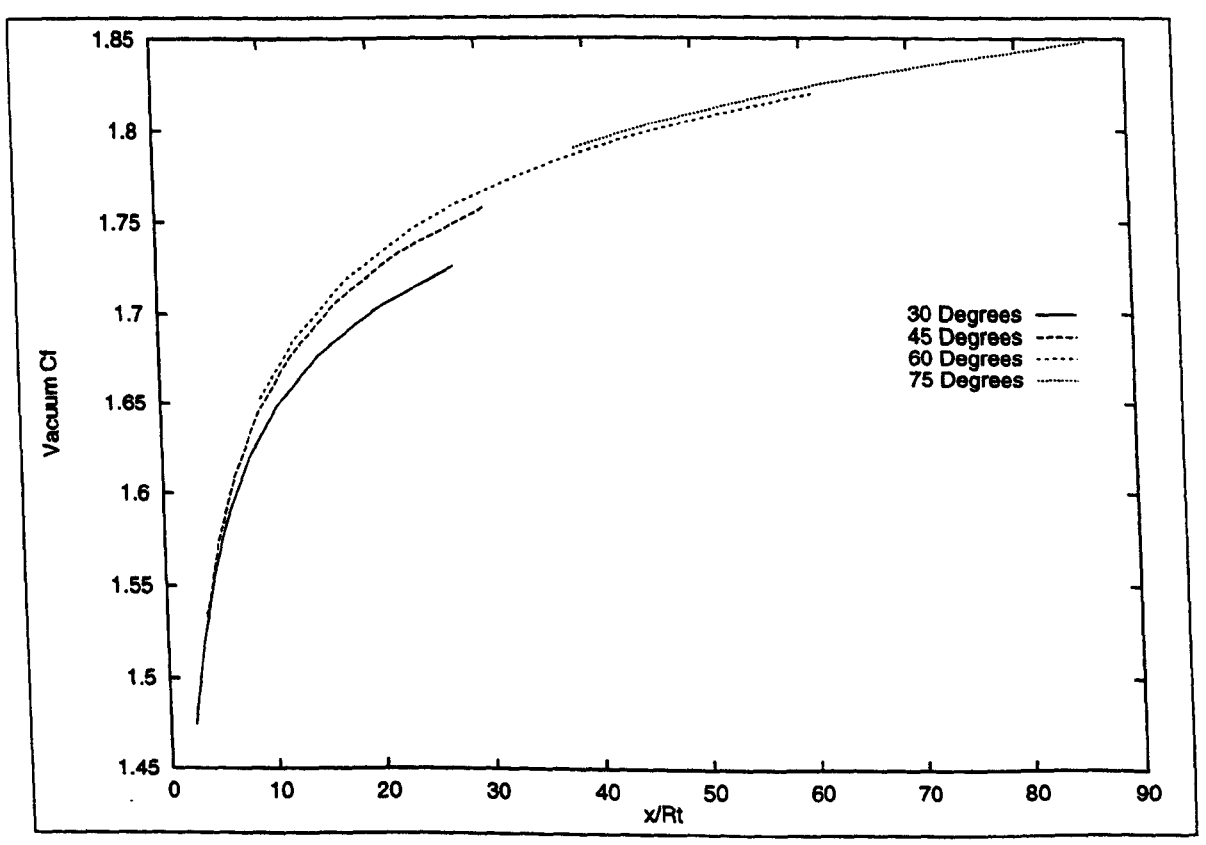

Figure 5.11: *Effect of θ_t on C_F^∞, Planar ED Nozzles, $R_w^+ = 1, R_p^+ = 2, R_=^- = 2G_t$*

5.2 Axisymmetric Nozzle Flows

Nearly all nozzles current or envisioned (with the exception of the failed X33 and similar programs based on the 'Linear Aerospike' concept) are of axisymmetric rather than planar design. A similar analysis of the impact of the primary design variables is therefore presented for ED nozzles of this type. As was the case for the planar nozzles, all the CFD grids used for generating the initial starting line for the MoC algorithms measured 256 by 64 cells, the ratio of specific heats was 1.23 to simulate LOx/LH products of combustion, and the pre throat wall radii of curvature on both the pintle and contour walls is set to an arbitrary value, this time of $5G_t$. In all results presented these values are implied, unless an alternative is specifically stated. Eqn. 5.1 is again used to ensure accuracy of results.

Before presenting this analysis in a similar fashion to that for planar flows, a review of the effect of the radial displacement of the geometric minimum gap (y_d) is required, as the value of this variable has a greater impact and more far reaching effects in axisymmetric nozzle configurations than on those of planar type.

5.2.1 Effect of y_d on Axisymmetric Nozzle Design

The relative performance of different nozzle designs are normally compared by examining the relationship between the C_F^∞ produced and nozzle length. For such a comparison to be meaningful, the coordinate system in which results are presented must result in an equal throat area for all nozzle types, in turn assuring equal mass flow through the nozzles in question. In conventional nozzles, comparison between bell and conical types is achieved by giving lengths in terms of R_t, the throat radius. To allow comparison of ED nozzles with conventional types, the coordinate system in which the nozzle contour is defined must also be non dimensionalised with respect to this variable, even though it may not have any physical meaning in the ED nozzle flow-field itself.

However, the equations used to define the location of the walls within the throat region of an ED nozzle were non dimensionalised with respect to the minimum separation of the nozzle walls, G_t. As this is the case, a mapping must be applied to the results of the CFD analysis to convert these dimensions into R_t units. This is achieved via the transformation

$$x(R_t) = \sigma x(G_t) \tag{5.2}$$

where x is any dimension, and σ is a constant for a particular nozzle geometry. In planar flows, setting σ to unity results in equal throat areas, and hence as was noted in the previous section there is a one to one correspondence between lengths in these two unit systems.

In axisymmetric flows, however, this relationship is lost due to the influence of y_d, the

arbitrary radial translation of the grid. The local cross sectional area of the flow is formed by the revolution about the nozzle centreline of the gap between the nozzle walls. This in effect decouples the location of the minimum cross sectional area (the geometric throat) from the location of the minimum wall separation. Therefore variation of y_d in axisymmetric flows has two effects not present in planar flows; the local cross sectional area along the entire length of the throat region will be altered, and the location of the geometric throat will also move in the streamwise direction.

Returning to Eqn. 5.2, consistency in throat areas requires that

$$\sigma = \sqrt{\frac{\pi}{A_t}} \tag{5.3}$$

A_t being the throat area of the ED nozzle in question in units of G_t^2, found from Eqn. 4.26. However, as a consequence of the dependency of A_t on y_d, σ will vary with changes in y_d, with the result that throat geometries which in G_t units differ only in y_d will possess different wall radii of curvature with respect to R_t units. This is also true if the value of y_d and wall radii input for two nozzles are the same, but the throat angle is different (larger throat angles tend to increase the radial location of the throat for equivalent wall radii in the G_t system). The situation is further complicated by the variation of the streamwise location of A_t with y_d, which renders the $\Delta\sigma$ associated with a given Δy_d unpredictable in advance.

This being the case, the only way in which a geometry for the throat region could be created which is predefined in R_t units is by an iterative procedure, adjusting the size of the minimum wall separation until the desired geometry is produced. However, this is a time consuming process with no guarantee of success, as the input parameters may not be compatible with each other (e.g. it would be impossible to specify $R_p^=$, θ_t and y_d in R_t units, one at least must be allowed to float). It is also possible that within the throat region of the nozzle, it is the the ratio of the wall radius to the local half channel height that exerts greatest influence on flow behaviour, and hence nozzles will present greater similarity in behaviour when wall radii are equal in terms of G_t units, even if the these radii are different on a physical nozzle.

For these reasons, the procedures for generating the throat region of axisymmetric nozzles outlined in Ch. 4 are used, where all parameters are defined in G_t units. Whilst this provides a similarity of approach with planar and conventional axisymmetric nozzles, it does mean that it is no longer possible to isolate the effect of an individual parameter to the same degree (e.g. varying θ_t while maintaining all other values constant will not actually isolate the effect of θ_t completely, as varying θ_t will also alter wall radii in R_t units). The difficulties outlined here in attempting to form a consistency of approach to the problem of ED throat geometry parameter variation should reinforce the point made in Sec. 4.1.1 that the number of variables within the throat region of ED nozzles, and indeed the amount of

Geometry Parameters					Allowable M_E Range					
θ_t	y_d	ζ_t	$R_=^-$		$R_w^+ : R_p^+$, in G_t					
deg	G_t	R_t	G_t	R_t	5:5	5:2.5	5:0	2.5:5	2.5:2.5	2.5:0
60	1.5	1.76	5	1.39	3.4-4.9	2.8-5.1	2.7-5.2	3.6-4.7	2.8-4.8	2.6-5.0
60	8	2.47	5	1.01	3.3-5.2	2.8-5.4	2.6-5.5	3.5-5.0	2.8-5.1	2.6-5.4
90	1.5	2.26	5	1.10	none	4.2-4.5	3.7-4.7	none	4.2-4.4	3.7-4.6
90	8	2.90	5	0.86	none	4.2-4.8	3.7-5.0	none	4.3-4.7	3.7-5.0
60	4.5	2.46	10	2.01	3.4-5.2	2.7-5.4	2.5-5.6	3.5-5.1	2.8-5.2	2.5-5.4

Table 5.1: *Allowable M_E Range for Various Nozzle Configurations*

variation possible within design principles, make for an almost infinite variety of potential ED nozzle throat configurations. This means that comparison of different designs is difficult, even within a unified design methodology. However some conclusions may still be drawn, if somewhat cautiously, as shall be demonstrated later in this chapter.

A second consequence of the relation of throat area to y_d is the effect it has upon the range of optimised nozzle contours that exist for any given throat configuration. As was noted in the previous section, in planar nozzle geometries the mass flow through the throat may restrict the minimum value of M_E for which an optimised nozzle contour exists. As explained in Ch. 4, this is a consequence of the optimisation formulation, and contours optimised to parameters other than length will exhibit different limits (this topic is re-addressed in the final chapter). However, for length optimised, axisymmetric ED nozzles, the problem is directly related to the location in the R_t coordinate system of the minimum throat area.

Table 5.1 presents the range of M_E for which an optimised solution exits for a selection of throat configurations. Before proceeding to discuss the implications of the results shown, it should be noted that whilst a strong correlation of M_E to length and thrust coefficient is assumed, the performance generated by any nozzle is not of primary concern (issues relating to performance being examined at length in subsequent sections). The only topic addressed here is the impact of the various throat parameters on the range of allowable M_E.

The most obvious conclusion that may be drawn from Table 5.1 is that the allowable size range of ED nozzles is very sensitive to modification of the parameters in the throat region. Only a relatively limited range of closely related configurations are shown, and yet the difference in possible M_E range varies from none whatsoever, to just under 3. The analysis of the impact of individual parameters may be divided into two subsets; those that primarily effect the location of the throat (θ_t and ζ_t), and those that primarily control the rate of change of the cross sectional area of the flow channel (the various radii of curvature).

Increasing the throat angle is shown to have a very detrimental effect, appreciably reducing the allowable range in all cases, as may be seen by comparing results in the first and second rows with those in the third and fourth. That this effect is primarily due to θ_t alone is demonstrated by a comparison of the results in the second and third row, where the difference in nozzle geometry in terms of ζ_t and $R_{=}^{-}$ (once transformed into R_t units) is minimal, yet the variation in allowable M_E range is large. Whilst both the minimum M_E is raised and the maximum reduced, it is notable that the former is the greater effect.

Whilst the radial step input (y_d) is user defined, the more direct relation to throat location is provided by ζ_t, the average radial distance of the geometric throat. This is given in terms of the transformed coordinate system, and is only controllable indirectly, through y_d. By comparing results in the first row with those in the second, and the third with the fourth, increasing ζ_t may be seen to increase the allowable Mach number range for a given θ_t, particularly with respect to the upper limit. However, it should be noted that due to the influence of y_d on both ζ_t and $R_{=}^{-}$, an increase in ζ_t is always accompanied by a reduction in $R_{=}^{-}$, and hence which of these variables is responsible for this effect must be ascertained.

To allow separation of these effects, the configuration presented in the final row has the same angle and radial displacement at the throat as that in the second, which results in an approximate equality of mass flow for these nozzles in the G_t unit system. This in turn means that σ is the same for both nozzles, and hence any radius that is equal in the G_t system will remain equal in R_t units. By doubling the pre throat radii, while maintaining all other properties, the effect of this variable has been isolated as far as is possible. Comparing the ranges in rows 2 and 5 reveal that $R_{=}^{-}$ appears to have little effect on either the upper or lower M_E limit. This in turn implies that the increase in range noted in the previous paragraph is indeed primarily related to the variation in ζ_t, rather than the coincidental drop in $R_{=}^{-}$.

The effects of the post throat radii may be determined by comparing results within the rows. R_w^+ is seen to have only a relatively minor impact; increasing this parameter raises the maximum M_E and lowers the minimum, but this small despite a doubling of R_w^+. The same is not true of R_p^+, which appears to have a greater effect than any other variable on the minimum permissible value of M_E. Halving R_p^+ slightly increases the maximum M_E, and greatly reduces the lowest. Reducing this radius still further to a sharp expansion corner continues the improvement in M_E range, although to a much lesser extent.

As has been noted, the results presented here represent only a small subset closely related ED nozzle throats. Before a detailed picture of the impact of each parameter can be produced, a considerably larger number of configurations must be examined. Of particular interest would be an attempt to isolate the wall and pintle pre throat radii, given the considerable difference in the magnitude of effect generated by the different post throat radii. Due to time constraints, such a survey has been left to the future. However, several issues may still be

addressed even from this limited analysis.

The results presented within this section give an overview of a design issue previously ignored in the literature, due to to the simpler models of the throat region previously used. However, the importance of this area in the design of ED nozzles is clear. This is particularly true when considering optimal throat angles. Previous investigations, relying upon simple linear approximations for the starting line, have found that optimum ED nozzle performance is achieved via large throat angles in the range of 75 to 90 degrees (primarily Rao [6], and Schorr [24]). However, the results presented in this dissertation demonstrate that increasing θ_t to such a level has severely detrimental effects of the range of sizes for which length optimised ED nozzles are possible.

Fortunately, the effect of increasing the displacement of the radial location of the throat may be seen to offset this problem, increasing the possible M_E range for both 60 and 90 degree throats for only relatively modest radial increments in ζ_t. This does indeed allow a wide range of nozzle contours to be considered, even for a large throat angle. However, it is at the cost of an increase in the radial location of the throat, which in turn will result in a reduction in the minimum separation of the nozzle walls, increasing the cooling and manufacturing problems associated.

5.2.2 Performance Analysis

As was the case for planar ED nozzles, only small selection of possible nozzle configurations is considered due to time constraints. Three different throat angles were examined, these being 30, 60 and 90 degrees. For the reasons explained in the preceding section, throat radii similarity was preserved in G_t units at the expense of similarity in R_t, and hence all the throat regions are formed from CFD grids with $R_{=}^{-} = 5G_t$, and $y_d = 1.5G_t$, unless otherwise stated. This produces throat areas of 20.5, 40.6, and 64.9 G_t^2 respectively, in turn resulting in σ values of 0.396, 0.278, and 0.220. Physically, σ is the minimum separation of nozzle walls in the R_t system, and hence gives an indication of the likely increase in heat flux transfer problems at the throat (for a conventional nozzle, this minimum separation is $2R_t$).

That the general effects of the wall radii on the relationship between C_F^∞ and length are similar in axisymmetric flows to that found previously for planar flows may be seen by comparing results shown in Figs. 5.12 and 5.13 with their planar counterparts, Figs. 5.1 and 5.3. In all cases, an increase in thrust is obtained by either reducing the outer wall radius, or increasing that of the pintle. Increasing the throat angle reduces the amount of thrust variation produced by this technique, as was found for planar nozzles.

That this is the case is of considerable importance in the light of the issues discussed in

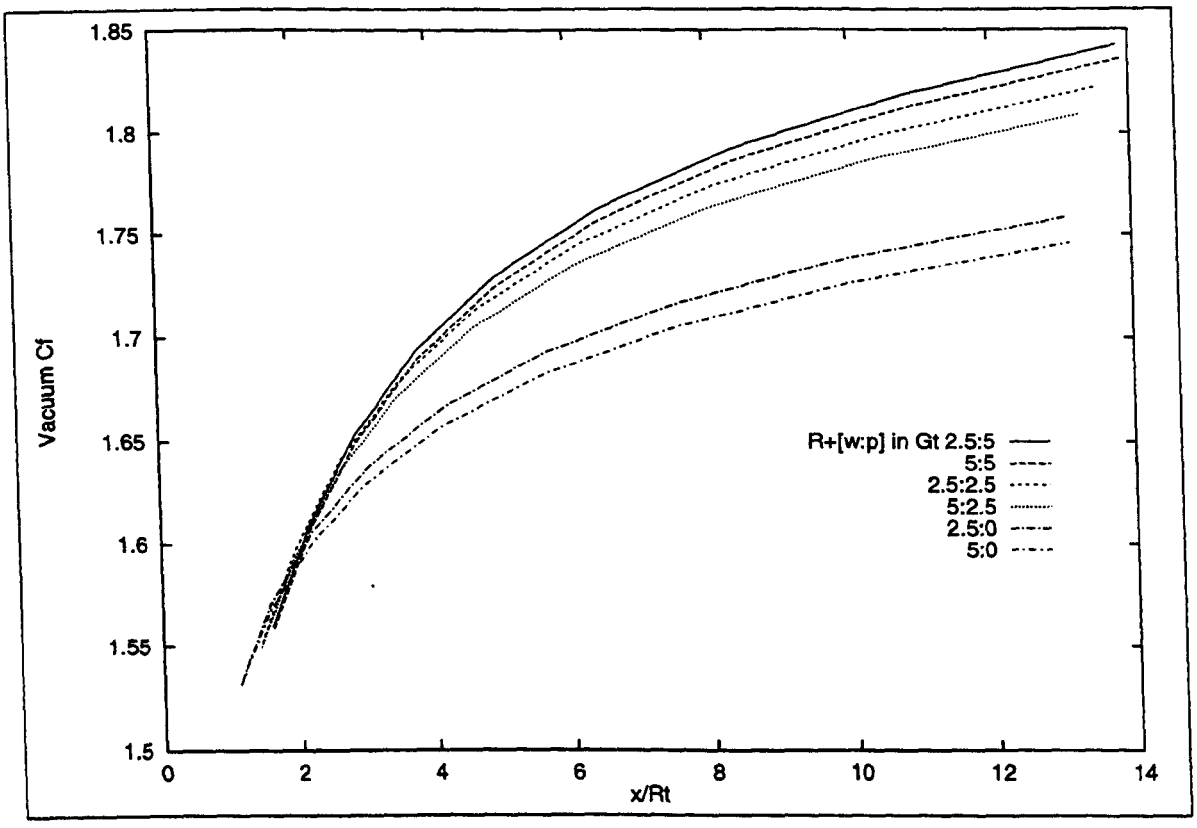

Figure 5.12: *Effect of R_w^+ and R_p^+ on C_F^∞, Axisymmetric ED Nozzles, $R_=^- = 5G_t$, $\theta_t = 30^0$*

the previous section, for it may clearly be seen that these are in opposition to the trends identified with respect to the range of physically allowable M_E created by the post throat curve combinations. In other words, if the post throat radii are varied to increase the performance

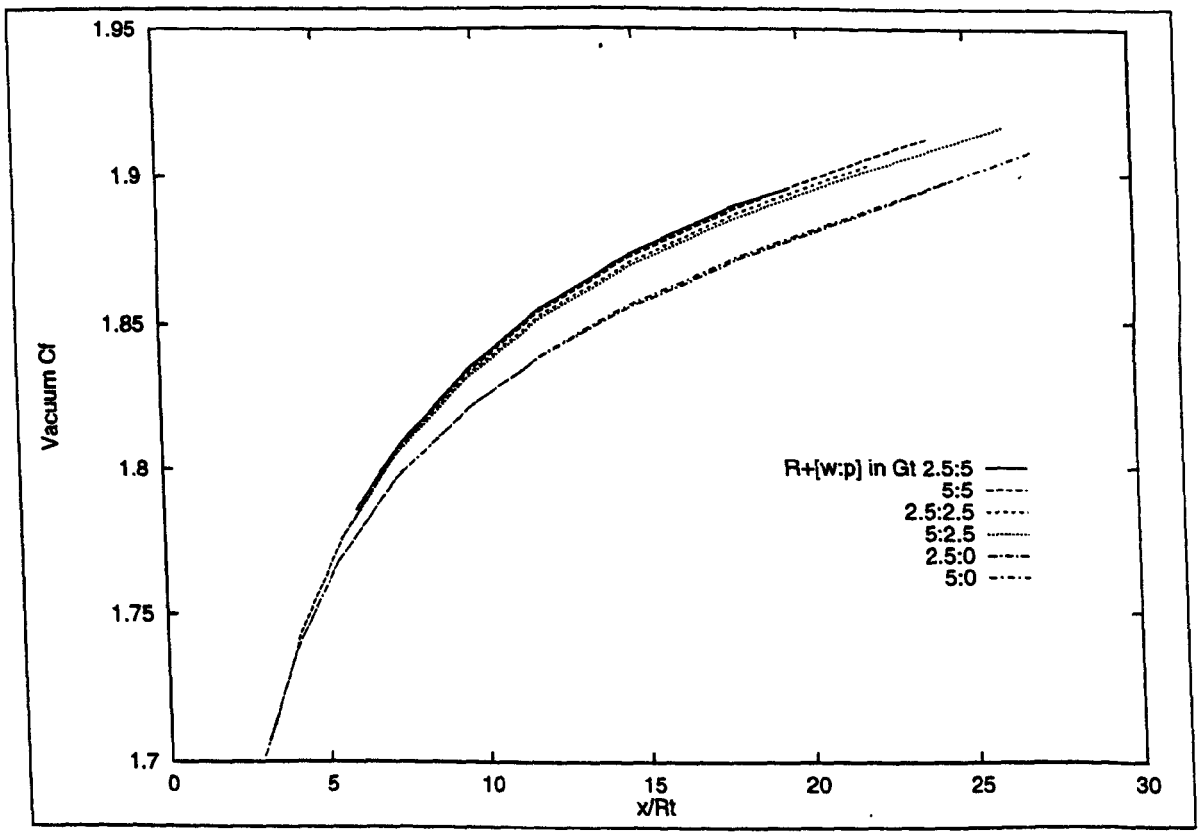

Figure 5.13: *Effect of R_w^+ and R_p^+ on C_F^∞, Axisymmetric ED Nozzles, $R_=^- = 5G_t$, $\theta_t = 60^0$*

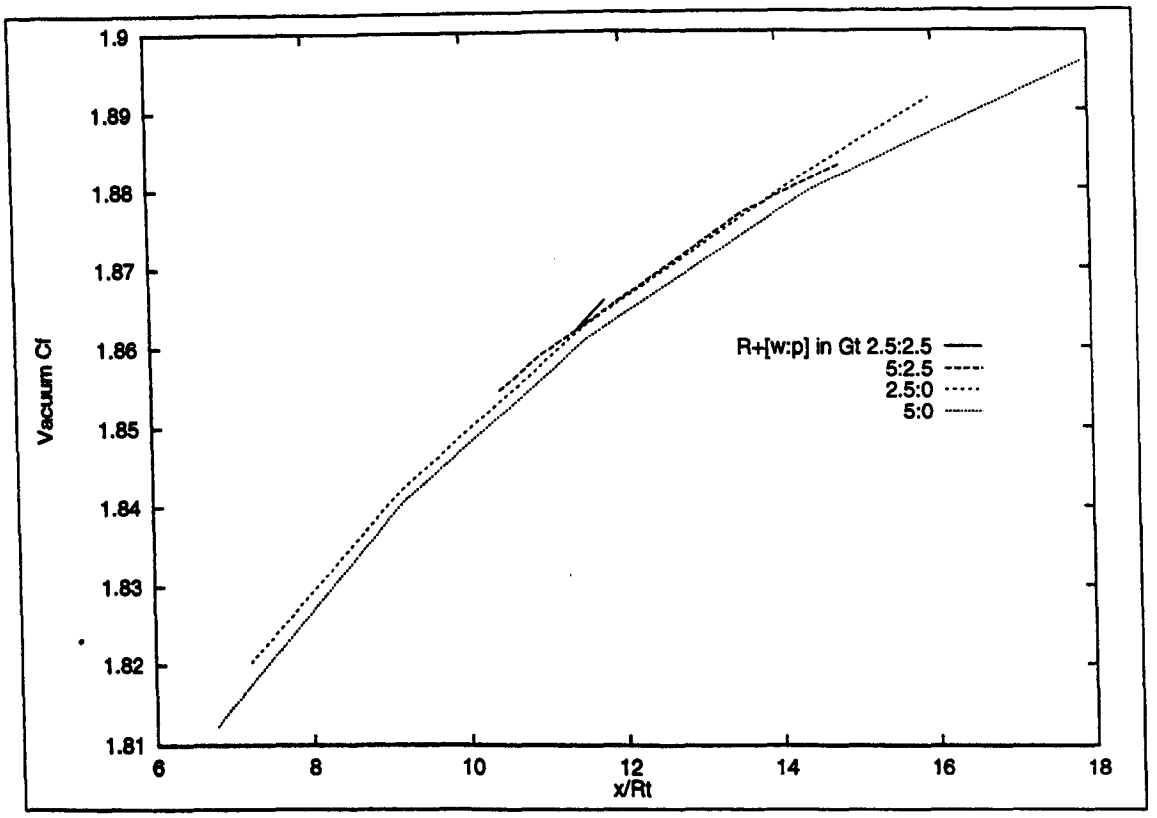

Figure 5.14: *Effect of R_w^+ and R_p^+ on C_F^∞, Axisymmetric ED Nozzles, $R_=^- = 5G_t$, $\theta_t = 90^0$*

in terms of thrust for a given length, the range of possible nozzle lengths reduce. This is even more clearly demonstrated in the results for the 90 degree throat presented in Fig. 5.14, where it may be seen that only a very small range of lengths have any possible contours, particularly if R_p^+ is increased (no results are presented for $R_p^+ = 5G_t$, as they do not exist).

Figs 5.15 and 5.16 show the effect of throat angle and post throat pintle radius on the respective base pressures and base area ratios of axisymmetric ED nozzles. As was found to be the case for planar nozzles, increased length reduces both base pressure and area ratio. However, whilst for planar nozzles, P_b was independent of θ_t, these results for axisymmetric nozzles do show a small dependence of P_b upon throat angle. This variation is minimal, and may in part be due to the different $R_=^-$ in terms of R_t units. It is therefore reasonable to conclude that the effect of throat angle is small.

The overall impact of the base pressure on total thrusts produced is negligible, except in the extreme (and unlikely) case of a very short nozzle with small throat angle (this again is similar to planar nozzle results). The accuracy of this statement is adequately demonstrated by Figs. 5.17 and 5.18. If anything, removing the effect of base pressure in vacuum conditions has even less of an effect than was the case for planar nozzles.

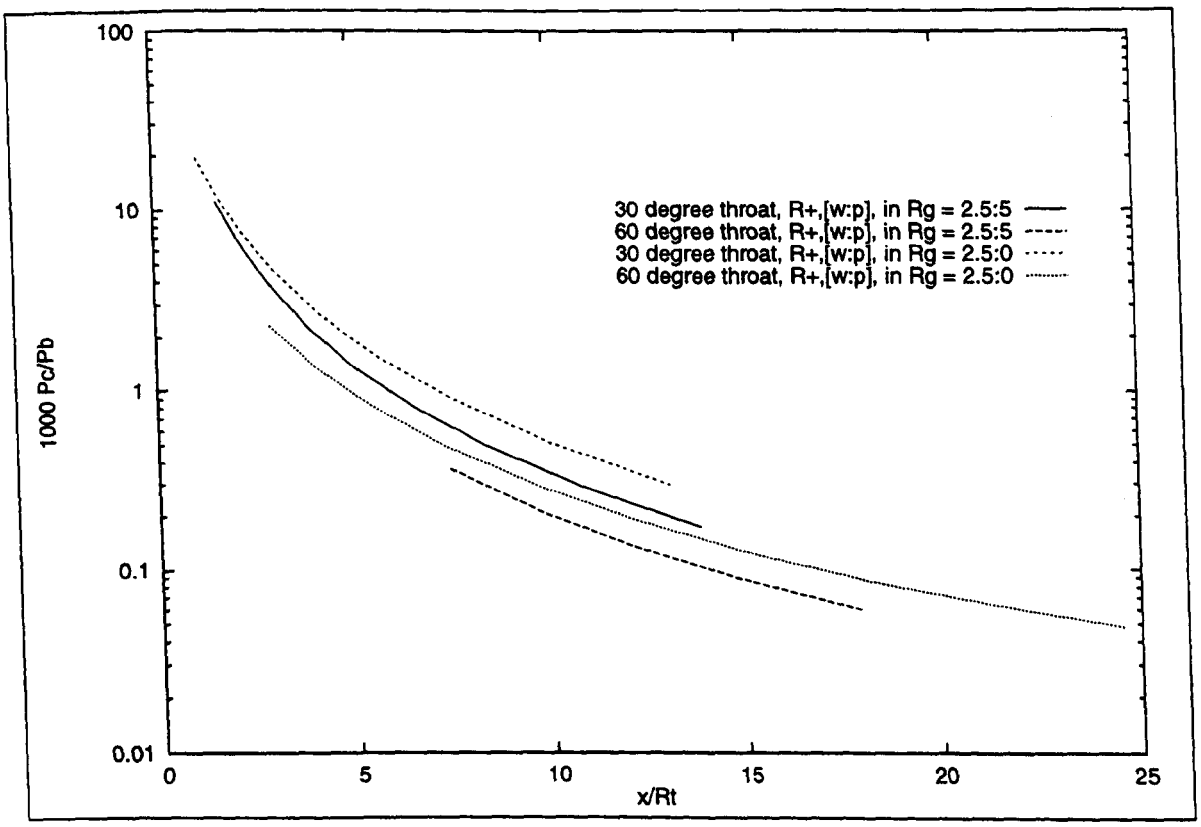

Figure 5.15: *Effect of θ_t and R_p^+ on P_b, Axisymmetric ED Nozzles, $R_w^+ = 2.5G_t$, $R_=^- = 5G_t$*

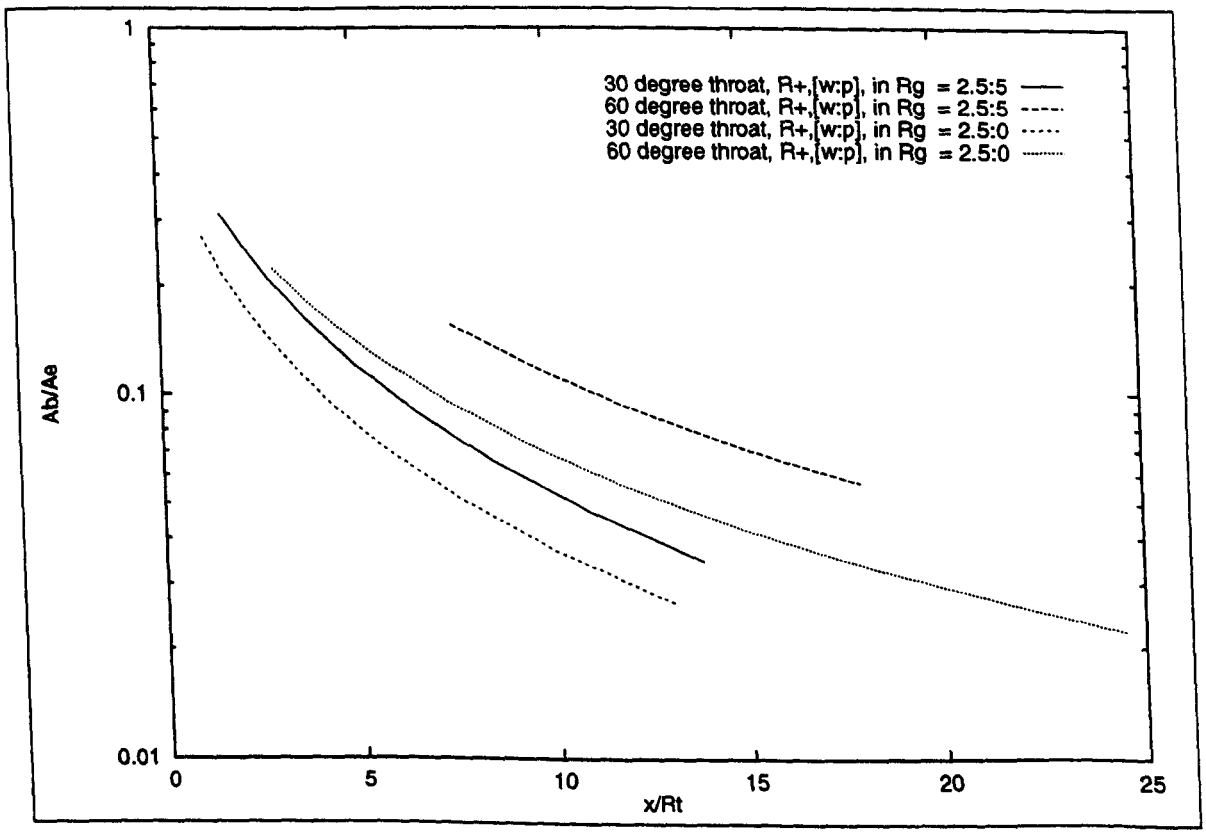

Figure 5.16: *Effect of θ_t and R_p^+ on A_b, Axisymmetric ED Nozzles, $R_w^+ = 2.5G_t$, $R_=^- = 5G_t$*

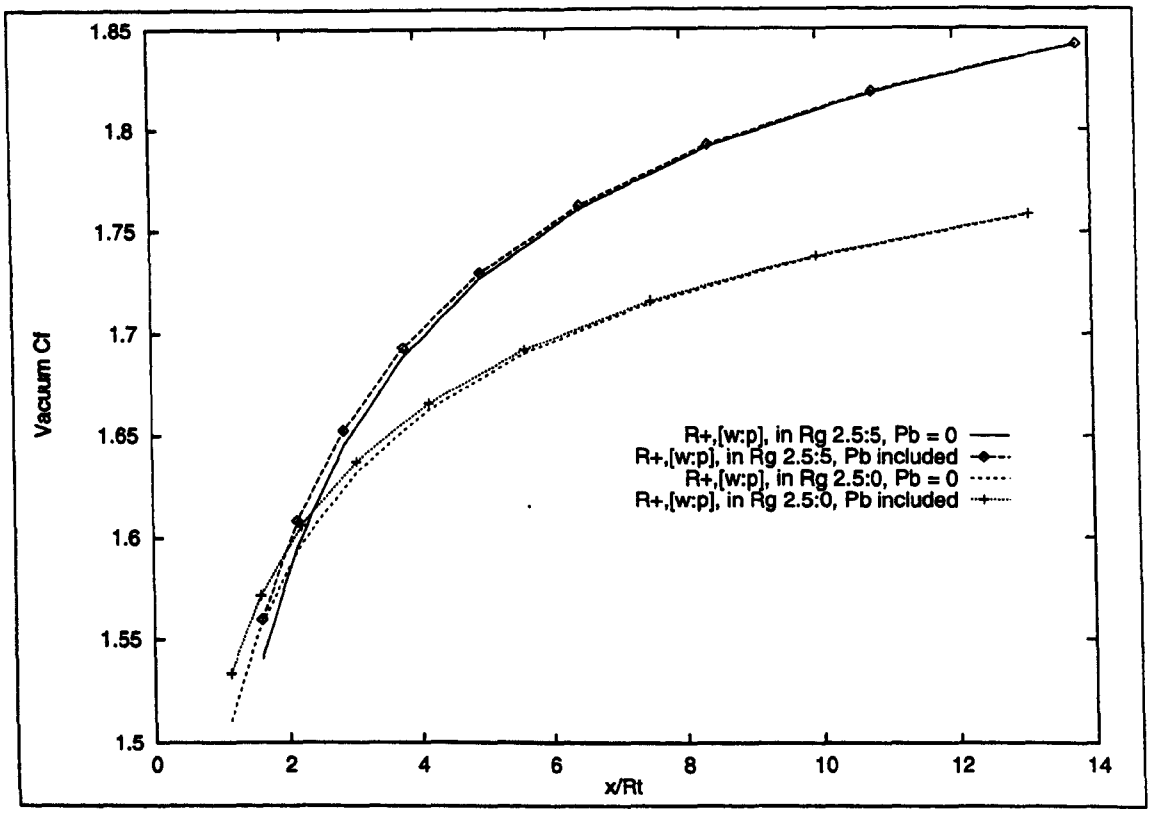

Figure 5.17: *Contribution of P_b to C_F^{∞}, Axisymmetric ED Nozzles, $\theta_t = 30$, $R_{=}^{-} = 5G_t$*

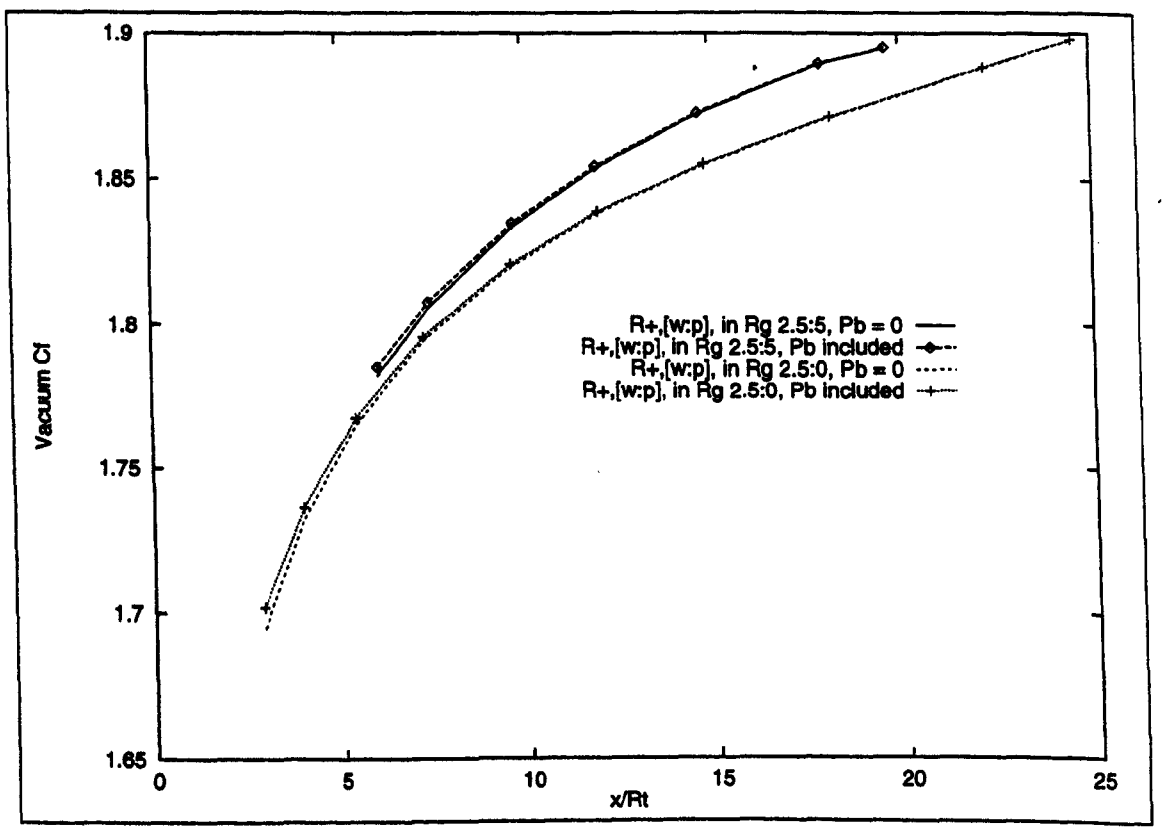

Figure 5.18: *Contribution of P_b to C_F^{∞}, Axisymmetric ED Nozzles, $\theta_t = 60$, $R_{=}^{-} = 5G_t$*

The Impact of Variations in y_d and $R_{=}^{-}$ on C_F^{∞}

It has already been demonstrated that y_d has a strong influence in axisymmetric nozzles on allowable M_E range. However, the impact of this variable on the relationship between C_F^{∞} and nozzle length has not yet been examined. This is achieved by comparing the results obtained from the 60 degree ED nozzle already discussed with those produced by a second 60 degree ED nozzle throat configuration, in all respects identical to the first except with a larger radial step ($y_d = 8G_t$, rather than $1.5G_t$). This raises the throat area from 40.6 to 77.5 G_t^2 respectively, and as a consequence reducing σ to 0.201.

Fig 5.19 presents an examination of the effect of R^+ on the relationship between C_F^{∞} and nozzle length for the second throat, and hence is directly comparable to Fig. 5.13. The trends produced by altering the post throat curves are clearly unchanged by this increase in radial distance, at least in a qualitative manner.

A more quantitative analysis of the effect of increasing y_d on thrust coefficient is provided in Fig. 5.20, where the thrust curves for the two throat configurations are shown side by side for a pair of R^+ combinations. Increasing y_d has already been shown to increase the allowable range of Mach numbers (and hence lengths) by the results provided in Table 5.1, and here the actual thrust produced for any specified length is also shown to be raised.

However, increasing y_d reduces the throat gap, increasing throat heat flux transfer problems. It also increases the average radial distance of the nozzle wall, which in turn increases

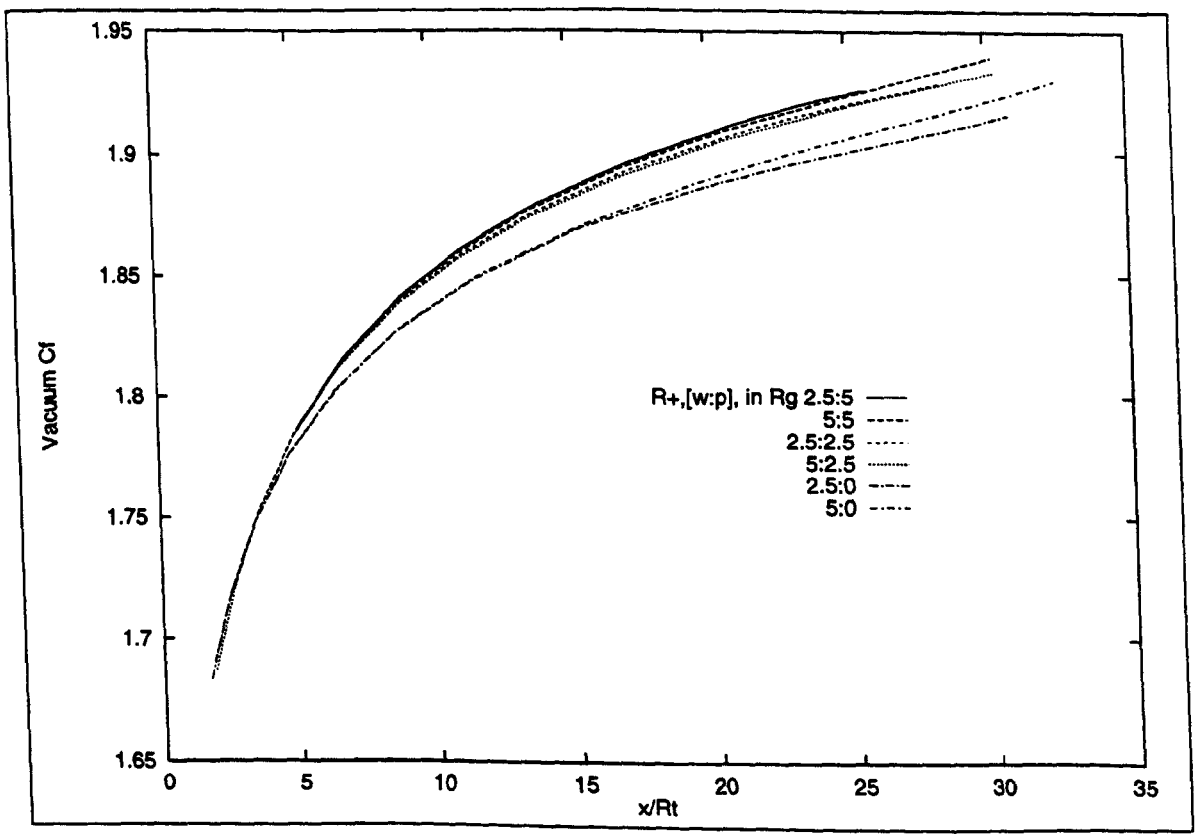

Figure 5.19: *Effect of R^+ on C_F^{∞}, Axisymmetric ED Nozzles, $R_{=}^{-} = 5G_t$, $\theta_t = 60^0$, $y_d = 8$*

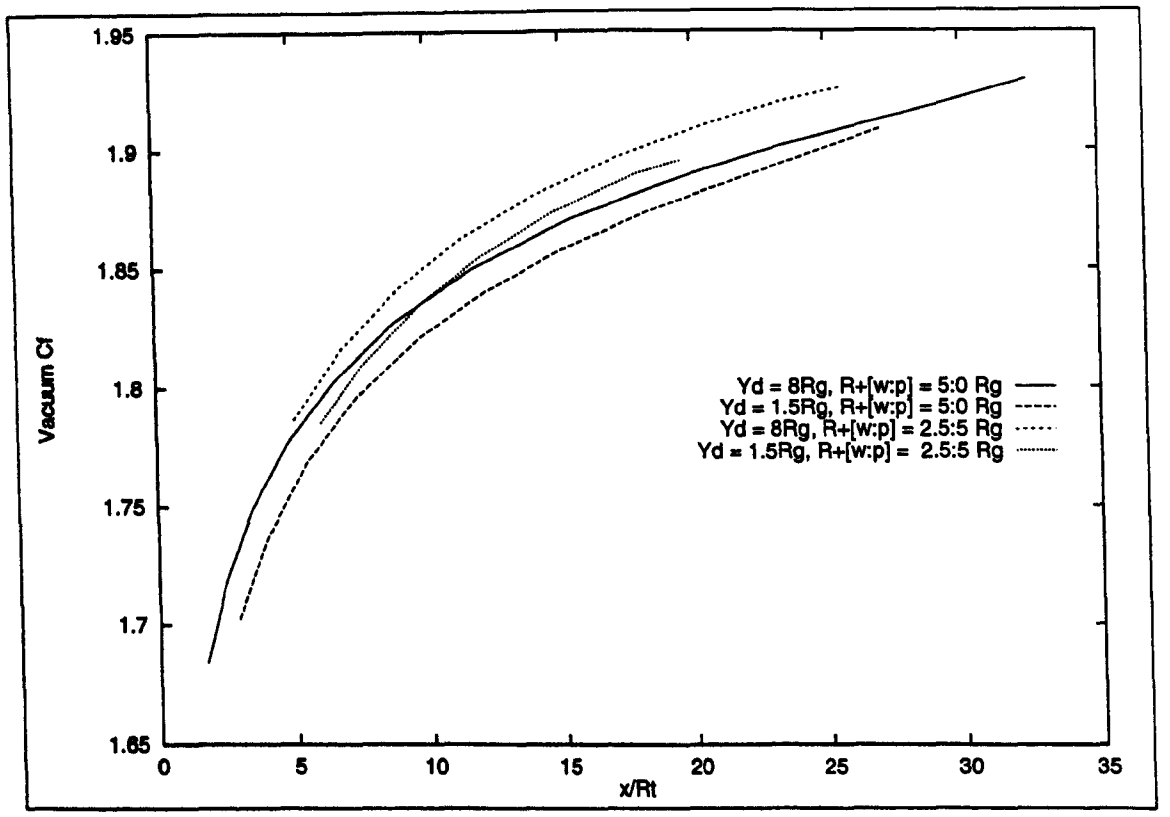

Figure 5.20: *Effect of y_d on C_F^∞, Axisymmetric ED Nozzles, $R_=^- = 5G_t, \theta_t = 60$*

the surface area produced by rotating the contour around the nozzle axis substantially. This has an impact on the usual assumption of approximately linear variation of mass with nozzle length implicit in the comparison between C_F^∞ and nozzle length. For these reasons, the advantage provided by increasing or decreasing y_d in terms of overall mass and costs is more difficult to assess than would be the case in a conventional nozzle. It is likely therefore that this variable would be increased as much as possible, until limited by either throat heat flux or total nozzle mass. Unfortunately, assessing both of these criteria is beyond the scope of the current project, and hence as yet no definitive statement may be made with respect to optimising this variable.

The influence of $R_=^-$ was also investigated using the 60 degree ED nozzle, as this throat angle appears to offer a good range of possible M_E combined with high C_F^∞. By setting y_d to 4.5 G_t, a 60 degree ED nozzle was obtained for $R_=^- = 10G_t$ which resulted in a throat area of 78.0 G_t^2. This is very nearly identical to the $y_d = 8G_t$ nozzle described above, and hence represents a doubling of the pre throat wall radii in both G_t and R_t coordinate systems.

The relation of C_F^∞ to length for these two nozzle throat configurations for a variety of R^+ values are shown in Fig. 5.21. For the $R_=^- = 10G_t$ configuration, the post throat variables are restricted to two combinations, an R_w^+ and R_p^+ of 5 and 10 G_t respectively, and secondly 5 and 0 G_t. The first of these represents the ratios of R^+ to $R_=^-$ found to generally produce maximum thrust, the later providing minimum thrust but greatest allowable M_E range. R^+ values for the $R_=^- = 5G_t$ nozzles are shown which correspond to these in ratios of R^+ to $R_=^-$,

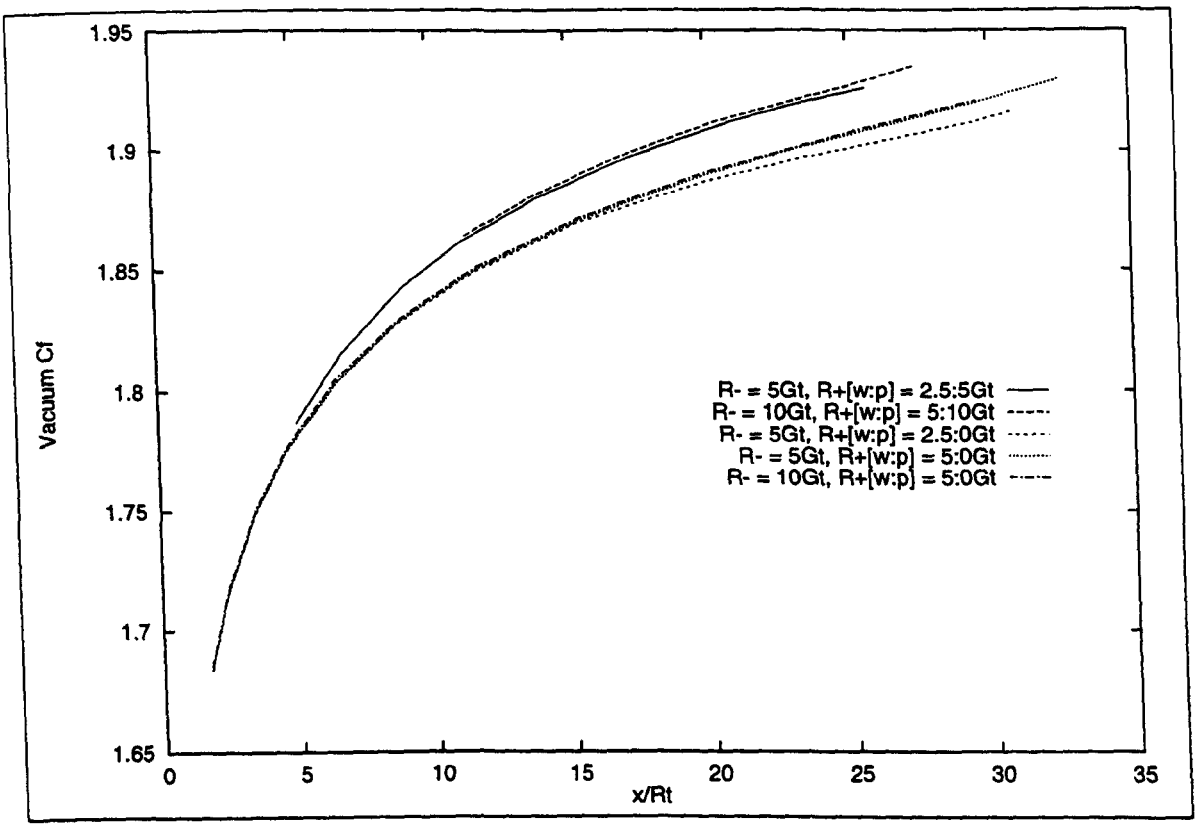

Figure 5.21: *Effect of* $R_{=}^{-}$ *on* C_F^{∞}, *Axisymmetric ED Nozzles,* $\theta_t = 60$

as well as a nozzle with $R_w^+, R_P^+ = 5 : 0G_t$ to allow comparison where the absolute value of the radii is preserved. It may be seen from this figure that the effect of doubling $R_{=}^{-}$ is minimal, especially if the absolute values of the post throat radii are preserved.

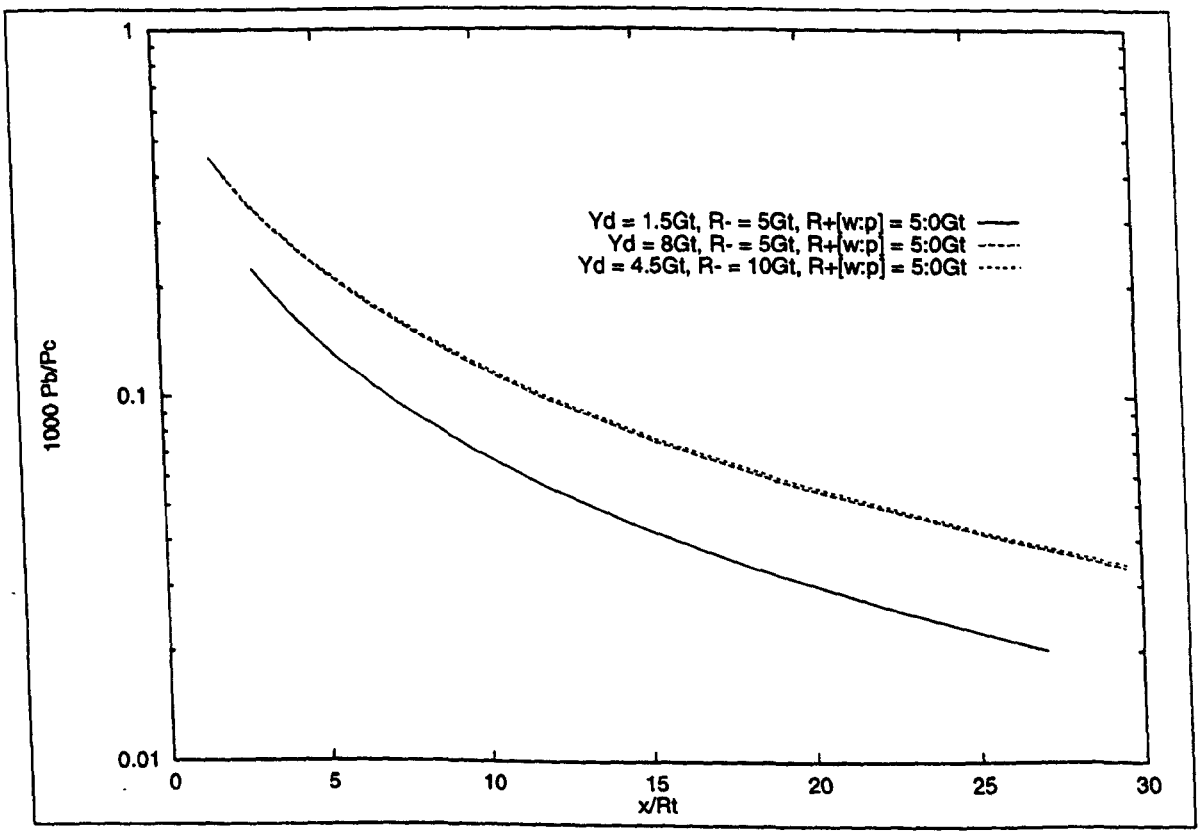

Figure 5.22: *Effect of* $R_{=}^{-}$ *on* $C_F^{\infty}, \theta_t = 60$

Finally, base pressures produced by all three 60 degree ED nozzle throat configurations discussed in this section (all with post throat radii of $R_w^+ = 5G_t$ and $R_p^+ = 0G_t$) are shown in Fig. 5.22. The results in this figure clearly show the independence of this variable from $R_=^-$, provided that the radial location of the throat is maintained in R_t units. However, increasing y_d increases the base pressure.

5.3 ED and Conventional Nozzle Vacuum Performance

The results thus far presented allow a comparison to be made between the ED nozzle and other conventional types with respect to vacuum performance.

5.3.1 Planar Nozzles

As the thrust for any given length ED nozzle will depend upon the throat angle, a generic variable throat angle ED nozzle may be created by selecting the maximum thrust coefficient produced by the throat angles studied for any given length. This gives a good approximation to the maximum thrust curve to that produced by an infinitely variable throat angle.

Fig. 5.23 presents the variation of C_F^∞ produced by this technique, both with and without the increment in thrust produced by the base pressure. The wall radii of curvature are $R_=^- = 2G_t$, and $R_w^+ = R_t$, $R_p^+ = 2R_t$, as the results described previously demonstrate this to be the optimum combination of those considered. Also shown on this figure are curves describing the variation of C_F^∞ with total nozzle length for the two conventional planar nozzle types examined in Ch. 3. The wall radii of the conventional nozzles are $3R_t$ for R_w^- and R_t for R_w^+, selected to be roughly equivalent to those utilised in the ED design.

The increment in thrust produced by the ED concept is obvious, and exists at all nozzle lengths. The increase in C_F^∞ over conventional length optimised nozzles is approximately constant for all nozzle lengths, being in the order of 0.04, or roughly 5 percent. This is an appreciable amount, and would no doubt increase slightly as methods by which the ED throat region may be optimised become better understood. Equally important is the fact that the increment in thrust is very nearly as large if the base pressure on the pintle is ignored, as this means that the accuracy of the current model used for prediction of this variable will have limited effect on the viability of the ED concept for high altitude applications.

Although the increase in C_F^∞ for a given length is significant, the reduction in length for a specified C_F^∞ is considerably larger, due to the oft noted low gradient of the thrust curve slope. By visual inspection alone, the reduction in length may be seen to be in the region of 25 percent. A more precise assessment is possible by determining the minimum length for

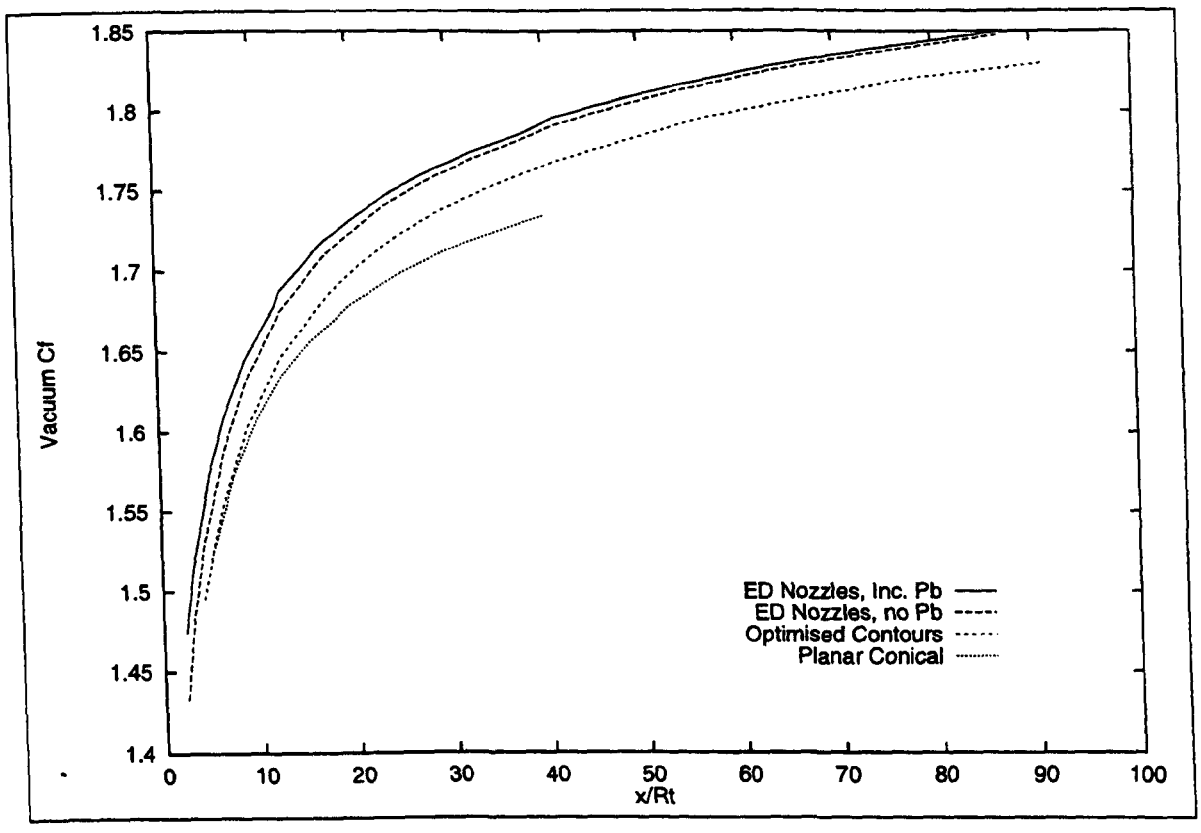

Figure 5.23: C_F^∞ *vs. Total Length, Planar ED, Bell and Conical Nozzles*

C_F^∞ of 1.7, allowing comparison with the results for conventional nozzle presented in Table 3.5.

This region of the thrust curve is produced from the 60 degree ED nozzle, and the length that gives a vacuum thrust coefficient of 1.7 for this throat configuration is 14.47 R_t, compared to 20.03 and 25.13 R_t for bell and wedge designs respectively. This provides a 28 and 42 percent reduction in length over each conventional type. Even if the base pressure is assumed zero, which in practise could never actually be the case, the reductions in length possible still amount to 20 and 37 percent reductions respectively. In other words, the length reduction achieved by replacing a planar length optimised nozzle with an ED is roughly the same as that created by replacing a planar conical with a length optimised design.

5.3.2 Axisymmetric Nozzles

The variation of C_F^∞ of various axisymmetric nozzle configurations are shown in Fig. 5.24, to provide a summary of the results in this section. The throat radii are chosen to offer the best performance out of the possible options considered. Generally, this results in small R_w^+ for both ED and conventional nozzles, combined with large R_p^+ for the ED type. However, as has already been noted, large values of θ_t will result in a very small range of M_E for such a combination. Therefore, the wall radii selected for the ED nozzles with 60 and 90 degree throats are in opposition to this, to increase the range of results presented. However,

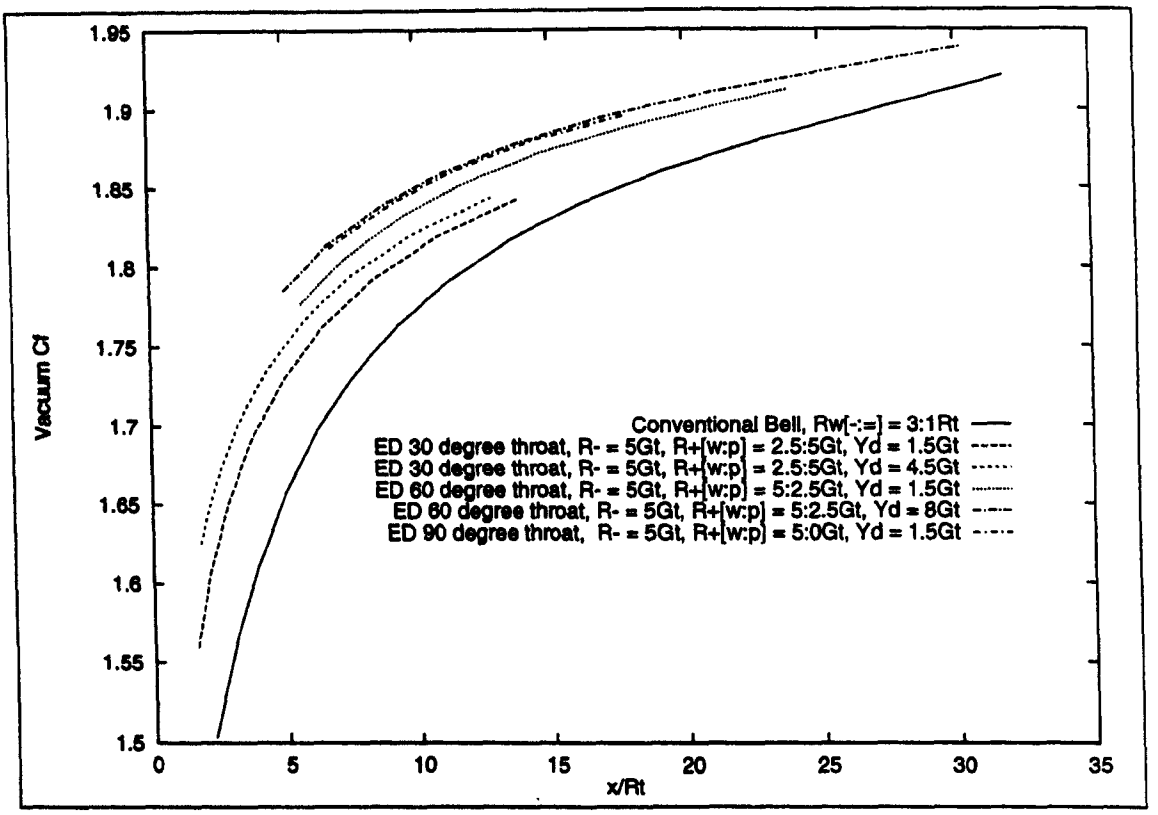

Figure 5.24: C_F^∞ *vs. Length, Various Nozzles*

as was noted earlier, as θ_t is increased the effect on the thrust curve of variations in wall radii reduces, and hence R_p^+ may be reduced without unduly compromising performance. The values of y_d are selected to examine the effect of this variable on the performance of the ED nozzles.

The results presented in this figure clearly demonstrate the opposing effects of increasing θ_t. Whilst the vacuum thrust is increased for a given nozzle length, the possible range of lengths the nozzle may take is restricted. This may be partly offset by an increase in y_d, increasing allowable range and C_F^∞.

The best performing of the nozzles presented is that of the 60 degree throat, with a radial grid step of $y_d = 8G_t$. This offers high thrust levels combined with a reasonable range of M_E. In general, a medium throat angle (such as 60 degrees) also maintains a reasonably sized minimum wall separation, although increasing y_d reduces this advantage.

No attempt has been made in this figure to present a composite curve representing an ED with an infinitely varying θ_t as was possible for the planar ED nozzle. This is because there is insufficient continuity between the various plots to allow a smooth curve to be derived, and hence little extra clarity would be gained by this approach. However, a length optimised bell nozzle thrust curve is shown, with $R_w^- = R_t, R_w^+ = 3R_t$. As may be seen, an ED nozzle which offers far greater performance than the conventional bell nozzle may be chosen for any given length. The increment in C_F^∞ is considerable, and appears to be more marked than was the case for planar flow types. This is in part explained by the decoupling of ϵ, the

expansion ratio of the nozzle, from the total nozzle length.

Whilst this reduces the meaningfulness of comparison between the nozzles, for completeness a length for the 60 degree, $y_d = 8G_t$ ED nozzle producing a C_F^∞ of 1.85 was calculated, to allow comparison with the conventional nozzle lengths presented for this vacuum thrust coefficients in Table 3.5. This nozzle produces a C_F^∞ of 1.85 if its length is 9.64 R_t. This compares to 17.34 and 23.18 R_t for bell and conical nozzles of the optimum throat wall radii combination considered in Table 3.5. This represents a reduction in length of 44 and 58 percent respectively. Although the contribution of base pressure is included, this has already been shown to have little impact.

Chapter 6

Altitude Performance Prediction for ED Nozzles

So far, only the performance of ED nozzles operating under vacuum conditions has been considered. Whilst it has been shown that this class offers potential advantages in terms of length reduction compared to conventional types, it has not yet been possible to assess the impact of the anticipated altitude compensating capabilities of the ED nozzle. To quantify the performance increment produced by this process it is necessary to be able to predict the flow-field and consequent forces produced at a variety of atmospheric pressures. To achieve this, it is in turn necessary to model the behaviour of the flow within an ED nozzle at all flight altitudes.

The prediction of the thrust produced by a conventional nozzle during atmospheric flight may be achieved by simple application of Eqn. 3.50, assuming that no separation of the flow from the nozzle walls occurs. For an ED nozzle however, the situation is more complex, due to the presence of the viscous region behind the pintle. Furthermore, three distinct modes of operation may be identified, these being open wake with altitude compensation, open wake but no altitude compensation, and the closed wake mode identified in the previous chapter. Each of these operating regimes present differing flow characteristics and hence require different approaches to the problem of thrust estimation.

As three possible operating modes exist within the nozzle, there lie between them two transitional flows. To ensure safe use of the ED nozzle type, it is necessary to be able to predict the range of chamber to ambient pressure ratios over which these transitions occur, and the likely effects they will have upon the thrust produced by the nozzle. This will allow the proportion of the flight envelope effected to be estimated, and give some insight into the likely effects on thrust and the structural integrity of the nozzle.

This chapter presents methods by which these operating modes and transitional regimes

may be analysed, allowing the complete atmospheric performance of an ED nozzle to be analysed (with some limitations, as will be discussed). The various operating regimes, and the transitions between them, will be considered in the order in which they occur during flight, i.e. from the relatively high ambient pressures associated with sea level performance to the transition to the vacuum flow performance analysed in the previous two chapters.

6.1 Open Wake, True Altitude Compensation

An ED nozzle altitude compensates by the interaction of pressure waves emanating from the internal free jet boundary with the nozzle wall. The pressure waves may travel in two different forms, these being compression waves and shock waves. Whilst the overall result - an increase in pressure at the nozzle wall - is similar, the details of the flow structures differ in some significant ways. Therefore, these two flow configurations are considered separately.

6.1.1 Shock-Free Compensation

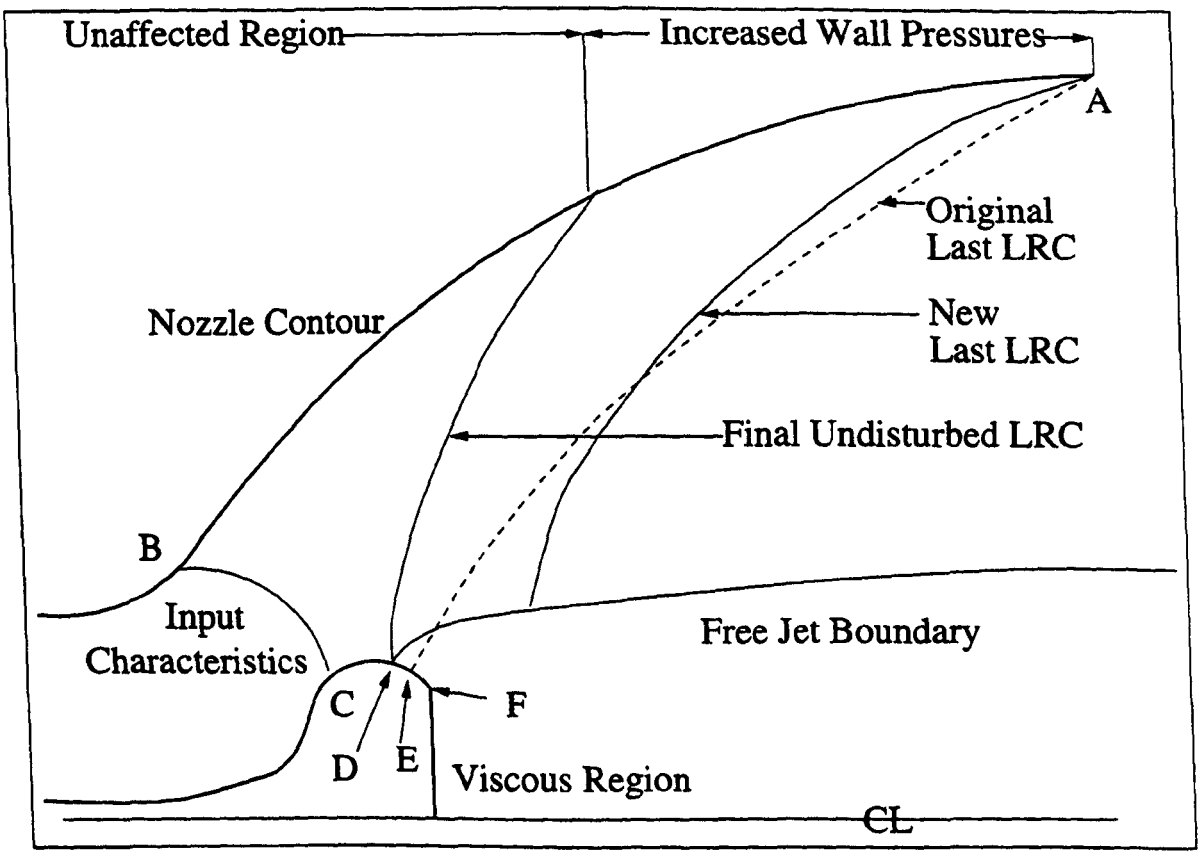

Figure 6.1: *ED Nozzle Flow Field, Low Altitude*

The general configuration of the flow-field within an ED nozzle operating at a low overall pressure ratio (P_c/P_a) is shown for a shock-free compensation in Fig. 6.1. The inflow boundary at the throat (BC) is provided by a pair of characteristics extracted from the CFD

analysis of the region, as was the case for the vacuum conditions addressed in the previous chapters. The flow expands around the pintle until it reaches D, at which point it separates from the pintle wall.

The free jet boundary reflects characteristics from the viscous interior as compression waves. When these waves intersect the nozzle wall, they increase the wall pressure relative to that which would otherwise occur, and hence increase the thrust generated by the nozzle. If the ambient pressure is sufficiently high, these compression waves reflected off the wall eventually intersect the free jet boundary once more. Here, they represent flow at a higher pressure than ambient, and hence generate expansion waves. These propagate back into the primary flow, and may reach the nozzle wall, reducing the pressure.

This process of compression and expansion continues the entire length of the nozzle, and produces the smoothly varying pressure profiles predicted by previous authors (e.g. Rao [6] and Schorr [24]), and typical of plug nozzle designs (as shown in Ref. 8). It should be remembered, however, that ED nozzles are normally designed with length optimised contours, whilst plug nozzles typically consist of truncated ideal contours. This results in the compression of the flow regimes within the ED nozzle, and hence increases the likelihood of shock wave formation within the type.

6.1.2 Shock-Induced Compensation

As the high pressure viscous region interacts with the inviscid flow by generating compression waves within the primary flow, the possibility of these gaining sufficient strength to coalesce into a shock wave must be considered. A shock wave is a discontinuity in the flow properties, and hence it may propagate through the flow-field at a steeper angle than the local characteristic angle (in fact it will always do so). This means that compensation through a shock wave may occur even if the flow separates from the pintle from a point beyond the origin of the last LRC in vacuum flow (as shown in Fig. 6.2.). Otherwise, the general configuration of the structures within the flow is similar to that described previously for shock-free compensation, with the shock wave substituted for compression waves.

There is no way of knowing in advance of flow-field calculation which form of compensation will occur, this being influenced by the nozzle contour design and overall pressure ratio. Therefore, when calculating the forces produced during open wake operation, the method used must allow for the formation of shock waves, even if in the final result they do not exist.

A flow containing shock waves may no longer be considered to be irrotational, and hence the irrotational MoC must be discarded and the rotational method introduced. In order for

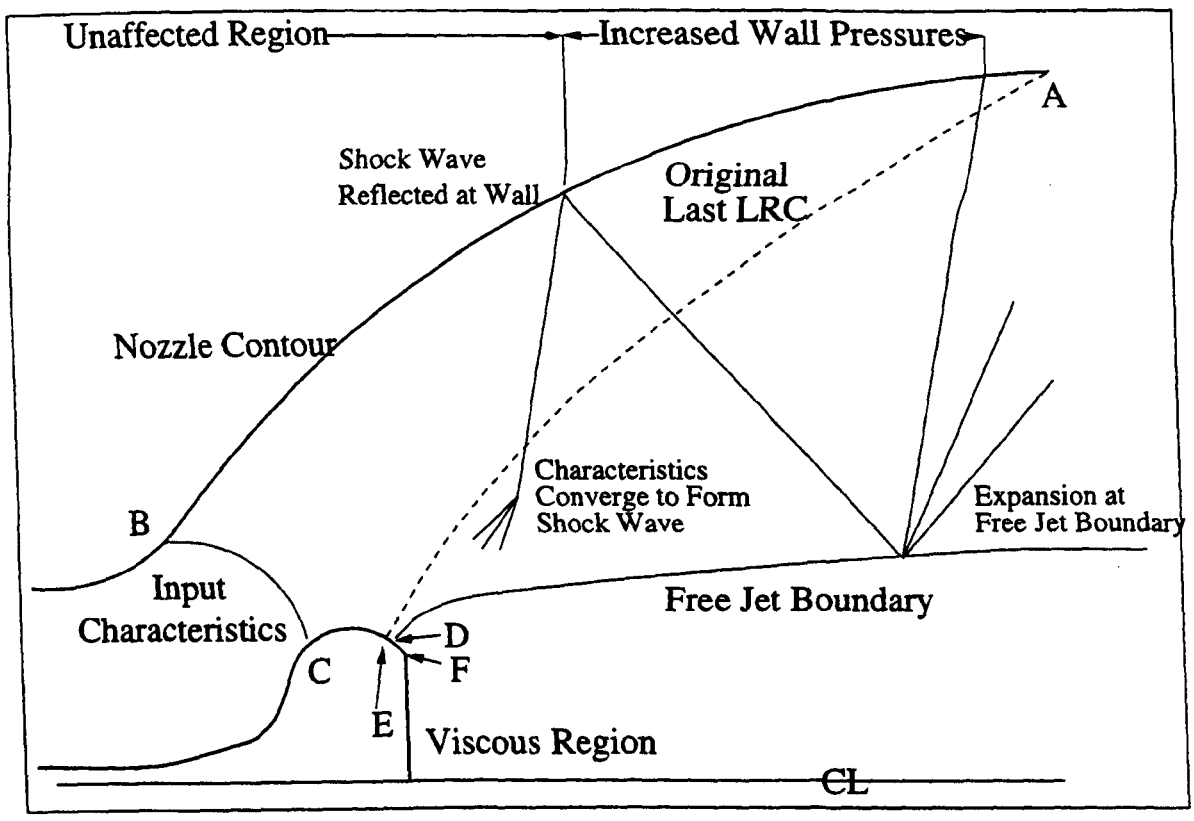

Figure 6.2: *ED Nozzle Flow Field, Low Altitude, Shock-Induced Compensation*

this method to be applied to the flow-field within the nozzle, an approximation of the pressure distribution along the free jet boundary must be made. Finally, the rotational method itself is not applicable through a shock wave, and hence appropriate equations to predict this flow phenomena must be included. These topics are now addressed.

6.1.3 The Rotational Method of Characteristics

The rotational MoC is less widely used than the irrotational form, and hence the derivation of the method is given for reference in App. C. However, the resulting equations are very similar to those for irrotational flow, and are summarised here. The characteristic directions are again

$$\frac{dy}{dx} = \tan(\theta \mp \mu) \tag{6.1}$$

and the flow variables ν, θ are given by

$$\nu_3 = F1 + F2 + F1i + F2i \tag{6.2}$$

$$\theta_3 = F1 - F2 + F1i - F2i \tag{6.3}$$

where $F1$ and $F2$ take the same definition as for irrotational conditions. The difference between the irrotational and rotational method is only revealed in the definitions of $F1i$ and

$F2i$, which are now given by

$$F1i_{Rot} = F1i_{Irrot} - \tilde{k}_{13}(\frac{\tilde{s_3}}{R} - \frac{\tilde{s_1}}{R}) \tag{6.4}$$

$$F2i_{Rot} = F2i_{Irrot} - \tilde{k}_{23}(\frac{\tilde{s_3}}{R} - \frac{\tilde{s_2}}{R}) \tag{6.5}$$

where 3 denominates a new calculation point joined by an RRC and an LRC to known points 1 and 2 respectively, and $\tilde{k}$ is the average of

$$k = \frac{\sin\mu\cos\mu}{\gamma} \tag{6.6}$$

between the respective points.

Calculation of the difference in specific entropies may be achieved from

$$\frac{1}{R}(\tilde{s_3} - \tilde{s_1}) = \frac{c_p}{R} ln[\frac{T_3}{T_1}] - ln[\frac{P_3}{P_1}] \tag{6.7}$$

Eqn. 6.7 requires two further variables, the local temperature and pressure, to be known. If the assumption of adiabatic flows is retained, local temperature may be calculated from the chamber value and local Mach number. However, the removal of the assumption of irrotational flow means that total pressure is not constant, and hence the pressures at all points within the flow must be stored, increasing the number of independent variables at each point from 4 to 5 (these being x, y, M, θ and now P).

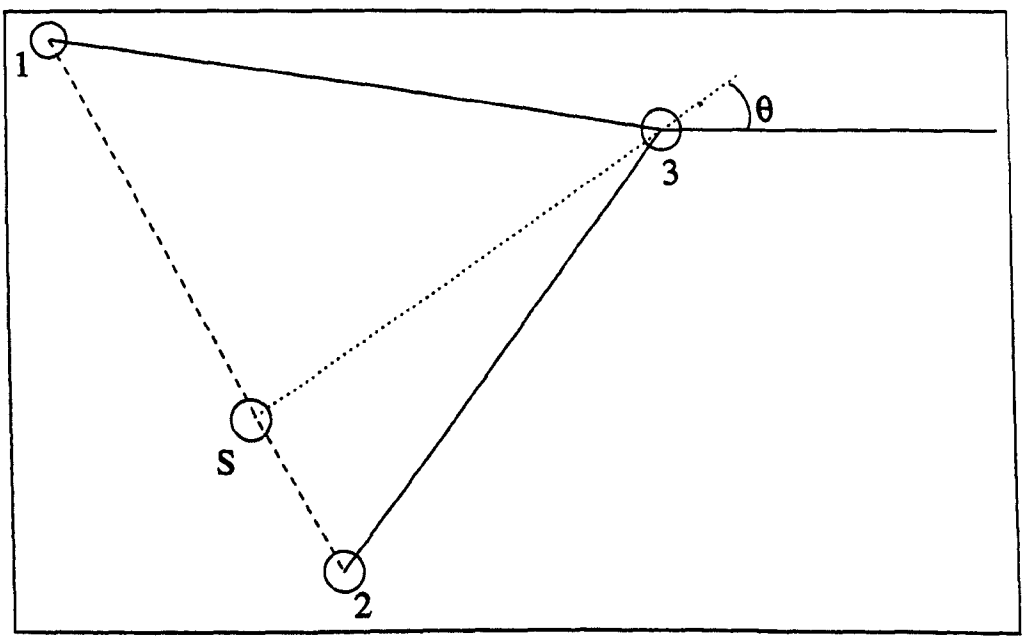

Figure 6.3: *Streamline and Characteristics, Rotational Flow*

The total pressure along a streamline may be assumed constant, provided that it does not pass through a shock wave. This allows calculation of the pressure at a new point (e.g. point 3 in Fig. 6.3) in the following manner. Assuming initial values of $F1i$ and $F2i$ of zero, the calculation method described in Ch. 3 may be used to produce an estimate for properties at point 3 assuming irrotational flow. The intersection of a line at the predicted flow angle

and the line joining the known points (1 and 2) may then be found, and thus the pressure and Mach number at this intersection point, S, interpolated. These values may then be substituted in the standard isentropic relationships, and P_3 calculated (using the estimated Mach number at 3). The solution process is iterative for both two-dimensional and axisymmetric flows, improved estimates for the flow quantities at point 3 being used to improve the estimate of $F1i$ and $F2i$ until convergence.

6.1.4 Free Pressure Boundary Estimation

In order to calculate the inviscid flow region within the nozzle, the location and pressure distribution of the free jet boundary must be known. This requires knowledge of the location of the point of separation of the flow from the pintle wall (D in Figs. 6.1 and 6.2), and an approximation of the pressure variation within the viscous region downstream of this point.

If the ambient pressure is below that associated with the flow at the sharp corner on the pintle (point F in Figs. 6.1 and 6.2), the sharp corner enforces separation, and points D and F are coincident. This removes the need to predict a pintle separation point and wall pressure distribution along the pintle, reducing the problem to that of estimating the base pressure and subsequent pressure distribution in the wake region.

Mueller and Sule present experimental evidence from Fig. 2 of Ref. 11 showing that for a plug nozzle with an open wake (a very similar flow-field to that within the open wake ED), the base pressure is very nearly equal to ambient (within 5 percent). This is confirmed by results for plug nozzles presented by Wasko in Fig. 8 of Ref. 12, although only a relatively small range of pressures which result in open wakes were considered here. In Ref. 29, Mueller *et al* claim that this behaviour is typical of all altitude compensating nozzles, and both Schorr [24] and Rao [6] claim initial experimental results from their respective programs suggesting that the base pressure behind an ED nozzle pintle is 'very nearly ambient'.

The experimental evidence presented by Mueller and Hall in Fig. 3 of Ref. 26 for a planar ED nozzle seems to show that the open wake base pressure is somewhat below ambient (about a third P_a). It is noted, however, that the wake of the nozzle in question closes at an extremely low overall pressure ratio, P_c/P_a being only about 2.2. As the flow will only turn supersonic for pressure ratios greater than about 1.9 (air being the working fluid), there is only a very small range of pressure ratios at which the open wake regime could exist, and hence these results may well be being influenced by the closure transition regime.

Whilst it may therefore be said that most authors appear to agree that the wake pressure near the base of the central body in altitude compensating nozzles is approximately ambient,

this view is challenged by Wasko in Ref. [12]. As was mentioned in the introductory chapter, this paper has been very influential, and hence a close examination of the issues raised is required. The base pressure for the ED nozzle tested are presented along side those for the plug nozzles already discussed, in Fig. 8 of that reference.

Although the open wake base pressure is shown to tend towards ambient, over the range of pressures examined it does not reach much above 0.6 of this pressure. It is also notable that the base pressure on the ED nozzle is lower than that of the plug nozzles tested at all pressure ratios. The argument employed by Wasko to explain the low base pressure is based on the assumption that the high velocity inviscid flow will act to aspirate the viscous region at low overall pressure ratios. As the ambient pressure decreases, and hence the volume of the inviscid flow increases, the recirculating flow-field becomes stronger, and decreases this aspiration. Whilst this explanation appears on the surface to be reasonable, there are a number of difficulties associated with it.

Primary among them is the lack of any evidence of a similar effect in available results for plug nozzles. The flow that develops behind the vertical face of a truncated plug nozzle before wake closure is almost identical to that behind the pintle of an ED in open wake mode. It too comprises a core of viscous flow surrounded by high velocity inviscid flow (in fact of even higher velocity, as the plug base occurs further downstream than an ED pintle). If the ejector action of this surrounding high velocity flow is the cause of the low base pressures, both plug and ED nozzles should be similarly effected. Mueller, however, has found experimentally that the effect for plug nozzles is not significant. Wasko's own results for plug nozzles do not extend very far into the open wake flow regime, but do tend to show the ratio between base pressure and atmospheric to be approximately equal to unity, if not slightly higher.

The ED nozzle tested by Wasko is of peculiar and unique design, as has been discussed in the introductory chapter. The phenomena of wake closure, and its effect on base pressure, is not referred to at any point, and its implications do not appear to have been considered. The pressure ratio at which Wasko identifies the strengthening of the recirculating region appears to more closely correspond to wake closure for the ED nozzle; for all higher pressure ratios the base pressure is approximately constant, a feature of closed-wake flow.

The extremely low throat angle (only 15 degrees) will lead to a relatively early wake closure (i.e. at a low overall pressure ratio), as will be shown in the following chapter. This low angle will also increase any ejector action the inviscid flow will produce, particularly at pressures near wake closure (this effect could be significant in certain conditions, as will be discussed in Sec. 6.3.2). The generally lower base pressures produced by the ED compared to plug nozzles may also be partly be explained by the peculiarities of the design. The nozzle has an internal expansion before the flow is expanded around the sharp corner of the pintle.

This will have the effect of increasing the onflow Mach number at separation, which in turn will reduce base pressure.

It is therefore argued that the low base pressures observed in the results of Wasko are actually related to the peculiarities of the design, and do not represent open wake operation of a typical ED nozzle. This being the case, it is assumed that there should be little difference between open wake base pressure for either plug or ED nozzles, and all other available experimental evidence for both types suggest this pressure is approximately atmospheric. Whilst this estimation is based on relatively limited amount of such data, and may in the future be revised with more experimental results, the present model therefore assumes a base pressure and subsequent free jet boundary at atmospheric pressure. It is accepted that this will inevitably result in an optimistic estimate for the thrust coefficient produced.

If the atmospheric pressure is sufficiently high that separation of the flow from the pintle wall ahead of the sharp corner occurs (only possible for nozzles where $R_p^+ \neq 0$), the pressure distribution in this region will become considerably more complex. It is highly probable that the flow will remain attached to the pintle wall for a range of pressures below atmospheric, as is generally the case for flow separations. The separation, when finally occurring, will be followed by a recompression region within the wake, returning the static pressure to near atmospheric.

By comparison with the wall pressures experienced within separated flows in conical nozzles (e.g. Ref. 7), it would be expected that recompression to a high percentage of atmospheric (approximately 90 percent or above) would occur in a short axial distance compared to the nozzle length. As this is the case, the detailed effects of the separation are ignored in the current analysis. Flow separation is assumed to occur at the wall pressure equal to atmospheric, and again the free jet boundary is assumed to be at atmospheric pressure.

This is a considerable simplification of the flow regime, but represents the best estimate possible, given the lack of any experimental data for this separation. The accurate theoretical prediction of flow separation from three dimensional curved walls is a complex process, and an area of active research. The current model of the open wake ED nozzle flow is insufficiently developed for the application of the time consuming techniques required for the solution of such flows to be warranted, although at a future date this may change as is discussed in the final chapter.

6.1.5 Open Wake Analysis Algorithm Initiation

As noted previously, whether the flow-field will contain a shock wave or not is unknown before the calculation process begins, and hence a single set of computational algorithms

is required that will compute the flow in either case. As the removal of the shock wave merely simplifies the process, the algorithms are constructed (and explained here) assuming the presence of a shock wave. The overview of the flow-field to be described has already been given in Fig. 6.2. This section begins the description of the flow calculation process in more detail.

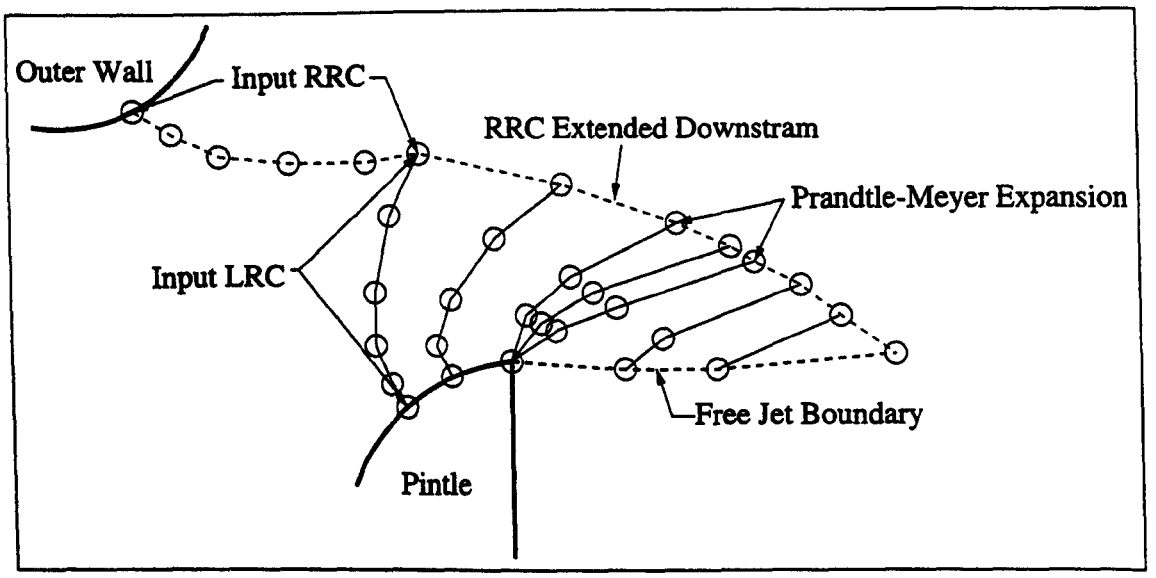

Figure 6.4: *Open Wake Kernel Calculation*

The open wake flow-field calculation takes as input the two characteristics derived from the CFD results for the throat flow. For reasons explained in the next section, it is preferable if the calculation follows consecutive RRC's from the nozzle wall to free jet boundary. Therefore, the input RRC is first extended to the free jet boundary in the following manner, shown graphically in Fig. 6.4.

The flow is expanded around the pintle wall from the input LRC. The last point in each LRC calculation is added to the input RRC, increasing its length. This continues until either a wall pressure equal to atmospheric is located, or the expansion reaches the sharp corner. If the latter, a Prandtle-Meyer expansion centred on this corner is calculated, until atmospheric pressure is reached. The LRC expansion continues, making use of the fact that ν is constant along the constant pressure boundary to provide enough equations to solve the characteristics. However, at each boundary point, the resulting LRC looses a point from its length, and eventually disappears. This results in the first RRC in the nozzle flow-field extending from the outer wall - geometric throat intersection to the free pressure boundary, as required.

6.1.6 Shock Waves

Compression waves within a flow-field cause characteristic waves of a family to converge. At the point where convergence is sufficiently strong that the characteristics cross, a shock wave forms. This process is shown graphically in Fig. 6.5, which shows the convergence of

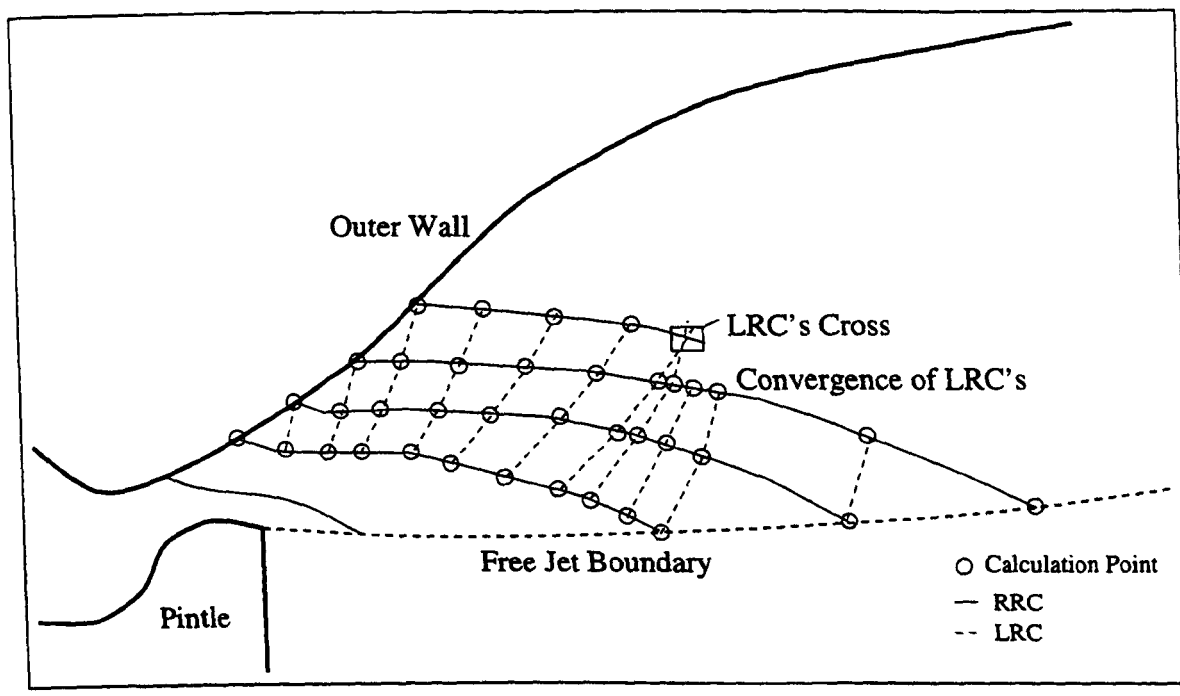

Figure 6.5: *Shock Wave Location*

LRC's within the ED nozzle flow-field. This is the most likely method of shock formation in an ED nozzle (see for instance the flows presented in Ref. 29 where complete analysis of closed wake ED nozzle flow-fields is attempted). It is generally easier to locate and track shock waves formed by the opposite family of those along which the characteristic calculation proceeds, and this is the reason behind the previously noted selection of RRC tracking.

As has already been noted, the MoC is invalid through a shock wave. Fortunately, standard shock relations may be incorporated within the calculation algorithms, allowing a flow with an embedded shock wave to be modelled via the processes which follow.

Location of the First Point

Fig. 6.6 shows a more detailed view of the shock formation region shown in Fig. 6.5. Calculation of RRC's in the nozzle continues until two LRC's cross (this may be identified as $x_{i,j'+1}$ will be less than $x_{i,j'}$). The shock wave will be weak in the initial region, and this allows a simplified version of the actual situation to be applied. For this first shock point, the LRC joining points i-1,j+1 and i,j'+1, and the initial shock wave section are assumed to be coincident. Therefore the intersection of this LRC and the RRC between i,j-1 and i,j' is assumed to be the first shock point, and a double point is formed. The first represents the flow just before passing through the shock wave (labelled i,j in the RHS of Fig. 6.5), and another coincident point, representing the flow just behind it i,j+1.

Linear interpolation of flow properties between i,j-1 and i,j' allows the Mach number, pressure, and flow direction just upstream of the shock wave to be estimated. A further

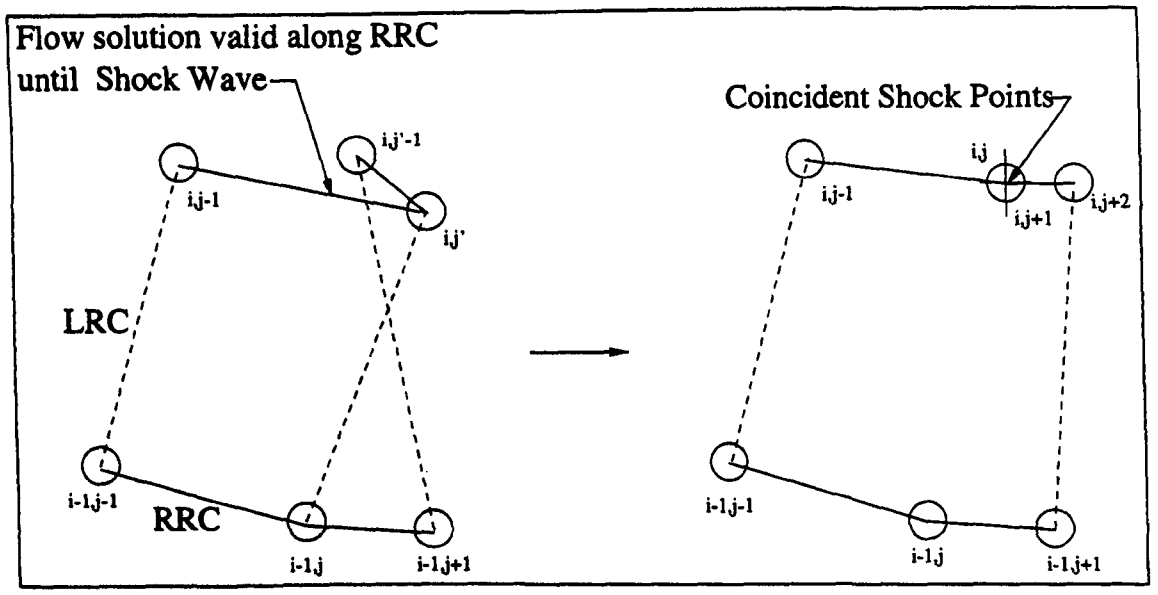

Figure 6.6: *Shock Wave Formation*

linear interpolation of the LRC flow properties between i-1,j+1 and i-1,j'+1 allows the flow direction behind the shock wave to be estimated, and this in turn produces the shock angle, δ, from

$$\delta = \theta_{i,j+1} - \theta_{i,j} \tag{6.8}$$

As δ and the onflow Mach number and angle are known, the standard shock relation

$$\tan\delta = 2\cot\beta\left[\frac{M_{i,j}^2 sin^2\beta - 1}{M_{i,j}^2(\gamma + \cos 2\beta) + 2}\right] \tag{6.9}$$

may be used to find the shock angle β via an iterative calculation. Once this is achieved, the properties on the far side of the shock wave follow from

$$M_{i,j+1} = \frac{1}{sin(\beta - \delta)}\sqrt{\frac{M_{i,j}^2 sin^2\beta + \frac{2}{\gamma-1}}{\frac{2\gamma}{\gamma-1}(M_{i,j}^2 sin^2\beta - 1)}} \tag{6.10}$$

and

$$P_{i,j+1} = P_{i,j}(1 + \frac{2\gamma}{\gamma+1}(M_{i,j}^2 sin^2\beta - 1)) \tag{6.11}$$

From these results it is then possible to continue the standard MoC algorithms downstream from point i,j+1 along the RRC to the constant pressure boundary in the usual manner. These shock relations are valid in both two-dimensional and axisymmetric flows.

Further Points

The method used to define the initial shock wave point in the ED nozzle flow-field results in the collocation in xy space of two points, one representing the flow immediately before

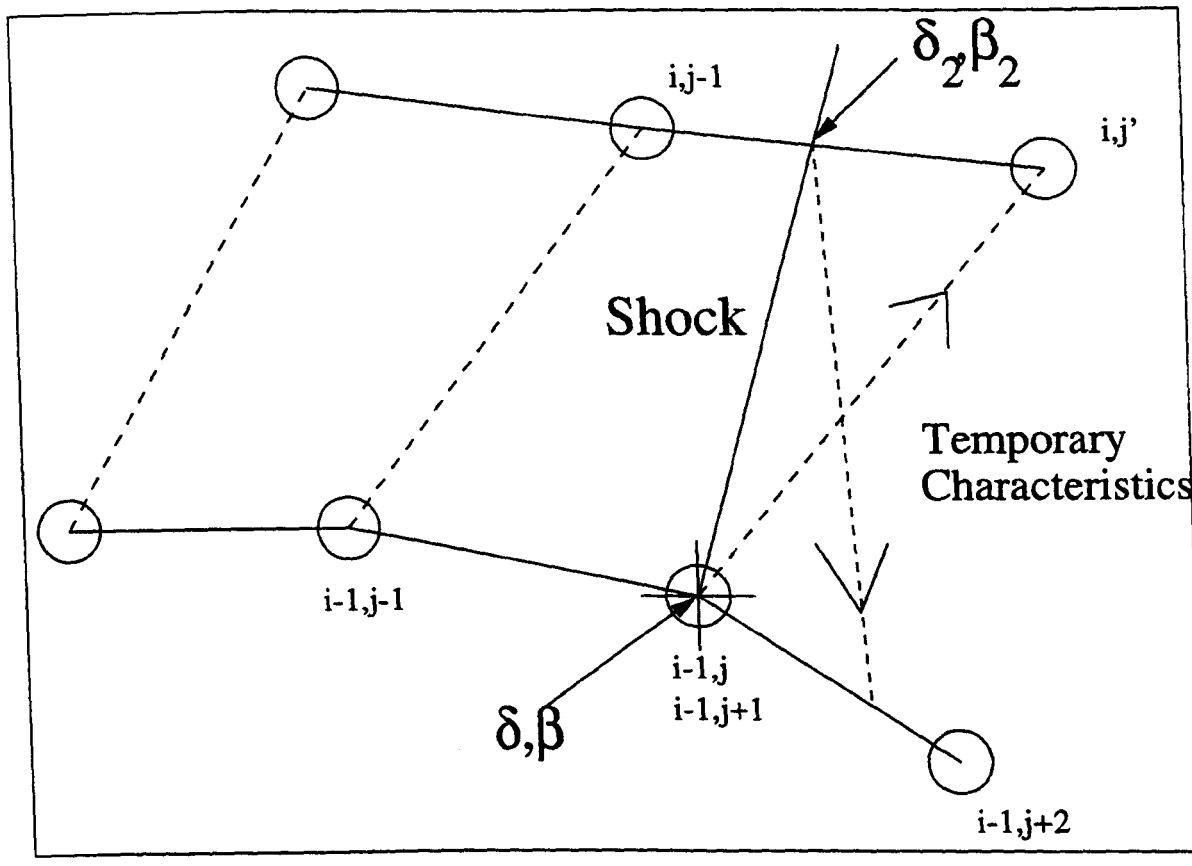

Figure 6.7: *Shock Wave Continuation*

the shock wave, and one immediately after. This fact is used in the generation of subsequent RRC's to locate the shock wave. Once two points with the same x coordinate are found, the standard MoC algorithm terminates, and a shock wave algorithm is initiated. Fig. 6.7 shows a graphical representation of the process.

A temporary point, i,j', is generated by finding the intersection of the RRC from (i,j-1) and the LRC from the coincident shock wave point containing the upstream, pre shock conditions (point i-1,j). The intersection of the shock wave and the RRC is then calculated from the flow angle at i-1,j, and the shock angle at this point, β. Once this location has been found, interpolation may be used to find the upstream properties, and the equations in the previous section used to find the flow properties immediately behind the shock wave.

The above process assumes that the shock wave maintains constant strength. As this is unlikely to be the case, an inverse LRC is produced from the flow properties just the other side of the proposed location of the shock wave, back to the (known) RRC i-1. Linear interpolation between points (i-1,j+1) and (i-1,j+2) is then used to determine if the postulated shock wave is compatible with the flow. If this is not the case, the value of δ_2 associated with the new point is incremented, resulting in new values of the shock angle β_2, and hence a change in the location of shock - RRC intersection. This of cause necessitates the recalculation of all other flow variables. This process continues until the flow properties interpolated along RRC i-1 are compatible with those previously calculated, at which time a double point is formed on RRC i, again representing flow in just in front and behind the shock wave. The

RRC is then completed to the constant pressure boundary, and the process repeats.

Shock Reflection from the Nozzle Wall

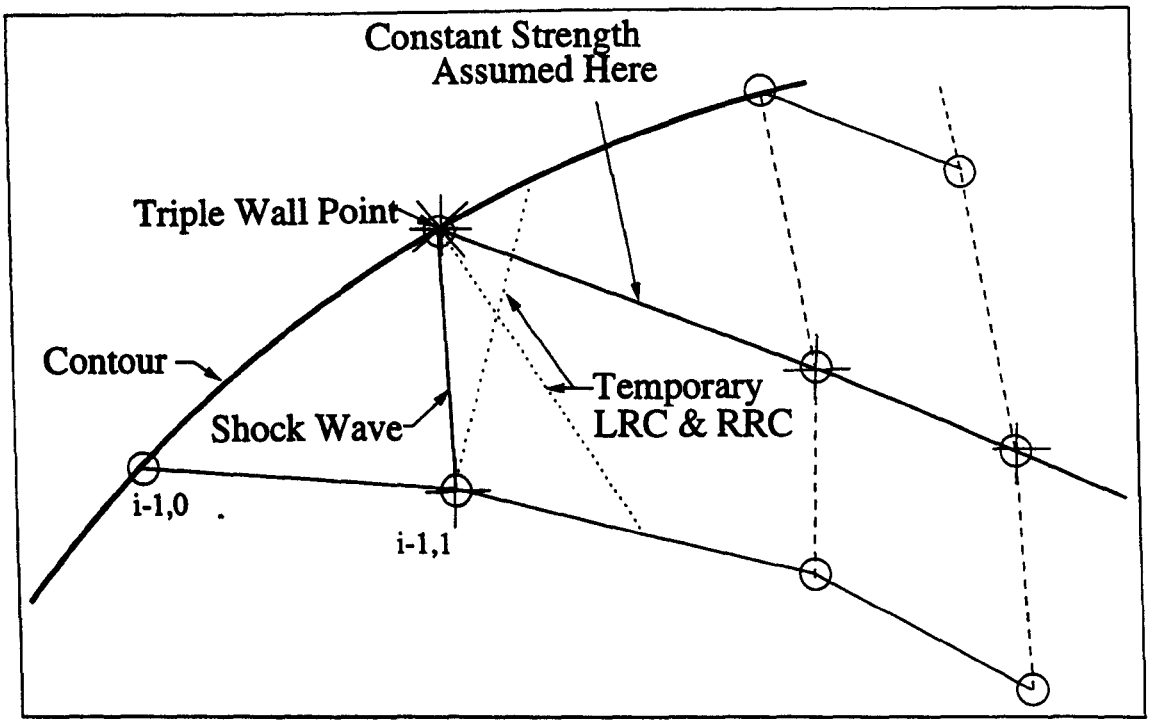

Figure 6.8: *Shock Wave Reflection*

As the shock wave is formed from the coalescence of LRC's, it lies above the local flow direction, and hence will propagate radially, towards the nozzle wall. If the ambient pressure is high enough, or the nozzle long enough, this shock wave will at some point reach the outer contour. A generalised diagram of the situation is shown in Fig. 6.8. The location of the triple shock point on the wall is found by calculating the point of intersection of the shock wave with the wall. Properties immediately upstream of this point (stored in the first of the three coincident points) are calculated by interpolation between the pre-existing wall point (i-1,0), and a temporary point created by an LRC from (i-1,1) intersecting the wall. The methods described in the previous subsection may then be used iteratively until a shock deflection that satisfies the shock relations and the temporary characteristic connecting the immediate downstream flow and the previous RRC. The properties immediately downstream of the shock wave are stored at the second point.

This results in a flow angle at this second point which is not parallel to the wall. This physical impossibility is removed by the construction of a second shock wave, of opposite deflection (i.e. the shock wave reflects off the wall). As all the properties of the flow are known at the second shock point, the third shock point is created using the same equations for flow through a shock wave, with the condition that the resulting flow direction must be parallel to the wall. This completes the definition of the triple point.

To continue calculation of the shock wave downstream, it is simplest if the program now switches to generation of successive LRC's. The first point of each are consecutive downstream points on the final RRC (i-1), and the last the intersection of the characteristic and the wall. This allows the shock wave to be calculated using the same methods previously described, but with LRC's substituted for RRC's, and vice-versa. One simplification is needed; there is insufficient data for the usual iterative procedure to be used to adjust the strength of the shock wave at the first double shock point after the reflection. The shock wave is therefore of necessity assumed to be of constant strength in this region. After this, the usual procedure may be resumed.

There is one further difficulty. As the shock wave is now of the RRC family, it will steepen, and penetrate the upstream region. It is possible that this will cause it to cross the RRC labelled i-1 in Fig. 6.8. If this is found to be the case, the RRC i-1 is discarded from this cross over point onwards, and the next oldest RRC (i.e. i-2) is used to produce the first point of subsequent LRC's. If the shock wave crosses this RRC, the next oldest is retrieved from storage, and so on. This of course requires storage of a number of RRC's as they are generated. This number is presently 4, although this could easily be increased. It should be noted that this process has no effect on wall pressures, as the results contained in the discarded sections of RRC are always downstream of the wall points already calculated.

This process continues until the shock wave reaches the free jet boundary. At this point, a Prandtle-Meyer expansion fan returns the post shock pressure to ambient. The last LRC in this fan is then emptied out against the constant pressure boundary, resulting in a new RRC from nozzle wall to free jet boundary in similar manner to that described for the first in Sec. 6.1.5. The whole process then repeats. If at any time the wall point associated with any RRC or LRC lies beyond the nozzle exit, the flow calculation ends and the flow properties at the exit plane are calculated by interpolation. If there is no shock wave within the nozzle (i.e. shock-free compensation), this condition will be reached before the location of the first shock point, and the entire shock wave calculation routine may simply be bypassed

6.1.7 Problems with Shock Wave Reflection

There are two primary areas of concern with the method for open wake flow calculation described in this chapter; the uncertain nature of the free jet boundary pressure distribution, and the accuracy of the shock wave reflection routine. The first of these has already been discussed. With regard to the second, whilst the method described reasonably accurately describes the behaviour of an inviscid flow, the reflection of shock waves from a solid surface in a real flow is heavily influenced by viscous effects. Rather than a neat reflection of the shock wave as described, due to the influence of the boundary layer and the impossibility

of flow angles at the wall which are not parallel to it, the actual flow will form a structure known as a λ-shock. This represents a more complex flow formation than allowed for in the current model.

Further to this, the impingement of a shock wave on the nozzle wall (or indeed any abrupt compression along the nozzle wall) may well lead to separation of the boundary layer. If the flow is sufficiently energetic, or the expansion emanating from the free jet boundary provides a sufficiently favourable pressure gradient, the flow may at some downstream point re-attach. This leads to the possibility of entrapped separation bubbles along the nozzle contour, leading to bursting of these bubbles with changing overall pressure ratios. The consequences of such behaviour are at present unknown.

The interaction of the shock wave with the wall may also cause local heating, leading to the possibility of holes being burned in the nozzle skin. However, as the transit through the atmosphere is fairly rapid, the location of the shock wave is unlikely to remain at the same point for sufficient time for this to be a problem. The exception to this is a static test facility, which would be likely to be fed from an approximately constant chamber pressure, resulting in a static shock location.

An alternative method for thrust coefficient prediction may be used if the shock wave is assumed to trip the boundary layer, separating the flow. The pressure distribution along the remainder of the nozzle wall may then be assumed to be atmospheric. Some altitude compensation will still occur, as the point of shock wave interaction gradually reduces the length and hence area ratio of the nozzle as overall pressure ratio drops and the shock wave moves upstream. As the pressure acting immediately behind the shock wave will be generally greater than atmospheric (this is demonstrated in the following chapter), this produces a pessimistic estimate of nozzle thrust.

6.1.8 Thrust Calculation

Calculation of the thrust produced in this mode of operation involves the integration of wall pressures on both the outer contour and pintle walls (only to the point of shock wave interaction if the enforced separation model is used), combined with the sum of the momentum flux and pressure forces across the input characteristics at the throat. The base pressure on the pintle is assumed atmospheric, and hence has no contribution to thrust.

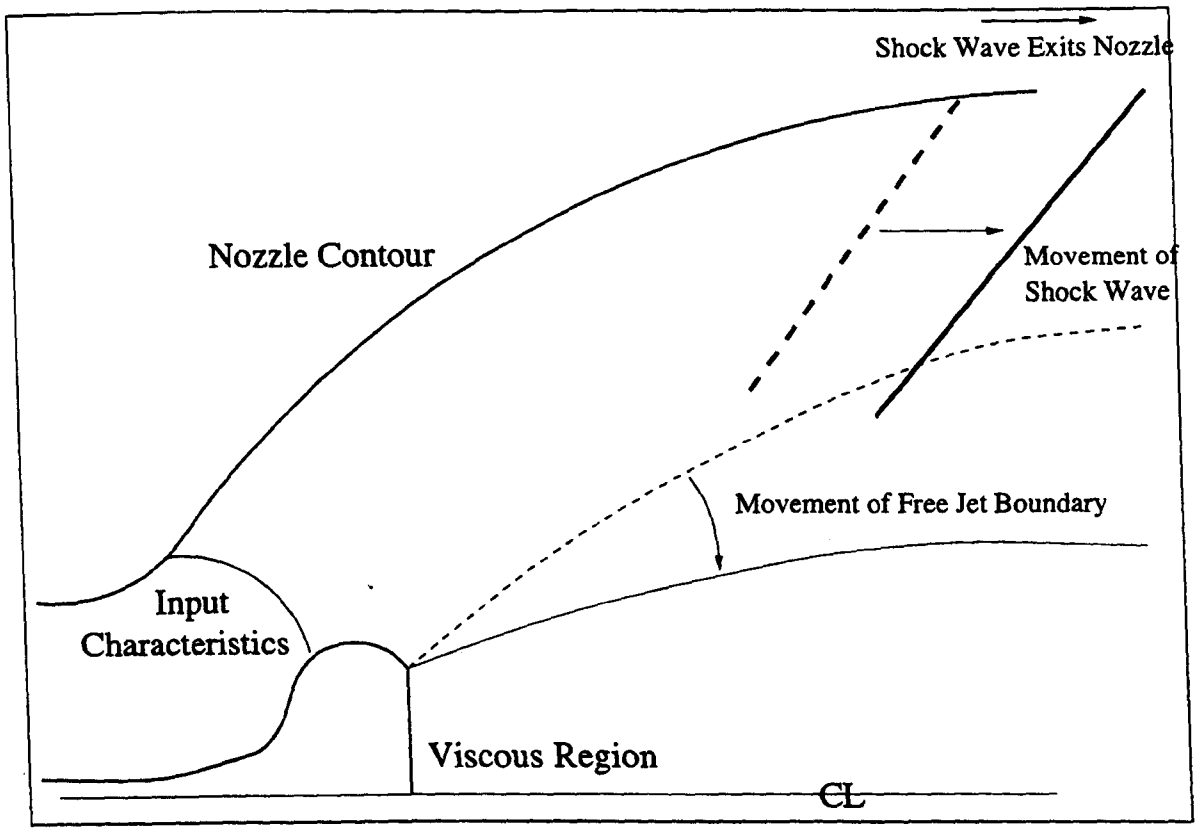

Figure 6.9: *ED Nozzle Flow Field, Intermediate Mode*

6.2 Open Wake, Non Altitude Compensating

As altitude is gained, the ambient pressure reduces and hence, assuming constant chamber pressure, the overall pressure ratio increases. This will cause the free jet boundary in the nozzle to move in towards the nozzle centreline. This in turn means that the point on the nozzle wall where the wall pressures are first effected by the pressure distribution on the free jet boundary, be the compensation achieved via compression or shock wave interaction, will move downstream. Eventually, this point will exit the nozzle, and true altitude compensation on the outer nozzle wall will cease. The general flow geometry is as shown in Fig. 6.9.

Whilst the fundamental flow processes in the nozzle remain the same, (e.g. compression waves still emanate from the free jet boundary, which may coalesce into shock waves, and the wake will remain in its open mode), the calculation of the thrust for such nozzles is considerably simplified. The forces acting on the nozzle walls are no longer effected by ambient conditions, and the thrust calculation simply becomes

$$C_F = (C_{Fw}^{\infty} + C_{Fc}^{\infty}) - \frac{P_a}{P_c}\frac{A_E - A_b}{A_t} + \frac{P_b - P_a}{P_c}A_b \tag{6.12}$$

where C_{Fw}^{∞} and C_{Fc}^{∞} are as defined in Eqns. 4.64 and 4.65, and A_b is the base area associated with the pintle. This equation is equally valid if the base pressure is no longer assumed to be equal to P_a, but some form of estimating this variable is required. In the results presented in this dissertation, P_b is assumed to be equal to P_a, and hence the last term in the equation disappears.

This removes the need to directly calculate the entire flow-field within the nozzle, as all the quantities in Eqn. 6.12 are calculated during vacuum thrust prediction. However, the pressure ratio at which the altitude compensation on the outer nozzle wall ceases is important for two reasons; not only does it mark the point at which the time consuming open wake calculations may cease, but is also vital when considering the effective range of the altitude compensation of the nozzle, and even whether altitude compensation occurs at all.

As noted in the introductory chapter, conventional bell nozzles are designed so that separation of the flow from the outer wall never occurs. It is likely that a similar restriction will be necessary to ensure stable flow within the ED nozzle. Therefore, the overall pressure ratio at which altitude compensation on this outer surface ceases is crucial. If it is lower than that associated with flow separation, the altitude compensating capability of the ED nozzle becomes useless, as flow separation will occur before any compression waves reach the nozzle wall. Finally, if the compensation at the outer wall is via a shock wave, there also exists the possibility of unusual and nonlinear effects due to the shock wave interactions at the exit plane at this transition pressure ratio, although such effects should be restricted to a narrow range of pressures.

Prediction of the pressure at which this transition regime occurs is not possible from the nozzle contour alone, and hence must be found by gradually increasing the overall pressure ratio from a true altitude compensating value, and calculating the entire flow-field using the method described in the previous section. However, this process would be required anyway, to produce a full picture of the nozzle performance throughout the atmospheric flight regime.

6.3 Transition between open and Closed Wake Modes

Two distinct flow-field compositions have been described within the ED nozzle, these being open and closed wake modes. The transitional regime between these modes of operation is not fully understood nor well documented, and is likely to be complex. It is known to exhibit oscillatory behaviour, at least in planar nozzle flows [27], [29]. It is also possible that the process will be prone to hysteresis, i.e. the ambient to chamber pressure at which the wake opens when moving from a low to high ambient pressure region will not necessarily be the same ratio at which the wake would close again when the traverse of pressure range is made in the opposite direction.

Experimental data suggests that the pressure range over which the wake transforms from open to closed is fairly narrow [26], and hence represents a limited part of the operating regime of the ED nozzle. However, it is still necessary to generate an estimate of this pressure range, as it marks a change in the equations used to determine thrust. More importantly, the

oscillatory nature of the flow observed during this transition could lead to vibration and hence have an impact upon the structural design of the nozzle. Therefore the altitude and flow regime at which it is likely to occur must be predicted, to allow an assessment of the magnitude and impact of the forces likely to be generated, and also the effectiveness of the application of possible alleviation techniques, discussed in more detail in the final chapter.

Before beginning a qualitative assessment of the processes involved, it is worth discussing the results presented by Mueller and Sule in Ref. 11. This paper is concerned solely with truncated plug nozzles, but as has already been discussed, the wake region behind the plug of such nozzles shares many similarities with that behind the pintle of an ED nozzle, and hence the qualitative behaviour of the nozzle types during wake closure would be expected to be similar. In Fig. 2 of this reference a series of curves showing a comparison of plug base pressure with ambient are presented for a plug nozzle truncated to various lengths. The result shown in this figure that the base pressure before wake closure is approximately ambient has already been referred to in Sec. 6.1.4. However, the effect of truncating the plug on vacuum base pressure and wake closure has not so far been examined.

Results are plotted for six different configurations, formed by different lengths of a conical plug inclined towards the centreline at an angle of 10 degrees. Whilst the open wake pressure for each of the plug lengths are similar (approximately ambient), the final closed wake base pressure of each varies. Examination of Eqn. 4.57 in Ch. 4 reveals that the base pressure is a function of both onflow Mach number and ratio of base to nozzle exit diameter, and as the plug length effects both of these variables, this behaviour would be expected. The overall pressure ratio, P_c/P_a, at which wake closure initiates, however, does not seem to be effected by plug length, and neither does the pressure ratio at which a stable closed wake regime is established (i.e. range over which the closure process occurs).

As the process of wake closure causes a rapid drop of the base pressure from approximately ambient to the final closed wake base pressure, wake closure causes the occurrence of a range of pressures for which the base pressure is considerably below ambient. The magnitude of this pressure deficit is increased by lengthening the plug (as the final base pressure drops). However, as the base pressure for a given nozzle is constant when a closed wake exists, eventually the ambient pressure drops to a level below that acting on the pintle base, and the base drag turns to a thrust. The range of overall pressures during which the wake closes is relatively narrow, although this is difficult to determine precisely from the figure.

There are very few other experimental investigations available for wake closure behaviour of either ED or plug nozzle flow-field in the literature. It does not seem to have been a specific area of interest, and even the summation discussed previously is interpreted from results targeted for analysis of other behaviours. Most such nozzles were designed specifically so that the wake closes at a low value of P_c/P_a (generally a benefit for plug

nozzles, but detrimental to ED performance), and hence very little data for the wake closure region is available. The range of pressures at which wake closure occurs is therefore estimated by consideration of the effect on the two flow modes as the ambient pressure changes to favour the other.

6.3.1 Wake Transition: Closed to Open

As an operating ED nozzle descends in the atmosphere from a high altitude to low altitude, the atmospheric pressure will rise from low to high. Initially, the wake will be closed, and the situation will be as shown in Fig. 6.10. The pressure immediately behind the shock wave S on the centreline is P_4. It is reasonable to assume that if the ambient pressure is below P_4 then this flow regime is stable.

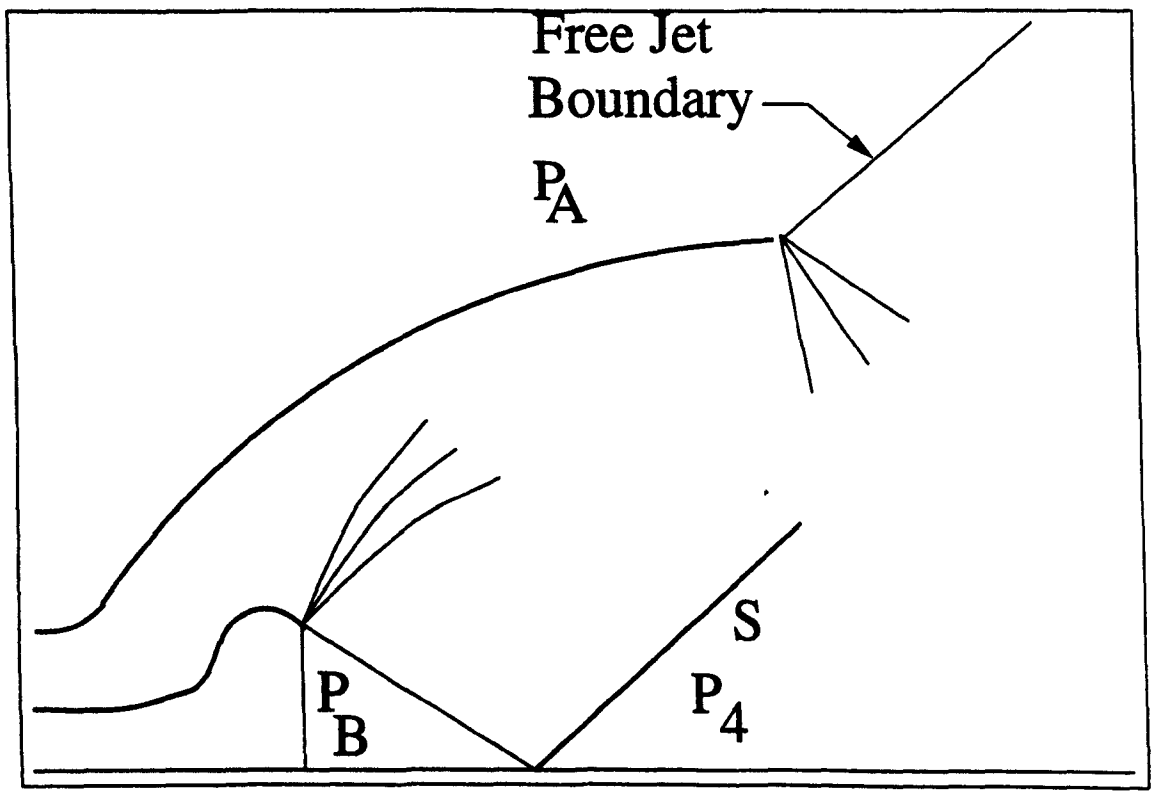

Figure 6.10: *ED Nozzle, Closed Wake*

However, if the ambient pressure is raised above this pressure, the shock wave as depicted will become incompatible with the flow-field created. Whilst secondary shocks within the exhaust flow downstream of S may sustain a closed wake for slightly higher ambient pressures than P_4, eventually the flow structure will collapse, and the wake will be forced open. The minimum possible ambient pressure at which the wake may open is therefore taken to be P_4, which is calculable from standard shock equations. If constant pressure mixing along the wake is assumed, this pressure is given by

$$P_4 = P_b\left[1 + \frac{2\gamma}{\gamma+1}(M_2^2 sin^2\beta - 1)\right] \tag{6.13}$$

and M_2 and β are calculated during the estimation of the base pressure for vacuum thrust calculation, and hence are already known.

As the ambient pressure would be considerably higher than the base pressure entrapped within the previously closed wake, this process is likely to be sudden. The ambient pressure, once gaining access to the pintle base, should rapidly increase the pressure acting on this face, and force the wake to open wide, rapidly changing the flow structures within the nozzle.

6.3.2 Wake Transition: Open to Closed

If the same nozzle moves from the high atmospheric pressure zone (i.e. by gaining altitude into a lower pressure region), the pressure within the viscous region drops. This allows the inviscid flow to expand, and occupy more of the volume within the nozzle. This in turn leads to a narrowing of the stream tube occupied by the viscous flow, as shown in Fig. 6.11.

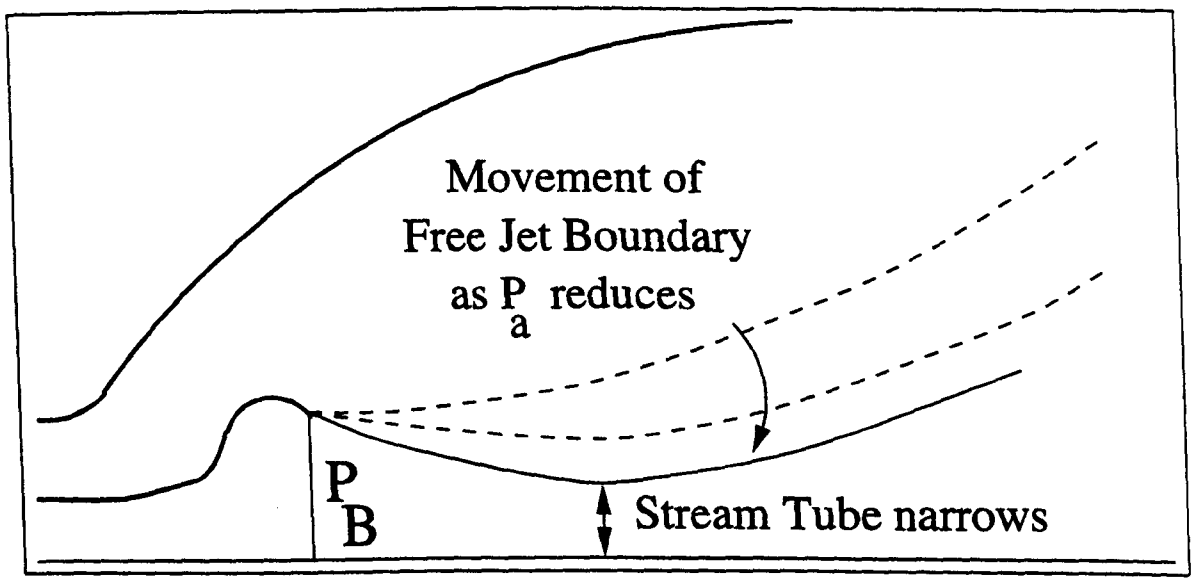

Figure 6.11: *ED Nozzle, Open Wake*

In Sec. 6.1.4, it was argued that the ejector action of the inviscid flow surrounding the viscous region under most conditions will be relatively weak. The supersonic flow will be contained within a thin layer near the wall of the nozzle, and hence have little effect on the viscous region near the centreline. However, as the boundary between these two flow regimes moves inwards, it is likely that the effect of this aspiration will increase, especially near the minimum cross section of the wake region. This will act as a contraction and accelerate the recirculating flow in the vicinity of it. It is likely that locally the pressure at this minima will drop below not only atmospheric pressure, but also that acting on the base of the pintle. This would further reduce the local wake radius, and thus create a positive feed back mechanism during wake closure.

As the minimum pressure in the viscous flow-field is likely to be below that at the base

of the pintle, it is possible that this wake closure may entrap the flow in such a way that the resulting pintle base pressure is greater than that which exists for the nozzle in a vacuum. If this is the case, the flow will be unstable, and the wake will burst open. This is a possible source of the oscillatory flows observed at certain pressure ranges in some experimental results.

The previously described flow cycle is one way in which unstable and oscillatory flow behaviour at wake closure pressure ratios could occur, but it is by no means the only possible mechanism. Unfortunately, the current understanding of the nozzle flow at such regimes is insufficient, and experimental results too sparse, for a precise model to be developed at this time. In the present work, the modelling of the wake closure is limited to defining a range of pressure ratios in which transition is likely, rather than an attempt to accurately define the narrow range for which it will occur.

This is estimated by a simple calculation of the minimum wake diameter for a given ambient pressure. As the open wake model described in Sec. 6.1 assumes an ambient pressure boundary, a cautious estimate that the wake will be prone to closure if the minimum diameter is anywhere less than half the pintle base diameter is used. This allows for the fact that the pressure boundary will in actual fact be at a considerably lower pressure, and hence the minima smaller.

This marks the beginning of the region of wake closure. The range of pressures over which uncertain behaviour may be expected may be estimated by consideration of the vacuum base pressure. If the ambient pressure is below this, the wake is assumed closed. This assumption is supported by all available experimental evidence so far discussed. In fact this data suggests that the wake will be closed at pressures considerably above this, and as an initial estimate the average of the vacuum base pressure and vacuum P_4 is used to mark the end of the wake closure region.

6.3.3 Wake Closure Summary

In summary, the wake closure process within ED nozzles is poorly understood, and insufficient experimental data exists to make anything more than broad estimates on the likely impact of the process. Whilst in the future it is hoped that an experimental program may allow significant improvements, the current basic model may be summarised as follows:

1. Wake closure occurs over a range of pressures, initiating at some point after the minimum diameter of the free stream boundary, calculated assuming inviscid flow and an atmospheric pressure along the wake length, is less than half that of the pintle base diameter. The process is assumed to be complete before the atmospheric pressure is less

than the average of the vacuum base pressure and post shock wave pressure (P_4). The actual closure process is probably prone to oscillatory and unstable behaviour, which is at present unpredictable.

2. Wake opening will occur at some point when the ambient pressure is (slightly) greater than the post shock pressure, P_4. This process is likely to be far more abrupt, but also more stable.

6.4 ED Nozzle Calculation Overview

The chapter which follows presents results for a series of ED nozzles over a wide range of flow configurations. Before proceeding, a brief summary of the design and analysis process of an ED nozzle is given on the following pages, providing a step by step description of the application of the techniques derived in this chapter, and the vacuum thrust predictive methods already discussed:

1. A set of throat geometry parameters, including throat angle, displacement, and wall radii of curvature are chosen, and a mesh generated according to the methods outlined in Sec. 4.1.1.

2. The CFD generated solution of this flow is then used to create input characteristics in the throat region of the nozzle.

3. These characteristics, along with a specified exit Mach number, are used as input to a standard optimisation routine and a contour of minimum length generated.

4. The wall pressures along this contour are integrated, and combined with the momentum and pressure forces on the throat. The vacuum base pressure is estimated using the methods described in the previous chapter. This allows Eqn. 4.67 (and hence C_F^∞) to be evaluated.

5. If the nozzle is to be used in atmospheric flight, the full open wake flow-field and wall forces are calculated for a range of P_c/P_a values, beginning with the lowest desired (i.e. lowest flight altitude). At some point one of two possibilities occur:

   (a) The compression wave within the nozzle exits the nozzle, or

   (b) The minimum wake radius reaches 0.5 of that of the pintle base.

6. In the case of 5(a), calculation of C_F continues until the pressure ratio at which 5(b) occurs using Eqn. 6.12

7. Wake closure is assumed to occur between the pressure associated with 5(b) above, and the average of P_b and P_4 calculated for vacuum conditions in step 4. For values of P_c/P_a greater than this, C_F may be evaluated using

$$C_F = C_F^{\infty} - \frac{P_a}{P_c}\frac{A_e}{A_t} \tag{6.14}$$

where $\frac{Ae}{At}$ is the maximum expansion ratio of the nozzle.

The above process allows a complete description of the performance of an ED nozzle to be estimated for a wide range of conditions. However, a considerable number of assumptions and simplifications have been necessary to allow this, particularly with respect to the techniques discussed in this chapter. The results which are presented in the following chapter for open wake results must therefore be viewed as a first approximation, until a considerable amount of experimental verification is undertaken.

Chapter 7

ED Nozzle Performance in Atmospheric Flight

There are several new and unique parts to the analysis described in the previous chapter, not least the ability to examine the effect for the first time of throat angle, and also the influence of shock wave formation on open wake altitude compensation (not previously discussed in any available literature). This should increase understanding of the processes occurring within such nozzles, and therefore also allow a more accurate targeting of future experimental work than previously possible. However, as these methods are new and not yet experimentally verified, the analysis presented within this chapter must be viewed as primarily qualitative in nature, and subject to a certain degree of uncertainty.

Available time and space again constrains the size of investigation possible, and hence the input characteristics generated by solving the flow-field within the throat geometries created for the results presented in Ch. 5 are reused, removing the time required for the CFD runs. This means that the input characteristics are interpolated from the output of the CFD model solving a mesh containing 256 by 64 cells, and the ratio of specific heats of all flows is 1.23. For planar flows an arbitrary value of y_d equal to G_t has been applied, combined with $R_{\equiv}^{-}$ equal to $2G_t$. Axisymmetric throat geometries have varying values of y_d, but in all cases $R_{\equiv}^{-} = 5G_t$. The use of two non dimensional lengths R_t and G_t is unfortunately again unavoidable.

The majority of the flight cases examined within this chapter involve conditions where the wake region in the nozzle is open to the atmosphere. However, the wake region will not be in this condition throughout the atmospheric flight regime, and indeed it is possible to design the ED nozzle such that the wake is never open, even at the lowest operating altitude. It is with this subset of ED nozzles that this chapter begins. This is followed by an examination of the thrust variation with altitude produced by compensating ED nozzles, combined with

a limited flow-field analysis of the type, concentrating on the wall pressures produced. The same methods are used to ensure an adequate number of points on the input characteristic to satisfy Eqn. 5.1

7.1 Closed Wake Atmospheric Flight Nozzles

An ED nozzle may be designed in such a way that the wake region behind the pintle remains closed throughout the operating range. Not only does this considerably simplify analysis, but also allows the complex behaviour of the wake closure phenomena to be ignored. Whilst this results in the loss of any altitude compensating capability, a significant reduction in length compared to a conventional bell nozzle of equivalent thrust remains theoretically possible. However, the maximum ambient pressure at which the nozzle may operate is limited by the need to ensure a closed wake flow-field, and this in turn restricts the maximum length and area ratio of a nozzle for a given chamber pressure and minimum operating altitude.

Two separate criteria for determining the pressure ratio at which wake transition occurs were described in Sec. 6.3.3, depending upon whether the wake is opening (overall pressure ratio dropping) or closing (overall pressure ratio dropping rising). In this case, it is the latter that is the more significant, as engine start up at low altitude will cause the flow within the nozzle to move rapidly from open to closed wake modes. This transition will occur at low thrust levels under controlled conditions, and hence will not generate the same level of vibration and related structural problems that gradual wake closure in free flight could produce (all nozzles, including bells, undergo such transients at start up without significant difficulties). However, to avoid any possibility of free flight wake closure, the wake behind the pintle must have finished all of the closure process at the lowest operating pressure of the nozzle. Therefore, the average of the base pressure and pressure behind the shock wave in vacuum flight of the nozzle must be greater than the highest ambient pressure in the operating envelope, as described in Sec. 6.3.2.

Whilst the need to ensure wake closure reduces the range of possible ED nozzle configurations, a similar restriction also limits the maximum permissible conventional nozzle size. The maximum Mach number occurring on the wall of a bell nozzle must not allow separation of the flow, as this would result in dangerous oscillations (this phenomena was discussed in more detail in Ch. 1). Therefore, the maximum value of M_E for a bell nozzle may be found from

$$(M_E)_{max} = \left[\left(\left(\frac{1}{S_c}\left(\frac{P_c}{P_a}\right)_{min}\right)^{\frac{\gamma-1}{\gamma}} - 1\right)\frac{2}{\gamma-1}\right]^{\frac{1}{2}} \tag{7.1}$$

Where S_c is a criterion related to the lowest wall pressure allowable which still avoids flow separation within the nozzle, relative to atmospheric pressure. In the work presented here, the

well known Summerfield Criterion is used, which simply states $S_c = 0.4$. This is standard practise in the design of current nozzles [8], and is used here for both planar and axisymmetric flow.

As chamber pressures of rocket motors are generally approximately constant during combustion [63], [5], the minimum ratio of chamber to atmospheric pressure will occur at the highest ambient pressure, i.e. the lowest operating altitude. Once this maximum exit Mach number has been calculated, an associated contour and vacuum thrust may be calculated using the nozzle optimisation procedures discussed in Ch. 3. It should be noted that the Summerfield Criterion is also assumed to apply to ED nozzles, and hence the maximum M_E number allowable for a closed wake ED nozzle may not exceed the value derived from Eqn. 7.1.

To allow a comparison between closed wake ED and bell nozzles, two example cases are considered. The first assumes a minimum operating pressure ratio of 150. This is typical of sea level conditions for high performance rocket motors (e.g. the planned chamber pressure of Skylon is 145 bar, that of the RS-68 on the Delta IV vehicle is 96 bar [64], and the LE-7 used on the HII launcher is 130 bar [5]), or alternatively may be viewed as equivalent to a second stage of a lower performance system. The second assumes a minimum pressure ratio of 600, which would roughly correspond to an altitude of 10 Km for a propulsion unit with a chamber pressure of 150 bar (i.e. representing a second stage of the first system). Both planar and axisymmetric variants are considered in turn.

7.1.1 Planar Nozzles

Planar flow analysis of bell nozzles is principally an academic exercise as no such nozzles are currently in use. However, planar analysis is more rapid than axisymmetric, and hence it is preferable to conduct a general investigation into this subset of ED nozzles in planar flow, provided of course that it is demonstrated that similar conclusions will be valid under axisymmetric conditions.

Table 7.1 presents the results for the same four throat angles examined in Ch. 5, each with two different post throat wall radii configurations. The exit Mach number for each nozzle is selected via an iterative procedure to find the maximum value that meets the previously discussed criteria for a closed wake at each pressure ratio. Also shown in the first row is the maximum thrust planar bell nozzle meeting the Summerfield Criterion, denoted by a throat angle of zero. The radii of curvature used for the throat region of this is $2:1R_t$.

As may be seen, the necessity of ensuring that the wake remains closed places a significant restriction on the allowable exit Mach number for the ED nozzle, and this in turn greatly

θ_t	R_w^+	R_p^+	$\frac{P_c}{P_a} = 150$				$\frac{P_c}{P_a} = 600$			
Deg.	G_t	G_t	M_e	$\frac{x}{R_t}$	$\frac{A_e}{A_t}$	C_F	M_e	$\frac{x}{R_t}$	$\frac{A_e}{A_t}$	C_F^∞
0	$1(R_t)$	-	4.20	124	49.1	1.85	5.04	439	147	1.93
30	1	2	2.92	13.3	10.0	1.67	-	-	-	-
30	2	0	3.07	13.4	9.54	1.64	-	-	-	-
45	1	2	2.83	12.7	10.8	1.68	3.64	45.5	25.8	1.79
45	2	0	2.95	12.8	10.4	1.68	3.74	45.3	24.4	1.76
60	1	2	2.79	12.5	11.9	1.68	3.58	43.6	26.8	1.80
60	2	0	2.84	11.9	11.1	1.69	3.59	44.5	25.9	1.79
75	1	2	-	-	-	-	3.57	43.6	28.6	1.80
75	2	0	-	-	-	-	3.60	43.1	27.3	1.80

Table 7.1: *Maximum Size for Closed Wake Only Planar ED Nozzles*

inhibits the overall expansion ratio and resulting thrust coefficient.

7.1.2 Axisymmetric Nozzles

Only axisymmetric ED nozzles with a throat angle of 60 degrees were considered, as this throat angle was found to offer not only a good range of possible M_E in Sec. 5.2.1 (see Table 5.1), but also a good performance relative to the other throat angles in the planar flow ED analysis presented in Table 7.1. Two throat configurations were selected for the ED nozzles, $R_w^+ = 2.5G_t$, $R_p^+ = 5G_t$ and $R_w^+ = 5G_t$, $R_p^+ = 0G_t$, shown in Ch. 5 to offer maximum C_F^∞ and range of M_E respectively. The bell nozzle throat geometry consists of R_w^- and R_w^+ of 3 and 1 R_t, as this was found to offer high vacuum performance in Ch. 3.

θ_t	y_d	R_w^+	R_p^+	$\frac{P_c}{P_a} = 150$				$\frac{P_c}{P_a} = 600$			
Deg.	(G_t)	G_t	G_t	M_E	$\frac{x}{R_t}$	$\frac{A_E}{A_t}$	C_F^∞	M_E	$\frac{x}{R_t}$	$\frac{A_E}{A_t}$	C_F^∞
0	0	$1(R_t)$	-	4.20	16.19	52.2	1.84	5.04	32.9	160	1.93
60	1.5	2.5	5	-	-	-	-	-	-	-	-
60	1.5	5	0	2.78	2.1881	10.9	1.67	3.57	6.02	25.2	1.78
60	8	2.5	5	-	-	-	-	3.46	4.80	29.2	1.78
60	8	5	0	2.80	1.85	14.12	1.69	3.58	5.35	28.4	1.79

Table 7.2: *Maximum Size for Closed Wake Only Axisymmetric ED Nozzles*

As was the case with the planar nozzle, the requirement that the wake remain closed places a severe restriction upon the performance of the ED nozzle, in many cases requiring

an exit Mach number below that identified as the minimum permissible. Further, the results for axisymmetric flow are similar in terms of thrust coefficient and exit Mach number to those for planar analysis, allowing the supposition that the use of throat angles other than 60 degrees would have no significant effect upon the viability of the closed wake ED nozzle to be made with a high degree of confidence. It may therefore be concluded that if the length (and hence expansion ratio) of a conventional nozzle is limited by the risk of separation from the walls at the exit, no advantage will arise from replacing the design with a closed wake ED nozzle.

7.2 Limits to Open Wake Nozzle Size

If the restriction on M_E imposed by the need to ensure a closed wake flow-field is removed, then not only are more efficient nozzles with larger expansion ratios available, but altitude compensating behaviour also becomes possible. This should provide a twofold improvement over conventional bell nozzles, as losses at low altitude are reduced, and larger overall expansion ratios may be used without separation at sea level. Before progressing to examine flow structures and thrusts produced during atmospheric operation, however, we must first consider certain limits imposed upon the maximum size of compensating ED nozzle.

Analysis of planar nozzles is again included, primarily for reasons of simplicity of both analysis, and (at some future date) testing. However, the evolution of the plug and aerospike nozzles from axisymmetric to linear form has taught the lesson that whilst at present the axisymmetric variant of the ED appears superior, presently unforeseen difficulties may arise which would result in the planar version being preferable. This means that the planar ED nozzle should be developed in parallel with the axisymmetric if this can be done without expenditure of undue extra resources.

Altitude compensation in length optimised ED nozzle contours occurs through the interaction of a compression wave at the nozzle walls, generally in the form of a shock wave. It has already been noted in the previous chapter that as the overall pressure ratio P_c/P_a increases, the point at which the compression wave first reaches the nozzle wall moves downstream. Eventually, at pressure ratio $(P_c/P_a)^{crit}$ it will reach the exit plane of the nozzle, at which point all altitude compensating behaviour ceases.

The Summerfield Criterion provides a means by which separation of the flow at the nozzle walls may be estimated in ED nozzles, in the same manner as is the case for bell types. As the flow will separate from the exit plane first, Eqn. 7.1 may be recast as

$$(\frac{P_c}{P_a})^{sep} = S_c(1 + \frac{\gamma - 1}{2} M_E^2)^{\frac{\gamma}{\gamma - 1}} \tag{7.2}$$

If the pressure ratio associated with the onset of separation $(P_c/P_a)^{sep}$ is higher than $(P_c/P_a)^{crit}$, the ED nozzle in question will not demonstrate any altitude compensating behaviour before the flow separates from the outer nozzle walls. As this behaviour is avoided in bell nozzles, it is assumed that it must also be prevented in nozzles of ED type (in fact arguments may be produced which suggest that this is not the case, but as these are speculative, they are reserved for the final chapter).

For small nozzles (low values of M_E), $(P_c/P_a)^{sep}$ is always less than $(P_c/P_a)^{crit}$. Increasing M_E increases both the length of the nozzle and $(P_c/P_a)^{sep}$. Whilst $(P_c/P_a)^{crit}$ is also raised, this is generally at a lower rate, and hence at some value of M_E a nozzle is produced where $(P_c/P_a)^{sep} = (P_c/P_a)^{crit}$. Any ED nozzle with a higher M_E will not altitude compensate before separation of the flow from the nozzle walls, and hence this restriction in effect places a maximum on the permissible length and area ratio of an ED nozzle that will altitude compensate over any of its operating range. Larger ED nozzles may be used, but only if restricted to pressure ratios above that at which interaction of the compression wave and nozzle wall occurs.

A second limit on the maximum M_E of a compensating ED nozzle is created by the onset of the wake closure process. It is impossible for any altitude compensation to occur if the wake is in closed form, as the access of the atmosphere to the pressure boundary is removed. If $(P_c/P_a)^{crit}$ is greater than that at which wake closure occurs, again the nozzle will not altitude compensate over any part of its operating range. As explained in the previous chapter, the mechanisms involved in the wake closure process are poorly understood, and the pressure range over which it occurs are difficult to predict. However, as an initial estimate the wake transition is assumed to initiate at the pressure ratio at which the minimum distance between the nozzle centreline and the inviscid flow-field is 50 percent of the base height of the pintle. The reasons for the choice of this value were explained in Ch. 6, although it must be admitted they are somewhat arbitrary.

7.2.1 Planar Nozzles

Table 7.3 shows results for various planar nozzle configurations, giving the maximum exit Mach number that still meets both these criteria, along with the associated nozzle length. These values will no doubt be reduced once viscous effects are included in the calculation. The ratio of the minimum radial distance of the wake to the radial distance at separation from the pintle (Γ) is given. Where a value of 0.50 appears in the table, the maximum M_E is created by the onset of wake closure, otherwise separation of the flow from the outer wall is the limiting factor.

The results presented in Table 7.3 reveal several notable trends. Variations in the throat

	$\theta_t = 30^0$			$\theta_t = 45^0$			$\theta_t = 60^0$		
$R_w^+ : R_p^+$	M_E^{max}	L (R_t)	Γ	M_E^{max}	L (R_t)	Γ	M_E^{max}	L (R_t)	Γ
2:2	2.93	13.2	0.95	4.16	99.5	0.50	4.80	282	0.50
1:2	3.32	24.9	0.74	4.17	104	0.50	4.87	330	0.50
2:1	2.53	6.49	1.00	3.55	36.5	0.77	4.41	152	0.50
1:1	2.69	8.49	0.97	3.78	53.5	0.57	4.45	162	0.50
2:0	2.52	5.59	1.00	2.99	13.7	0.99	4.18	102	0.61
1:0	2.52	5.70	1.00	3.15	17.9	0.93	4.22	108	0.58

Table 7.3: *Maximum M_E for Altitude Compensating Planar ED Nozzles*

angle have a considerable effect, greatly increasing the permissible nozzle size across all throat configurations. Whilst varying R_w^+ has only a small effect on the maximum M_E (reducing this variable appears to slightly increase the M_E limit), that of the pintle is much more pronounced. For all throat angles and outer wall radii, reducing R_p^+ considerably reduces the maximum allowable exit Mach number. It is also worth noting that the combination of throat radii offering the greatest range of altitude compensating nozzles (i.e. $R_w^+ = G_t, R_p^+ = 2G_t$) is the same combination that was found to provide the greatest vacuum thrust in the analysis presented in Sec. 5.1.

The increased range of M_E available for such throat configurations is primarily related to the Mach number associated with the point at which the flow separates from the pintle. If all variables are held constant except R_p^+, which is reduced, this Mach number will also fall (again, the pintle curve is assumed to terminate at the point of origin of the last LRC in the vacuum flow-field of the nozzle). As the total pressure of the flow in this region is constant (the shock wave not forming until a distance downstream), a lowering of the Mach number results in an increase in pressure. As the atmospheric pressure is constant, the flow must expand a greater amount immediately after separation, delaying the recompression of the higher velocity flow downstream. This in turn means that the shock wave forms a greater distance from the pintle, and hence will interact with the nozzle wall at a greater downstream location.

This effect is demonstrated in Figs. 7.1 to 7.3, where flow boundaries and shock wave locations are shown for three nozzles. Each nozzle has a throat angle of 45 degrees, and an exit Mach number of 3.5. The pressure ratio for the all flow-fields shown is 50:1. The outer (wall) and inner (free jet) flow boundaries are shown for each value of R_p^+. In between these flow boundaries the shock wave associated is displayed. As the pintle radius is reduced, the location of the shock wave is clearly shown to move downstream. Only the nozzle formed from a pintle with radius $2G_t$ has an interaction between the shock wave and the nozzle wall,

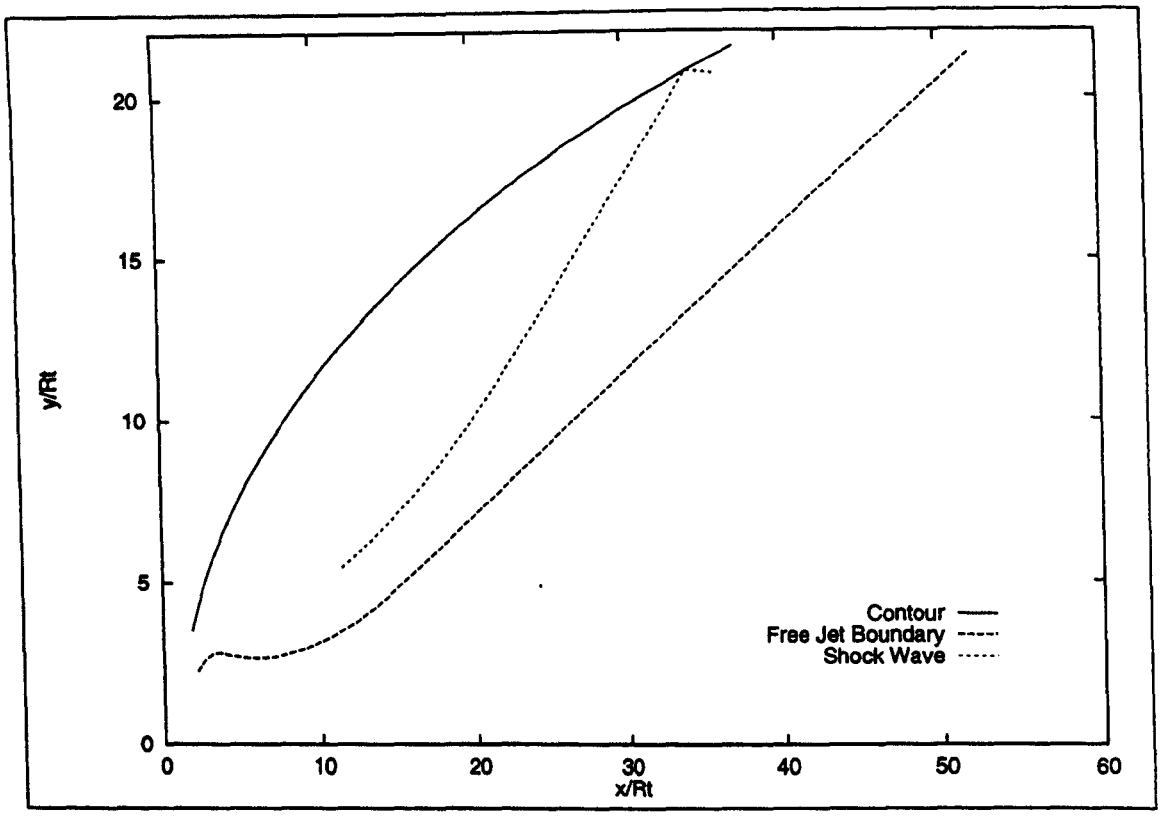

Figure 7.1: *Position of Shock waves,* $M_E = 3.5, \frac{P_c}{P_a} = 50, R_w^+ = 2G_t, R_p^+ = 2G_t$

and hence is the only nozzle compensating for the atmospheric pressure.

These figures also demonstrate the movement of the free jet boundary caused by variation in R_p^+. As the pintle radius reduces, this boundary moves towards the nozzle centreline. As

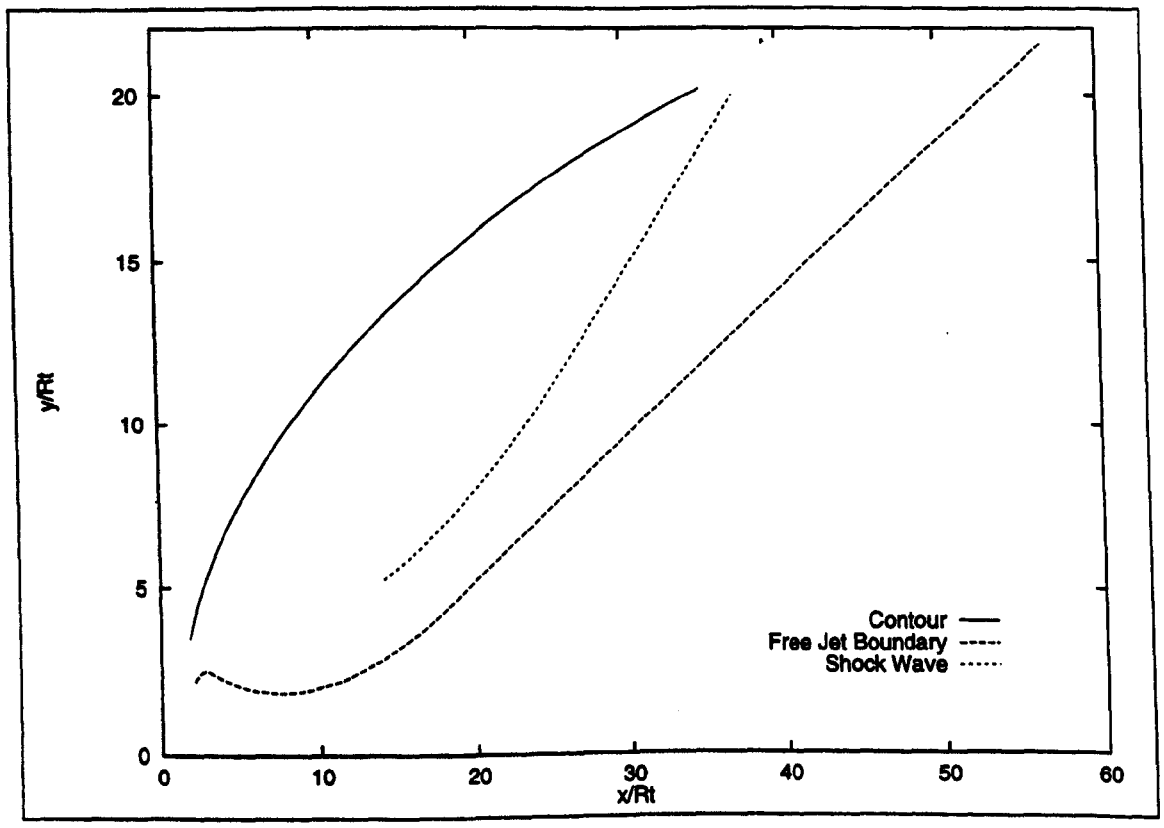

Figure 7.2: *Position of Shock waves,*$M_E = 3.5, \frac{P_c}{P_a} = 50, R_w^+ = 2G_t, R_p^+ = 1G_t$

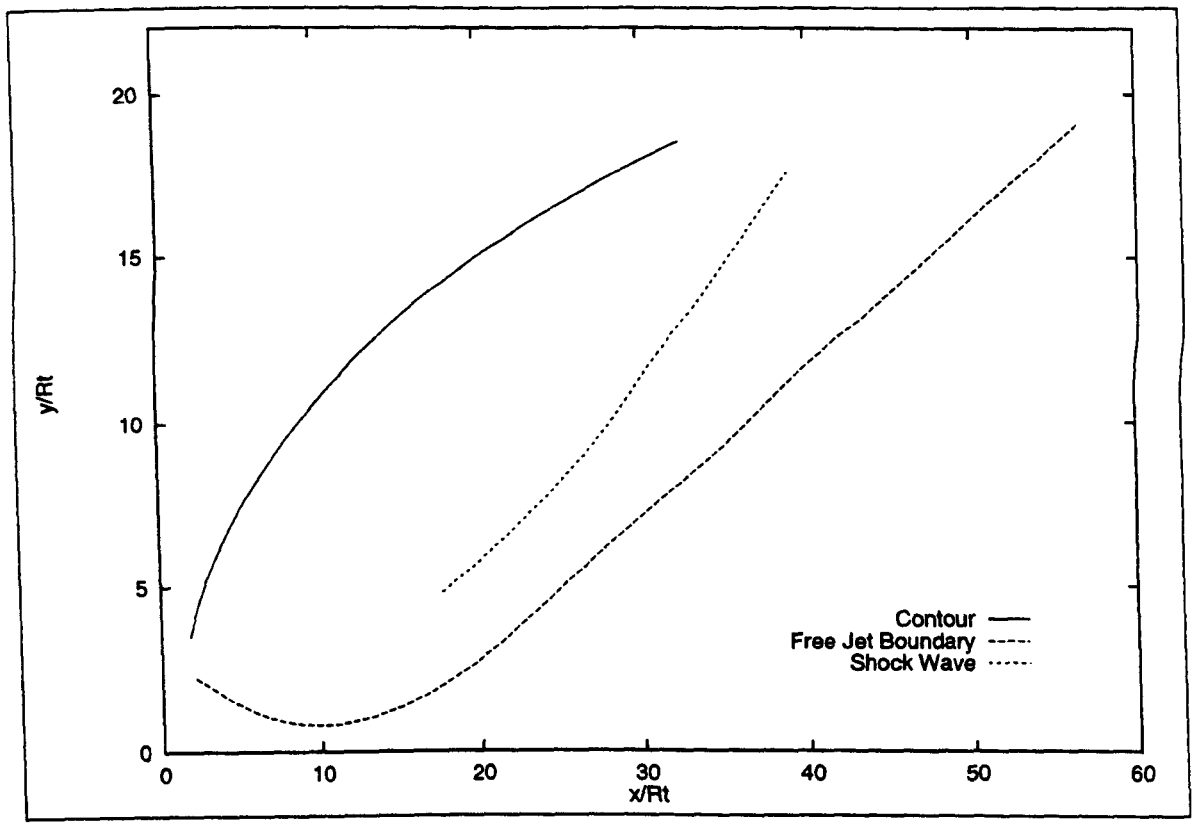

Figure 7.3: *Position of Shock waves,* $M_E = 3.5$, $\frac{P_c}{P_a} = 50$, $R_w^+ = 2G_t$, $R_p^+ = 0G_t$

has been explained previously in this section, this increases the likelihood of wake closure at any overall pressure ratio. In fact, the free pressure boundary associated with $R_p^+ = 0G_t$ flow-field (Fig. 7.3) has a minima much nearer to the nozzle centreline than half of the pintle base height. As such, by the criteria used to calculate the values in Table 7.3 it would be considered to be operating in a closed wake mode at the pressure ratio shown.

The results presented in Tab 7.3 also demonstrate that the nature of the phenomenon limiting the maximum size of the nozzle alters with increased throat angle. For a 30 degree throat, the maximum exit Mach number is limited by the shock interaction exiting the nozzle for all throat configurations. As the throat angle increases, first nozzles with $R_p^+ = 2G_t$ then those where $R_p^+ = G_t$, and finally (presumably, at angles greater than 60 degrees) those with a sharp cornered pintle, are limited by the onset of wake closure. It also appears that once this is the case, the outer wall throat radius ceases to have any significant impact on the maximum M_E.

However, it should be noted that the maximum length associated with each throat configuration is greater than that at which the next higher throat angle produces greater thrust (e.g. compare Fig. 5.11 with the lengths in the second row of data). This means that the limit on the exit Mach number for altitude compensating nozzles discussed here are unlikely to play a significant factor in the design of planar ED nozzles. If a nozzle is desired with a higher M_E than allowed by Table 7.3, the limitation may be removed simply by increasing the throat angle, which would also increase vacuum thrust.

7.2.2 Axisymmetric Nozzles

The same sources of limitation to the maximum length possible for an axisymmetric altitude compensating nozzle exist in axisymmetric form as planar, i.e. the shock wave (or compression wave) must intersect the nozzle wall before the flow will separate from the outer wall, and the minimum wake diameter must never be less than 50 percent of the pintle base diameter before altitude compensation begins. The limit to M_E imposed by the contour optimisation also play a more significant role in restricting the maximum size of axisymmetric compensating nozzle, as a possible contour must of course exist to allow compensation (refer to Sec. 5.2.1, and Table 5.1 on page 138 in particular for these limits).

	$\theta_t = 60^0, y_d = 1.5G_t$				$\theta_t = 60^0, y_d = 8G_t$			
$R_w^+ : R_p^+$	M_E^{max}	Reason	L (R_t)	Γ	M_E^{max}	Reason	L (R_t)	Γ
5:5	4.94	Max M_E	25.2	1.0	5.23	Max M_E	31.7	1.0
2.5:5	4.69	Max M_E	19.6	1.0	4.96	S_c	24.7	0.87
5:0	4.34	Wake	14.0	0.5	4.55	Wake	16.2	0.5
2.5:0	4.36	Wake	8.1	0.5	4.57	Wake	16.4	0.50

Table 7.4: *Maximum M_E for Altitude Compensating Axisymmetric ED Nozzles*

The maximum M_E allowing altitude compensation for a range of 60 degree throat ED nozzle configurations are presented in Table 7.4. The three possible reasons for limiting M_E are indicated by 'max M_E' if the largest possible ED nozzle altitude compensates effectively, 'S_c' if the Summerfield Criterion indicates separation of the flow from the outer wall before the shock wave interaction, and 'Wake' if the limit is due to the reduction of the minimum wake radius to 50 percent of the pintle base radius.

A study of Table 7.4 reveals that all three of these limits do occur, depending upon the throat wall radii. However, as was noted in Ch. 5, the M_E limit imposed by the optimisation process is always most severe for nozzle radii combinations that otherwise produce the best performance, both in terms of C_F^∞ and allowable range for altitude compensation. This is evident from the low M_E permissible for the low R_w^+, high R_p^+ combinations that generally produced the largest altitude compensating range for planar flows. Instead of being limited by separation at the walls, these nozzles are now limited by the requirement that an optimised contour exist. This in turn leads to reduction in R_w^+ having a restrictive, rather than beneficial effect on the allowable Mach number range. The Mach number limit is, however, increased in all cases by raising y_d.

There are, however, some similarities between the axisymmetric and planar results. If only 60 degree throats are considered, the $Y_d = 1.5$ axisymmetric nozzle limits are very sim-

ilar to those of the planar nozzle. In fact the axisymmetric nozzles actually have a slightly larger allowable maximum M_E, even though the associated length is much shorter. As the thrust coefficient of the nozzle is closely related to this M_E, it follows that the ED nozzles permit higher thrusts in axisymmetric form. This encourages the speculation that the effect of throat angle on allowable ranges will also be similar, increasing θ_t allowing larger nozzles. However, the range of M_E producing optimised contours was found to be severely reduced by increasing the throat angle (again see Table. 5.1), and hence will require further investigation with a greater range of ED throat configurations.

The impact that these restrictions may have on the viability of the ED concept is difficult to determine at present. One of the key advantages that the type theoretically possesses is a removal of any limit imposed by separation at sea level, allowing much greater expansion ratio nozzles to be used, increasing vacuum performance. The restrictions discussed in this section would reduce this advantage. However, the wide variation caused by altering the throat design parameters in the maximum possible M_E produces the possibility that the range of nozzles could be extended by careful design of the throat region. This is therefore an important area for future research.

7.3 Altitude Performance: Planar Nozzles

It is now possible to establish some design principles applicable to the planar ED nozzle if maximising altitude compensating performance is desired. First, a large radius of curvature on the pintle provides a significant advantage, as it not only tends to increase vacuum thrust (Figs. 5.1 to 5.4), but also increases the range of lengths for which an altitude compensating nozzle is possible (Table 7.3). R_w^+ has a lesser impact on performance, but it would appear that in general reducing this radius is beneficial both in terms of vacuum performance and altitude compensating range.

The throat angle of the nozzle should be selected to maximise the vacuum thrust, large angles being suited to longer, high thrust nozzles and allowing a greater range of lengths of altitude compensating nozzle. The maximum length of such a nozzle will be governed either by the maximum value of M_E as described in the previous section, or by independent structural considerations (i.e. a maximum length permissible due to staging, etc.). In either case, the limit on conventional bell nozzles relating to the risk of overexpansion is removed, allowing the potential of higher vacuum thrusts.

Making use of these guidelines, it is now possible to compare the ED with conventional nozzle performance in atmospheric flight. Figs. 7.4 and 7.5 show the thrust coefficients produced over a range of chamber to ambient pressure ratios for a selection of ED and con-

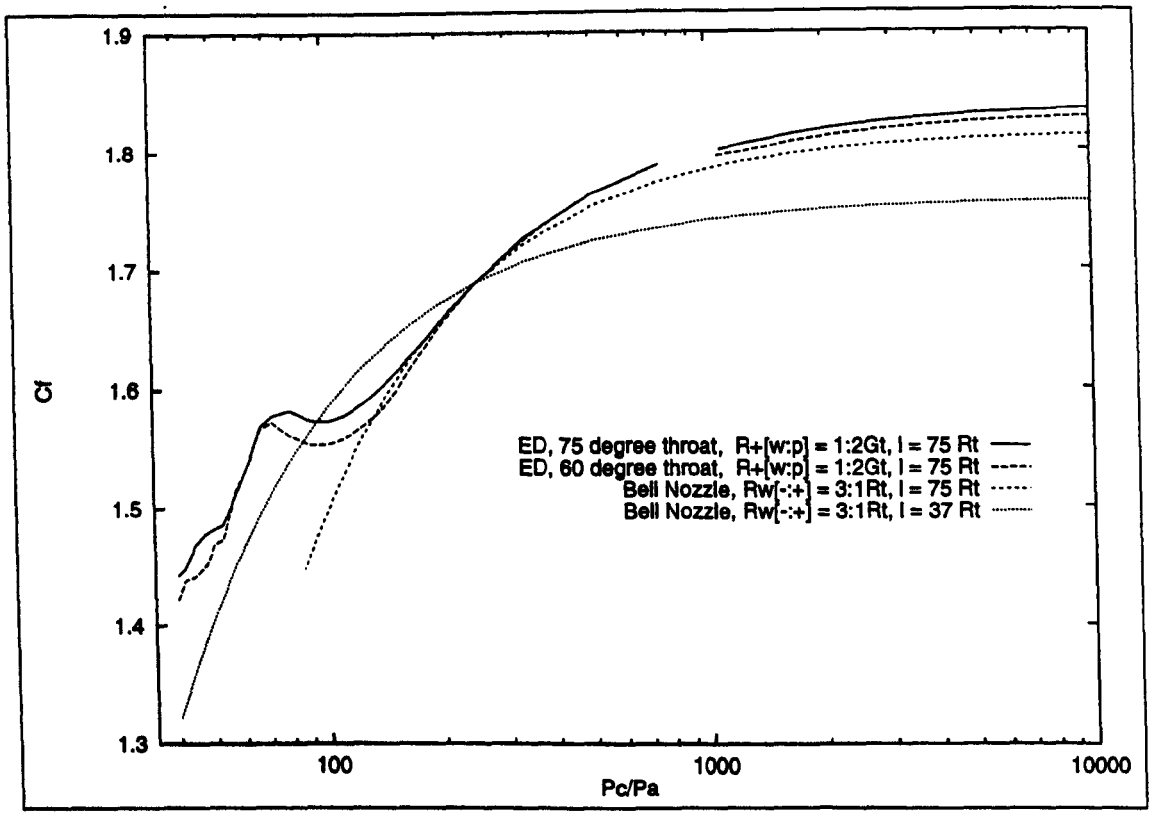

Figure 7.4: *Altitude Performance, Planar Nozzles, L = 75*

ventional nozzles, of lengths 75 and 125 R_t respectively. In each figure, the thrust curves of a pair of ED nozzles with $R_w^+ = 1G_t$, $R_p^+ = 2G_t$ and throat angles of 60 and 75 degrees are shown. Gaps in the plots for these nozzles represent the wake closure region, where thrust coefficient prediction is at present impossible.

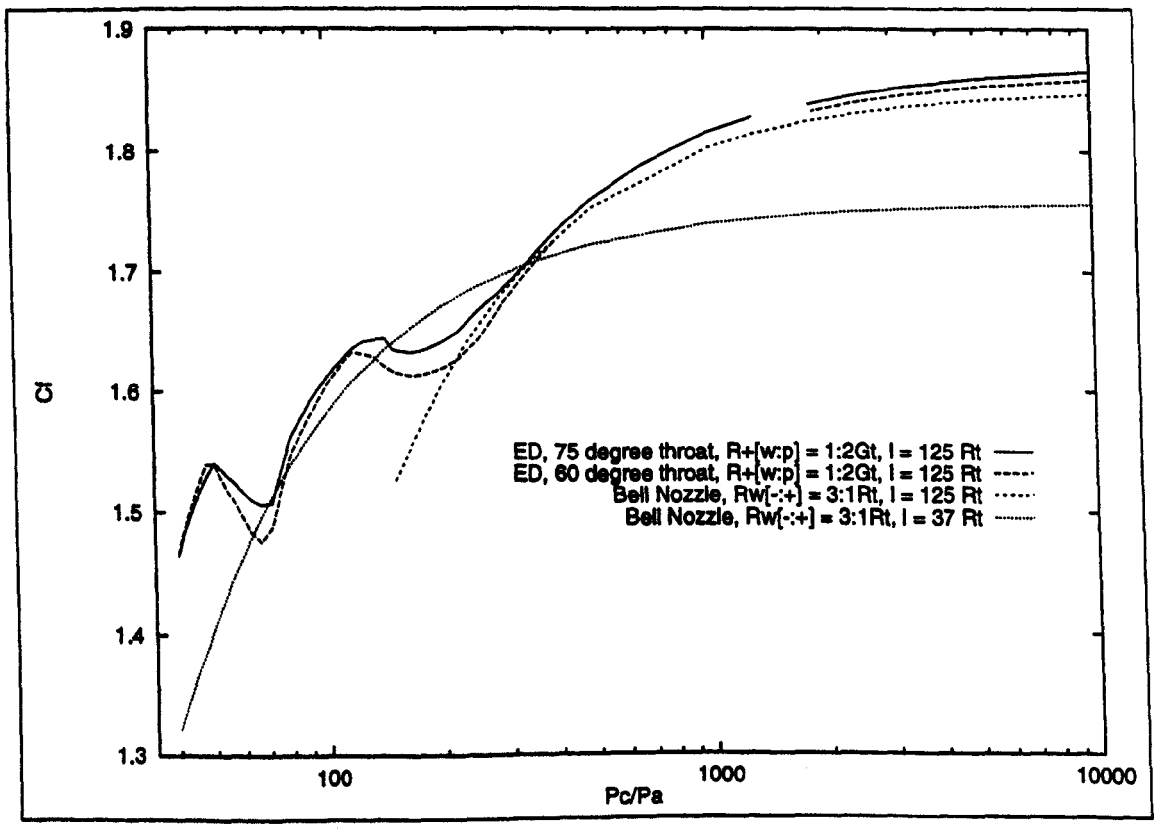

Figure 7.5: *Altitude Performance, Planar Nozzles, L = 125*

In each figure, a curve produced by a bell nozzle of equal length, with R_w^- and R_w^+ of 3 and 1 R_t respectively is shown. The minimum pressure ratio for which results are presented for these nozzles lies at the point at which the Summerfield Criterion indicates that separation of the flow from the nozzle walls would occur. This is not the case for the ED nozzles, the minimum pressure ratio here is entirely arbitrarily selected to be 40:1. If a bell nozzle were required that would function at this pressure ratio, a maximum length of 37 R_t is imposed by the Summerfield Criterion. The thrust curve of such a bell nozzle is shown on both figures.

There are several features present in these two figures that are worthy of note. First, the cross altitude performance of the ED nozzle with a 60 degree throat is very similar to that of a 75 degree ED nozzle of the same length, although in general the latter offers slightly greater performance. However, both the thrust curves produced by the ED nozzles differ considerably from the smooth arc produced by a conventional bell nozzle of the same length, particularly at low pressure ratios. Here, the C_F values produced by the ED nozzles vary rapidly with overall pressure ratio, passing through a series of fluctuations, although at all ratios exhibiting a greater C_F than that of the equivalent length bell nozzle. The increase in vacuum thrust produced by the ED nozzles may also be inferred from extrapolation of values at high pressure ratios.

The gaps in the plots for the ED nozzles which denote the range of pressures predicted for the wake closure process reduce when the 75 degree throat is used. Unfortunately, it is impossible to tell without experimental evidence whether this effect is real, or solely a consequence of the models used for this analysis (and hence possibly an error). Finally, comparison with the shorter ($x_E = 37R_t$) bell nozzle shows that whilst at some pressure ratios the C_F produced by this nozzle is greater than that of any of the ED nozzles under consideration, overall the much higher C_F^∞ and high altitude performance of the larger nozzles considerably offsets this.

The fluctuations in C_F at low altitude noted in Figs. 7.4 and 7.5 are a result of the interaction of alternating compression and expansion waves from the free pressure boundary. Figs. 7.6 and 7.7 show the wall pressures developed along the length of the two 75 degree throat ED nozzles at various overall pressure ratios. These figures clearly show the sharp increase in wall pressures due to the shock wave impingement upon the nozzle wall. Behind the initial discontinuity, the wall pressure continues to rise in a fairly linear fashion, until expansion waves reflected from the free pressure boundary reach the nozzle wall. This causes a rapid initial drop in wall pressure, followed by a flatter curve which has a similar gradient profile to the undisturbed wall pressures, though at a higher pressure level. At high ambient pressures, the shock wave forms a considerable distance upstream of the exit plane of the nozzle, and if the pressure is sufficiently high, a second compression wave forms behind it. This explains the periodic nature of the thrust curve revealed in Figs. 7.4 and 7.5.

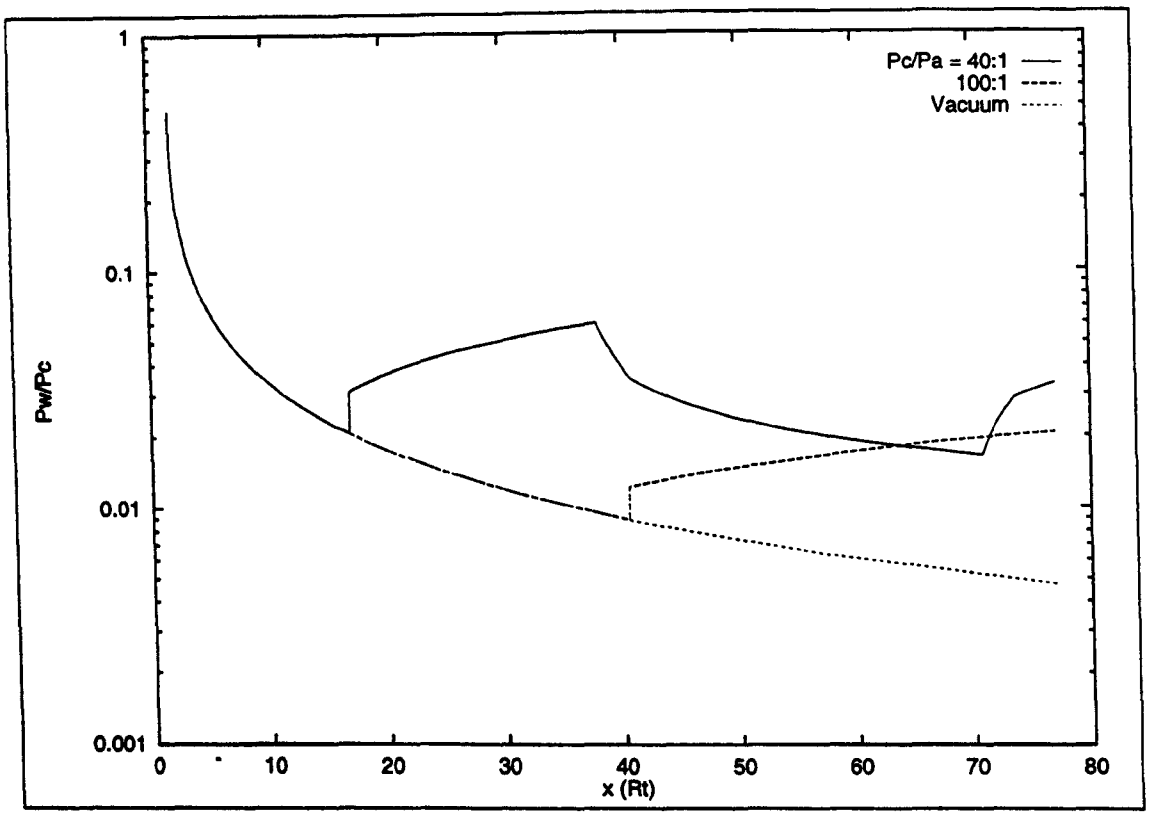

Figure 7.6: *Wall Pressures at Various Pressure Ratios, L = 75 R_t*

Increasing the ambient pressure also causes the ramp in pressure behind the shock wave steepen and shorten. The secondary compression wave does not take the form of a shock

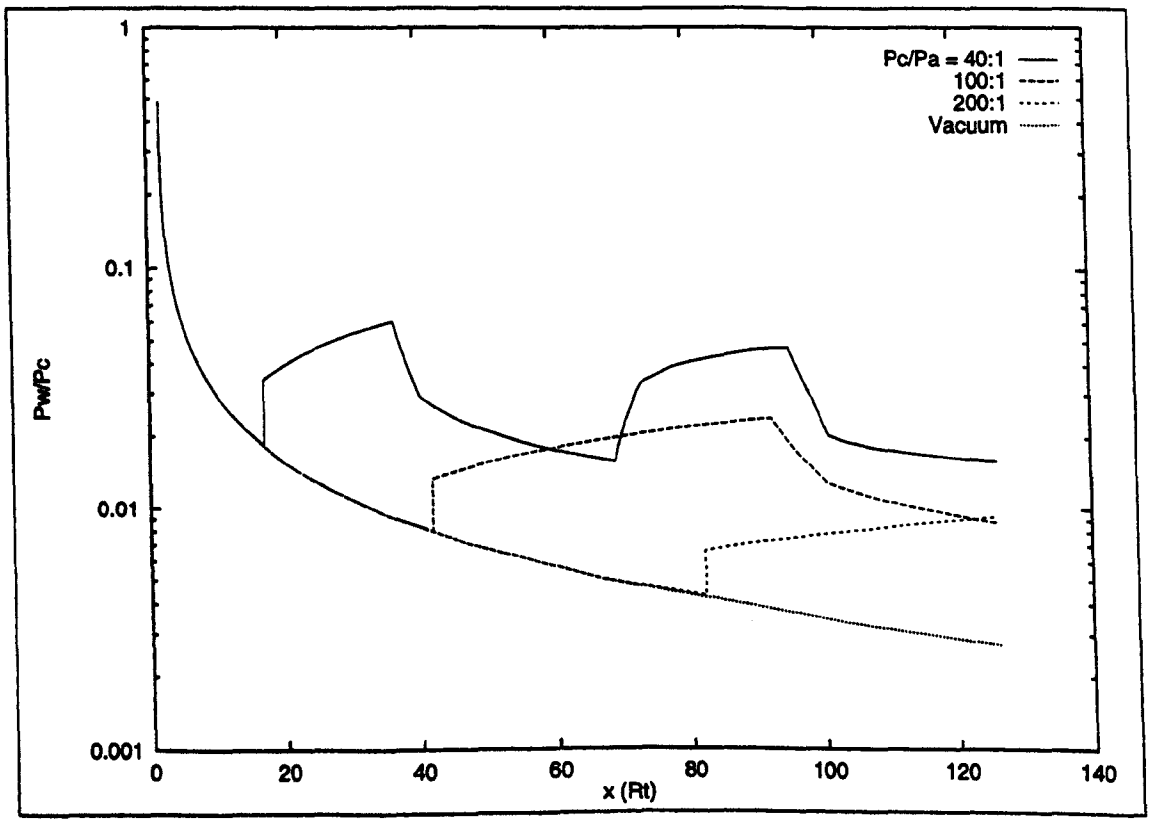

Figure 7.7: *Wall Pressures at Various Pressure Ratios, L = 125 R_t*

wave, although there it still is a clearly two stage phenomena; an initial rapid rise in wall pressure, followed by a more gentle increment behind. This may explain why the right hand

peak visible at low pressure ratios in Fig. 7.5 is flatter in profile than that immediately to its left. Finally, it should be noted that the streamwise location of each change in wall pressure behaviour is dependent on overall pressure ratio alone, and is independent of the total nozzle length.

7.4 Altitude Performance: Axisymmetric Nozzles

Whilst planar bell nozzles are not currently in use, axisymmetric bells are common. In this section, the replacement of the existing nozzle on a hypothetical propulsion system with an ED design is examined. This allows a comparison to be made not only between the bell and ED in atmospheric flight, but also a limited evaluation of the impact of throat geometry on the viability of the ED concept. The nozzle to be replaced is arbitrarily conceived to be a bell nozzle of length $15R_t$, with a throat geometry consisting of a R_w^- of 3 R_t, and a R_w^+ of R_t. Using the methods described in Ch. 3, it may be calculated that ignoring viscous flow phenomena and other losses, this nozzle configuration yields a vacuum thrust coefficient of 1.8298, and an area ratio of 46.1.

7.4.1 Maintaining Length

Again, due to the greater range of lengths generally available from ED nozzles with 60 degree throats, only nozzles of this throat angle were considered. Assuming that maintaining the maximum length of the nozzle is the most important concern, a series of candidate ED nozzles of this length may be created and analysed. This length requirement in itself removes several throat configurations, as no possible contours exist (Table 5.1). However, a fairly broad range is still possible, and four were selected. All of these have $R_=^-$ of $5G_t$, but differ either in the post throat wall radii, or magnitude of radial step y_d. The details of each of these nozzles is presented in Table 7.5, and the thrust curves produced are displayed in Fig. 7.8.

θ_t	y_d	R_w^-	R_w^+	R_p^-	R_p^+	C_F^∞	A_e/A_t
0^0	n/a	$3R_t$	R_t	n/a	n/a	1.8298	46.1
60^0	$1.5G_t$	$5G_t$	$5G_t$	$5G_t$	$5G_t$	1.8744	83.3
60^0	$8G_t$	$5G_t$	$5G_t$	$5G_t$	$5G_t$	1.8841	90.2
60^0	$8G_t$	$5G_t$	$5G_t$	$5G_t$	$0G_t$	1.8702	77.8
60^0	$8G_t$	$5G_t$	$5G_t$	$2.5G_t$	$5G_t$	1.8861	90.7

Table 7.5: *Characteristics of Axisymmetric Nozzles, Length* = $15R_t$

As was the case for planar nozzle altitude comparison, the minimum pressure ratio thrust coefficient shown for the conventional nozzle marks the point at which the Summerfield Criterion limits nozzle operation (i.e. the nozzle may not be used at lower pressure ratios without separation from the walls), whereas no such restriction applies to the ED, and any of the nozzles may be used at any lower pressure ratio. However, the plots have not been extended significantly, as the replacement of an existing nozzle is being considered, and hence the range of pressure ratios will have already been determined when the conventional nozzle was designed.

Considering first the comparison between the ED nozzles shown, the most obvious feature is the considerable drop in performance produced by the sharp expansion corner (i.e. $R_p^+ = 0Gt$) design. A slight reduction in thrust is notable at very high altitude, as would be expected given the vacuum thrust performance examined in Ch. 5. Coupled to this, the nozzle suffers from a much lower pressure ratio at which altitude compensation ceases, due to the earlier closure of the wake region. This means that the full area ratio of the ED nozzle is used much earlier in flight, and as this area ratio is considerably larger than that of the conventional nozzle, the low altitude performance suffers.

The other ED throats have generally similar performance. The larger y_d does slightly increase the high altitude performance (again as would be expected given the vacuum thrusts discussed previously). Other than this, the largest difference is visible in the region behind

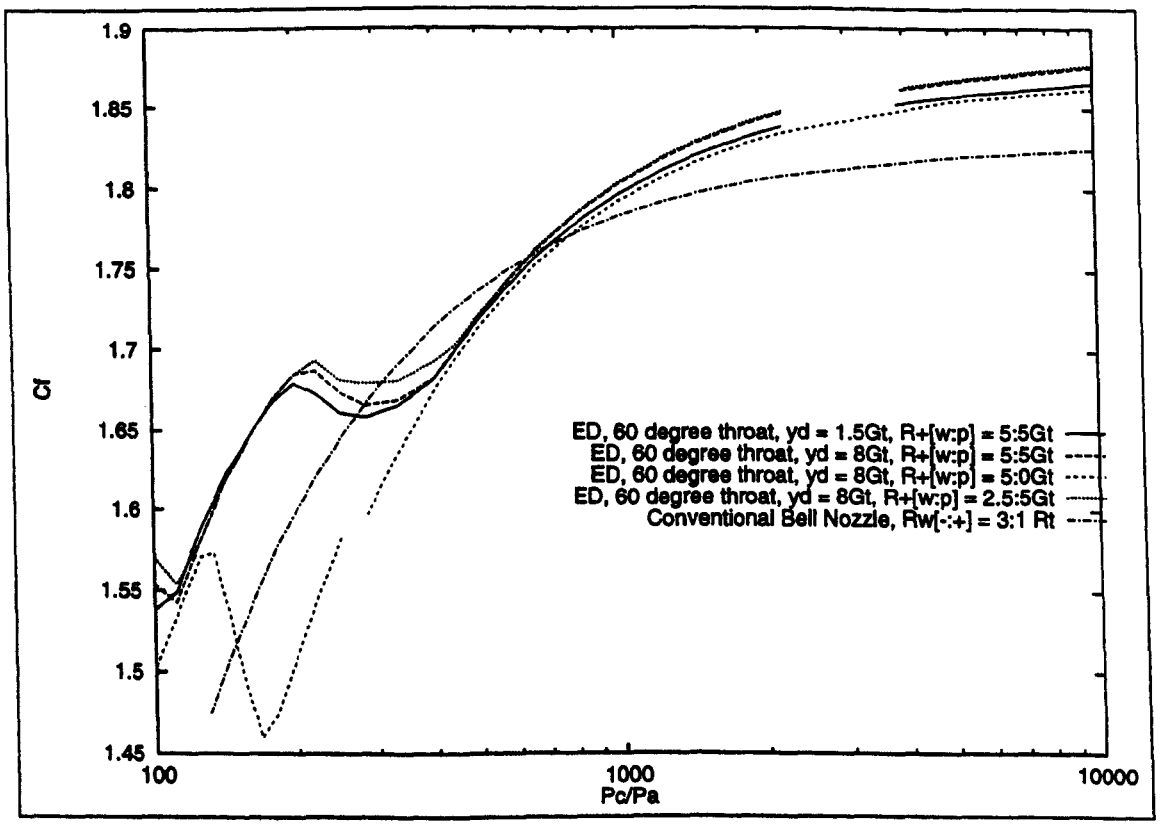

Figure 7.8: *Altitude Performance, Axisymmetric Nozzles, Length = $15R_t$*

the first peak on the left of thrust curve. Here, maximum thrust at the peak is raised if y_d is

increased, whilst the altitude at which altitude compensation ceases is delayed by reducing R_w^+.

The reasons for this behaviour become clear when the wall pressures along the nozzles at various pressure ratios are compared. Figs. 7.9 to 7.12 show the effect increasing the overall pressure ratio has on the pressure distribution along the wall of each of the ED nozzles considered.

The most striking feature is the very strong shock wave interaction with the nozzle wall occurring in the $R_p^+ = 0G_t$ nozzle at an overall pressure ratio of 100. This is clearly a much more powerful flow phenomenon than the shock waves occurring in the other ED nozzles. However, it rapidly moves down the contour as the pressure ratio rises, and by the time the pressure ratio reaches 200, the point of interaction with the wall has passed the exit plane. This explains the more dramatic fall in C_F visible for this nozzle type in Fig. 7.8.

Not only are the less severe shock waves generated by the other nozzles less likely to trigger separation, they are also more gradual in their movements with pressure ratio, maintaining contact with the nozzle wall until a pressure ratio of just over 400. Closer examination of these figures also reveals the reason for the slight difference in thrust curves already noted; the shock waves in the higher performing $R_p^+ = 2.5G_t$, $R_w^+ = 5G_t$, $Y_d = 8G_t$ nozzle forms further up the nozzle for a given pressure ratio, and hence increasing the thrust across a greater wall length. This also results in the shock wave remaining within the nozzle to a

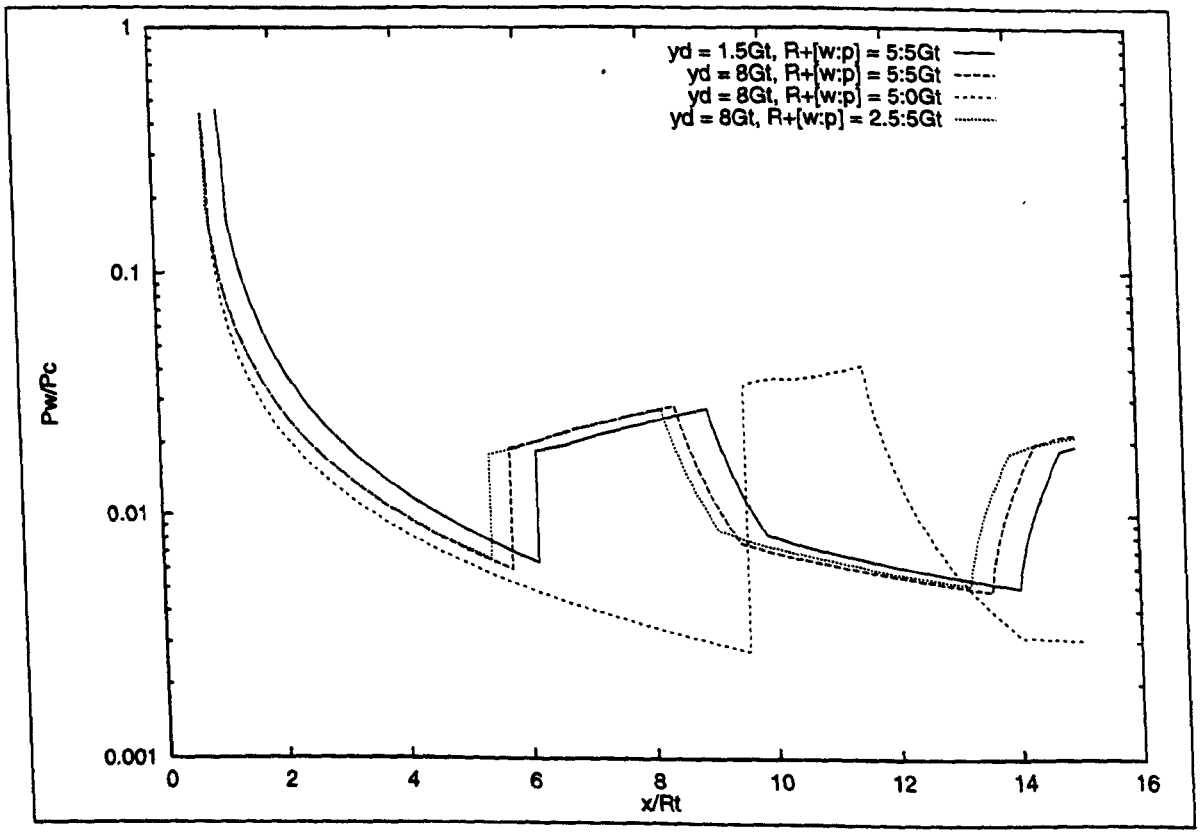

Figure 7.9: *Wall Pressures at $P_c/P_a = 100$, Axisymmetric 60 degree Throat ED Nozzles*

higher overall pressure ratio.

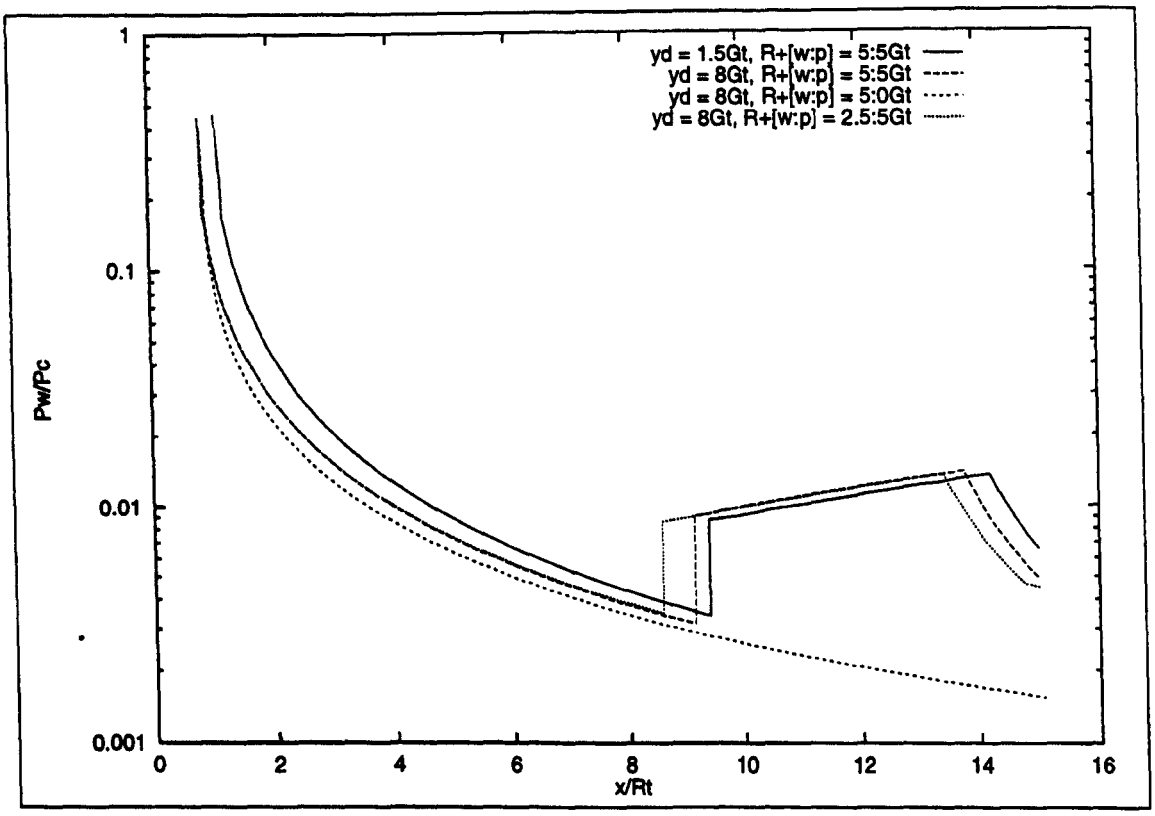

Figure 7.10: *Wall Pressures at $P_c/P_a = 200$, Axisymmetric 60 degree Throat ED Nozzles*

The larger planar nozzle examined in Sec. 7.3 displayed a pair of peaks in the thrust curve, as a secondary compression wave reached the exit plane of the nozzle and moved

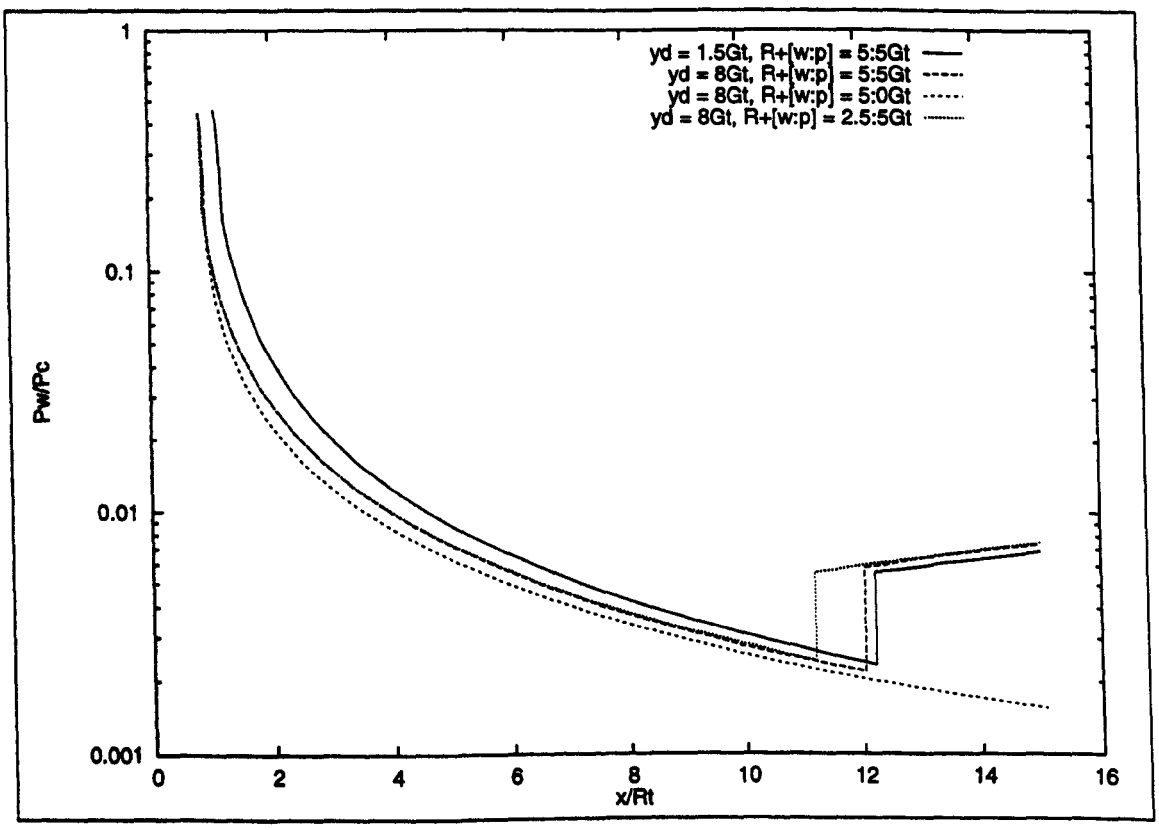

Figure 7.11: *Wall Pressures at $P_c/P_a = 300$, Axisymmetric 60 degree Throat ED Nozzles*

gradually upstream. A similar situation appears to be occurring at the extreme low altitude range of the ED plots in Fig. 7.8, most noticeably for the nozzles with larger y_d. These

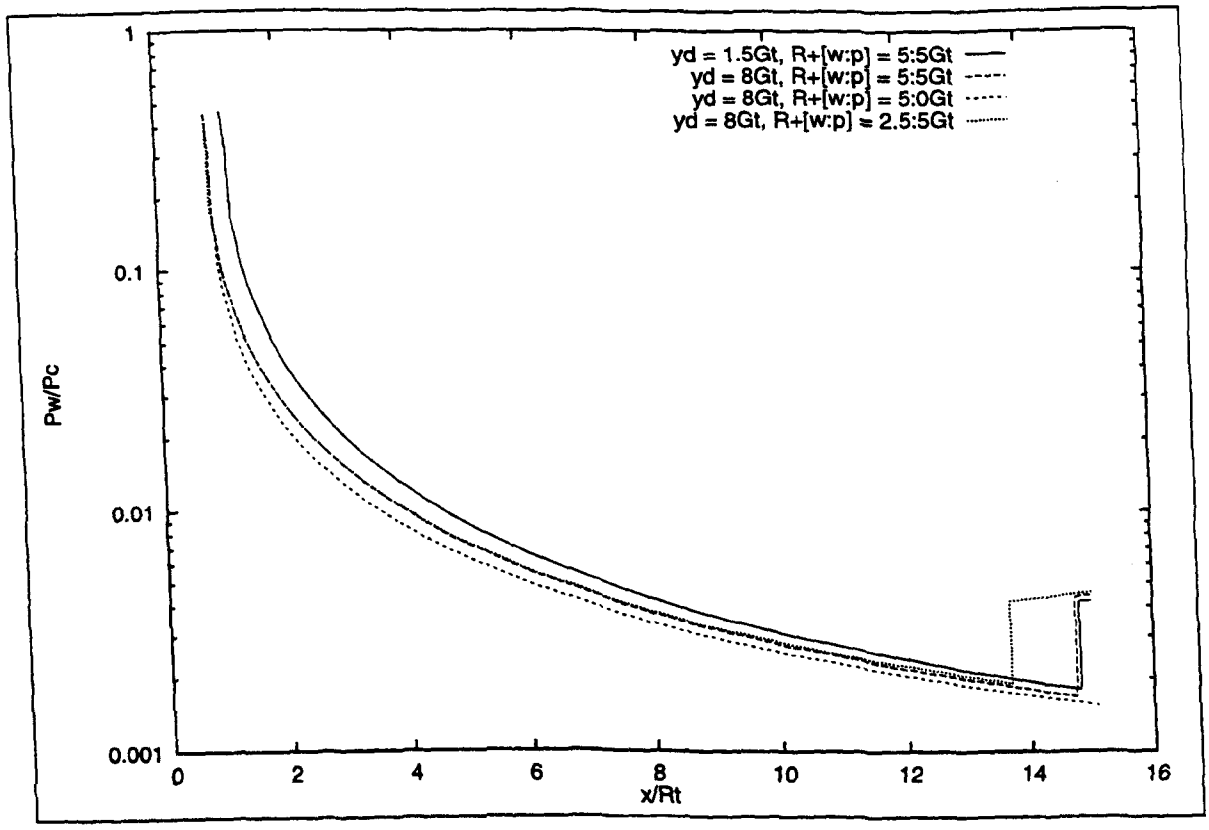

Figure 7.12: *Wall Pressures at $P_c/P_a = 400$, Axisymmetric 60 degree Throat ED Nozzles*

secondary waves are clearly visible for all ED nozzles (with the exception of the pintle sharp expansion corner) on Fig. 7.9. As was the case for planar flows, it is noticeable that these secondary compression waves are not shock waves, but weaker structures.

The difference between the thrust curves produced by the conventional bell and the ED nozzles is considerable. An ED nozzle of equal length generally improves the thrust coefficient produced over the entire operating range. Compared to the results for planar nozzles, however, there is a larger region where the conventional nozzle actually out performs any of the ED's considered. Despite this, it is a relatively modest increment in C_F, and the much higher sea level thrust, combined with far superior vacuum thrusts of all the ED nozzles would clearly make them favoured if this were the only design criterion.

However, there are other issues that should be taken into consideration. As has been made clear the methods used to predict the open wake thrust coefficient of the ED nozzles is of uncertain accuracy, and more importantly will be optimistic, as it includes an assumption of atmospheric base and free boundary pressures. It is unlikely that this is actually the case, and hence a slight reduction in performance may be expected.

It is also possible that the interaction of the shock wave at the nozzle wall may result in separation of the flow there. If this is the case, the performance will also be reduced. Fig. 7.13 presents two thrust curves for an ED nozzle with $R_w^+ = 5G_t$ and $R_p^+ = 2.5G_t$. The first is that created using the inviscid flow model, and hence is identical to that already presented in Fig. 7.8. The second, however, is created by integrating wall pressures only as far as the

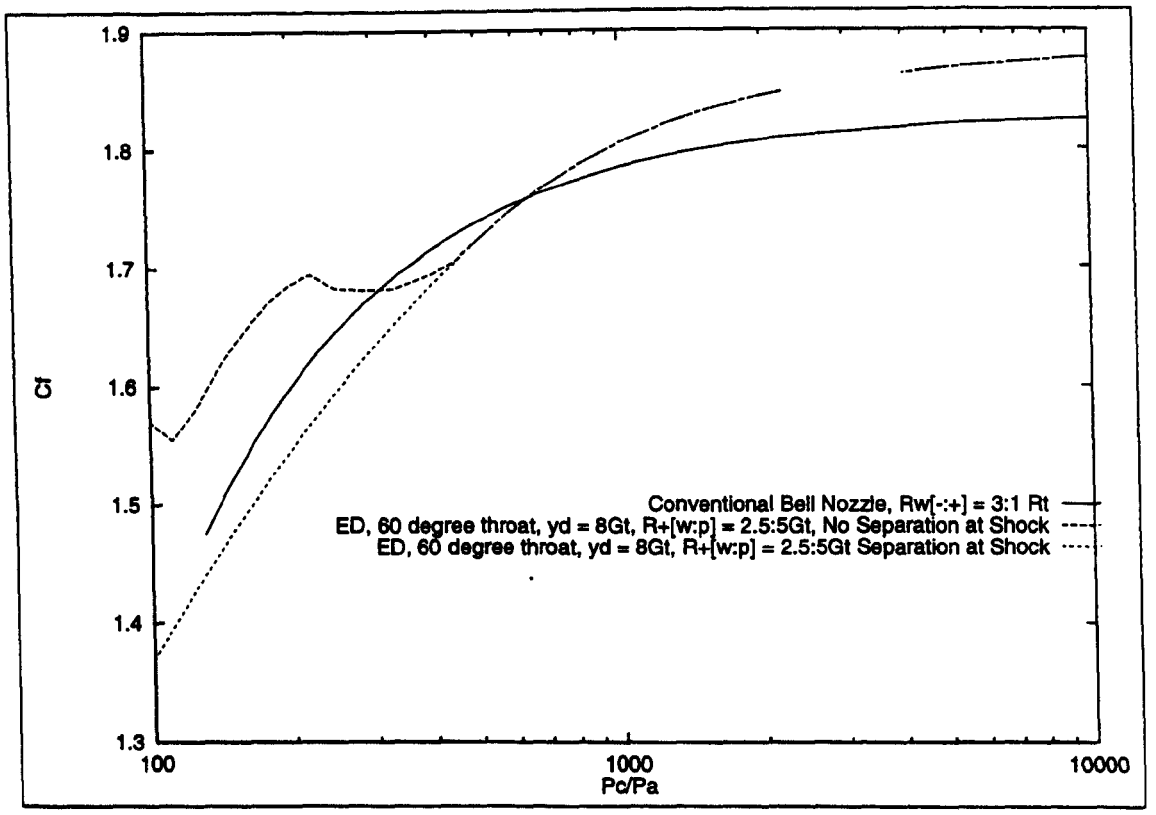

Figure 7.13: *Altitude Performance of Separating and Non separating ED Nozzles, Length = $15R_t$*

shock wave interaction. In effect, it is assumed that the shock wave trips separation of the boundary layer, and that the remainder of the nozzle wall is at atmospheric pressure. As has been discussed in Sec. 6.1.7, this represents a pessimistic prediction in thrusts, and hence the actual thrust produced by the real nozzle will lie somewhere between these two curves. Also shown is the thrust curve of the bell nozzle to be replaced.

Obviously the vacuum thrust and high altitude performance of the nozzle is unaffected by which method is used for open wake flow prediction. However, at low altitudes, a considerable amount of thrust will be lost if the flow does separate from the nozzle walls. The nozzle will still to some extent altitude compensate, as the movement of the shock wave will reduce the effective length and hence area ratio of the ED nozzle as overall pressure ratio drops. This means that the ED will still produce slightly greater low altitude thrust than a bell nozzle of equal area ratio. More importantly, if as anticipated the shock wave induced separation is a more stable separation phenomena than the pressure induced separation typical of bell nozzles, the restriction on maximum expansion ratio imposed by the Summerfield Criterion is removed.

Finally, Fig. 7.14 presents a comparison of the outer contours of three nozzles, the conventional bell, and two ED's, each with throat angles of 60 degrees and $R_{=}^{+} = 5G_t$, but with differing values of y_d. This demonstrates that whilst the length of the ED is indeed equal to the conventional bell to be replaced, the radial distance to the nozzle wall is generally far

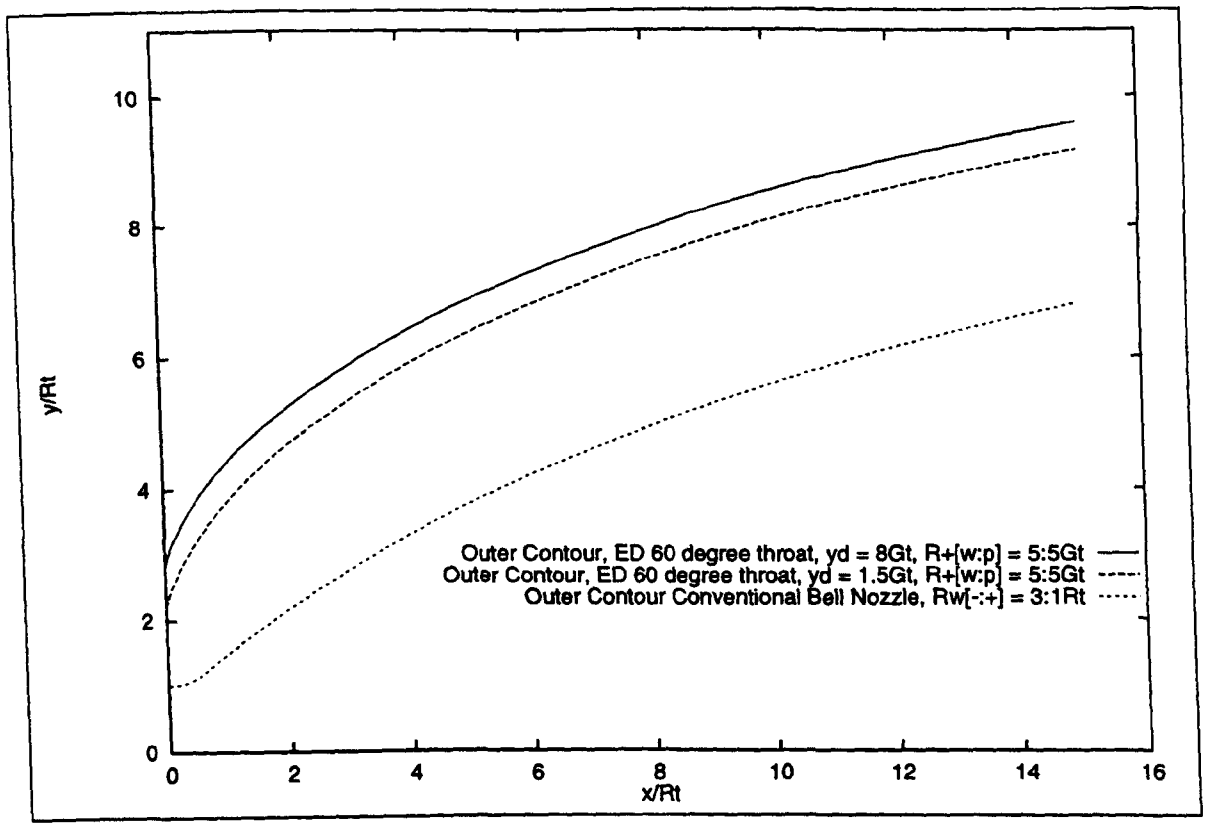

Figure 7.14: *Contours, Axisymmetric Nozzles, Length = $15R_t$*

greater. As these contours are rotated through 360 degrees to produce the actual nozzle, they are considerably larger, at least in terms of surface area. The mass of the pintle must also be allowed for, although being much nearer the axis of revolution, it will have a lesser impact. Comparison between the two ED contours also demonstrates that y_d must be increased significantly in G_t units before a notable increase in the radial position of the throat in global R_t coordinates is achieved.

7.4.2 Maintaining Vacuum Thrust

If instead of maintaining the length of the bell nozzle, the vacuum thrust is of primary concern, then the ED nozzle concept may be used to shorten the nozzle length. Selecting throat radii of $R_w^+ = 2.5G_t$ and $R_p^+ = 5G_t$ as generally offering higher vacuum and altitude performance, a series of three candidate nozzles were created, as defined in Table. 7.6

θ_t	y_d	R_w^-	R_w^+	R_p^-	R_p^+	x_E, R_t	A_e/A_t
0^0	n/a	$3R_t$	R_t	n/a	n/a	15.0	46.1
30^0	$4.5G_t$	$5G_t$	$5G_t$	$5G_t$	$2.5G_t$	10.9433	46.8
60^0	$1.5G_t$	$5G_t$	$5G_t$	$5G_t$	$2.5G_t$	9.2048	46.8
60^0	$8G_t$	$5G_t$	$5G_t$	$5G_t$	$2.5G_t$	7.8228	45.4

Table 7.6: *Characteristics of Axisymmetric Nozzles, $C_F^\infty = 1.8298$*

The thrust produced by each nozzle is compared with that of the bell nozzles in Fig. 7.15 for the full inviscid analysis. The thrust produced by all three ED nozzles is greater than that of the conventional bell at all altitudes, although that of the 30 degree throat is barely so. This is in contrast to the $l = 15R_t$ nozzles discussed previously, where at some altitudes the bell nozzle out-performed the ED. This is primarily because the area ratio of all the nozzles is approximately the same, so when the ED nozzle is not altitude compensating, there is still no penalty due to a larger area ratio.

In fact, if the wake is open there is some advantage for the ED nozzle type even if the shock wave does not reach the nozzle wall, as the area ratio is effectively reduced by the base area of the pintle. This causes the nozzle to act as though it were of a slightly smaller area ratio. This effect is dependent upon the pressure acting at the base of the pintle, assumed ambient in this analysis. However, even if it is found that this pressure is in fact somewhat below ambient, only if it were zero (which is obviously impossible) would the advantage be totally lost.

It is only at very low overall pressure ratios where true altitude occurs that the increase in thrust produced is very significant, and then only for ED nozzles with a 60 degree throat. Wall pressures are shown for the highest performing nozzle in Fig. 7.16 for a range of

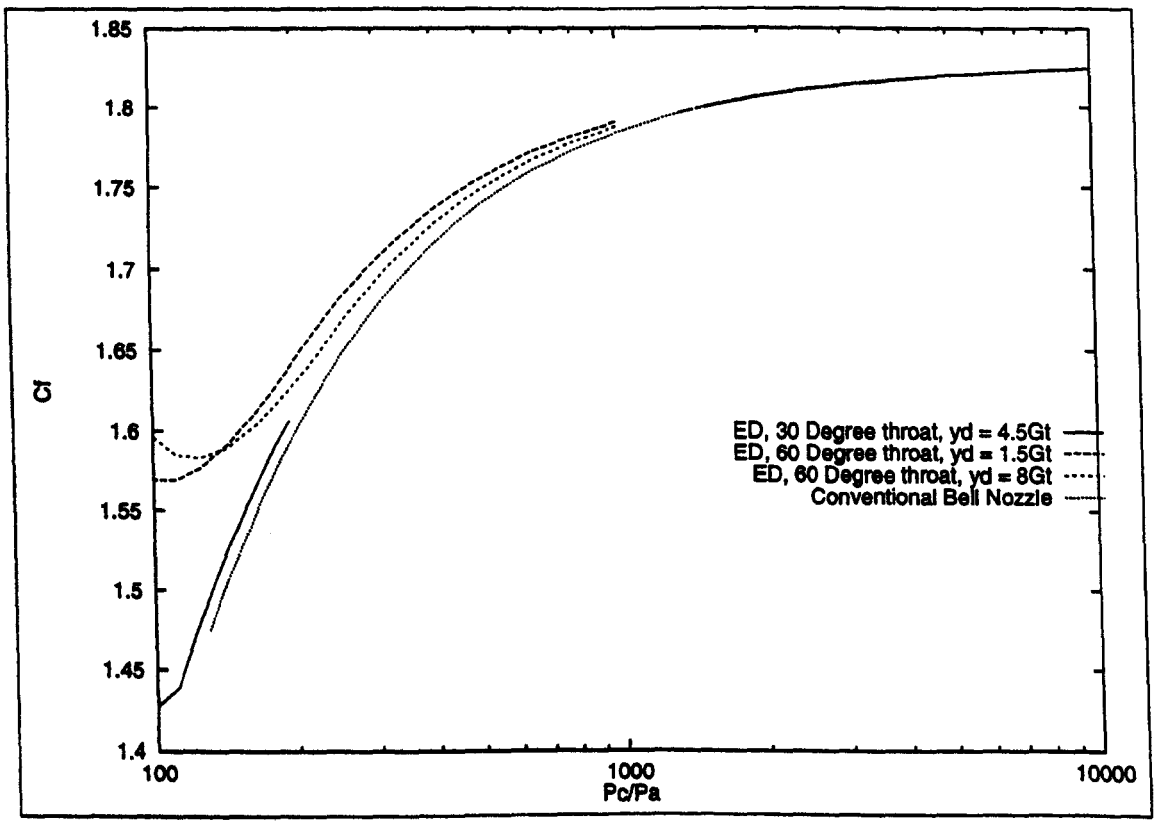

Figure 7.15: *Altitude Performance, Axisymmetric Nozzles* $C_F^\infty = 1.8298$, *No Separation*

pressure ratios. Not only may it be seen that the shock wave is of a lesser strength than for the larger nozzles discussed in the previous section, but also that the shock wave passes the exit plane of the nozzle at a much lower P_c to P_a ratio of 200:1. Even this nozzle will

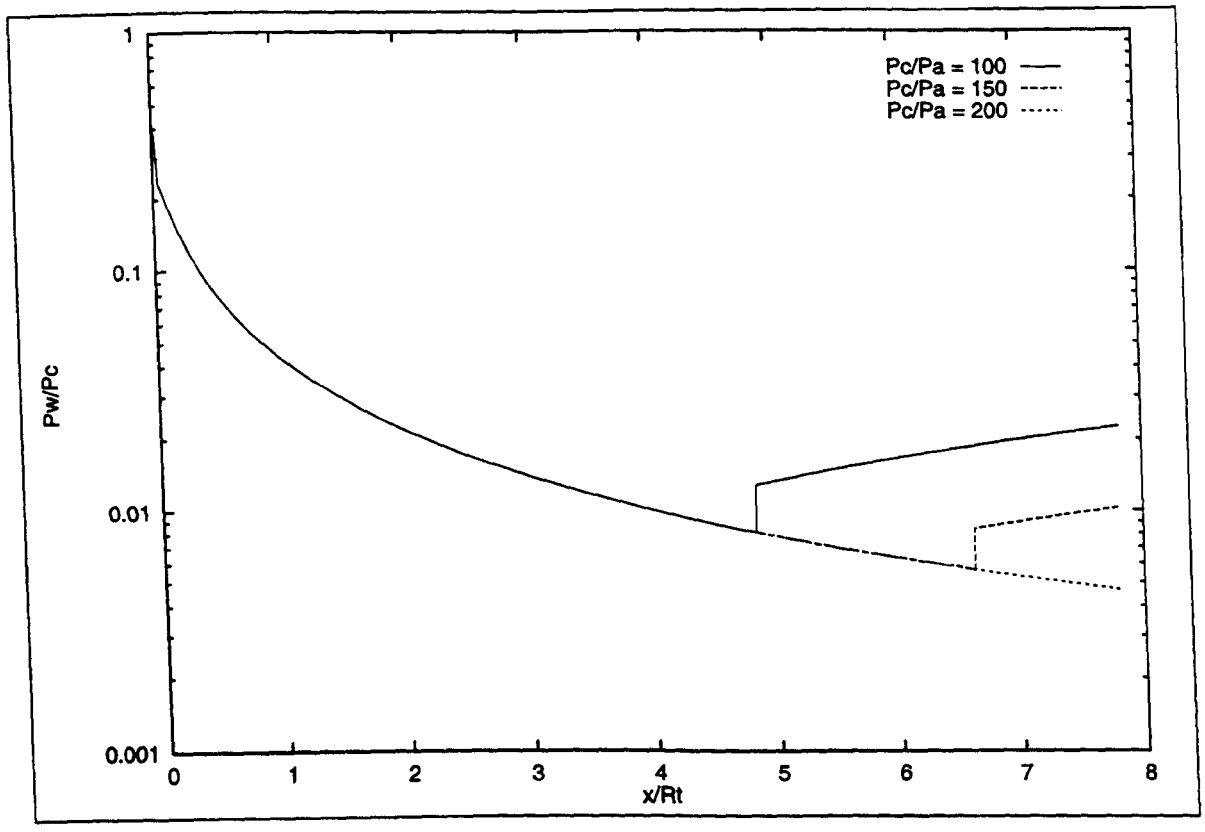

Figure 7.16: *Wall Pressures,* $\theta_t = 60, y_d = 8G_t, R_w^+ = 2.5G_t, R_p^+ 5G_t$

therefore only altitude compensate for a relatively limited altitude range.

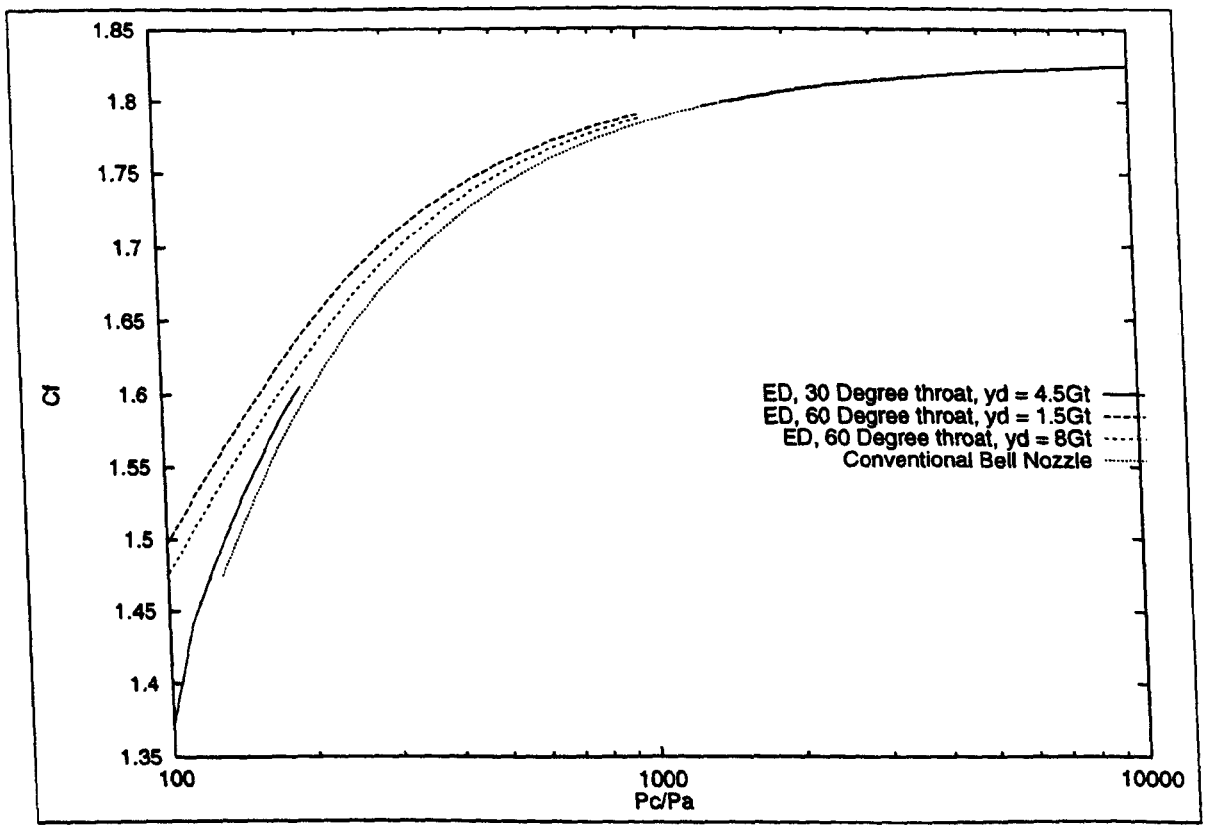

Figure 7.17: *Altitude Performance, Axisymmetric Nozzles* $C_F^\infty = 1.8298$, *Separation*

If the shock wave does cause flow separation at the wall, the majority of the performance advantage offered by the ED in atmospheric flight is lost, as is demonstrated by Fig. 7.17.

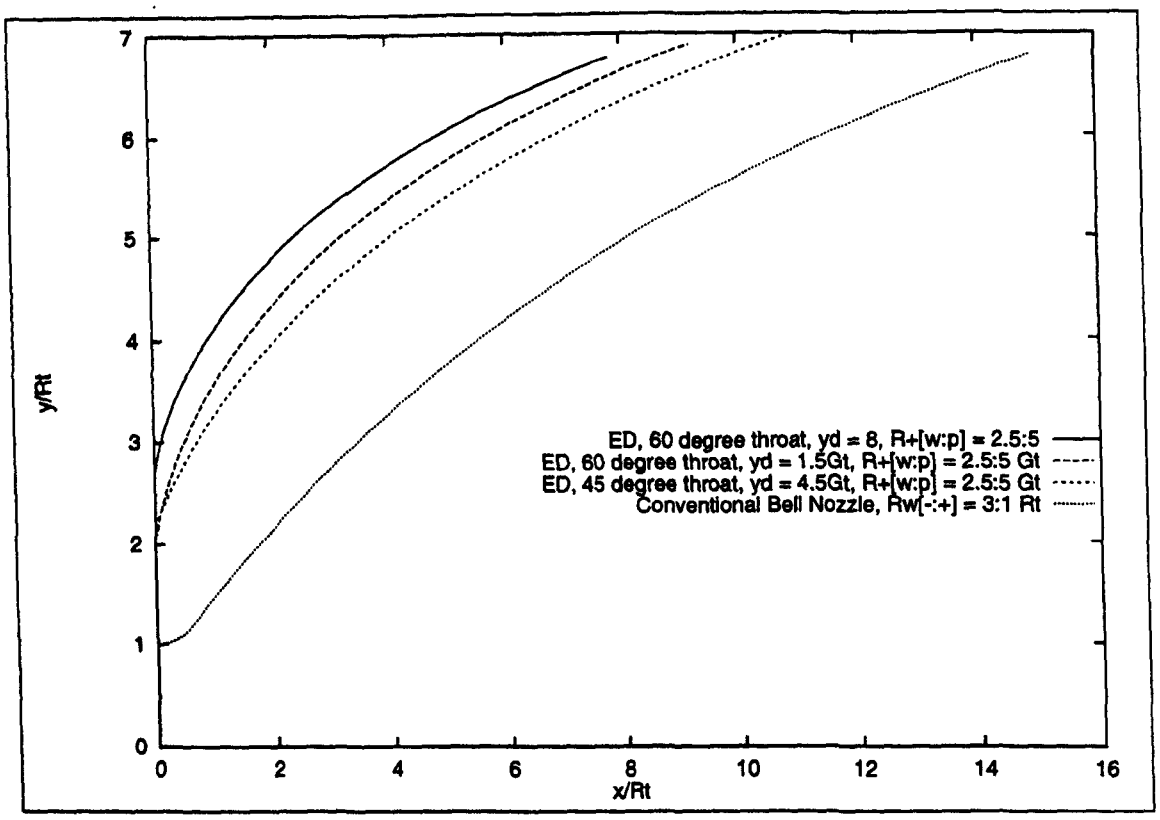

Figure 7.18: *Contours, Axisymmetric Nozzles,* $C_F^\infty = 1.8298$, *Separation*

However, the contours of each nozzle (displayed in Fig. 7.18) are seen to be shorter whilst of similar radial extent, and should therefore not only reduce length but also mass. This means that even if the altitude compensation be limited, it will provide a secondary advantage over bell nozzles, which is combined with a reduced length and mass.

7.5 Summary of Results

The magnitude of performance increment provided by the replacement of an existing bell nozzle design with an ED will depend upon which of three criteria govern the design of the conventional nozzle. If the design specifies a vacuum thrust, the bell may be replaced with a shorter ED nozzle of the same C_F^∞. The reduction in length is difficult to predict at this stage, but appears to be roughly in the region of 25 to 50 percent. Increasing the radial location of the throat reduces the length of the nozzle, but without altering the area ratio significantly. However, it will result in a smaller throat gap.

If the maximum length of the nozzle is limited, the use of an ED nozzle of equal length will increase vacuum thrust, and provide a notable increment over the whole operating range, although the overall nozzle area ratio and surface area are considerably increased. This would be likely to cause a noticeable increase in mass of the nozzle relative to the existing bell. However, this should be more than offset by the performance increments when the vehicle as a whole is considered.

If the necessity of avoiding flow separation at low altitude is the primary limiting factor on bell nozzle design, the most significant advantages are available. A longer nozzle may be used, considerably increasing vacuum and high altitude thrust, as may be seen by comparing the planar ED nozzle results with the bell nozzle limited by separation to 37 R_t. Initial thrust will also be increased, important in achieving rapid accelerations and overcoming gravity at low altitudes. The mass of the nozzle will of course be considerably increased, but again this should be offset when the knock on impact on the vehicle as a whole is considered.

Set against these advantages is the increased complexity of the design, and increase in heat flux transfer at the walls of the throat (a planar ED nozzle with equivalent mass flow at the throat will have a minimum separation of the walls equal to a half that of a conventional planar nozzle, the axisymmetric nozzles even less, dependent upon throat geometry detail). It should also be re-emphasised that the thrusts presented within this chapter represent optimistic values, and will be reduced if the free pressure boundary is less than atmospheric, or if the pressure recovery at the wall suffers from losses due to the shock wave - boundary layer interaction. Finally, the fluctuations in C_F at low pressure ratios could also have undesirable consequences, resulting in a rapid variations in thrust in some parts of the flight envelope, and the problems associated with wake closure are yet to be considered.

The choice of parameters at the throat has been shown to have a considerable effect on the performance of the nozzle, particularly in axisymmetric form. These parameters effect not only the range of possible contours, but also the behaviour of the wall pressures during open wake mode, both in terms of the strength of the shock wave produced and the pressure ratio at which altitude compensation ceases. Of particular concern is the restrictions found on allowable lengths for the high throat angle nozzles which offer otherwise generally better performance. However, the fact that at present only an extremely limited number of possible throat configurations have been examined means that it is probable that those selected are far from optimum, and hence even greater increments in performance may be achieved once the effect of throat region parameters is better understood.

Finally, the criteria used to optimise the contour design may also require re-evaluation. Minimising length is generally assumed to be of highest priority, due to its impact on staging lengths, etc. However, if the altitude compensating capability of the ED nozzle is to be seriously exploited, it is likely to be used on SSTO vehicles. If this is the case, then the overall mass of the nozzle, combined with the efficiency of the altitude compensation will be of paramount importance. As has been seen, very short high vacuum thrust ED nozzles are possible, but are likely to be larger and heavier than bell nozzles of equivalent length.

An alternative contour geometry, being longer but of generally smaller radius, could well produce similar thrusts at similar weights. Further the lengthening of the nozzle would be likely to stretch out the compression waves, reducing the likelihood of shock formation. This

would be of considerable importance if it is found that the shock wave does indeed trip the boundary layer, as it has been shown that this would seriously reduce the altitude compensating capability of the ED nozzle. The limits imposed on the maximum and minimum exit Mach number are also likely to be relaxed by a less demanding contour design.

Chapter 8

Conclusions

In the introductory chapter it was noted that a considerable amount of work was required before the ED nozzle could be considered as a viable alternative to conventional bell nozzles. The objective set for this project was therefore limited to advancing the current level of knowledge, rather than attempting a complete definition of the concept. Within this chapter, a summary of the advances made in the understanding of ED nozzle performance achieved by the work detailed previously in this thesis is presented, followed in the subsequent and final chapter by a discussion of areas deserving of possible attention in the future.

Previous research has tended to concentrate on one particular area of the ED problem (Rao on contour design, Mueller on base pressure), primarily due to the limited computational power available at the time of the research. Unfortunately, this meant that the work at times either presented an extremely simplified model of parts of the flow-field, or detailed analysis of one area of the flow obscured the overall objective, which is to provide a more efficient replacement for current conventional nozzles.

Due to recent advances in computing technology, more detailed models of the flow may be modelled much more rapidly, and the advent of CFD techniques has allowed the modelling of the throat region to be attempted with a far greater expectation of success. Therefore, it was decided early on that a complete model of all flow regimes and modes of operation would be developed, rather than focus attention on any one a single area. Whilst this inevitably lead to a more superficial treatment of any particular area than would have been possible had specialisation been attempted, it was felt that it was a more sensible approach due to the immature current state of knowledge with respect to the ED nozzle. It allowed the interactions of the various flow regimes and operating modes to be examined, and hence the factors which were most important in determining nozzle performance could be identified.

A strong feature of the results presented in this dissertation is the clear delineation of the general ED concept in two separate sub classes, each having different design philosophies,

applications, and levels of current knowledge. ED nozzles designed solely for high altitude applications (and hence only having closed wakes) are considerably nearer to possible application, being more similar to conventional nozzles, and with less uncertainties in design methodology and performance prediction. However, the greatest benefits will be produced by a true altitude compensating design, which requires more work, and possibly a radical reassessment of nozzle design criteria.

The vacuum thrust of length optimised ED nozzles has been shown to be little effected by the pintle base pressure, and some optimising parameters with respect to the throat configuration have been identified. More importantly, the performance benefits compared to conventional nozzles, in terms of reduced length for a given thrust, have been clearly demonstrated with a high degree of confidence for a wider range of configurations than previously possible.

The open wake performance of altitude compensating nozzle designs is on a less sound footing, and as yet could require considerable modification. However, the combination of CFD methods for analysis of the throat region with the MoC for the remainder of the flow have allowed a more detailed insight to be gained into the behaviour of the ED nozzle. In particular, the shock induced pressure rise along the wall of length optimised ED nozzles had not previously been noted, but has been found to be a common method through which altitude compensation occurs. The great sensitivity of ED nozzle performance to throat geometry parameters has also been demonstrated. Finally, the various modes of operation have been distinguished more precisely than in previous studies, including an open wake regime between vacuum conditions and altitude compensating flight.

Whilst a distinction between these two nozzle sub groups is clear, there remain significant similarities. The successful implementation of one type will be hastened by use of the other. It is therefore felt that the high altitude variety in particular is sufficiently validated that an experimental program to test the type is warranted, combined with an extension of the modelling methods to allow an assessment of the critical remaining issues of heat transfer in the throat region and development of boundary layers along the nozzle walls (both these issues are considered in more detail in the following chapter). The previously unsuspected impact of throat configuration upon the allowable range of axisymmetric nozzle size has been shown to be possibly severe, but is likely to be avoidable if the throat region is designed carefully.

The introduction of an effective altitude compensating variant is further off, and may require a change in the way in which the contours of such nozzles are designed. This is by no means a certainty, however, as further experimental and theoretical analysis of the type may well result in the current model being shown to be satisfactory to a sufficient degree. If this is the case, then the results of the nozzle analysis within this dissertation alone are

sufficient to warrant further investigation of the type, and yet these represent only a small sample of the possible forms.

It is perhaps this final point that is most important with respect to altitude compensating designs. The variations available within the the selection of throat variables and contour generation techniques mean that the possible ED nozzle configurations are virtually endless. This should allow performance to be tailored to individual design cases in a way not possible with conventional bell nozzles, as well as provide considerable performance increments over the limited and largely arbitrary combinations thus far examined.

This of course means that a complete investigation and definition of the type is a large and challenging exercise, well beyond the scope of the investigation presented here. However, a basic framework for design and analysis has been established, opening up new areas of interest. The performance of the nozzles examined within this dissertation have been shown with a high degree of confidence (particularly the closed wake model) to offer the potential of significant gains, despite representing only a fraction of the possible configurations.

Chapter 9

Recommendations for Future Work

Whilst this investigation has increased understanding of the flow behaviour within ED nozzles considerably, accurate methods for flow-field analysis of all modes and flight conditions remain some way off. The research has opened up many unexpected areas, and in fact a complete model appears to be a greater challenge than it did at the start. The questions that need to be asked, however, may now be phrased in a manner that should allow solutions to be found, and it is this topic that is now addressed.

The areas requiring future work may be split into two primary topics, although the boundaries between the two are a little blurred. The first is updating the models used for analysis and design of the nozzle type themselves, and the second a revision of the design philosophy of ED nozzles as a group. These topics are now considered in turn.

9.1 Modelling

Each of the primary areas within the current model are now reviewed, and areas involving uncertainties or possible areas for future investigation emphasised.

9.1.1 The ED Throat Model

A high priority for any follow on work from this investigation into either the high altitude or compensating ED designs would be the improvement of the CFD technique used to model the throat region of the ED nozzle. Accurate modelling of this region has been shown to be of great importance, particularly with respect to axisymmetric nozzle flows. There are a large number of parameters which could have a significant effect on the viability and performance of ED nozzles, particularly with respect to the limits to M_E ranges identified. Before the ED

nozzle may be seriously considered as an alternative to conventional bell nozzles, the flow-field within this region must be fully understood, both to allow correct selection of these diverse design parameters, and also to ensure a high level of confidence in the initial line used for contour generation.

In order to achieve this, examination of a considerably greater number of throat geometries than has thus far been achieved is required. However, the present CFD model was selected for speed and ease of implementation rather than operation. As a result, it is somewhat slow and cumbersome, and represents a significantly simplified model of the flow. It could be improved, both in terms of accuracy and speed, in a number of ways. Reducing the time spent on the CFD solution would remove a bottle neck in the modelling of ED nozzles, allowing a more comprehensive investigation into the ED concept to advance rapidly.

Model Improvements: Speed

The time taken to find the solution of a flow could be reduced in two ways; improving the accuracy of the initial conditions, and refining the mesh geometry. Initial conditions are at present derived assuming one dimensional flow. Whilst this is a good first approximation to the flow through planar and axisymmetric conventional nozzles, it is less accurate for planar ED nozzles, and far less accurate for the axisymmetric ED. A more representative initial state could be derived using the potential methods often utilised to find a starting flow for transonic aerofoil flows. Such methods would require some adaption, as the combined internal and external nature of the flow through the channel is more complex than the purely external flow surrounding aerofoils. However, this would significantly reduce the time taken to calculate a flow solution, as the initial conditions would be much closer to the converged result.

Improvements in both solution times and accuracy could be achieved by a revision of the grid generation technique. The formulation currently used is extremely basic, and was chosen primarily for ease of implementation. However, the essentially linear, constant density mesh is not necessarily the most efficient type. Variable density grids (possibly adaptive) could be used to target the density of the mesh more appropriately, and further reduce run-time. Developing algorithms which ensure perpendicular alignment of the cell boundaries at the nozzle walls and centreline would also improve the accuracy of the solution.

Model Improvements: Accuracy

The CFD scheme itself may be altered to more accurately model the flow by including the effects of chemical reactions, turbulence, and heat transfer. Incorporating reacting gas flows

and turbulence effects, the latter within both the main flow and in the form of boundary layer analysis, are complex issues requiring considerable revision of the basic Jameson model. However, whilst such processes would undoubtedly be important when considering the detail design stage it is unlikely that the magnitude of the effects would be significant enough to influence the viability of the ED nozzle concept as a whole. This work would therefore need only be attempted once the current models have been experimentally verified and proved reliable.

The analysis of heat transfer in the throat region is a higher priority. As noted in the introductory chapter, problems associated with cooling the region in the immediate vicinity of the throat were found to be insurmountable in axisymmetric plug nozzles, and are the primary reason why little interest is currently shown in that type. Whilst the minimum separation of the nozzle walls in axisymmetric ED nozzles is likely to be at least an order of magnitude greater than that typical of an equivalent plug, the minimum wall surface separation in the throat configurations examined within this dissertation vary from about a fifth to a tenth of the separation of a conventional bell. It must also be remembered that both surfaces require cooling, and that of the pintle is internal, presenting a greater difficulty with respect to manufacturing. It is possible that the need to maintain the maximum possible separation of these walls is such that it will impact upon the optimisation criteria used for nozzle contour generation, or at least be the primary factor in deciding the throat configuration and flow angle (see Sec. 9.2 below). It is therefore felt that this issue is now the most important obstacle to implementation of the ED nozzle, at least with respect to its non-altitude compensating, high altitude only variant.

Fortunately, the CFD based technique is particularly suited to this task, as wall temperatures are produced as a by product of the solution method. This provides a simple method by which an initial estimate of the magnitude of the heat transfer could be achieved. However, in order to produce a more accurate model, the current assumption of constant enthalpy must be removed, and a formulation for representing the heat transfer capabilities of the nozzle wall applied. Neither of these improvements should prove to be of great difficulty, especially if an appropriate complementary experimental program is implemented.

9.1.2 Viscous Flow Model

The treatment of the viscous region behind the pintle in ED nozzles may be split into two sections, that of the wake in its closed form, and the currently much simpler open wake free pressure boundary formulation.

Closed Wake Model

The closed wake model has been shown to provide at least broad agreement with the admittedly limited amount of experimental evidence available. The thrust contributed by the base pressure during vacuum operations has been shown to be a relatively small proportion of the total thrust, particularly in large expansion area ratio nozzles. For this reason, the improvement of this area of the ED model is less urgent than some others. That being said, detailed design and comparison of possible ED nozzle designs will eventually require a more accurate model of the closed wake flow to be produced. Although the amount of thrust produced is small, it is still important to get as good an estimate as possible of the thrust to allow accurate calculation of trajectories.

The framework of the method implemented allows improvements to be made as knowledge of the flow in the throat region increases, particularly with respect to boundary layer effects. An iterative procedure could also be devised to increase the accuracy of the calculation of the effective onflow Mach number. Experimental work would play an important part, as not only is there little currently available, but CFD based alternatives for analysing such flows as yet do not exist, although an active area of research.

Open Wake Mode

The model used to approximate the viscous region in the open wake mode is far more simplistic, being a straight forward assumption of a constant pressure boundary. Whilst a strong case has been made in support of this assumption from comparison with experimental results from studies on plug nozzles with open wakes, there will remain a question mark over the reliability of this assumption until an experimental program dedicated to answering this question has been completed.

A detailed examination of the problem would require pressure and velocity variation in the longtitudional direction from the pintle base to exit plane of the nozzle, and radially from the nozzle centreline to the free jet boundary, throughout the entire viscous field. These measurements would have to be taken over a range of operating pressure ratios. Alternatively, the accuracy of the assumption may be inferred from a successful prediction of wall pressures for a range of operating pressures, as the behaviour of the free jet boundary will effect the axial location and strength of the pressure rises at the nozzle wall. In practise, some combination of both these approaches is probably required.

Whatever the approach, the results should allow a more accurate semi empirical pressure distribution along the free jet boundary to be devised. Incorporation of a non constant pressure boundary within the MoC should not require considerable revision of the current

algorithms. This work is of a high priority for altitude compensating ED nozzles, as the accuracy of the assumption of atmospheric boundary is critical to the effectiveness of the altitude compensation. If this is found not to be the case, the ED nozzle in its present form may not altitude compensate sufficiently to warrant further examination for use as such, without considerable revision of the contour design methodology. However, the effectiveness or otherwise of the open wake mode is obviously irrelevant for continuation of the high altitude variant.

9.1.3 Supersonic Flow Model

The supersonic flow-field of the ED nozzle is modelled using either the irrotational or rotational MoC, depending upon whether a shock free, full flowing nozzle may or may not be assumed. These have been proven to be effective methods for the design and analysis of nozzle contours, and would probably be maintained even if the calculus of variations optimising method is removed (see Sec. 9.2). However, before the results of this analysis could be transformed into actual nozzle contours, a boundary layer calculation must be incorporated at the design stage to allow for the thickness of this viscous layer. The influence of the boundary layer with regard to the wall - shock wave interactions during altitude compensation may have a profound effect upon the performance prediction at low altitudes, and could effect flow stability and generate other unusual phenomena. Both these issues are now addressed

Boundary Layer Thickness Correction

Corrections for the thickness of boundary layers on bell nozzles are generally applied after optimisation of the contour. A detailed analysis of the boundary layers occurring along nozzle walls is extremely complex [5], and generally considered unnecessary. Instead, a simplified semi empirical approach is usual (e.g. that presented in Ref. 65).

ED nozzle contours are similar in many ways to those of bell nozzles, and hence a similar method would likely be effective. In fact, the rate of curvature of ED nozzles is generally much higher (as the flow must pass through a considerably greater angle change in about half the distance). This may create a slight decrease in the rate of growth of the boundary layer, as the nozzle cross sectional area is increased more rapidly, thinning the boundary layer (c.f. plug nozzles [4]). In vacuum flight this effect is likely to be added to by the accompanying increase in the favourable pressure gradient. Inclusion of an appropriate boundary layer correction factor in the design process is not therefore seen as a major obstacle in the path of the development of the ED concept, a simple adaption of a related method from bell nozzles should suffice. The compensating variant faces a more serious problem, however, when the

implications of altitude compensation on the boundary layer are considered.

Boundary layer - Compression Wave Interaction

Altitude compensation by definition requires an increase in pressure at the nozzle walls over that which would otherwise occur. This inevitably will cause a rise in wall pressure in the axial direction. Such a phenomenon is known as an adverse pressure gradient, and has a detrimental effect on nozzle performance as it causes the growth of the boundary layer and resultant momentum deficit. In some cases it may even trigger separation of the flow from the walls.

Even without shock wave interaction or separation, the prediction of the growth of such a boundary layer is difficult, as the standard methods by which boundary layer growth on conventional bell nozzles is estimated do not account for an adverse pressure gradient. Although plug and linear aerospike nozzles will also be effected by this phenomenon, no method to account for these losses has yet been widely published. An accurate prediction of the loss in thrust produced would require the development of a boundary layer method capable of dealing with the double curved surface and varying pressure gradients. However this is a detail design issue that may initially be allowed for via an empirical method, before a more accurate technique is developed. It is unlikely to be sufficiently detrimental to destroy the ED concept.

Unfortunately, one of the most striking and unexpected features of the behaviour of the altitude compensating ED nozzles analysed in this dissertation could have more serious implications. The most common method by which altitude compensation is achieved is through the interaction of shock waves with the nozzle walls, and this presents a challenging problem, for which the rotational MoC alone is not suitable. The interactions of shock waves with a boundary layer are complex, and an area of current research.

The probable result of the impact of the shock wave on the nozzle wall is the separation of the primary supersonic flow. Whether this has a beneficial effect depends upon the pressure recovery along the wall, and whether the flow subsequently re-attaches. If re-attachment does occur, there is the possibility that small separation bubbles would form along the contour. As the ambient pressure changes, these bubbles would move longtitudionally, generating the possibility of sudden changes in thrust when they burst at the nozzle exit.

A key factor in the consideration of such issues is the stability of the interaction. Flow separation is generally prevented on bell nozzles due to the risk of structurally damaging vibrations caused by the instability of the separation point. However, shock induced separation would likely form a more stable and robust phenomena.

As has been mentioned, the subject of shock wave - boundary layer interaction is a complex one, with no simple modelling technique available. Investigation of this phenomenon would have to proceed in an experimental manner, at least initially. Fortunately, the majority of the possible flow behaviour outlined above would produce noticeable effects on the wall pressures, reducing the complexity of the experimental analysis. How severe the effects are could have serious implications for the applicability of the compensating variant of the ED nozzle, particularly of minimum length design.

Other Separation Criteria

As mentioned above, bell nozzles are designed such that the primary supersonic flow never separates from the walls. This removes the risk of unwanted structural vibrations. The Summerfield criterion discussed throughout this dissertation provides a simple method by which separation may be avoided, and has been applied to both the bell and ED nozzle types.

However, conical nozzles are generally not required to meet this criterion, as flow separation from the walls is stable due to the constant wall angle. In fact the primary reason for unstable separation in bell nozzles is the low wall angles in the vicinity of the nozzle exit plane, which allow the point of separation to move easily. In ED nozzles, the wall angles and rate of change of wall angle with length are greater, which may increase the stability of the separation point. If this is the case, the Summerfield criteria represents an overly conservative approach to the separation problem, and may be abandoned in favour of a more optimistic alternative

This would raise the maximum exit Mach number for any compensating ED nozzle where separation of the flow from the outer walls before interaction of the compensating shock wave is the limiting factor. However, this idea is yet to be seriously tested.

9.2 Philosophy Revision: Contour Optimisation

Historically, all rocket nozzles have been designed to optimise the ratio of vacuum thrust to total nozzle length. This provides a simple criterion allowing comparison of nozzles within a class, and between competing concepts. For nozzles which are stored within the main structure before use (e.g. upper stages, satellite propulsion), minimising length is of critical importance, as reducing this will reduce inter staging lengths, which will have a higher mass per unit length than the nozzle itself. In this case, reducing the nozzle length will reduce overall system mass, even if a shorter nozzle is slightly heavier. The case for minimising length

is less strong for conventional nozzles which are not subject to such storage restrictions, and here it may be argued that an alternative criteria should be used. However, for simplicity a high degree of dependence of mass to length is assumed, and the criteria retained.

ED nozzles, however, complicate the situation considerably. The high altitude variant of ED nozzle would be subject to the same storage restrictions as conventional upper stage nozzles, and hence minimising length is still a sensible optimisation criteria. However, optimisation of the nozzle contour may be effected by the heat transfer in the throat region and the decoupling of nozzle mass and length produced by the independence of the throat radius from nozzle length. The optimisation of altitude compensating nozzles may need a more complete review, primarily due to uncertainties over the relationship of length to mass, and the shock wave interaction with the boundary layer that produces the compensating phenomenon.

9.2.1 Limits Due to Heat Transfer

The modelling problem associated with heat transfer was discussed in the previous section, and as was noted the impact on optimising ED nozzle contours could be significant. The size of the minimum separation of nozzle walls in the throat region is highly dependent on the throat angle and radial location. Essentially increasing either of these variables results in a reduced minimum separation of the nozzle walls, but also tends to improve the vacuum thrust coefficient for a given nozzle length, particularly for high area ratio engines. This therefore represents an extra criteria which must be factored in when optimising for length, as left unchecked pure length optimisation would result in a very small wall separation at the throat. However, an accurate assessment of the impact of the heat transfer requirements at the throat on the optimisation process obviously requires an improved throat flow model which incorporates such transfer to be devised first.

9.2.2 Decoupling of Length and Mass

Minimising length to minimise mass assumes a very high correlation between mass and length. There is reason to doubt the validity of this assumption even for bell and conical nozzles, as the mass of a nozzle will be related not just to its length, but to the surface area of the solid of revolution formed by the contour (in axisymmetric flow), and the thickness of material required to resist the local wall pressure.

The ED nozzle will have an even lower correlation between these two factors, due to the displacement of the throat from the nozzle centreline. This has the effect of decoupling to a far greater extent the nozzle area ratio (and hence C_F) and nozzle length, and allows

very short nozzles of high thrust to be designed simply by increasing the radius of the throat. The seeming performance gain is only apparent, as not only would the greater throat radius exacerbate the problem of cooling the pintle, but the increased radius of all parts of the nozzle (pintle base, outer nozzle wall, etc.) will result in an appreciable increase in the mass per unit length.

It is therefore recommended that an alternative method for optimisation be developed that is based on a parameter(s) that directly relate to mass. Unfortunately, this would almost certainly require the abandonment of the calculus of variations based technique in favour of a direct method (e.g. that proposed in Ref. 66), increasing the complexity and time required for the task of contour generation. However, the potential benefits could be significant. These would undoubtedly feed back to conventional bell nozzle design, creating lighter nozzles where minimising length is unnecessary. The implications would be even more important if a method for incorporating the effect of boundary layers into the optimisation routine could be achieved. These represent significant losses for large expansion ratio nozzles, but are currently only included in the form of a correction after contour optimisation.

It is also worth remembering that the limits on the range of possible M_E found to be restrictive as far as axisymmetric nozzles are concerned are a function of the equations used to optimise the nozzle length. If these optimisation criteria are relaxed, the range of possible contour solutions will rise.

9.2.3 Optimising for Altitude Compensation

The rise in pressure along the nozzle wall caused by pressure compensation will occur in both plug and ED nozzles of planar or axisymmetric design. In fact it will occur in any altitude compensating design which relies on variations in the flow-field to produce the compensating effect, rather than a mechanical devise (e.g. translating inserts). However, no work as yet appears to have been carried out to analyse the impact that this adverse pressure gradient will have on the nozzle flow-field.

Experimental results from planar plug nozzles appear to show a reasonable match between wall pressures predicted using the irrotational MoC and experimental results [8]. This reveals that neither shock wave compression nor boundary layer separation due to the adverse pressure gradient occur in the nozzles experimented upon, for if either of these phenomena were present, the experimental and theoretical wall pressure profiles would differ considerably. However, sufficient margin for error does exist within the results to allow for the possibility that the boundary layer is increasing rapidly in thickness, creating a significant performance drop.

The ED nozzles examined in this dissertation differ from the plug contours in Ref. [8] in several significant ways. As was noted in the introductory chapter, plug nozzle designs are generally of ideal contour type. This is necessary to ensure parallel flow at the exit of the full length plug (important because the radial distance of the plug tip is zero). This results in a smaller deviation of the throat angle form the horizontal, and a longer contour for a given exit Mach number. It also means that the last characteristic in the nozzle flow-field is at the Mach angle.

A full length plug nozzle will therefore be of greater length than an equivalent thrust ED. However, the low throat angle and greater length combine to reduce the rate of change of wall gradient, and this in turn spaces out the compression waves. This is primarily due to the last characteristic being a Mach wave, which means that any disturbance in the flow at the point of the external expansion will propagate immediately to the nozzle wall at the exit plane. The combined effect of this design philosophy is a longer nozzle that compensates at a lower atmospheric pressure and in a more gradual fashion. Truncating the nozzle reduces the length back down to a similar length as that of an ED, whilst retaining the gradual nature of the wall pressure rise. However, this will result in less effective altitude compensation, and the atmospheric pressure at which altitude compensation initiates will rise.

The shock wave reflection at the wall is therefore a phenomenon related to the length optimisation of the ED nozzle. Even if a direct mass parameter as advocated in the previous subsection could be found, it may not provide the best solution to the contour design of compensating ED nozzles. Both the strength of the compression wave interaction with the boundary layer, and the pressure range of altitude compensation, may be manipulated by careful contour design, and hence even if the minimum length ED nozzle is found to be unsatisfactory, an alternative design philosophy may well allow the ED nozzle to be successful.

9.3 Wake Transition Behaviour

The behaviour of the wake flow-field during transition between open and closed wake modes has largely been ignored in this dissertation. Whilst it is only an area of concern for the generally less well defined compensating ED variant, it is still an important issue that will require analysis before altitude compensating ED nozzles become a reality. Issues relating to this flow phenomena include the possibility of hysteresis, and unstable oscillations resulting in high structural loads, particularly on the pintle. It may be possible to control the wake closure actively, through injection of mass into the base region to inhibit wake closure until an overall pressure ratio is reached which ensures rapid and complete closure, or translation of the pintle itself. The subject of wake transition requires considerable attention, but this will be an inevitable by-product of research into other aspects of the compensating ED design.

Appendix A

Axisymmetric and Two-dimensional Dutton Addy Throat Flow Equations.

Presented here are the equations used to generate the flow in the throat region of conventional nozzles, based on the Dutton Addy expansion method. Given input parameters γ, $R_w^=$, and an arbitrary expansion coefficient η, using the expansion

$$\epsilon = \frac{1}{R_w^= + \eta} \tag{A.1}$$

and the transformed z coordinate

$$z = \left[\frac{\gamma+1}{2}\epsilon\right]^{-\frac{1}{2}} x \tag{A.2}$$

The velocity expansion in axisymmetric flow is then

$$u_1(z,y) = \frac{1}{2}y^2 - \frac{1}{4} + z \tag{A.3}$$

$$v_1(z,y) = \frac{1}{4}y^3 - \frac{1}{4}y + yz \tag{A.4}$$

$$u_2(z,y) = \frac{2\gamma+9}{24}y^4 - \frac{4\gamma+15-12\eta}{24}y^2 + \frac{10\gamma+57-72\eta}{288} + \left(y^2 + \frac{4\eta-5}{8}\right)z - \frac{2\gamma-3}{6}z^2 \tag{A.5}$$

$$v_2(z,y) = \frac{\gamma+3}{9}y^5 - \frac{20\gamma+63-36\eta}{96}y^3 + \frac{28\gamma+93-108\eta}{288}y + \left(\frac{2\gamma+9}{6}y^3 - \frac{4\gamma+15-12\eta}{12}y\right)z + yz^2 \tag{A.6}$$

$$
\begin{aligned}
u_3(z,y) = & \frac{566\gamma^2+1737\gamma+3069}{10368}y^6 \\
& - \frac{388\gamma^2+(1161-384\eta)\gamma+1881-1728\eta}{2304}y^4 \\
& + \frac{304\gamma^2+(831-576\eta)\gamma+1242-2160\eta+864\eta^2}{1728}y^2 \\
& - \frac{2708\gamma^2+(7839-5760\eta)\gamma+14211-32832\eta+20736\eta^2}{82944} \\
& + \Big[\frac{52\gamma^2+51\gamma+327}{384}y^4 - \frac{52\gamma^2+75\gamma+279-288\eta}{192}y^2 \\
& \qquad + \frac{92\gamma^2+180\gamma+639-1080\eta+432\eta^2}{1152}\Big]z \\
& + \Big[-\frac{7\gamma-3}{8}y^2 + \frac{(13-16\eta)\gamma-27+24\eta}{48}\Big]z^2 + \frac{4\gamma^2-57\gamma+27}{144}z^3
\end{aligned}
\tag{A.7}
$$

$$
\begin{aligned}
v_3(z,y) = & \frac{6836\gamma^2+23031\gamma+30627}{82944}y^7 \\
& - \frac{3380\gamma^2+(11391-3840\eta)\gamma+15291-11520\eta}{13824}y^5 \\
& + \frac{3424\gamma^2+(11271-7200\eta)\gamma+15228-22680\eta+6480\eta^2}{13824}y^3 \\
& - \frac{7100\gamma^2+(22311-20160\eta)\gamma+30249-66960\eta+38880\eta^2}{82944}y \\
& + \Big[\frac{556\gamma^2+1737\gamma+3069}{1728}y^5 - \frac{388\gamma^2+(1161-384\eta)\gamma+1881-1728\eta}{576}y^3 \\
& \qquad + \frac{304\gamma^2+(831-576\eta)\gamma+1242-2160\eta+864\eta^2}{864}y\Big]z \\
& + \Big[\frac{52\gamma^2+51\gamma+327}{192}y^3 - \frac{52\gamma^2+75\gamma+279-288\eta}{192}y\Big]z - \frac{7\gamma-3}{12}yz^3
\end{aligned}
\tag{A.8}
$$

Which is identical to that given by Dutton and Addy in Ref. 35. As

$$u(z,y) = 1 + u_1\epsilon + u_2\epsilon^2 + u_3\epsilon^3 + \ldots \tag{A.9}$$

$$v(z,y) = \Phi(v_1\epsilon + v_2\epsilon^2 + v_3\epsilon^3 + \ldots) \tag{A.10}$$

where

$$\Phi = \Big[\frac{\gamma+1}{2}\epsilon\Big]^{\frac{1}{2}}$$

the important flow properties M and θ may be solved for directly from

$$
\begin{aligned}
M(z,y) = 1 + \frac{\gamma+1}{2}\Big(u_1\epsilon + \Big[u_2 + \frac{3}{4}(\gamma-1)u_1^2\Big]\epsilon^2 + \Big[u_3 + \frac{\gamma+1}{4}v_1^2 \\
+ \frac{3}{2}(\gamma-1)u_1u_2 + \frac{5\gamma^2-8\gamma+3}{8}u_1^3\Big]\epsilon^3 + \ldots\Big)
\end{aligned}
\tag{A.11}
$$

$$\theta(z,y) = \Phi\big(v_1\epsilon + (v_2 - u_1v_1)\epsilon^2 + (v_3 - u_1v_2 - u_2v_1 + u_1^2v_1)\epsilon^3 + ..\big) \tag{A.12}$$

As mentioned in Ch. 2, no attempt was made in the original paper by Dutton and Addy to allow for two-dimensional flow, presumably because at the time there were no real world applications for such geometries. However, for the work in this dissertation, a two-dimensional method was developed, using the same technique.

As before

$$\epsilon = \frac{1}{R_w^{\equiv} + \eta} \tag{A.13}$$

However the transformed z coordinate is given by

$$z = [(\gamma + 1)\epsilon]^{-\frac{1}{2}} x \tag{A.14}$$

The velocity expansion in two-dimensional flow is then

$$u_1(z, y) = \frac{1}{2}y^2 - \frac{1}{6} + z \tag{A.15}$$

$$v_1(z, y) = \frac{1}{6}y^3 - \frac{1}{6}y + yz \tag{A.16}$$

$$u_2(z, y) = \frac{\gamma + 6}{18}y^4 - \frac{2\gamma + 9 - 9\eta}{18}y^2 + \frac{4\gamma + 120 - 195\eta}{1080} + \left[y^2 + \frac{\eta - 1}{2}\right]z - \frac{2\gamma - 3}{6}z^2 \tag{A.17}$$

$$v_2(z, y) = \frac{22\gamma + 75}{360}y^5 - \frac{10\gamma + 42 - 27\eta}{108}y^3 + \frac{34\gamma + 195 - 270\eta}{1080}y + \left[\frac{4\gamma + 24}{18}y^3 - \frac{4\gamma + 18 - 18\eta}{18}y\right]z + yz^2 \tag{A.18}$$

$$\begin{aligned} u_3(z, y) = {} & \frac{362\gamma^2 + 1449\gamma + 3177}{12960}y^6 \\ & - \frac{194\gamma^2 + (837 - 396\eta)\gamma + 1665 - 1620\eta}{2592}y^4 \\ & + \frac{854\gamma^2 + (3687 - 3960\eta)\gamma + 6759 - 11970\eta + 6480\eta^2}{12960}y^2 \\ & - \frac{782\gamma^2 + (5523 - 7308\eta)\gamma + 22887 - 55188\eta + 43470\eta^2}{272160} \\ & + \left[\frac{26\gamma^2 + 27\gamma + 237}{288}y^4 - \frac{26\gamma^2 + 51\gamma + 189 - 216\eta}{144}y^2 \right. \\ & \qquad \left. + \frac{134\gamma^2 + (429 - 350\eta)\gamma + 1743 - 2880\eta + 1620\eta^2}{4320}\right]z \\ & + \left[-\frac{5\gamma}{4}y^2 + \frac{(7 - 12\eta)\gamma - 18 + 18\eta}{36}\right]z^2 + \frac{2\gamma^2 - 33\gamma + 9}{72}z^3 \end{aligned} \tag{A.19}$$

$$
\begin{aligned}
v_3(z,y) = & \frac{6574\gamma^2 + 26481\gamma + 40059}{181440} y^7 \\
& - \frac{2254\gamma^2 + (10113 - 4176\eta)\gamma + 16479 - 13284\eta}{25920} y^5 \\
& + \frac{5026\gamma^2 + (25551 - 21390\eta)\gamma + 46377 - 72900\eta + 24300\eta^2}{77760} y^3 \\
& - \frac{7570\gamma^2 + (45927 - 62034\eta)\gamma + 98757 - 231336\eta + 170100\eta^2}{544320} y \\
& + \left[\frac{362\gamma^2 + 1449\gamma + 3177}{2160} y^5 - \frac{194\gamma^2 + (837 - 396\eta)\gamma + 1665 - 1620\eta}{648} y^3 \right. \\
& \qquad \left. + \frac{854\gamma^2 + (3687 - 3960\eta)\gamma + 6759 - 11970\eta + 6480\eta^2}{6480} y \right] z \\
& + = \left[\frac{26\gamma^2 + 27\gamma + 237}{144} y^3 - \frac{26\gamma^2 + 51\gamma + 189 - 216\eta}{144} y \right] z^2 - \frac{5\gamma}{6} y z^3
\end{aligned}
\tag{A.20}
$$

Eqns. A.9 to A12 are equally valid in two-dimensional flow, with the exception that

$$\Phi = [(\gamma + 1)\epsilon]^{\frac{1}{2}}$$

Appendix B

Rao's Optimisation Method

As was noted in Ch. 3, the method used by Rao for optimising the length of bell nozzles is widely used. However, due to the limited length of the paper in which it appears, the details of the calculation are not provided. This Appendix therefore contains a full derivation of the resulting equations (3.25 to 3.29 in the main body of the text), beginning with the integral to be maximised:

$$I = \int_C^E (f_1 + \lambda_2 f_2 + \lambda_3 f_3) dy \tag{B.1}$$

where

$$f_1 = [(P - P_a) + \rho u^2 \frac{\sin(\phi - \theta)\cos\theta}{\sin\phi}] y \tag{B.2}$$

$$f_2 = \rho u \frac{\sin(\phi - \theta)}{\sin\phi} y \tag{B.3}$$

$$f_3 = \cot\phi \tag{B.4}$$

As in Ch. 3, point D denotes the point on the control surface coinciding with the edge of the 'kernel' (refer to Fig. 3.4 on page 59), and for an optimisation problem, the LRC between C and D is therefore fixed. This results in δC, δM and $\delta\theta$ all being zero in this region. $\phi = (\mu + \theta)$ is then a known quantity, leading to $\delta\phi$ being zero. This leaves only δD as unknown. Between D and E all the previous are non zero, as is δy_E. M and θ are continuous in the interior of the flow, and ϕ is continuous along CDE. This means that the integrand in the above equation is continuous, resulting in the variation of D not entering into the first variation of the integral. Setting this first variation to zero will result in the required maximisation. Therefore

$$\delta I = 0 = \int_{y_D}^{Y_E} \Big[(f_{1M} + \lambda_2 f_{2M} + \lambda_3 f_{3M})\delta M + (f_{1\theta} + \lambda_2 f_{2\theta} + \lambda_3 f_{3\theta})\delta\theta + (f_{1\phi} + \lambda_2 f_{2\phi} + \lambda_3 f_{3\phi})\delta\phi \Big] dy + \delta y_E (f_1 + \lambda_2 f_2 + \lambda_3 f_3)_{at\,E} \tag{B.5}$$

where subscripts refer to partial differentiation with respect to that variable. As variations in M, θ, ϕ, and y_E are arbitrary, Eqn. B.5 requires

$$f_{1M} + \lambda_2 f_{2M} + \lambda_3 f_{3M} = 0 \tag{B.6}$$

$$f_{1\theta} + \lambda_2 f_{2\theta} + \lambda_3 f_{3\theta} = 0 \tag{B.7}$$

$$f_{1\phi} + \lambda_2 f_{2\phi} + \lambda_3 f_{3\phi} = 0 \tag{B.8}$$

$$f_1 + \lambda_2 f_2 + \lambda_3 f_3 = 0 \text{ at E} \tag{B.9}$$

Inspection of Eqn. B.4 reveals that both f_{3M} and $f_{3\theta}$ are zero, and hence equating Eqns. B.6 and B.7 gives

$$f_{1M} f_{2\theta} = f_{1\theta} f_{2M} \tag{B.10}$$

Substituting the standard isentropic relations

$$P = P_c(1 + \frac{\gamma - 1}{2} M^2)^{\frac{-\gamma}{\gamma-1}} \tag{B.11}$$

$$\rho = \rho_c(1 + \frac{\gamma - 1}{2} M^2)^{\frac{-1}{\gamma-1}} \tag{B.12}$$

$$u^2 = M^2 a^2 = M^2 \gamma R T_c (1 + \frac{\gamma - 1}{2} M^2)^{-1} \tag{B.13}$$

into Eqn. B.2 results in

$$\begin{aligned} f_1 &= \Big[P_c(1 + \frac{\gamma - 1}{2} M^2)^{\frac{-\gamma}{\gamma-1}} - P_a \\ &\qquad + \rho_c(1 + \frac{\gamma - 1}{2} M^2)^{\frac{-1}{\gamma-1}} M^2 \gamma R T_c (1 + \frac{\gamma - 1}{2} M^2)^{-1} \frac{\sin(\phi - \theta)\cos\theta}{\sin\phi}\Big] y \\ &= \Big[P_c(1 + \frac{\gamma - 1}{2} M^2)^{\frac{-\gamma}{\gamma-1}} - P_a + M^2 \gamma R T_c \rho_c \frac{\sin(\phi - \theta)\cos\theta}{\sin\phi}(1 + \frac{\gamma - 1}{2} M^2) - \frac{\gamma}{\gamma - 1}\Big] y \\ &= \Big[P_c(1 + \frac{\gamma - 1}{2} M^2)^{\frac{-\gamma}{\gamma-1}}(1 + M^2 \gamma \frac{\sin(\phi - \theta)\cos\theta}{\sin\phi}) - P_a\Big] y \end{aligned} \tag{B.14}$$

Partial differentiating with respect to M and θ produces

$$\begin{aligned} f_{1M} = P_c y \Big[&\frac{\partial}{\partial M}(1 + \frac{\gamma - 1}{2} M^2)^{\frac{-\gamma}{\gamma-1}}(1 + M^2 \gamma \frac{\sin(\phi - \theta)\cos\theta}{\sin\phi}) \\ &+ (1 + \frac{\gamma - 1}{2} M^2)^{\frac{-\gamma}{\gamma-1}} 2M\gamma \frac{\sin(\phi - \theta)\cos\theta}{\sin\phi}\Big] \end{aligned} \tag{B.15}$$

and

$$f_{1\theta} = P_c y (1 + \frac{\gamma - 1}{2} M^2)^{\frac{-\gamma}{\gamma-1}} M^2 \gamma \Big(\frac{-\cos(\phi - \theta)}{\sin\phi} - \frac{\sin(\phi - \theta)\sin\theta}{\sin(\phi)}\Big) \tag{B.16}$$

The same substitutions may be made into Eqn. B.3 :

$$\begin{aligned} f_2 &= \rho_c(1 + \frac{\gamma - 1}{2} M^2)^{\frac{-1}{\gamma-1}} M \sqrt{\gamma R T_c}(1 + \frac{\gamma - 1}{2} M^2)^{\frac{-1}{2}} \frac{\sin(\phi - \theta)}{\sin\phi} y \\ &= \rho_c \sqrt{\gamma R T_c}\, y \frac{\sin(\phi - \theta)}{\sin\phi} M(1 + \frac{\gamma - 1}{2} M^2)^{\frac{-(\gamma+1)}{2(\gamma-1)}} \end{aligned} \tag{B.17}$$

and partial differentiation results in

$$f_{2M} = \rho_c \sqrt{\gamma R T_c} y \frac{\sin(\phi-\theta)}{\sin\phi}\left[(1+\frac{\gamma-1}{2}M^2)^{\frac{-(\gamma+1)}{2(\gamma-1)}} + M\frac{\partial}{\partial M}(1+\frac{\gamma-1}{2}M^2)^{\frac{-(\gamma+1)}{2(\gamma-1)}}\right] \tag{B.18}$$

and

$$f_{2\theta} = \rho_c \sqrt{\gamma R T_c} y \frac{-\cos(\phi-\theta)}{\sin\phi} M(1+\frac{\gamma-1}{2}M^2)^{\frac{-(\gamma+1)}{2(\gamma-1)}} \tag{B.19}$$

The LHS of Eqn. B.10 may now be calculated from Eqns. B.15 and B.19, and the RHS from B.16 and B.18. Equating these and cancelling the common factor $-P_c y^2 \rho_c \sqrt{\gamma R T_c} M/\sin\phi$ results in

$$\begin{aligned}
&\Big[\frac{\partial}{\partial M}(1+\frac{\gamma-1}{2}M^2)^{\frac{-\gamma}{\gamma-1}}(1+M^2\gamma\frac{\sin(\phi-\theta)\cos\theta}{\sin\phi}) \\
&\quad + (1+\frac{\gamma-1}{2}M^2)^{\frac{-\gamma}{\gamma-1}} 2M\gamma\frac{\sin(\phi-\theta)\cos\theta}{\sin\phi}\Big]\cos(\phi-\theta)(1+\frac{\gamma-1}{2}M^2)^{\frac{-(\gamma+1)}{2(\gamma-1)}} \\
&= \Big[(1+\frac{\gamma-1}{2}M^2)^{\frac{-\gamma}{\gamma-1}} M\gamma\Big(\frac{\cos(\phi-\theta)\cos\theta}{\sin\phi} + \frac{\sin(\phi-\theta)\sin\theta}{\sin\phi}\Big)\sin(\phi-\theta)\Big] \\
&\qquad \Big[(1+\frac{\gamma-1}{2}M^2)^{\frac{-(\gamma+1)}{2(\gamma-1)}} + M\frac{\partial}{\partial M}(1+\frac{\gamma-1}{2}M^2)^{\frac{-(\gamma+1)}{2(\gamma-1)}}\Big]
\end{aligned} \tag{B.20}$$

Substituting

$$\frac{\partial}{\partial M}(1+\frac{\gamma-1}{2}M^2)^{\frac{-\gamma}{\gamma-1}} = -\gamma M(1+\frac{\gamma-1}{2}M^2)^{\frac{-\gamma}{\gamma-1}}(1+\frac{\gamma-1}{2}M^2)^{-1} \tag{B.21}$$

into the LHS of Eqn. B.20 results in

$$\begin{aligned}
\gamma M(1+\frac{\gamma-1}{2}M^2)^{\frac{-\gamma}{\gamma-1}}\Big[&-(1+\frac{\gamma-1}{2}M^2)^{-1}(1+M^2\gamma\frac{\sin(\phi-\theta)\sin\theta}{\sin\phi}) \\
&+\frac{2\sin(\phi-\theta)\sin\theta}{\sin\phi}\Big]\cos(\phi-\theta)(1+\frac{\gamma-1}{2}M^2)^{\frac{-(\gamma+1)}{2(\gamma-1)}}
\end{aligned} \tag{B.22}$$

It is now possible to divide both sides of Eqn. B.20 by $\gamma M(1+\frac{\gamma-1}{2}M^2)^{\frac{-\gamma}{\gamma-1}}$ to give

$$\begin{aligned}
&\Big[-(1+\frac{\gamma-1}{2}M^2)^{-1}(1+M^2\gamma\frac{\sin(\phi-\theta)\sin\theta}{\sin\phi}) \\
&\qquad +\frac{2\sin(\phi-\theta)\sin\theta}{\sin\phi}\Big]\cos(\phi-\theta)(1+\frac{\gamma-1}{2}M^2)^{\frac{-(\gamma+1)}{2(\gamma-1)}} \\
&\quad = \Big(\frac{\cos(\phi-\theta)\cos\theta}{\sin\phi} + \frac{\sin(\phi-\theta)\sin\theta}{\sin\phi}\Big)\sin(\phi-\theta) \\
&\qquad \Big[(1+\frac{\gamma-1}{2}M^2)^{\frac{-(\gamma+1)}{2(\gamma-1)}} + M\frac{\partial}{\partial M}(1+\frac{\gamma-1}{2}M^2)^{\frac{-(\gamma+1)}{2(\gamma-1)}}\Big]
\end{aligned} \tag{B.23}$$

As

$$\frac{\partial}{\partial M}(1+\frac{\gamma-1}{2}M^2)^{\frac{-(\gamma+1)}{2(\gamma-1)}} = \frac{-(\gamma+1)}{2}M(1+\frac{\gamma-1}{2}M^2)^{\frac{-(\gamma+1)}{2(\gamma-1)}}(1+\frac{\gamma-1}{2}M^2)^{-1} \tag{B.24}$$

the RHS of Eqn. B.23 may be rewritten

$$\left(\frac{\cos(\phi-\theta)\cos\theta}{\sin\phi}+\frac{\sin(\phi-\theta)\sin\theta}{\sin\phi}\right)\sin(\phi-\theta)$$
$$(1+\frac{\gamma-1}{2}M^2)^{\frac{-(\gamma+1)}{2(\gamma-1)}}\left[1-M^2\frac{\gamma+1}{2}(1+\frac{\gamma-1}{2}M^2)^{-1}\right] \quad \text{(B.25)}$$

Dividing both sides of Eqn. B.23 by $(1+\frac{\gamma-1}{2}M^2)^{\frac{-(\gamma+1)}{2(\gamma-1)}}$ therefore results in

$$\left[\frac{2\sin(\phi-\theta)\sin\theta}{\sin\phi}-(1+\frac{\gamma-1}{2}M^2)^{-1}\left(1+M^2\gamma\frac{\sin(\phi-\theta)\sin\theta}{\sin\phi}\right)\right]\cos(\phi-\theta)$$
$$=\left(\frac{\cos(\phi-\theta)\cos\theta}{\sin\phi}+\frac{\sin(\phi-\theta)\sin\theta}{\sin\phi}\right)\sin(\phi-\theta)\left[1-M^2\frac{\gamma+1}{2}(1+\frac{\gamma-1}{2}M^2)^{-1}\right] \quad \text{(B.26)}$$

Multiplying through by $(1+\frac{\gamma-1}{2}M^2)\sin\phi$ reduces this to

$$\left[(2+(\gamma-1)M^2)\sin(\phi-\theta)\cos\theta-(\sin\phi+M^2\gamma\sin(\phi-\theta)\cos\theta\right]\cos(\phi-\theta)$$
$$=\left[\cos(\phi-\theta)\cos\theta+\sin(\phi-\theta)\sin\theta\right]\sin(\phi-\theta)(1+\frac{\gamma-1}{2}M^2-\frac{\gamma+1}{2}M^2) \quad \text{(B.27)}$$

Expanding:

$$2\sin(\phi-\theta)\cos\theta\cos(\phi-\theta)-M^2\sin(\phi-\theta)\cos\theta\cos(\phi-\theta)-\sin\phi\cos(\phi-\theta)$$
$$=\left[\cos(\phi-\theta)\cos\theta\sin(\phi-\theta)+\sin^2(\phi-\theta)\sin\theta\right](1-M^2) \quad \text{(B.28)}$$

and collecting and cancelling terms

$$\begin{aligned}M^2\sin^2(\phi-\theta)\sin\theta &= \sin^2(\phi-\theta)\sin\theta+\sin\phi\cos(\phi-\theta)-\sin(\phi-\theta)\cos\theta\cos(\phi-\theta)\\ &= -\sin(\phi-\theta)\left(\cos\theta\cos(\phi-\theta)-\sin(\phi-\theta)\sin\theta\right)+\sin\phi\cos(\phi-\theta)\\ &= -\sin(\phi-\theta)\cos\phi+\sin\phi\cos(\phi-\theta)\\ &= \sin\theta\end{aligned} \quad \text{(B.29)}$$

Hence

$$\sin^2(\phi-\theta)=\frac{1}{M^2} \quad \text{(B.30)}$$

and therefore

$$\phi-\theta=\sin^{-1}\frac{1}{M}=\mu \quad \text{(B.31)}$$

Eqn. B.31 shows that between D and E, the control surface follows the last LRC in the nozzle, and is the same as Eqn. 3.25. The next stage is to find the values of the LaGrangian multipliers, λ_2 and λ_3.

It has already been noted that $f_{3\theta}$ is zero. Eqn. B.7 may therefore be written as

$$-\lambda_2 = \frac{f_{1\theta}}{f_{2\theta}} \tag{B.32}$$

Differentiating Eqns. B.2 and B.3 with respect to θ (without substituting for u) allows this calculation to be made

$$\begin{aligned} -\lambda_2 &= \frac{-\rho u^2 y\left(\frac{\cos(\phi-\theta)\cos\theta}{\sin\phi} + \frac{\sin(\phi-\theta)\sin\theta}{\sin\phi}\right)}{-\rho u y \frac{\cos(\phi-\theta)}{\sin\phi}} \\ &= u\frac{\cos(\phi-\theta)\cos\theta + \sin(\phi-\theta)\sin\theta}{\cos(\phi-\theta)} \end{aligned} \tag{B.33}$$

Substituting for ϕ using Eqn. B.31 results in.

$$\begin{aligned} -\lambda_2 &= u\frac{\cos\mu\cos\theta + \sin\mu\sin\theta}{\cos\mu} \\ &= \frac{u\cos(\theta-\mu)}{\cos\mu} \end{aligned} \tag{B.34}$$

which is Eqn. 3.26, as was desired.

Turning to λ_3, Eqn. B.4 may be expressed as

$$-\lambda_3 = \frac{f_{1\phi} + \lambda_2 f_{2\phi}}{f_{3\phi}} \tag{B.35}$$

Differentiation of Eqns. B.2, B.3 and B.4 with respect to ϕ produces

$$f_{1\phi} = \rho u^2 y\left(\frac{\cos(\phi-\theta)\cos\theta}{\sin\phi} - \frac{\cos\phi\sin(\phi-\theta)\cos\theta}{\sin^2\phi}\right) \tag{B.36}$$

$$f_{2\phi} = \rho u y\left(\frac{\cos(\phi-\theta)}{\sin\phi} - \frac{\cos\phi\sin(\phi-\theta)}{\sin^2\theta}\right) \tag{B.37}$$

$$f_{3\phi} = \frac{-1}{\sin^2\phi} \tag{B.38}$$

Substituting these values into Eqn. B.35 results in

$$\begin{aligned} -\lambda_3 = \rho u^2 y\Big[&\big(-\cos(\phi-\theta)\cos\theta\sin\phi - \cos\phi\cos\theta\sin(\phi-\theta)\big) \\ &+ \big(\cos(\phi-\theta)\sin\phi - \cos\phi\sin(\phi-\theta)\big)\frac{\cos(\theta-\mu}{\cos\mu}\Big] \end{aligned} \tag{B.39}$$

Then substituting for ϕ using Eqn. B.31 gives

$$
\begin{aligned}
-\lambda_3 = y\rho u^2\Big[&\big(-\cos\mu\cos\theta\sin(\theta+\mu)+\cos(\theta+\mu)\cos\theta\sin\mu\big)\\
&+\big(\cos\mu\sin(\theta+\mu)-\cos(\theta+\mu)\sin\mu\big)\frac{\cos(\theta-\mu)}{\cos\mu}\Big]\\
=\Big[&-\cos\mu\cos\theta\sin(\theta+\mu)+\cos(\theta+\mu)\cos\theta\sin\mu\\
&+\cos(\theta-\mu)\sin(\theta+\mu)-\cos(\theta+\mu)\cos(\theta-\mu)\tan\mu\Big]\\
= y\rho u^2\tan\mu\Big[&-\cos^2\mu\cos\theta\frac{\sin(\theta+\mu)}{\sin\mu}+\cos(\theta+\mu)\cos\theta\cos\mu\\
&+\frac{\cos(\theta-\mu)\sin(\theta+\mu)\cos\mu}{\sin\mu}-\cos(\theta+\mu)\cos(\theta-\mu)\Big]\\
= \rho u^2\tan\mu\Big[&\cos\theta\cos\mu\cos(\theta+\mu)+\sin\theta\cos\mu\sin\theta\cos\mu\\
&+\sin\theta\cos\mu\cos\theta\sin\mu-(\cos\theta\cos\mu-\sin\theta\sin\mu)(\cos\theta\cos\mu-\sin\theta\sin\mu)\Big]\\
= \rho u^2\tan\mu\Big[&\cos\theta\cos\mu(\cos(\theta+\mu)+\sin\theta\sin\mu-\cos\theta\cos\mu)+\sin^2\theta(\sin^2\mu+\cos^2\mu)\Big]\\
= \rho u^2\tan\mu\Big[&\cos\theta\cos\mu(\cos(\theta+\mu)-(\cos\theta\cos\mu-\sin\theta\sin\mu))+\sin^2\theta\Big]
\end{aligned}
\tag{B.40}
$$

and hence

$$
-\lambda_3 = y\rho u^2\sin^2\theta\tan\mu \tag{B.41}
$$

and this is Eqn. 3.27.

Next, substituting for the LaGrangian multipliers in Eqn. B.9 will allow flow conditions at E to be predicted:

$$
\begin{aligned}
&\Big[(P-P_a)+\rho u^2\frac{\sin(\phi-\theta)\cos\theta}{\sin\phi}\Big]y\\
&\qquad-u\frac{\cos(\theta-\mu)}{\cos\mu}\frac{\rho u\sin(\phi-\theta)}{\sin\phi}y-y\rho u^2\sin^2\theta\tan\mu\cot\phi=0
\end{aligned}
\tag{B.42}
$$

Dividing by $\rho u^2 y$ will give

$$
\begin{aligned}
&\frac{P-P_a}{\rho u^2}+\frac{\sin\mu\cos\theta}{\sin(\theta+\mu)}-\frac{\cos(\theta-\mu)\sin\mu}{\cos\mu\sin(\theta+\mu)}-\frac{\sin^2\theta\sin\mu\cos(\theta+\mu)}{\cos\mu\sin(\theta+\mu)}=0\\
\Rightarrow&\frac{P-P_a}{\rho u^2}+\frac{\sin\mu\cos\theta\cos\mu-\cos(\theta-\mu)\sin\mu-\sin^2\theta\sin\mu\cos(\theta+\mu)}{\cos\mu\sin(\theta+\mu)}=0\\
\Rightarrow&\frac{P-P_a}{\rho u^2}+\frac{\tan\mu}{\sin(\theta+\mu)}\big(\cos\theta\cos\mu-\cos(\theta-\mu)-\sin^2\theta\cos(\theta+\mu)\big)=0
\end{aligned}
\tag{B.43}
$$

and then by $\frac{1}{2}\tan\mu$ results in

$$
\begin{aligned}
&\frac{P-P_a}{\frac{1}{2}\rho u^2}\cot\mu+2\Big(\frac{\cos\theta\cos\mu-(\cos\theta\cos\mu+\sin\theta\sin\mu)}{\sin(\theta+\mu)}\Big)\\
&\qquad-2\Big(\frac{\sin^2\theta(\cos\theta\cos\mu-\sin\theta\sin\mu)}{\sin(\theta+\mu)}\Big)=0
\end{aligned}
\tag{B.44}
$$

which may be simplified to

$$\frac{P-P_a}{\frac{1}{2}\rho u^2}\cot\mu + 2\frac{\sin\theta\cos\theta}{\sin(\theta+\mu)}\left(\frac{-\sin\theta}{\cos\theta} - \sin\theta\cos\mu + \sin^2\theta\frac{\sin\mu}{\cos\theta}\right) = 0$$

$$\Rightarrow \frac{P-P_a}{\frac{1}{2}\rho u^2}\cot\mu - \frac{\sin 2\theta}{\sin(\theta+\mu)}\left(\frac{\sin\mu}{\cos\theta}(1-\sin^2\theta) + \sin\theta\cos\mu\right) = 0 \qquad \text{(B.45)}$$

$$\Rightarrow \frac{P-P_a}{\frac{1}{2}\rho u^2}\cot\mu - \frac{\sin 2\theta}{\sin(\theta+\mu)}\left(\sin\mu\cos\theta + \sin\theta\cos\mu\right) = 0$$

and hence, at E

$$\frac{P-P_a}{\frac{1}{2}\rho u^2}\cot\mu = \sin 2\theta \qquad \text{(B.46)}$$

which is Eqn. 3.28.

The final task is to show that the control surface, already shown to lie physically coincident with the last LRC in the nozzle, obeys the compatibility equation of the LRC (i.e. derive Eqn. 3.29). Examining the equations that define the LaGrangian Multipliers λ_2 and λ_3 (Eqns. B.34 and B.41), it is obvious that the LaGrangian multipliers are functions of M, y and θ. However, along the LRC DE, both M and θ will be functions of y only. Hence differentiating with respect to y will give ordinary differentials, more specifically

$$\frac{d(-\lambda_2)}{dy} = \frac{\partial(-\lambda_2)}{\partial\theta}\frac{d\theta}{dy} + \frac{\partial(-\lambda_2)}{\partial M}\frac{dM}{dy} \qquad \text{(B.47)}$$

$$\frac{d(-\lambda_3)}{dy} = \frac{\partial(-\lambda_3)}{\partial y} + \frac{d\theta}{dy} + \frac{\partial(-\lambda_3)}{\partial M}\frac{dM}{dy} \qquad \text{(B.48)}$$

It has already been established that along the control surface, the LaGrangian multipliers are constants, and hence both Eqns. B.47 and B.48 are zero. This means that

$$-u\frac{\sin(\theta-\mu)}{\cos\mu}\frac{d\theta}{dy} + \frac{\partial}{\partial M}\left(u\frac{\cos(\theta-\mu)}{\cos\mu}\right)\frac{dM}{dy} = 0 \qquad \text{(B.49)}$$

$$\rho u^2\sin^2\theta\tan\mu + 2\sin\theta\cos\theta y\rho u^2\tan\mu\frac{d\theta}{dy} + \frac{\partial}{\partial M}(y\rho u^2\sin^2\theta\tan\mu)\frac{dM}{dy} = 0 \qquad \text{(B.50)}$$

Now

$$u\frac{\cos(\theta-\mu)}{\cos\mu} = u\left(\frac{\cos\theta\cos\mu+\sin\theta\sin\mu}{\cos\mu}\right) = u(\cos\theta+\sin\theta\tan\mu) \qquad \text{(B.51)}$$

Substituting this into Eqn. B.49 and multiplying by $-\rho uy\sin\theta$ produces

$$\rho u^2 y\sin\theta\frac{\sin(\theta-\mu)}{\cos\mu}\frac{d\theta}{dy} - \rho uy\sin\theta\frac{\partial}{\partial M}\left(u(\cos\theta+\sin\theta\tan\mu)\right)\frac{dM}{dy} = 0 \qquad \text{(B.52)}$$

Summing Eqn. B.50 and Eqn.B.52 then gives

$$\rho u^2\sin^2\theta\tan\mu + y\rho u^2\sin\theta\left(\frac{\sin(\theta-\mu)}{\cos\mu} + 2\cos\theta\tan\mu\right)\frac{d\theta}{dy}$$
$$+\left(\frac{\partial}{\partial M}(y\rho u^2\sin^2\theta\tan\mu) - \rho uy\sin\theta\left((\cos\theta\right.\right.$$
$$\left.\left.+\sin\theta\tan\mu)\frac{\partial u}{\partial M} + u\sin\theta\frac{\partial\tan\mu}{\partial M}\right)\right)\frac{dM}{dy} = 0 \qquad \text{(B.53)}$$

Expanding the coefficient of $\frac{dM}{dy}$

$$\rho u^2 \sin^2\theta \tan\mu + y\rho u^2 \sin\theta \Big(\frac{\sin\theta\cos\mu - \cos\theta\sin\mu + 2\cos\theta\sin\mu}{\cos\mu}\Big)\frac{d\theta}{dy}$$
$$+ \Big[u^2 y \sin^2\theta \tan\mu \frac{\partial P}{\partial M} + 2\rho u y \sin^2\theta \tan\mu \frac{\partial u}{\partial M} + \rho u^2 y \sin^2\theta \frac{\partial \tan\mu}{\partial M}$$
$$- \rho u y \sin\theta(\cos\theta + \sin\theta\tan\mu)\frac{\partial u}{\partial M} - \rho u^2 y \sin^2\theta \frac{\partial \tan\mu}{\partial M}\Big]\frac{dM}{dy} = 0 \quad \text{(B.54)}$$

Cancelling the derivatives of $\tan\mu$, and dividing by $\rho u^2 y \sin\theta \frac{\tan\mu}{\sin\mu}$ reduces this to

$$\frac{\sin\theta\sin\mu}{y} + \sin(\theta+\mu)\frac{d\theta}{dy} + \Big(\frac{\sin\theta\sin\mu}{\rho}\frac{\partial\rho}{\partial M} + \frac{2\sin\mu\sin\theta}{u}\frac{\partial u}{\partial M}$$
$$- \frac{\sin\mu}{u}\Big(\frac{\cos\theta}{\tan\mu} + \sin\theta\Big)\frac{\partial u}{\partial M}\Big)\frac{dM}{dy} = 0 \quad \text{(B.55)}$$

As

$$\begin{aligned}\frac{1}{u}\frac{\partial u}{\partial M} &= \frac{1}{Ma}\frac{\partial Ma}{\partial M} \\ &= \frac{1}{Ma}\Big(\sqrt{\frac{\gamma RT}{1+\frac{\gamma-1}{2}M^2}} - \frac{\gamma-1}{2}M^2\frac{1}{1+\frac{\gamma-1}{2}M^2}\sqrt{\frac{\gamma RT}{1+\frac{\gamma-1}{2}M^2}}\Big) \\ &= \frac{1}{M}\Big(\frac{1+\frac{\gamma-1}{2}M^2 - \frac{\gamma-1}{2}M^2}{1+\frac{\gamma-1}{2}}\Big) \\ &= \frac{1}{M\big(1+\frac{\gamma-1}{2}M^2\big)}\end{aligned} \quad \text{(B.56)}$$

and similarly it may be shown that

$$\frac{1}{\rho}\frac{\partial\rho}{\partial M} = \frac{-M}{1+\frac{\gamma-1}{2}M^2} \quad \text{(B.57)}$$

Eqn. B.55 may be expressed as

$$\frac{\sin\theta\sin\mu}{y} + \sin(\theta+\mu)\frac{d\theta}{dy} - \Big(\frac{M\sin\theta\sin\mu}{1+\frac{\gamma-1}{2}M^2} +$$
$$\Big(\frac{\cos\theta\cos\mu}{\sin\mu} + \sin\theta\Big)\frac{\sin\mu}{M(1+\frac{\gamma-1}{2}M^2)}\Big)\frac{dM}{dy} = 0 \quad \text{(B.58)}$$

which reduces to

$$\begin{aligned}&\frac{\sin\theta\sin\mu}{y} + \sin(\theta+\mu)\frac{d\theta}{dy} - \Big(\frac{M^2\sin\theta\sin\mu + \cos\theta\cos\mu - \sin\theta\sin\mu}{M(1+\frac{\gamma-1}{2}M^2)}\Big)\frac{dM}{dy} = 0 \\ \Rightarrow &\frac{\sin\theta\sin\mu}{y} + \sin(\theta+\mu)\frac{d\theta}{dy} - \Big(\frac{(M^2-1)\sin\theta\sin\mu + \cos\theta\cos\mu}{M(1+\frac{\gamma-1}{2}M^2)}\Big)\frac{dM}{dy} = 0\end{aligned} \quad \text{(B.59)}$$

As

$$\tan\mu = \frac{1}{\sqrt{M^2-1}} \quad \text{(B.60)}$$

this may be written

$$(M^2-1)\sin\theta\sin\mu = \sqrt{M^2-1}\frac{\cos\mu}{\sin\mu}\sin\theta\sin\mu = \sqrt{M^2-1}\cos\mu\sin\theta \tag{B.61}$$

Further, as

$$\cos\mu = \frac{\sqrt{M^2-1}}{M} \tag{B.62}$$

and

$$\sin\mu = \frac{1}{M} \tag{B.63}$$

we may write

$$\cos\theta\cos\mu = \cos\theta\frac{\sqrt{M^2-1}}{M} = \sqrt{M^2-1}\frac{1}{M}\cos\theta = \sqrt{M^2-1}\cos\theta\sin\mu \tag{B.64}$$

And substituting this into Eqn. B.61

$$\frac{\sin\theta\sin\mu}{y} + \sin(\theta-\mu)\frac{d\theta}{dy} - \left(\frac{\sqrt{M^2-1}(\cos\mu\sin\theta+\cos\theta\sin\mu)}{M(1+\frac{\gamma-1}{2}M^2)}\right)\frac{dM}{dy} = 0 \tag{B.65}$$

Finally, dividing by $\sin(\theta+\mu)$ and rearranging produces

$$\frac{d\theta}{dy} - \frac{\sqrt{M^2-1}}{M(1+\frac{\gamma-1}{2}M^2)}\frac{dM}{dy} + \frac{\sin\theta\sin\mu}{y\sin(\theta+\mu)} = 0 \tag{B.66}$$

which is the compatibility equation for an LRC in axisymmetric, irrotational flow, and of course identical to Eqn. 3.29.

Appendix C

Derivation of the Axisymmetric Rotational Method of Characteristics

In a portion of the flow bounded by streamlines, of thickness Δn, the axisymmetric continuity equation may be expressed as

$$\rho \underline{V} \Delta n 2\pi y = const \tag{C.1}$$

where y is the radial coordinate. If Δs lies in the flow direction

$$\rho \underline{V} \Delta n 2\pi y = (\rho \underline{V} + \frac{\partial \rho \underline{V}}{\partial s}\Delta s)(\Delta n + \frac{\partial \Delta n}{\partial s}\Delta s)2\pi(y + \frac{\partial y}{\partial s}\Delta s) \tag{C.2}$$

Expanding, and allowing $\Delta s \rightarrow 0$,

$$\begin{aligned} \rho \underline{V} \Delta n 2\pi y &= (\rho \underline{V} \Delta n + \rho \underline{V} \frac{\partial n}{\partial s}\Delta s + \frac{\partial \rho \underline{V}}{\partial s}\Delta s \Delta n)2\pi(y + \frac{\partial y}{\partial s}\Delta s) \\ \Rightarrow \rho \underline{V} \Delta n y &= \rho \underline{V} \Delta n y + \rho \underline{V} \Delta n \frac{\partial y}{\partial s}\Delta s + \rho \underline{V} y \frac{\partial \Delta n}{\partial s}\Delta s + \frac{\partial \rho \underline{V}}{\partial s}\Delta s \Delta n y \\ \Rightarrow 0 &= \rho \underline{V} \Delta n y \Delta s (\frac{1}{y}\frac{\partial y}{\partial s} + \frac{1}{\Delta n}\frac{\partial \Delta n}{\partial s} + \frac{1}{\underline{V}}\frac{\partial \underline{V}}{\partial s} + \frac{1}{\rho}\frac{\partial \rho}{\partial s}) \end{aligned} \tag{C.3}$$

As

$$\frac{\partial y}{\partial s} = \sin\theta \tag{C.4}$$

and

$$\frac{\partial(\Delta n)}{\partial s} = \Delta n \frac{\partial \theta}{\partial n} \tag{C.5}$$

Eqn. C.3 becomes

$$\frac{\sin\theta}{y} + \frac{\partial \theta}{\partial n} + \frac{1}{\underline{V}}\frac{\partial \underline{V}}{\partial s} + \frac{1}{\rho}\frac{\partial \rho}{\partial s} = 0 \tag{C.6}$$

For isentropic flow, the s momentum equation may be written as

$$\frac{1}{\rho}\frac{\partial \rho}{\partial s} = -\frac{\underline{V}}{a^2}\frac{\partial \underline{V}}{\partial s} \tag{C.7}$$

substituting this into Eqn. C.6 gives

$$\frac{\sin\theta}{y} + \frac{\partial \theta}{\partial n} + \frac{1}{\underline{V}}\frac{\partial \underline{V}}{\partial s} - \frac{\underline{V}}{a^2}\frac{\partial \underline{V}}{\partial s} = 0 \tag{C.8}$$

which reduces to

$$\frac{\sin\theta}{y} = (M^2 - 1)\frac{1}{\underline{V}}\frac{\partial \underline{V}}{\partial s} - \frac{\partial \theta}{\partial n} \tag{C.9}$$

Now,

$$\tan\mu = \frac{1}{\sqrt{M^2 - 1}} \tag{C.10}$$

so, multiplying through by $\tan\mu$ gives

$$\frac{\sin\theta}{y}\tan\mu = \cot\mu\frac{1}{\underline{V}}\frac{\partial \underline{V}}{\partial s} - \frac{\partial \theta}{\partial n}\tan\mu \tag{C.11}$$

Entropy is assumed constant along a streamline, but may vary from streamline to streamline. The enthalpy equation may be expressed as

$$dh = Td\tilde{s} + \frac{dp}{\rho} \tag{C.12}$$

and as n lies along the flow direction, the n momentum equation is

$$\frac{\partial p}{\partial n} = -\rho\underline{V}^2\frac{\partial \theta}{\partial s} \tag{C.13}$$

Substituting Eqn. C.13 into C.12 results in

$$\frac{dh}{dn} - T\frac{d\tilde{s}}{dn} = -\underline{V}^2\frac{\partial \theta}{\partial s} \tag{C.14}$$

The adiabatic energy equation may be written as

$$h_0 = h + \frac{\underline{V}^2}{2} \tag{C.15}$$

and by differentiating with respect to n we find

$$\frac{dh}{dn} = -\underline{V}\frac{d\underline{V}}{dn} \tag{C.16}$$

Substituting this into Eqn. C.14, and rearranging gives

$$\frac{1}{\underline{V}}\frac{\partial \underline{V}}{\partial n} - \frac{\partial \theta}{\partial s} = -\frac{T}{\underline{V}^2}\frac{d\tilde{s}}{dn} \tag{C.17}$$

Now,

$$\nu = \int_{M=1}^{M} (M^2 - 1)^{\frac{1}{2}} \frac{d\underline{V}}{\underline{V}} \tag{C.18}$$

and hence

$$\frac{\partial \nu}{\partial s} = \frac{\partial \nu}{\partial \underline{V}} \frac{\partial \underline{V}}{\partial s} = \cot \mu \frac{1}{\underline{V}} \frac{\partial \underline{V}}{\partial s} \tag{C.19}$$

Substituting into Eqns. C.11 and C.17 produces

$$\frac{\sin \theta}{y} \tan \mu = \frac{\partial \nu}{\partial s} - \frac{\partial \theta}{\partial n} \tan \mu \tag{C.20}$$

and

$$\frac{\partial \nu}{\partial n} \tan \mu - \frac{\partial \theta}{\partial s} = -\frac{T}{\underline{V}^2} \frac{\partial \tilde{s}}{\partial n} \tag{C.21}$$

Adding these gives

$$\frac{\partial(\nu - \theta)}{\partial s} + \tan \mu \frac{\partial(\nu - \theta)}{\partial n} = \tan \mu \frac{\sin \theta}{y} - \frac{T}{\underline{V}^2} \frac{d\tilde{s}}{dn} \tag{C.22}$$

and subtracting gives

$$\frac{\partial(\nu + \theta)}{\partial s} - \tan \mu \frac{\partial(\nu + \theta)}{\partial n} = \tan \mu \frac{\sin \theta}{y} + \frac{T}{\underline{V}^2} \frac{d\tilde{s}}{dn} \tag{C.23}$$

It can be shown [29] that for any function F, the characteristics equations may be written as

$$\frac{\partial F}{\partial s} + \tan \mu \frac{\partial F}{\partial n} = \frac{\partial F}{\partial \eta} \sec \mu \tag{C.24}$$

and

$$\frac{\partial F}{\partial s} - \tan \mu \frac{\partial F}{\partial n} = \frac{\partial F}{\partial \xi} \sec \mu \tag{C.25}$$

By comparing the above four equations, it is easy to see that

$$\frac{\partial(\nu - \theta)}{\partial \eta} = \sin \mu \frac{\sin \theta}{y} - \cos \mu \frac{T}{\underline{V}^2} \frac{d\tilde{s}}{dn} \tag{C.26}$$

and

$$\frac{\partial(\nu + \theta)}{\partial \xi} = \sin \mu \frac{\sin \theta}{y} + \cos \mu \frac{T}{\underline{V}^2} \frac{d\tilde{s}}{dn} \tag{C.27}$$

where η and ξ are the directions of the left and right running characteristics respectively. Assuming that along the characteristics, the partial derivatives may be considered to be ordinary allows integration of these equations, resulting in

$$(\nu_3 - \theta_3) - (\nu_2 - \theta_2) = \int_2^3 \sin \mu \frac{\sin \theta}{y} d\eta - \cot \mu \frac{T}{\underline{V}^2} (\tilde{s}_3 - \tilde{s}_2) \tag{C.28}$$

along a LRC from point 2 to 3, and

$$(\nu_3 + \theta_3) - (\nu_1 + \theta_1) = \int_1^3 \sin\mu \frac{\sin\theta}{y} d\xi - \cot\mu \frac{T}{\underline{V}^2}(\tilde{s}_3 - \tilde{s}_1) \tag{C.29}$$

on a RRC from point 1 to 3. Now,

$$\frac{T}{\underline{V}^2} = \frac{a^2}{\gamma R \underline{V}^2} = \frac{1}{\gamma R M^2} \tag{C.30}$$

but

$$\frac{1}{M} = \sin\mu \tag{C.31}$$

so

$$\cot\mu \frac{T}{\underline{V}^2} = \frac{\cos\mu \sin\mu}{\gamma R} \tag{C.32}$$

hence we can rewrite the above equations as

$$(\nu_3 - \theta_3) - (\nu_2 - \theta_2) = \tilde{c}_{23}\Delta\eta_{23} - \tilde{k}_{23}\left(\frac{\tilde{s}_3}{R} - \frac{\tilde{s}_2}{R}\right) \tag{C.33}$$

and

$$(\nu_3 + \theta_3) - (\nu_1 - \theta_1) = \tilde{c}_{13}\Delta\xi_{13} - \tilde{k}_{13}\left(\frac{\tilde{s}_3}{R} - \frac{\tilde{s}_1}{R}\right) \tag{C.34}$$

where $\tilde{c}$ denotes the average of the integrand, i.e.

$$c = \sin\mu \frac{\sin\theta}{y} \tag{C.35}$$

and $\tilde{k}$ is the average of

$$k = \frac{\sin\mu\cos\mu}{\gamma} \tag{C.36}$$

References

[1] C.E. Franklin. The early rockets of william congreve in british service. *JBIS*, 54:300–310, 2001.

[2] N. Hill and D. Wright. Derivatives of the black night technology. *JBIS*, 53:307–318, 2000.

[3] G.V.R. Rao. Exhaust nozzle contour for optimum thrust. *Journal of Jet Propulsion*, 28(6):377–382, Jun 1958.

[4] G.V.R. Rao. Nozzle contours. *Journal of Propulsion*, 20:69–75, 1960.

[5] G. P. Sutton. *Rocket Propulsion Elements*. John Wiley and Sons. Inc., sixth edition, 1992.

[6] G.V.R. Rao. Analysis of a new concept rocket nozzle. *Journal of Liquid Rockets and Propellants*, 2:669–682, 1960.

[7] M. Arens and E. Spiegler. Shock-induced boundary layer separation in overexpanded conical exhaust nozzles. *AIAA Journal*, 1(3):578–581, Mar 1963.

[8] G. Hagemann H. Immich T.V. Nguyen and G.E. Dumnov. Advanced rocket nozzles. *Journal of Propulsion and Power*, 14(5):620–634, sept. 1998.

[9] E. Mayer. Analysis of convective heat transfer in rocket nozzles. *ARS Journal*, pages 911–916, Dec 1960.

[10] R. Beichel. Nozzle concepts for single stage shuttles. *Astronautics and Aeronautics*, pages 16–27, Jun 1975.

[11] T.J. Mueller and W.P. Sule. Annular truncated plug nozzle flowfield and base pressure characteristics. *Journal of Spacecraft*, 10(11):689–695, Nov 1973.

[12] R.A. Wasko. Performance of annular plug and expansion-deflection nozzles including external flow effects at transonic mach numbers. Technical Report NASA-TN-D-4462, NASA, Apr 1968.

[13] T. Rommel G. Hagemann C.A. Schely G. Krulle and D. Manski. Plug nozzle flowfield analysis. *Journal of Propulsion and Power*, 13(5):629–634, September 1997.

[14] T.J. Mueller C.R. Hall Jr. and P.J. Roache. Influence of initial flow direction on the turbulent base pressure in supersonic axisymmetric flow. *Journal of Spacecraft*, 7(12):1484–1487, Dec 1970.

[15] F. Nasuti and M. Onofri. Theoretical analysis and engineering modelling of flowfields in clustered module plug nozzles. *Journal of Propulsion and Power*, 15(4):544–551, Jul-Aug 1999.

[16] G.V.R. Rao. Recent developments in rocket nozzle configurations. *ARS Journal*, pages 1488–1494, Nov 1961.

[17] F. Nasuti and M. Onofri. Analysis of in flight behaviour of truncated plug nozzles. *Journal of Propulsion and Power*, 17(4):809–817, Jul-Aug 2001.

[18] N. I. Tillyayeva A. N. Kraiko and S. V. Baftalovskii. Optimal design of plug nozzles and their thrust determiniation at start. *Journal of Propulsion and Power*, 17(6):1347–1352, Nov-Dec 2001.

[19] A. Kumakawa and Y. Watanbe. A study of reusable launcher/demonstrator powered by aerospike engines. IAF paper IAF-99-V.4.05, Oct 1999.

[20] A. Pruess. An analytical approach for the flowfield analysis of overexpanded rocket nozzles. IAF paper IAF-00-W.2.08, Oct 2000.

[21] M. Frey and G. Hagemann. Critical assessement of dual-bell nozzles. *Journal of Propulsion and Power*, 15(1):137–143, Jan-Feb 1999.

[22] G. Manski, D. Hagemenn and H.D. Sassnick. Optimisation of dual-expander rocket engines in single-stage-to-orbit vehicles. IAF paper IAF-96-S.2.05, Oct 1996.

[23] R. Sauer. General characterisitcs of the flow through nozzles at near critical speeds. Technical Report TM1147, NACA, Sep 1944.

[24] C. Schorr. Constant chamber pressure throttling of an expansion-deflection nozzle. *Journal of Spacecraft*, 7(7):843–847, Jul 1970.

[25] T.J. Mueller. Determination of the turbulent base pressure in supersonic axisymmetric flow. *Journal of Spacecraft*, 5(1):101–107, Jan 1968.

[26] T.J. Mueller and C. R. Hall Jr. Separated flow region within a planar expansion-deflection nozzle. *Journal of Spacecraft*, 5(6):738–740, Jun 1968.

[27] T.J. Mueller and W.L. Oberkampf. Hydraulic analog for the expansion deflection nozzle. *AIAA Journal*, 5(6):1200–1202, Jun 1967.

[28] T.J. Mueller C.R. Hall Jr. and W.P. Sule. Supersonic wake flow visualisation. *AIAA Journal*, 7(11):2151–2153, Nov 1969.

[29] T.J. Mueller W.P. Sule and C.R. Hall Jr. Characteristics of separated flow regions within altitude compensating nozzles. Technical Report NASA-CR-116875, NASA, Jan 1971.

[30] H.H. Korst. A theory for base pressures in transonic and supersonic flow. *Journal of Applied Mechanics*, 23(4):593–599, Dec 1956.

[31] M. Tanner. Two different theoretical approaches to the base pressure problem in two-dimensional flow. Technical report, DFVLR, Germany, May 1978.

[32] I.M. Hall. Transonic flow in two-dimensional and axially symmetric nozzles. *Quarterly Journal of Mechanics and Applied Mechanics*, XV(4):487–508, 1962.

[33] J.R. Kliegel and J.N. Levine. Transonic flow in small throat radius of curvature nozzles. *AIAA Journal*, 7(7):1375–1378, Jul 1969.

[34] J.N Levine and D.E. Coates. Transonic flow in a converging - diverging nozzle. Technical Report CR111104, NASA, Sept 1970.

[35] J.C. Dutton and A.L. Addy. Transonic Flow in the Throat Region of Axisymmetric Nozzles. *AIAA Journal*, 19(6):801–804, Jun 1981.

[36] D.F. Hopkins and D.E. Hill. Effect of small radius of curvature on transonic flow in axisymmetric nozzles. *AIAA Journal*, 4(8):1337–1343, Aug 1966.

[37] Ron-Ho Ni. A multiple-grid scheme for solving the euler equations. *AIAA Journal*, 20(11):1565–1571, Nov 1982.

[38] R.W. MacCormack. The effects of viscosity in hypervelocity impact cratering. AIAA Paper 60-345, May 1969.

[39] A. Jameson. Transonic aerofoil calculations using the euler equations. In P.L. Roe, editor, *Numerical Methods in Aeronautical Fluid Dynamics*, pages 289–309, 24/28 Oval Road London, 1982. The Institute of Mathematics and its Applications, Academic Press.

[40] Gaitonde A.L. A dual-time method for the solution of the unsteady euler equations. University of Bristol, Report 496, Jun 1994.

[41] W.H. Press S.A. Teukolsky W.T Vetterling and B.P. Flannery. *Numerical Recipes in Fortran 77*. Cambridge University Press, The Pitt Building, Trumpigton street, Cambridge, 1986.

[42] C.B. Allen. Multigrid convergence for an upwind euler method for hovering rotor flows. *Aeronautical Journal*, 105(1051):517–524, 2001.

[43] Cuffel R.F. Back L.H. and P.F. Massier. Transonic flowfield in a supersonic nozzle with small throat radius of curvature. *AIAA Journal*, 7(7):1364–1366, Jul 1969.

[44] J. D. Anderson Jr. *Fundamentals of Aerodynamics*. McGraw-Hill Book Co, Singapore, 1985.

[45] J. D. Anderson Jr. *Modern Compressible Flow*. McGraw-Hill Book Co, Singapore, 1985.

[46] H. M. Darwell and H. Badham. Shock formation in conical nozzles. *AIAA Journal*, 1(8):1932–1934, Aug 1963.

[47] J.C. Dutton and A.L. Addy. Transonic flow in the throat region of annular supersonic nozzles. *AIAA Journal*, 1982.

[48] B.F. Carroll and J.C. Dutton. Transonic flow in the throat region of radial or nearly radial supersonic nozzles. *AIAA Journal*, 23(7):1127–1129, 23 1985.

[49] D.F. Hopkins and D.E. Hill. Transonic flow in unconventional nozzles. *AIAA Journal*, 6(5):838–842, May 1968.

[50] D.R. Chapman. An analysis of base pressure at supersonic velocities and comparison with experiments. Technical Report 1051, NACA, 1951.

[51] J.H. Fox. Simple recompression model for the korst base pressure theory. *AIAA Journal*, 17(3):312–313, Mar 1979.

[52] R.S. Channapragada. Compressible jet spread parameter for mixing zone analyses. *AIAA Journal*, 1(9):2188–2189, Sep 1963.

[53] M. Tanner. Steady base flows. *Progress in Aerospace Sciences*, 21:81–157, 1984.

[54] C. Berner. Supersonic base flow investigation over axisymmetric afterbodies. Technical report, French-German Research Institute (ISL), 68310 Saint-Louis Cedex, France, August 1993.

[55] S. Y. Yang. Adaptive analysis of the inviscid supersonic flow over a backward-facing step. *Journal of Propulsion and Power*, 17(4):938–940, 2001.

[56] M. A. Badrinarayanan. An experimental investigation of base flows at supersonic speeds. *Journal of the Royal Aeronautical Society*, 65:475–481, Feb 1970.

[57] W.L. Hwang, C. Chow and D. Moslemian. Base pressure of a sudden expansion from a conical converging nozzle. *AIAA Journal*, 31(4):657–661, Apr 1993.

[58] W.L. Chow. Base pressure of a projectile within the transonic flight regime. *AIAA*, 3:388–395, March 1985.

[59] A.D. Young. *Boundary Layers*. BSP Professional Books, Osney Mead, Oxford OX2 OEL, 1989.

[60] M Tanner. Base pressure in supersonic flow: Further thoughts about a theory. *AIAA*, 30(2):565–565, Feb 1992.

[61] F.R. Hama. Experimental studies on the lip shock. *AIAA Journal*, 6(2):212–219, Feb 1968.

[62] F. C. Magi and S.L. Gai. Supersonic base pressure and lip shock. *AIAA*, 26(3):370–372, March 1988.

[63] P. Fortescue and J. Stark, editors. *Spacecraft Systems Engineering*. John Wiley and Sons Ltd, Baffins Lane, Chichester, West Sussex, England, 1995.

[64] Boeing. Rs-68 propulsion system, 2001. Promosional Literature for the Delta IV vehicle.

[65] W. Buschulte and W. Hartung. The influence of the boundary layer on the thrust especially with respect to small rocket engines and high expansion ratios. In *ICAF Congress*, number 10791 in A66, pages 55–77. IAF, 1965.

[66] D. Allman. Design of maximum thrust nozzle contours by direct optimisation methods. *AIAA*, page 750, June 1981.